STUDY OF THE MECHANICAL PROPERTIES OF Mg-8.5wt%Al BY IN-SITU NEUTRON DIFFRACTION

By

MICHAEL GHARGHOURI, B.A.Sc.

A Thesis
Submitted to the School of Graduate Studies
in Partial Fulfilment of the Requirements
for the Degree
Doctor of Philosophy

McMaster University

MECHANICAL PROPERTIES OF Mg - 8.5 wt% Al

DOCTOR OF PHILOSOPHY (1997)
Materials Science and Engineering

McMaster University
Hamilton, Ontario

TITLE: Study of the Mechanical Properties of Mg-8.5wt%Al by In-situ Neutron Diffraction.

AUTHOR: Michael Gharghouri, B.A.Sc. (University of Toronto)

SUPERVISORS: Professor J.D. Embury
Professor G.C. Weatherly

NUMBER OF PAGES: xv, 179

ABSTRACT

The mechanical behaviour in uniaxial tension and compression of extruded and aged Mg-8.5wt%Al was studied. In-situ neutron diffraction was used to follow the elastic lattice strains under load in the matrix and the precipitates. The internal stresses determined from these measurements are highest in grains unfavourably oriented for both basal slip and $\{10\bar{1}2\}$ twinning, lowest in grains oriented favourably for both, and in between for grains oriented favourably for $\{10\bar{1}2\}$ twinning only. Most variations in scattered peak intensity are due to the lattice reorientation produced by $\{10\bar{1}2\}$ twinning. A critical resolved shear stress criterion is shown to apply for twinning. Intensity variations which cannot be explained by $\{10\bar{1}2\}$ twinning occurred in some grains during tensile loading. They are likely due to $\{10\bar{1}1\}$ twinning which produces **c**-axis compression, unlike $\{10\bar{1}2\}$ twinning.

Transmission electron microscopy revealed the presence of **c**- and non-basal **a**-dislocations in the undeformed alloy. Basal slip is the most common slip system, though non-basal **a**-slip also occurs. Only $\{10\bar{1}2\}$ twinning was observed by TEM. Twins often traversed grains completely, despite the presence of the precipitates. Schmid factor considerations show that pure magnesium yields first by basal slip. The early portion of the stress-strain curve should thus be considered a region of rapid strain hardening due to basal dislocation pile-ups at grain boundaries. In compression $\{10\bar{1}2\}$ twinning can also occur at very low applied stress. Strengthening in the alloy before yield is explained using a Brown and Clarke mean-stress hardening model. Beyond yield, relaxation mechanisms reduce the mean stress contribution essentially to zero in tension.

The mechanical and physical properties of the intermetallic were obtained from experiments on a single crystal. Property correlations have been used to estimate the fracture toughness and yield stress, assuming its behaviour is similar to that of a ceramic.

ACKNOWLEDGEMENTS

I am indebted to more people than I can count. My only concern is that I not forget anyone. I am of course indebted to my supervisors, Drs. Embury and Weatherly for their unflagging support and confidence, and for their monumental patience. I can't say enough about them.

Prof. Bruce Gaulin kindly agreed to be part of my supervisory committee. His comments have been very helpful and have contributed significantly to this thesis.

Thanks also to Dr. John Root of AECL Research for his kindness and help in performing the neutron diffraction experiments, and in understanding what they meant. He was always available, even at ungodly hours, and made my experience at AECL very enjoyable. Perry Clarke filled in when John wasn't around.

I would like to thank the people at Pechiney for supplying the material for this project, which they kindly prepared for me despite abandoning this line of research. This project was begun in Grenoble, France, under the guidance of Prof. Yves Bréchet and I thank him for a pleasant experience, and also for making certain that Pechiney processed enough material for me to finish my thesis!

Special thanks to Jim Garrett and Bruce Collier at IMR. They taught me a great deal about crystal growth, heat treatment, machining, temperature measurement, vacuum systems, silver-soldering, glass-working, as well as how to take verbal abuse. Special thanks also to Ed McCaffery. He can fix anything, whether it has a motor, hydraulic cylinder, or computer chips, and is always willing to do so.

Transmission electron microscopy is probably one of the things I am least suited for: I find it fascinating, but it kills me. Muriel Veron had the patience to answer all of my questions concerning the operation of the damn thing, and I am greatly indebted to her. Thanks also to Andy Duft and Teresa Castillo for helping to prepare my TEM foils. No small feat!

I must also thank Dr. N.D. Patel (Prof. Nicholson's group) for the single crystal elastic constant measurements.

The 204/206 graduate students in the Materials Department at McMaster have always been good company. They were a fun crowd to be with.

I have been blessed with parents who have always encouraged and helped me in every conceivable way. I can express my love for them, but is it possible to thank them enough?

Meeting my wife Rosaura is the best thing that has ever happened to me. With her I find myself living and enjoying life to the fullest. This thesis is dedicated to her.

TABLE OF CONTENTS

LIST OF FIGURES

LIST OF TABLES

1. INTRODUCTION

Magnesium is one of the 'light metals', a designation it shares with aluminium and titanium. These materials have relative densities of 1.7 (magnesium), 2.1 (aluminium), and 4.5 (titanium), compared with 7.9 and 8.9 for the older structural metals, iron and copper. The property of lightness makes these materials suitable for the transportation industry, for which the strength to weight ratio is of primary concern, particularly in engineering design when parameters such as stiffness or resistance to buckling are involved. The potential weight reduction which can be realised through the use of these materials can be illustrated by considering the weight of similar beams of different materials for equal values of stiffness. A steel beam weighing 10 kg will have the same stiffness as beams of equal width and length weighing 7 kg in titanium, 4.9 kg in aluminium, and 3.8 kg in magnesium.

Today, more than half the magnesium produced is used as alloying additions to aluminium and nodular cast iron, rather than as a base for structural materials, despite the availability of commercial structural alloys since approximately the First World War. In fact, considerable effort was expended on research into the development of structural magnesium alloys in the 50's and 60's, in the hope that the performance improvements obtained by precipitation strengthening in aluminium alloys could also be achieved in magnesium alloys. Unfortunately, though cast magnesium alloys are in fact comparable (and sometimes superior) in performance to cast aluminium alloys, this is not so of the wrought alloys, which has severely limited the use of magnesium as a base for structural materials. This failure in developing high performance magnesium alloys is due to the fact that the fine scale precipitation and Guinier-Preston zones necessary to yield high strength in general does not occur in magnesium alloys.

With the current drive towards ever lighter materials for the automobile and aerospace industries, there is a resurgence in interest in magnesium alloys. Current work on conventional alloys aims to find new alloying additions which can modify the scale of the precipitation obtained during heat treatment. In addition, magnesium alloys are being studied as matrix materials for metal matrix composites.

Magnesium is also a fascinating material from a fundamental point of view. It has a hexagonal-close-packed structure with a close to ideal c/a ratio. Young's modulus depends very weakly on crystallographic direction, as does the coefficient of thermal expansion. In addition, there is only one easily activated slip system and only one ubiquitously observed twinning mode which makes it an interesting material in which to study grain interactions and texture effects. Despite these severe limitations, magnesium polycrystals show considerable ductility, which raises questions as to how many deformation

modes, and how much slip on any given system, is really required for a metal to show some ductility. Pure single crystals have been used to study stage one work hardening because it is very easy to induce single slip.

The current study is concerned with the way in which second phase particles affect the mechanical properties of a binary magnesium-aluminium alloy. The particles are produced by a very long heat treatment which produces a coarse distribution. In-situ neutron diffraction is used to measure the internal stresses in the second phase and in the matrix during deformation, and optical and transmission electron microscopy provide information on the slip and twinning modes which contribute to deformation as well as on the way in which the particles interact with the various systems. A single crystal of the intermetallic prepared at McMaster University is used to study its mechanical and physical properties.

This report is organised as follows. A literature review is presented in Chapter Two. The basic crystallography of HCP metals is presented as well as a detailed consideration of how the various possible slip and twinning modes can contribute to deformation. A summary of the deformation modes observed in pure magnesium and its alloys is then presented, followed by a description of the precipitation observed in the binary alloy studied. The chapter concludes with a description of the neutron diffraction technique for the determination of internal stresses. A description of the experimental methods used in this study is presented in Chapter Three. Chapter Four contains all of the experimental results obtained. Stress-strain curves and in-situ neutron diffraction data are presented first, followed by observations by optical and transmission electron microscopy, followed by the results from experiments performed on the intermetallic single crystal. In Chapter Five a discussion of the results is presented. The stresses in various textural components of the magnesium matrix and in the second phase particles are calculated and a suitable activation criterion for twinning derived. A general semi-quantitative analysis of yielding is then presented. A simple continuum model is used to rationalise the effects of the second phase on the mechanical properties of the alloy, and some simple notions are used to explain twin-particle interactions observed by transmission electron microscopy. Finally, Ashby's property correlation tables are used to rationalise the properties of the intermetallic phase. Chapter Six contains a summary of the experimental observations, conclusions derived from the study, and suggestions for future work.

2. LITERATURE REVIEW

2.1 Introduction

In this project I have used transmission electron microscopy, conventional metallography, and in-situ neutron diffraction techniques to study the deformation behaviour of a two-phase polycrystalline magnesium-aluminium alloy under various strain paths. This review begins with a brief description of the crystallography of hexagonal-close-packed (HCP) metals, in which the important planes and directions are illustrated. This is followed by a discussion of the deformation of HCP metals in which elastic and plastic anisotropy, slip modes, and twinning are considered. Having addressed the basics of deformation in HCP metals, the available literature on the deformation of magnesium and magnesium alloy single and poly-crystals is discussed in detail.

Strain reversal experiments (Bauschinger tests) have been used as a method of determining the magnitude and directionality of internal stresses built up in the material during the course of deformation. It is thus instructive to review the literature pertaining to the Bauschinger Effect (BE).

Finally, the chapter concludes with a description of the type of information available and of the literature on neutron diffraction as this technique provides a great deal of the experimental data used in modelling the behaviour of the magnesium alloy under study.

2.2 Crystallography of HCP Metals

An excellent discussion of the crystallography of HCP metals is provided by Partridge, 1967. The primitive hexagonal unit cell has axes $\mathbf{a}_1$, $\mathbf{a}_2$, and $\mathbf{c}$ as shown in Figure 2.1 (heavy lines). The HCP structure has two atoms associated with each lattice point - one at (0,0,0), and the other at (2/3,1/3,1/2). The hexagonal symmetry is usually illustrated by means of the hexagonal prism shown in Figure 2.1 (solid lines) in which the ABAB stacking sequence of the basal planes is also illustrated. Important directions and planes are given in Figure 2.2. In order to avoid confusion, only 4-digit Miller-Bravais indices based on the axes $\mathbf{a}_1$, $\mathbf{a}_2$, $\mathbf{a}_3$, and $\mathbf{c}$ shown in Figure 2.1 will be used in this report when referring to planes and directions in the HCP structure.

When dealing with non-basal planes in the HCP structure it is important to realise that they include atoms in both A and B layers in (0002) planes (Figure 2.3). This is an important consideration when dealing with non-basal slip as the slip surface is in fact corrugated rather than planar. Note, however, that non-basal planes give rise to a single well defined Bragg reflection in diffraction experiments.

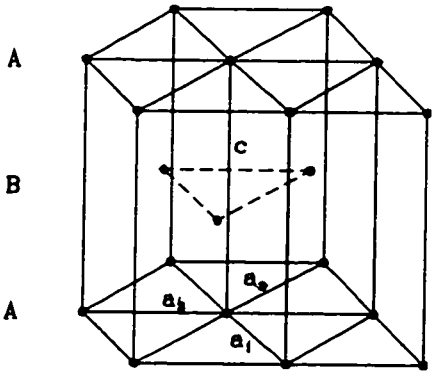

Figure 2.1: The hexagonal unit cell.

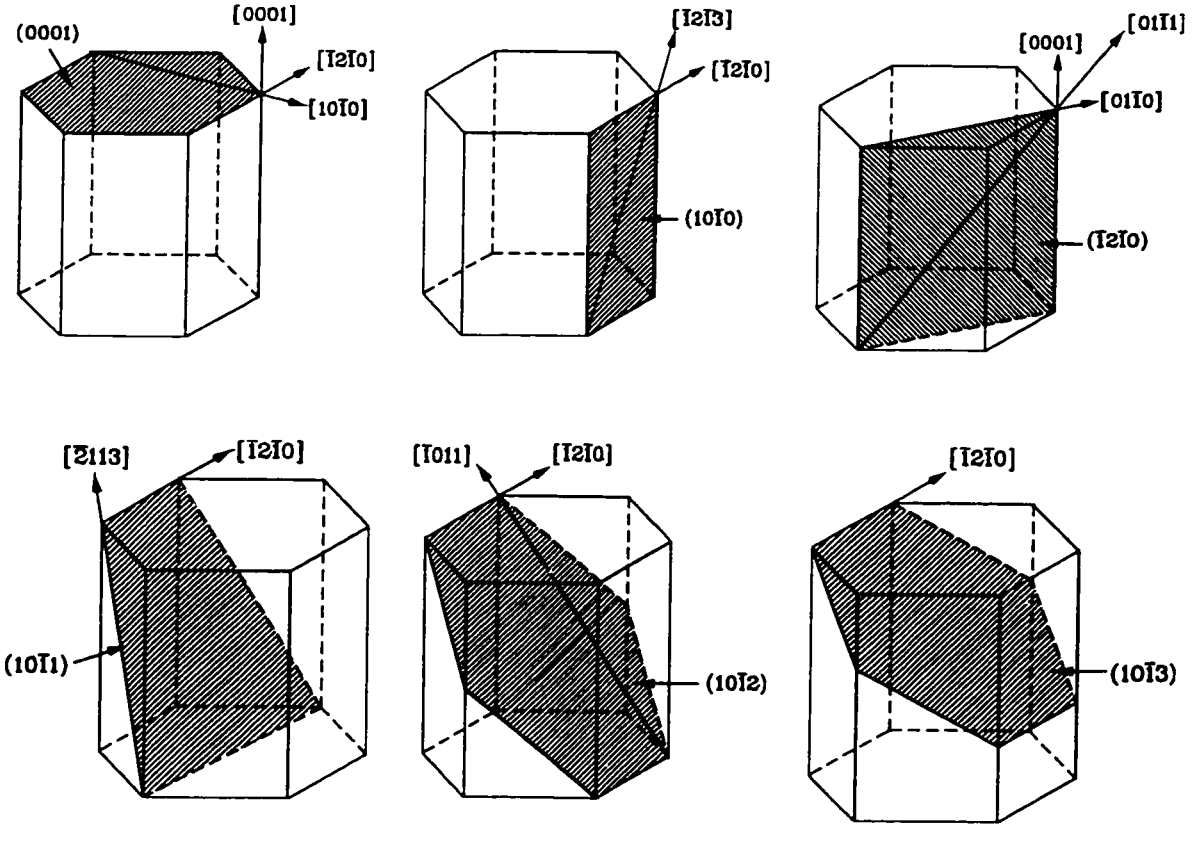

Figure 2.2: Important planes and directions in the hexagonal system.

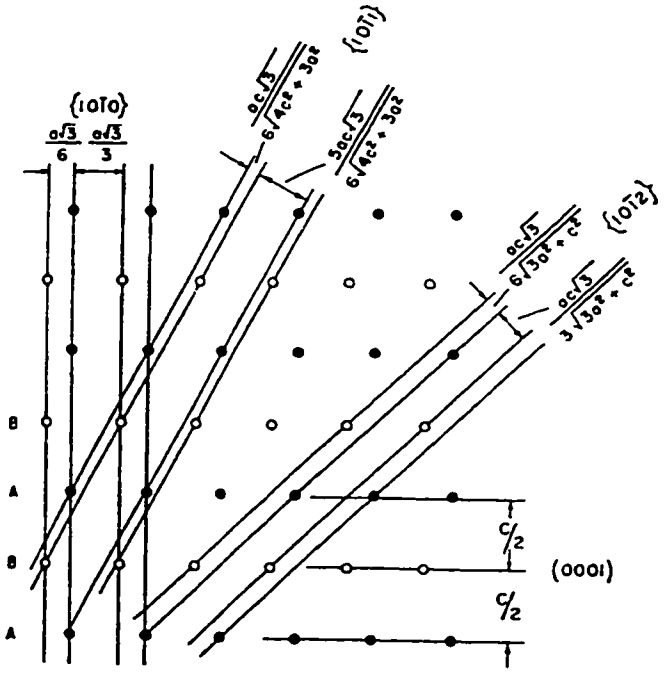

Projection of atoms in (1$\bar{2}$10), showing traces and interplanar spacings of (0001), (10$\bar{1}$2), (10$\bar{1}$1), and (10$\bar{1}$0) planes in magnesium.
● atoms in A layer; ○ atoms in B layer.

Figure 2.3: Diagram illustrating the corrugated nature of non-basal planes in the HCP structure (Partridge, 1967).

If the atoms are assumed to be hard spheres in contact with one another, then in the ideal close-packed structure the co-ordination number is twelve and the c/a ratio is $\sqrt{(8/3)} = 1.633$. None of the pure hexagonal metals exhibit this ideal c/a ratio, but cobalt and magnesium are quite close (Table 2.1). If c/a is greater than the ideal value, the $\{10\bar{1}0\}$ planes have the smallest spacing; each atom then has six nearest neighbours in the basal plane and three next-nearest neighbours above and below the basal plane at a slightly greater distance. If c/a is less than the ideal value, the (0002) planes have the smallest spacing; each atom then has three nearest neighbours above and below the basal plane at a slightly smaller distance than the next-nearest neighbours which are in the basal plane.

2.3 Deformation of HCP Metals

Having discussed the basic crystallography of HCP metals, it is useful to consider how it affects their elastic behaviour as well as the number and types of possible slip and twinning systems.

2.3.1 Elastic deformation

Due to the symmetry of the HCP lattice, five elastic constants are required to completely

characterise the elastic behaviour, as shown in Equation 2.1.

$$\begin{bmatrix}\sigma_1\\ \sigma_2\\ \sigma_3\\ \sigma_4\\ \sigma_5\\ \sigma_6\end{bmatrix}=\begin{bmatrix}c_{11} & c_{12} & c_{13} & 0 & 0 & 0\\ c_{12} & c_{11} & c_{13} & 0 & 0 & 0\\ c_{13} & c_{13} & c_{33} & 0 & 0 & 0\\ 0 & 0 & 0 & c_{44} & 0 & 0\\ 0 & 0 & 0 & 0 & c_{44} & 0\\ 0 & 0 & 0 & 0 & 0 & (c_{11}-c_{12})/2\end{bmatrix}\begin{bmatrix}\varepsilon_1\\ \varepsilon_2\\ \varepsilon_3\\ \varepsilon_4\\ \varepsilon_5\\ \varepsilon_6\end{bmatrix} \qquad (2.1)$$

Table 2.1: Crystallographic data for some HCP metals (Partridge, 1967).

Metal	a (Å)	c (Å)	c/a	Ratio of interplanar spacings $d_{\{10\bar{1}0\}}/d_{(0002)}$
Cd	2.972	5.605	1.8859	0.918
Zn	2.659	4.936	1.8563	0.933
IDEAL	-----	-----	1.6330	1.061
Co	2.502	4.061	1.6230	1.067
Mg	3.203	5.200	1.6230	1.067
Re	2.760	4.458	1.6150	1.072
Zr	3.231	5.147	1.5930	1.087
Ti	2.950	4.683	1.5873	1.091
Hf	3.194	5.051	1.5810	1.095
Be	2.281	3.576	1.5680	1.105

All HCP metals are elastically isotropic in the basal plane; however, the elastic properties parallel to the c-axis can vary considerably from those perpendicular to it, resulting in a pronounced elastic anisotropy. As a result of this, the way in which a particular grain deforms when a polycrystalline aggregate is strained may depend strongly on the orientation of the crystallographic axes of the grain with respect to the stress axes, and it is to be expected that the Young's modulus exhibited by a polycrystal will depend on the degree of preferred orientation in the material. The degree of elastic anisotropy can vary considerably from metal to metal as illustrated in Figure 2.4 which shows how the modulus of elasticity varies with crystallographic direction in magnesium and in zinc.

2.3.2 Dislocations in HCP metals

Burgers vectors in the HCP structure can be described using the bi-pyramid shown in Figure 2.5 (Berghezan et al., 1961) which is similar to the Thompson tetrahedron for FCC metals.

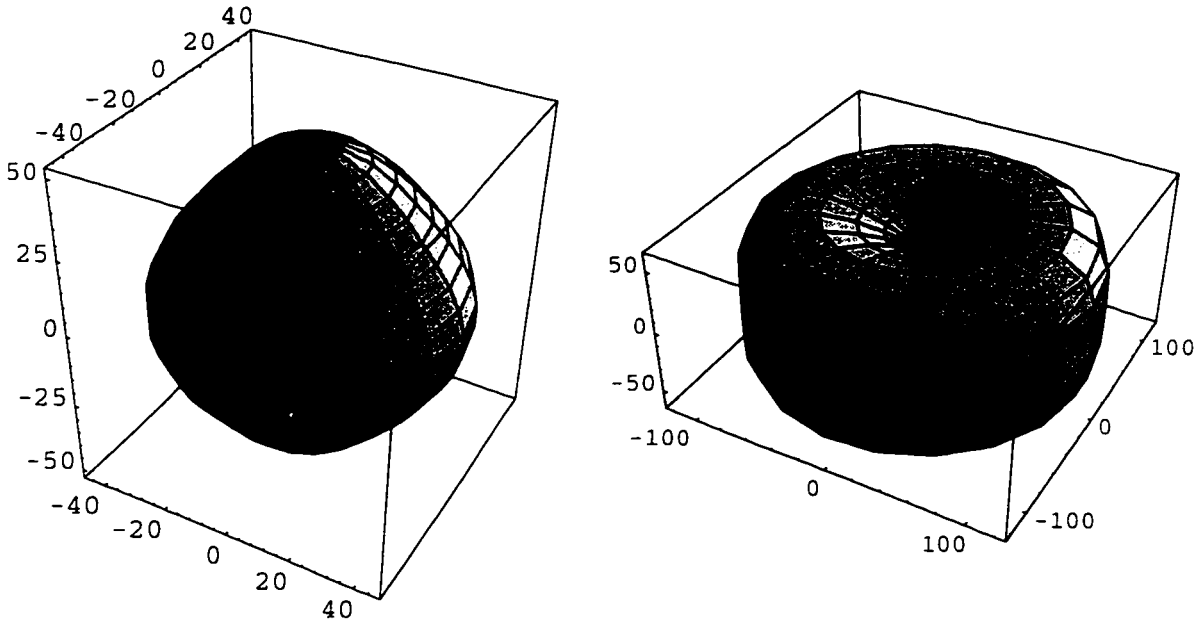

(a) (b)

Figure 2.4: Anisotropy of Young's modulus in (a) magnesium and (b) zinc (Schmid & Boas, 1950).

Table 2.2 lists the Miller-Bravais indices, lengths b, and energies (assumed proportional to b^2) of some of the possible Burgers vectors in the HCP lattice. Note that three glide directions are coplanar and are associated with the shortest Burgers vectors, **a**, lying in the close-packed directions in the basal plane. The other important Burgers vectors, **c** and **c+a**, do not lie in a close-packed direction.

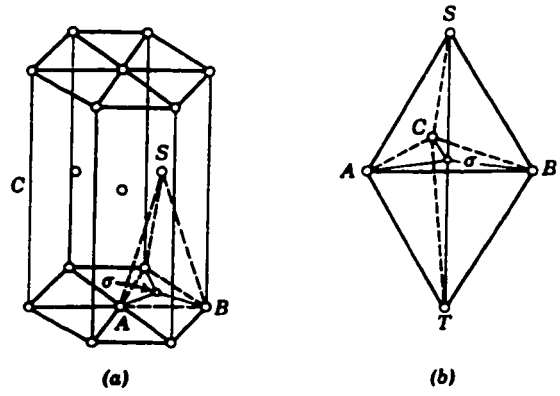

(a) (b)

Figure 2.5: Dislocation bi-pyramid construction for the HCP lattice (Berghezan et al., 1961).

Table 2.2: Dislocations in the HCP structure (Partridge, 1967).

Number	1	2	3	4	5	6
Bi-pyramid designation	AB (perfect)	TS (perfect)	ST+AB (perfect)	Aσ (partial)	σS (partial)	AS (partial)
b	$1/3\langle 11\bar{2}0\rangle$	[0001]	$1/3\langle 11\bar{2}3\rangle$	$1/3\langle 10\bar{1}0\rangle$	½[0001]	$1/6\langle \bar{2}203\rangle$
b	$\mathbf{a_1}, \mathbf{a_2}, \mathbf{a_3}$	**c**	**c + a**	$\mathbf{½(2a_1 + a_2)}$	**c/2**	**(4) + (5)**
b^2	a^2	c^2	(c^2+a^2)	$a^2/3$	$c^2/4$	$(a^2/3+c^2/4)$
Total #	3	1	6	3	2	6

Dislocations having **a**-type Burgers vectors can dissociate into two low energy Shockley partials of the type **A**σ surrounding a stacking fault which violates two next-nearest neighbours in the stacking sequence (Figure 2.6). The Burgers vector reaction is:

$$\begin{gathered}\mathbf{AB} \rightarrow \mathbf{A}\sigma + \sigma\mathbf{B} \\ \mathbf{1/3[11\bar{2}0]} \rightarrow \mathbf{1/3[10\bar{1}0]} + \mathbf{1/3[01\bar{1}0]} \\ a^2 \rightarrow a^2/3 + a^2/3\end{gathered} \tag{2.2}$$

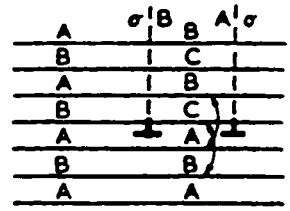

Figure 2.6: Stacking fault due to dislocation dissociation (Partridge, 1967).

The dissociated dislocation is restricted to slip in the basal plane but constriction of screw segments will enable cross-slip to occur on $\{10\bar{1}n\}$-type planes . Other dissociations can produce faults in $\{10\bar{1}0\}$, $\{11\bar{2}2\}$, and $\{11\bar{2}0\}$ planes as discussed by Partridge, 1967.

2.3.3 Slip systems in HCP metals

A slip system is defined by its Burgers vector and slip plane. In order for a crystal to undergo an arbitrary strain by slip, at least five independent shear systems are required to account for the five independent components of the general strain tensor if constancy of volume is assumed and diffusional processes are negligible. A set of shear systems is independent provided the operation of any one system produces a change in shape of the crystal which cannot be duplicated by any linear combination of shears produced by the remaining systems. The concept can be extended to polycrystals if it is assumed that the plastic deformation of a polycrystalline specimen can proceed without the formation of voids if and only if each grain can undergo a general constant-volume strain (see e.g. Groves & Kelly, 1963).

The six types of slip system which have been observed in hexagonal metals are listed in Table 2.3. Types 1 and 2, acting simultaneously, provide a total of four independent slip modes. The shape change provided by 1 and 2 acting together is equivalent to 3 acting alone. In addition, none of 1, 2, or 3 can produce strain parallel to the **c** direction since they all involve $<11\bar{2}0>$ slip directions which are normal to the **c** axis. Thus at least one of 4, 5, and 6 must operate if a general constant-volume strain is to be produced.

Poirier & Le Hazif, 1976 discuss the contribution of transmission electron microscopy to the study of slip systems in HCP metals. They point out that each HCP metal has a primary slip system which is easy to activate as well as one or more secondary systems which have a considerably higher critical resolved shear stress. The primary system is either $(0001)<11\bar{2}0>$ or $\{10\bar{1}0\}<11\bar{2}0>$, and a fundamental problem is determining why a particular metal 'chooses' one or the other as its primary system. The authors also indicate that the stress-strain curves and the dislocation configurations are very similar whether the principal system is basal or prismatic. More details concerning primary slip in HCP metals are provided in section 2.4, in which the deformation of magnesium is considered in detail.

Table 2.3: Independent slip systems in HCP metals (Partridge, 1967)

Slip system	Burgers vector type	Slip direction	Slip plane	No. of slip systems	
				Total	Independent
1	**a**	$<11\bar{2}0>$	B: (0001)	3	2
2	**a**	$<11\bar{2}0>$	P_1: $\{10\bar{1}0\}$	3	2
3	**a**	$<11\bar{2}0>$	Π_1: $\{10\bar{1}1\}$	6	4
4	**c + a**	$<11\bar{2}3>$	Π_2: $\{11\bar{2}2\}$	6	5
5	**c**	<0001>	P_1: $\{10\bar{1}0\}$	3	2
6	**c**	<0001>	P_2: $\{11\bar{2}0\}$	3	2

2.3.4 Deformation twinning in HCP metals

This section contains an account of the crystallography and a brief discussion of some of the issues in mechanical twinning, with special reference to twinning in HCP metals, and magnesium in particular. More detailed accounts can be found in the following review articles: Clark & Craig, 1952, Cahn, 1954, Partridge, 1967, and Mahajan & Williams, 1973.

2.3.4.1 Crystallography of twinning

In mechanical twinning, a portion of the lattice homogeneously shears in response to an applied stress such that the lattice orientation in the twinned region is a mirror image of that of the matrix. Twinning thus differs from slip in which strain is accommodated by translating undeformed blocks of a crystal relative to one another across a single lattice plane in multiples of the Burgers vector. In twinning, the displacement of any plane within the twin is proportional to its distance from the twin-matrix interface. In addition, twinning is polar i.e. the shear occurs in only one sense. Finally, twinning results in an abrupt reorientation of the crystal lattice, whereas the reorientation caused by slip is much more gradual, occurring over a large strain interval.

Twins can be uniquely described by defining four elements as shown in Figure 2.7. K_1, called the composition or twin plane, denotes the first undistorted plane. It is unchanged by the shear and is the identical plane defined in both the twin and the matrix. The direction of shear, η_1, creates the twin and is contained in the plane K_1. The plane of shear, S, is defined by η_1 and the normal to K_1. There is a second undistorted plane, denoted K_2, which is unchanged in size or shape but which is rotated about K_1 during twinning. K_2 intersects K_1 in a line perpendicular to η_1 and makes equal angles with K_1 before and after the shear. The intersection of S and K_2 is labelled η_2 and has two positions corresponding to before and after shearing.

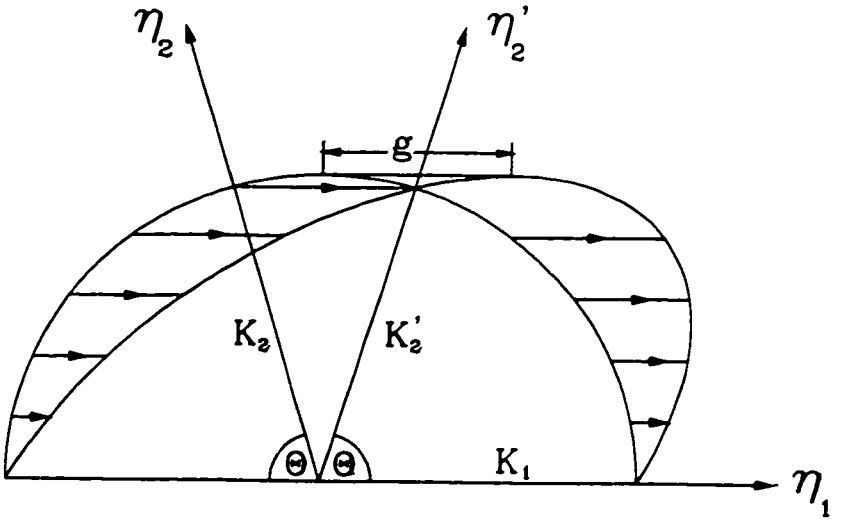

Figure 2.7: Twinning elements.

The magnitude of the twinning shear , g, is given by:

$$g = 2 \cot \theta \qquad (2.3)$$

where θ is the angle between K_1 and K_2. In HCP crystals a simple shear will not complete the twin relationship, leaving some atoms out of the proper position for a true mirror configuration with respect to

K_1; it is then necessary either to shuffle local arrangements of atoms or undergo secondary twinning. An example of such a shuffle is shown in Figure 2.8 for $\{10\bar{1}2\}\langle 10\bar{1}\bar{1}\rangle$ twinning .

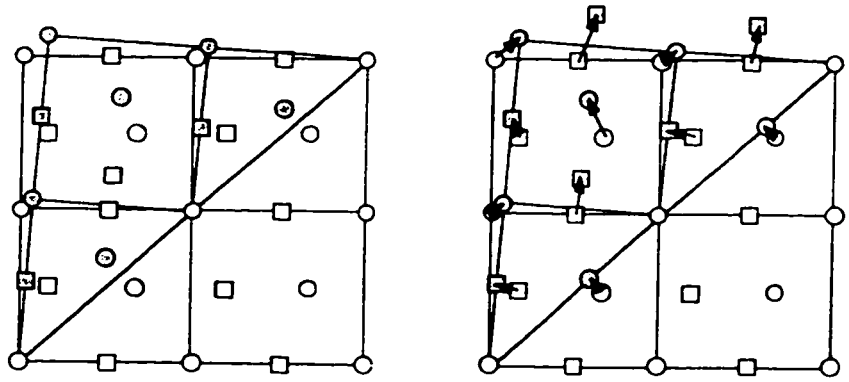

Figure 2.8: Atomic shuffling for $\{10\bar{1}2\}\langle 10\bar{1}\bar{1}\rangle$ twinning (Hosford, 1993).

2.3.4.2 Strain produced by twinning

The concept of the strain ellipsoid is helpful in analysing twinning (Figure 2.7). Twinning causes a sphere to become an ellipsoid and this shape change can be conveniently illustrated by sections parallel to the plane of shear S. When a single crystal is *completely* converted to a twin, the crystal will contract in the directions lying in the initially acute sector between K_1 and K_2, while it will extend in all directions lying in the obtuse sector. However, if only a thin lamella of twin on the K_1 plane is formed in the crystal then the distance between two points initially separated by a distance large compared with the thickness of the lamella increases or decreases according as the line joining them lies in one or other of the quadrants bounded by K_1 and the plane normal to K_1 and η_1 (Frank & Thompson, 1955).

The following expression for the theoretical tensile strain due to the complete transformation of a single crystal into a twin is given in Schmid & Boas, 1950.

$$\varepsilon_t = \sqrt{1 + 2g\sin\chi_0\cos\lambda_0 + g^2\sin^2\chi_0} - 1 \qquad (2.4)$$

where ε_t is the tensile strain due to twinning, g is the twinning shear, λ_0 is the angle between the tensile stress axis and the twinning shear direction, and χ_0 is the angle between the twinning plane and the tensile axis. For a crystal initially oriented so that both χ_0 and λ_0 are 45°, Equation 2.4 reduces to:

$$\varepsilon_t^{max} = \sqrt{1 + g + \frac{g^2}{2}} - 1 \qquad (2.5)$$

This expression gives the maximum tensile strain obtainable when a crystal twins completely on a plane originally oriented so as to have the maximum shear stress applied to it. Reed-Hill, 1973 provided a list of ε_t^{max} for some of the twinning modes observed in HCP metals (Table 2.4). It is clear that twinning can typically produce between about 7% and 10% elongation, and as much as 35% elongation in one case ($\{11\bar{2}1\}$ twinning in Zr). This table does not consider the effect of second and higher order twinning which may contribute significantly to the tensile strain (see section 2.4).

Table 2.4: Maximum tensile strain resulting from various twinning modes in HCP metals (Reed-Hill, 1973).

Metal	Twin mode		Twinning shear g	Maximum tensile strain single crystal
Be	$\{10\bar{1}2\}$	$<10\bar{1}1>$	0.19	0.095
Ti	$\{10\bar{1}2\}$	$<10\bar{1}1>$	0.18	0.09
Ti	$\{10\bar{1}1\}$	$<10\bar{1}2>$	0.10	0.05
Ti	$\{11\bar{2}2\}$	$<11\bar{2}3>$	0.22	0.11
Ti	$\{11\bar{2}4\}$	$<22\bar{4}3>$	0.22	0.11
Zr	$\{10\bar{1}2\}$	$<10\bar{1}1>$	0.17	0.085
Zr	$\{11\bar{2}2\}$	$<11\bar{2}3>$	0.63	0.35
Zr	$\{11\bar{2}2\}$	$<11\bar{2}3>$	0.23	0.12
Mg	$\{10\bar{1}2\}$	$<10\bar{1}1>$	0.13	0.065
Mg	$\{10\bar{1}1\}$	$<10\bar{1}2>$	0.14	0.07
Zn	$\{10\bar{1}2\}$	$<10\bar{1}1>$	0.14	0.07
Cd	$\{10\bar{1}2\}$	$<10\bar{1}1>$	0.17	0.085

All HCP metals undergo $\{10\bar{1}2\}<10\bar{1}\bar{1}>$ twinning. The sense of the shear depends on the c/a ratio: when c/a is larger than the ideal value the result is c-axis contraction, but when c/a is less than the ideal value twinning causes c-axis extension. In magnesium, this type of twinning results in a reorientation of the lattice of approximately 87°.

2.3.4.3 Twin morphology

Deformation twins are generally lenticular. When a grain twins it is not converted entirely into the twin orientation but consists of thin lenticular plates separated by strips of parent material. The twins do not necessarily traverse the entire grain but can taper to a point within the grain. Due to their lenticular shape, the boundaries between the twinned and untwinned regions do not coincide exactly with the K_1 plane. Their central plane is, however, approximately parallel to K_1. The shape of deformation twins is

probably related to the overall energy change as a twin forms. There are two main contributions to this energy change:

- The surface energy associated with the formation of the twin boundary.
- The strain energy due to the inhomogeneous plastic deformation in the twinned and untwinned regions. The mismatch between the twins and the matrix must be accommodated by elastic distortion of the parent and/or slip in the parent phase.

The accommodation energy is minimised when the aspect ratio (ratio of length to thickness) of the twins is high. Conversely, the surface energy is minimised when the aspect ratio is unity (a spherical shape). The final shape of the twin will therefore depend on the relative magnitudes of the surface energy and accommodation energy terms.

2.3.4.4 Twin formation

Deformation twins form very rapidly and can produce sharp load drops in a tensile test as the deformation of the material overtakes the crosshead motion of the test rig. This can cause the stress-strain curve of the material to be serrated (Figure 2.9).

It is not clear what yield criterion is appropriate for twinning. In most analytical treatments a critical resolved shear stress criterion has been assumed, but some investigations have questioned the validity of such a criterion. Deviations from a shear stress criterion may be due to the necessity for some slip to nucleate twinning or to a dependence on the stress normal to the twin plane as well as the resolved shear stress. This could be particularly important for twinning in HCP metals in which the atoms do not all move in the direction of the shear but have a component of their displacement normal to the twin plane.

It is important to recognise that the stress required to nucleate a twin may be very different from that for twin growth. The nucleation stress may be high because as a twin is nucleated its surface to volume ratio is very high and the work to produce the surface must come from the mechanical work expended. On a per volume basis, this can be expressed as:

$$dw = \sigma d\varepsilon = \tau g df \qquad (2.6)$$

where dw is the incremental work per unit volume expended in causing an incremental volume fraction df to undergo twinning, g is the twinning shear, and τ is the required shear stress. For small twins, dw/df will be high, so $\tau = (1/g)dw/df$ must also be high (Hosford, 1993).

Anything which limits the size of a twin, such as a fine grain size or a second phase within the grains which cannot be easily sheared by the twins, will result in a higher shear stress for nucleation.

It is possible that twin nucleation is sensitive to the normal stress across the twin plane. According to the principle of normality, which states that the strain vector must be normal to the yield locus, if the shear stress for twinning depends on the normal stress, there must be a plastic strain normal to

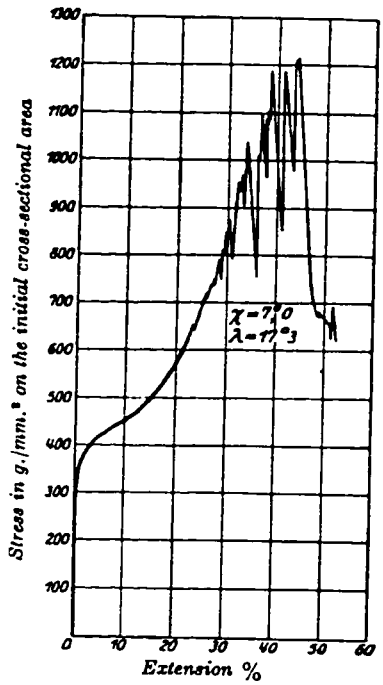

Figure 2.9: Stress-strain curve of a cadmium single crystal. Each serration corresponds to the formation of a twin (Schmid & Boas, 1950).

the twin plane. Conversely, a strain normal to the twin plane would imply that twin formation is sensitive to the normal stress across the twin plane. The atomic misfit at the twin boundary may cause a small dilation. As the twin thickens, the dilated region simply moves with the boundary which implies that even if the twin nucleation stress depends on the normal stress, the stress for twin propagation should not.

2.3.4.5 Twinning in polycrystals

The grain size and texture of a polycrystal can have a profound influence on the formation and growth of twins. In addition to the higher average stress required to nucleate twins in fine-grained materials discussed above, decreasing grain size also tends to lessen the jerkiness of the macroscopic stress-strain curves. This is because the twins that form are smaller in fine-grained material so that the relaxation caused by the formation of a twin does not produce an appreciable load drop as would occur when a large twin forms in a single crystal. Fine twins can form at grain boundaries which relax intergranular stresses that occur as a result of intergranular incompatibility.

As discussed previously, the shear occurs in only one sense for twinning. As a result, a strong anisotropy in the flow curves for tension and compression may be observed in textured materials. Indeed, if a majority of grains are oriented favourably for twinning in compression, this process will not occur when the material is strained along the same axis in tension. This is shown for extruded magnesium in Figure 2.10. The material has a strong texture, with the basal poles oriented preferentially in a plane normal to the

extrusion axis and the stress is applied parallel to the extrusion direction. $\{10\bar{1}2\}\langle 10\bar{1}\bar{1}\rangle$ twinning is favoured in compression but not in tension.

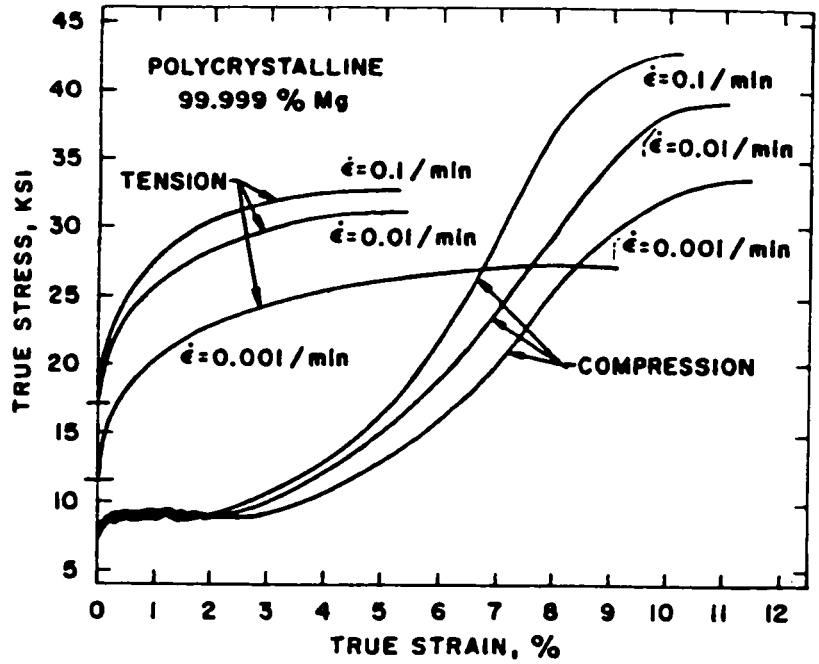

Figure 2.10: Effect of texture on the stress-strain curves of highly textured pure magnesium (Reed-Hill, 1973).

In compression, yielding occurs by a Lüders process involving twinning. Deformation tends to occur at constant stress since the twins are nucleated at the Lüders front. The Lüders band may or may not be preceded by a sharp load drop. Thus in this case, previously formed twins have only a secondary effect on those that form subsequently and the work hardening is negligible. Eventually, however, as deformation proceeds by a combination of slip and twinning, or by slip in a heavily twinned matrix, a high work hardening rate can result as the twin boundaries constitute obstacles to slip.

It is also important to realise that in general a tensile (or compressive) stress applied in a given direction is not equivalent to a compressive (or tensile) stress applied in a perpendicular direction. For example, in HCP metals a tensile (or compressive) stress applied parallel to the basal plane is not equivalent, with regard to the activation of twinning modes, to a compressive (or tensile) stress applied perpendicular to the basal plane. This can be seen in Figure 2.11 in which the $\{10\bar{1}2\}$ planes of a HCP crystal are arranged in a six-sided pyramid. It can be seen that a stress perpendicular to the basal plane should produce equal shear stress components on all six twinning planes, but that a stress parallel to (0002) and along $\langle 10\bar{1}0\rangle$ places a larger stress on two planes than on the other four.

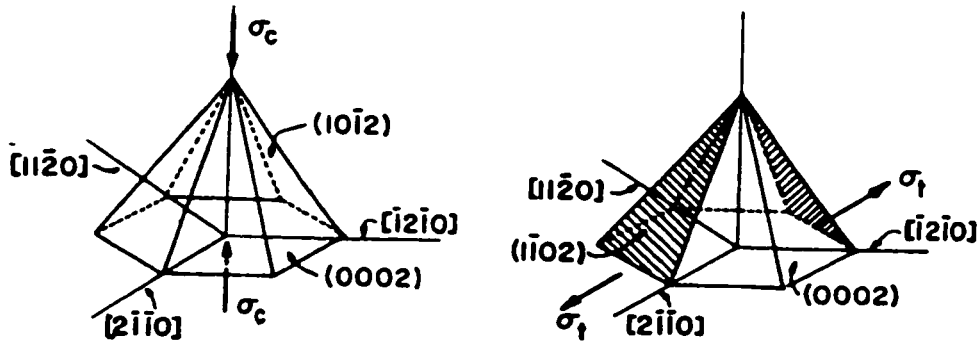

Figure 2.11: Diagram illustrating that (a) a compressive stress normal to the basal plane in a HCP metal is not equivalent in its effects on activating twinning modes to (b) a tensile stress parallel to the basal plane (Reed-Hill, 1973).

2.3.5 Summary

A large variety of deformation modes are possible in HCP metals. It is important to note in particular that only if at least one non-basal slip mode with a c-component Burgers vector is active can slip alone provide five independent shear modes. Twinning can contribute significantly to plastic deformation, but may be limited to particular stress conditions because of its polar nature if the material has a pronounced texture.

2.4 Deformation of Magnesium

This section contains a review of the work reported in the literature which discusses the deformation modes which can occur in magnesium and its alloys and how these vary with temperature and stress state. Work on both single and polycrystals is reviewed.

2.4.1 Deformation of pure magnesium

2.4.1.1 Single crystals: basal slip

Burke & Hibbard, 1952, tested high purity single crystals of various orientations in tension at room temperature, using X-ray techniques and optical microscopy to analyse the deformation markings on a polished surface. They found basal slip (0001)<11$\bar{2}$0> to be the only slip mode in crystals for which the basal plane was between 6° and 72° from the tensile axis. When the basal plane was inclined at greater than 72° to the stress axis, basal slip still occurred but was accompanied by fine {10$\bar{1}$2}<10$\bar{1}$1> twins as deformation proceeded due to grip constraints. The authors calculated a critical resolved shear stress for basal slip of 0.46 MPa.

Hirsch & Lally, 1965 studied the deformation of magnesium single crystals strained in tension at room temperature. Dislocation distributions were determined by transmission electron microscopy on sections of crystals deformed by various amounts. The angle between the slip direction and the stress axis was kept between 40° and 60°, thus avoiding grip-constraint-related effects. An example of the stress-strain curves obtained is shown in Figure 2.12.

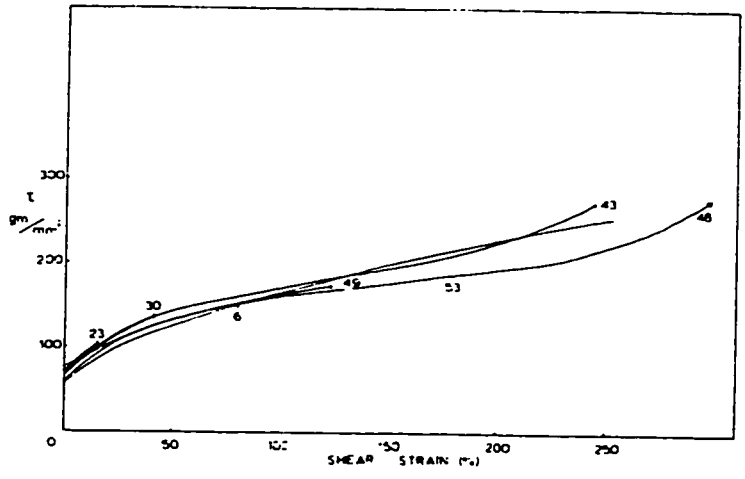

Figure 2.12: Stress-strain curve for magnesium single crystals at room temperature (Hirsch & Lally, 1965).

The curve is divided into two stages, A and B. In stage A, which extends up to about 250% strain in crystals with no initial sub-structure, the rate of work hardening is of the order of $2x10^{-5}G$ where G is the shear modulus of magnesium. The dislocations consisted mainly of bands of edge dipoles with only about 10% of the dislocations having non-primary Burgers vectors. No dislocations with non-basal Burgers vectors were found. The density of dislocations varied linearly with strain. At intermediate and higher strains (i.e. 80% to 250%), the dislocations tended to be clustered, the size and number of the groupings increasing with strain. The authors proposed a model for stage A in which dislocations from sources operating simultaneously trap one another and form dipole bands for edges and screws; the screws cross-slip and annihilate leaving the edges and an excess of screws of one sign. The flow stress is thus controlled by the internal stress field from edge clusters, residual screws, and dislocations with non-primary Burgers vectors. The work hardening rate is low because most of the dislocations annihilate (screws) or form dipoles which have a relatively small radius of interaction and hardening effect. As a result of this process, the density of effective obstacles rises only slowly. In stage B, the rate of work hardening is typically $6x10^{-4}G$. This stage is characterised by twinning and the production of networks and tangles in which the three basal Burgers vectors are equally represented.

2.4.1.2 Single crystals: non-basal slip

Reed-Hill & Robertson, 1957, 1958 studied non-basal slip by straining single crystals at -190°C, 25°C, 150°C, and 286°C in tension with the stress axis within 2°±1° from a <10$\bar{1}$0> direction so that basal slip and {10$\bar{1}$2}<10$\bar{1}$1> twinning were suppressed. {10$\bar{1}$0}<11$\bar{2}$0> prism slip was found to be dominant at -190°C, with cross-slip occurring on the basal planes. At 25°C, prismatic-basal cross-slip was observed in the highly strained regions close to fractures.

Reed-Hill and Robertson also found {10$\bar{1}$1}<11$\bar{2}$0> slip at 25°C near fillets, grips, and fractures on straining single crystals with the stress axis inclined at 85° and 18° to the <0002> and <10$\bar{1}$0> directions, respectively. Specimens exhibiting pyramidal slip showed negligible ductility, suggesting that it is unlikely that pyramidal slip is important in producing plastic deformation at room temperature.

Stohr & Poirier, 1972. studied single crystals of pure magnesium compressed parallel to the c-axis using optical microscopy as well as transmission electron microscopy. {11$\bar{2}$2}<11$\bar{2}$3> second order pyramidal slip was obtained from 77K to 450K. At room temperature, the c+a dislocations consist of large edge loops which are elongated parallel to the <10$\bar{1}$0> direction. The c+a edge segments as well as the dislocation loops are dissociated into partials according to the following reaction:

$$\frac{1}{3}[11\bar{2}3] \rightarrow \frac{1}{6}[20\bar{2}3] + \frac{1}{6}[02\bar{2}3] \qquad (2.7)$$

2.4.1.3 Single crystals: deformation twinning

Twinning was recognised in the earliest work on magnesium, the dominant mode being {10$\bar{1}$2}<10$\bar{1}\bar{1}$>. As discussed in section 2.2, this type of twin results in c-axis extension in magnesium.

Burke & Hibbard, 1952 found that when single crystals of magnesium were pulled in tension with the basal plane inclined at greater than 72° to the stress axis, basal slip occurred first. As deformation proceeded, rotation of the basal plane in conjunction with grip constraints caused a bend plane to form at which point fine {10$\bar{1}$2}<10$\bar{1}\bar{1}$> twins were visible near the bend plane with slip occurring on the reoriented basal plane of the twins. The amount of twinning increased with the degree of bending, which led the authors to suggest that twinning occurred primarily as a stress relief mechanism arising from the bending accommodation of the basal plane to grip (or other) constraints.

Reed-Hill & Robertson, 1957 and Reed-Hill, 1960 studied deformation twinning in crystals strained in tension with the stress axis in the basal plane by optical microscopy and X-ray analysis. At 25°C, 150°C, and 286°C, large bands consisting of tightly grouped clusters of twins were observed. They were initially identified as {30$\bar{3}$4}<20$\bar{2}$3> twins but it was then realised that the structures observed corresponded to {10$\bar{1}$1}<10$\bar{1}$2> twins which were then subject to almost complete second order twinning on the {10$\bar{1}$2} plane of the first order twin. The mechanism is illustrated in Figure 2.13. At 150°C and

286°C, small {10$\bar{1}$3} twins were observed near the region of fracture and in the vicinity of {10$\bar{1}$1}<10$\bar{1}$2> twins. An electron microscopy analysis using replicas confirmed this double-twinning mechanism (Hart & Reed-Hill, 1967).

The '{30$\bar{3}$4}' twins were responsible for failure at room temperature with the tensile axis in the basal plane, because the reoriented crystal structure of a lamella was well-aligned for slip while the parent crystal was not. Extensive deformation thus occurred within the lamella while the matrix was still almost undeformed, thereby producing a ductile rupture running the length of the lamella (Reed-Hill & Robertson, 1957). Since the volume fraction of these lamellae was quite small, fracture occurred at low overall strains, hence the low ductility which was observed. This double twinning mechanism can, however, produce remarkable ductility in rolling in certain magnesium alloys (Couling et al., 1959).

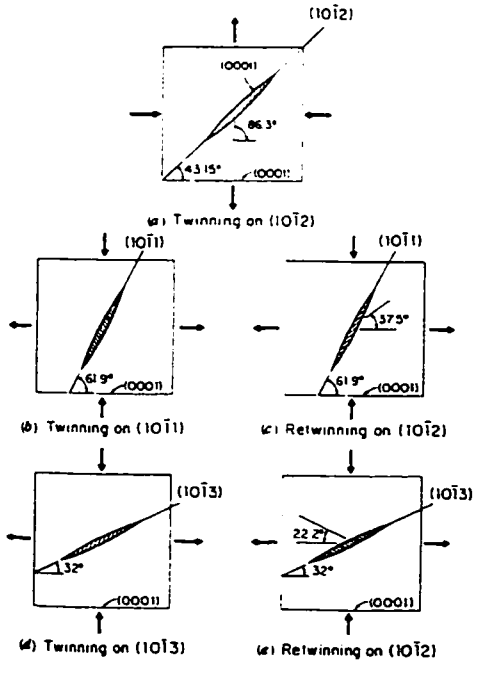

Figure 2.13: Second order twinning process in magnesium (Wonsiewicz & Backofen, 1967).

2.4.1.4 Single crystals: channel die compression

Wonsiewicz & Backofen, 1967 tested single crystals of pure magnesium in channel die compression. When the crystals were compressed parallel to the c-direction, with expansion limited to either the <10$\bar{1}$0> or <11$\bar{2}$0> directions, the applied stress rose rapidly and fracture occurred at about 6% strain at a stress of 324 to 365 MPa (Figure 2.14). The authors attributed the rapid increase in stress to the occurrence of basal slip with the operative Schmid factor being very low but not zero. Only at the very end

of straining was the previously described double-twinning mechanism observed, so that it contributed very little to the overall deformation.

For crystals compressed perpendicular to the c-axis, with expansion restricted parallel to the c-axis, the stress-strain curves varied significantly depending on whether the stress axis was parallel to <10$\bar{1}$ 0> or <11$\bar{2}$0> (Figure 2.15). {10$\bar{1}$2} twins, which produce c-axis expansion, appeared during the initial linear region of the stress-strain curve. The slightly higher rate of work hardening associated with crystals compressed along <10$\bar{1}$0> was attributed to the fact that the basal planes in the twinned material were unfavourably oriented for basal slip whereas this was not so for the crystals compressed along the <11$\bar{2}$0> direction. The more horizontal regions of the stress-strain curves were associated with the occurrence of double twinning which acted to relieve the c-axis expansion which had been generated by {10$\bar{1}$2} twinning.

Channel die compression was also carried out on pure magnesium single crystals by Kelley & Hosford, 1968. Their stress-strain curves for pure magnesium are shown in Figure 2.16. It is clear from a comparison of these observations that the stress-strain behaviour depends strongly on the compression direction and constraint directions.

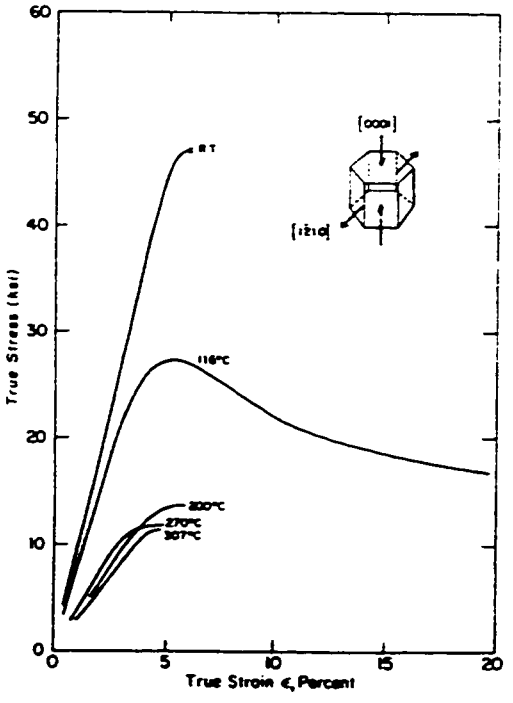

Figure 2.14: Stress-strain curves for magnesium crystals compressed along [0001] with expansion limited to [11$\bar{2}$0] (Wonsiewicz & Backofen, 1967).

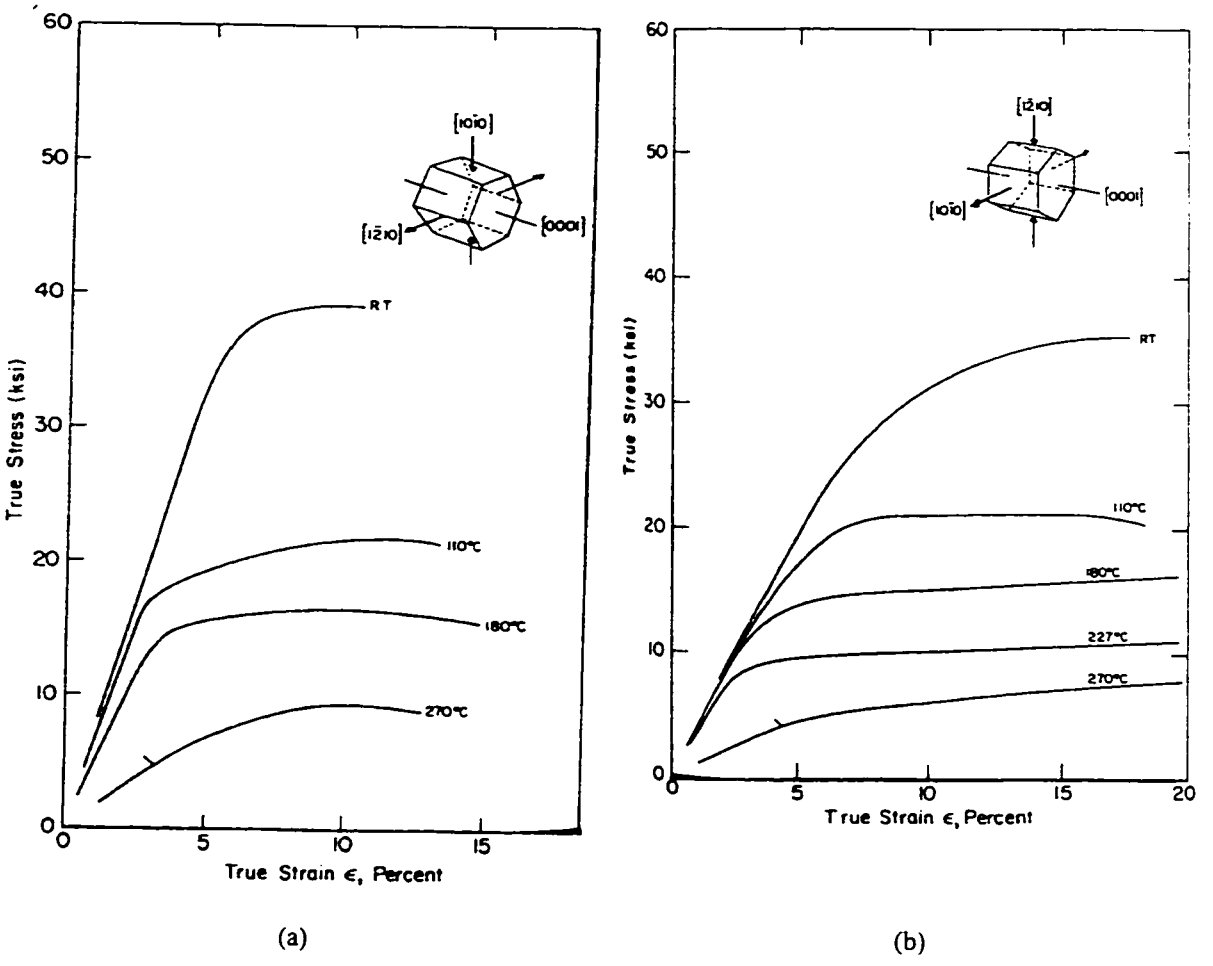

Figure 2.15: Stress-strain curves for magnesium crystals compressed along (a) <10$\bar{1}$0> and (b) <11$\bar{2}$0> with expansion restricted parallel to the c-axis (Wonsiewicz & Backofen, 1967).

The results for compression parallel to the c-axis with expansion limited to <10$\bar{1}$0> and <11$\bar{2}$0>, and for compression perpendicular to the c-axis with expansion restricted parallel to the c-axis, agreed well with those of Wonsiewicz & Backofen, 1967. In addition to these two classes, Kelley and Hosford also compressed single crystals perpendicular to the c-axis with expansion allowed parallel to that axis (orientations E and F in Figure 2.16). In this case, {10$\bar{1}$2} twinning was favoured and it proceeded to completion to about 6% strain. After twinning was complete, orientation E was only about 3.7° from a B orientation and deformation proceeded as described for this orientation according to Wonsiewicz and Backofen. For the F orientation, the twinned material was favourably oriented for basal slip which was resisted by the side constraint. Near the end of the deformation, the double twinning mechanism became operative but contributed very little to the overall deformation. {10$\bar{1}$0}<11$\bar{2}$0> slip traces were never observed.

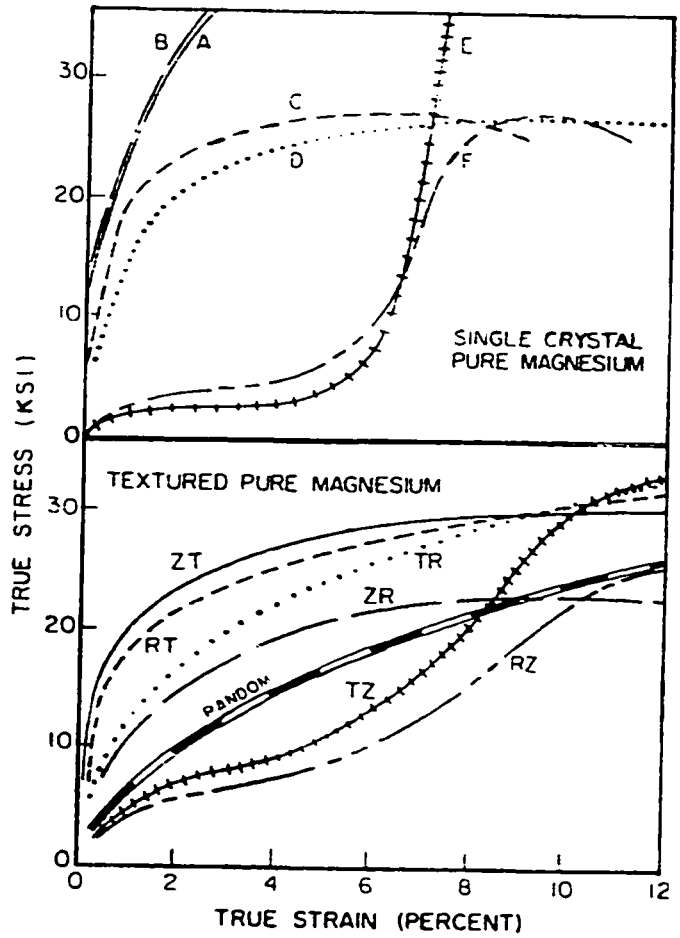

Figure 2.16: Stress-strain curves for pure magnesium (Kelley & Hosford, 1968).

2.4.1.5 Deformation of polycrystalline magnesium

Mote & Dorn, 1960 studied the deformation and fracture of magnesium bicrystals in tension having the orientations shown in Figure 2.17. The investigation showed clearly that the relative orientations of adjacent grains can have a profound effect on the overall deformation behaviour in a material such as magnesium which displays considerable plastic anisotropy.

The bicrystals exhibited ductilities that were consistent with the fact that only basal slip and $\{10\bar{1}2\}$ twinning can produce appreciable deformation in magnesium. In particular, they found the following:

a) When one grain was so oriented that it could neither slip nor twin, (orientation C in Figure 2.17), the bicrystal exhibited zero ductility.

b) When one grain was so oriented that it could only twin (orientation D in Figure 2.17), the strain to fracture was only slightly greater than that which would be obtained if the grain was completely converted into the twin orientation.

c) When slip could occur in both grains (orientations B and E in Figure 2.17), cracking occurred in the grain boundary.

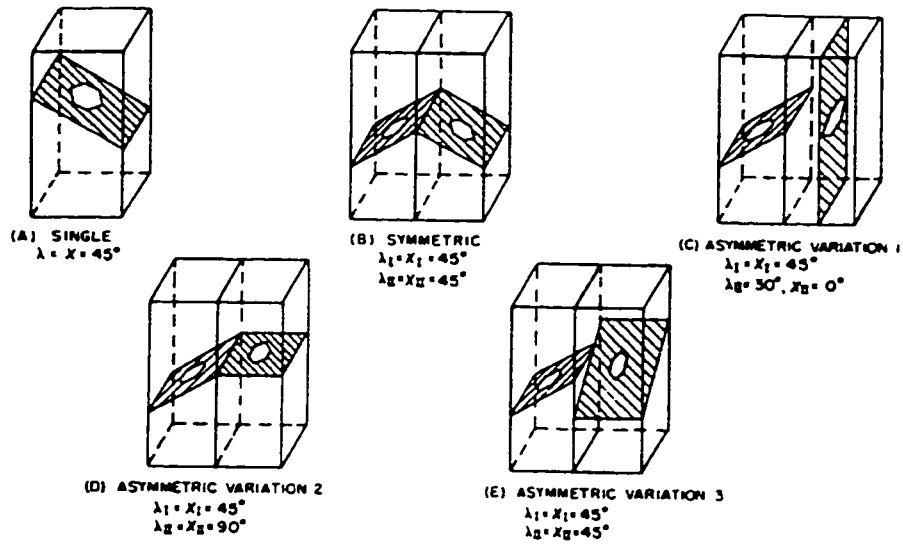

Figure 2.17: Schematic illustration of magnesium bicrystals used by Mote & Dorn, 1960.

This study is also interesting because it showed that for the conditions tested, no slip systems other than basal slip contributed significantly to the overall deformation despite the stress states in the vicinity of the grain boundary.

Hauser et al., 1955 studied the deformation of polycrystalline magnesium at room temperature in tension by X-ray techniques and optical microscopy. The texture was such that the basal plane normals were oriented at high angles (≈90°) to the extrusion direction; for this orientation, neither {10$\bar{1}$2} twinning nor basal slip were favoured. In all the specimens tested, only basal slip traces were observed within the grains, even in grains very unfavourably oriented for basal slip. The authors found exclusively {10$\bar{1}$2} twinning in deformed specimens. Untwinning was found to occur even when extensive slip took place on the reoriented basal plane of the twins. Rupture generally occurred at grain boundaries.

Kelley & Hosford, 1968 studied the deformation of variously oriented textured magnesium samples by channel die compression as well as uniaxial tension and compression. The stress-strain curves obtained were similar in their general form of anisotropy and stress levels to those obtained from single crystals (Kelley & Hosford, 1968). The degree of anisotropy was lower, however, in the polycrystalline material, and could be correlated with the intensity of the basal texture.

2.4.1.6 Summary

The literature reviewed in this section indicates that basal slip is by far the easiest and most

common slip mode in magnesium at room temperature. Prismatic slip and pyramidal slip appear to contribute very little to macroscopic deformation. {10$\bar{1}$2} twinning and {10$\bar{1}$1}-{10$\bar{1}$2} double twinning can produce limited deformation parallel to the c-axis, the former producing extension and the latter compression. {10$\bar{1}$2} twinning, in particular, can untwin when the stress is reversed.

2.4.2 Deformation of magnesium alloys

2.4.2.1 Deformation of single crystals

Byrne, 1963 studied the deformation behaviour of Mg-1.24% Mn single crystals. The alloy was heat treated to produce precipitate ribbons normal to the basal plane which were not resolvable in the electron microscope using carbon replicas. Both the solid solution and the precipitated alloy were studied. The CRSS of the solid solution was approximately five times that of pure magnesium at room temperature and was attributed to the clustering of solute atoms during quenching (42% atom size difference between Mg and Mn). The CRSS of the aged alloy was approximately twice that of the solid solution. The alloy strength in this case was attributed to a combination of the solid solution in equilibrium with the precipitate and a particle shearing process. The precipitates were not strong enough to inhibit twinning in this alloy.

Chun & Byrne, 1969 studied precipitate strengthening mechanisms in quenched (i.e. solution treated) and fully aged Mg-5.1%Zn. All the crystals were oriented favourably for basal slip. In the fully aged condition, the precipitates consisted of long rod-like particles with an average interparticle spacing of 330 to 660 Å, a width of 150 to 300 Å, and an aspect ratio of about 20. The quenched and fully aged crystals exhibited a room-temperature CRSS approximately ten, and forty times that of pure magnesium, respectively. However, in both cases, the rate of work hardening was similar to that of pure magnesium. In addition, slip lines in quenched crystals were finer and more closely spaced than for fully aged crystals. Chun et al., 1969 tested these Mg-Zn crystals in tension with the stress axis aligned close to [0001] in order to prevent basal slip and favour twinning. They found that twinning was inhibited at room temperature in the fully aged crystals. Though some small twins were present in fully aged crystals, they were short and never traversed the entire crystal. In comparison, twins formed in the underaged crystals invariably spanned the entire crystal.

2.4.2.2 Deformation of polycrystals

Couling et al., 1959 discussed the deformation and ageing characteristics of some magnesium alloys (e.g. Mg-Ca, Mg-Zr, Mg-Th) which exhibit extensive cold-rollability under certain conditions. The interesting observation in this work is that it appears that the double twinning mechanism discussed in section 2.4.1 is capable of producing a great deal of plastic deformation. This is in contrast to the ductile fracture (at low macroscopic strains) which is associated with this deformation mode in pure magnesium.

2.4.2.3 Precipitation reactions and deformation of binary Mg-Al alloys

Precipitation reactions

It is useful at this point to consider in detail the types of precipitation that can occur in binary Mg-Al alloys, as well as the work which has already been done to elucidate the ways in which they affect the deformation of magnesium.

The binary Mg-Al phase diagram is shown in Figure 2.18.

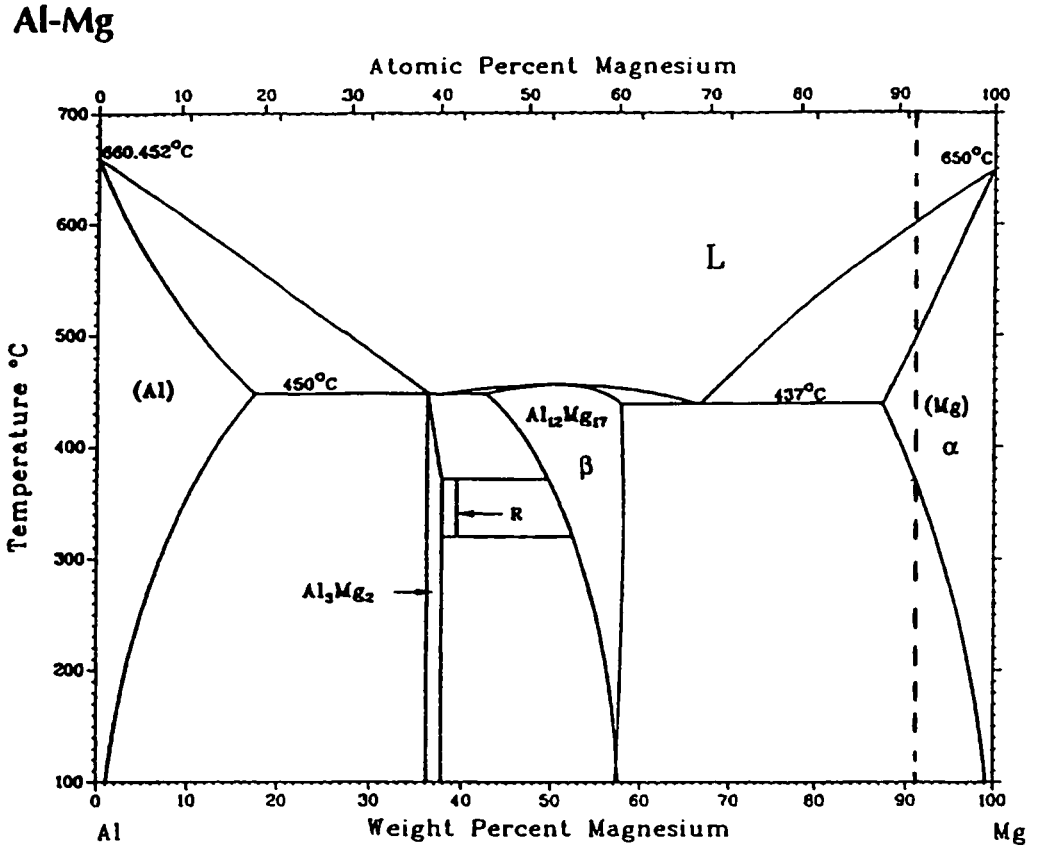

Figure 2.18: The Al-Mg binary phase diagram (Murray, 1982). The composition of the alloy used in this study is indicated by a dotted line.

The supersaturated α' solid solution (SSSS) can decompose into the equilibrium α solid solution and the intermetallic β phase $Mg_{17}Al_{12}$ by two mechanisms (Duly, 1992):

In *continuous* precipitation, the formation of the β phase is accompanied by a progressive reduction in solute content of the SSSS. The intragranular platelets which result are homogeneously distributed.

In *discontinuous* precipitation, the transformed zone is separated from the original SSSS by an interface which migrates during the course of the reaction (this is the reaction front). The SSSS is unchanged until it

is swept by the reaction front and all the diffusion processes which occur during the reaction are concentrated at the migrating interface. In the regions which have been swept by the reaction front, one finds alternating lamellae of α solid solution and β phase. The reaction front consists of a migrating grain boundary.

Duly, 1992 studied the type of precipitation which occurs in Mg-Al alloys as a function of aluminium content and ageing temperature. For all the alloys studied he was able to define temperature ranges as follows (Figure 2.19):

- For $T < T_{c1}$, only continuous precipitation is observed.
- For $T_{c1} < T < T_{d1}$, both types of precipitation are present. In this temperature range, the volume fraction of discontinuous precipitation increases with temperature.
- For $T_{d1} < T < T_{d2}$, only discontinuous precipitation is observed.
- For $T_{d2} < T < T_{c2}$, both types of precipitation are again observed. In this temperature range, the volume fraction of discontinuous precipitation decreases with increasing temperature.
- For $T_{c2} < T < T_S$, only continuous precipitation is observed (T_S is the temperature at which the solid solution is the equilibrium configuration).

T_{c1} was only observed for the alloy containing 18.8at% Al, but the author suggests that it may in fact exist for alloys having lower Al content because he found that for Mg-10at%Al and Mg-7.7at%Al the volume fraction of discontinuous precipitation decreases rapidly with temperature.

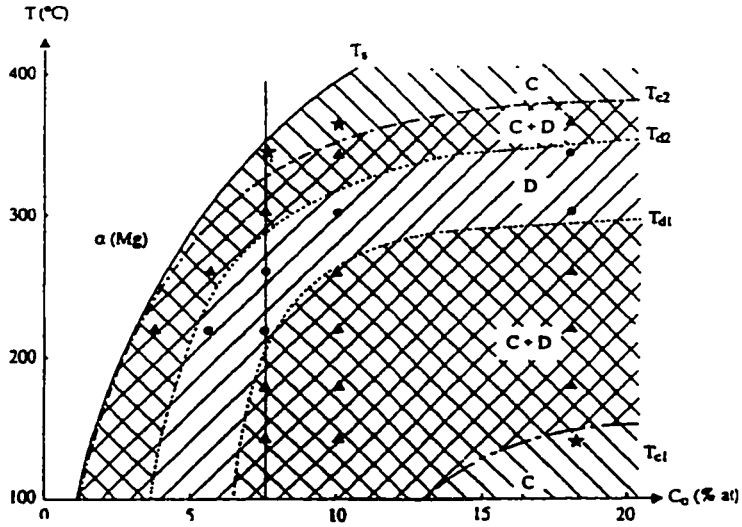

Figure 2.19: Diagram showing how the type of precipitation occurring in binary Mg-Al alloys varies with ageing temperature (T) and aluminium content (C_0) (Duly, 1992).
Circles = only discontinuous precipitation (D).
Triangles = continuous and discontinuous precipitation (C + D).
Stars = only continuous precipitation (C).

As mentioned previously, discontinuous precipitation appears as lamellae which extend from the grain boundaries into the grains. However, the morphology of these lamellae can be quite complex as illustrated in Figure 2.20.

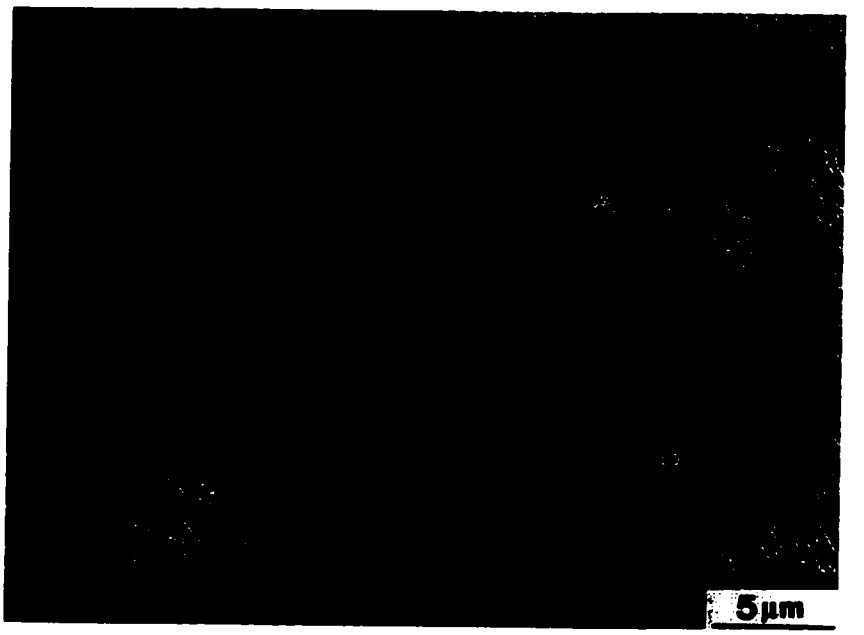

Figure 2.20: Different morphologies in a nodule of discontinuous precipitation showing (A and B) zones of parallel growth, and (C) zones where the lamellae appear to grow radially outward in a bush morphology (Duly, 1992).

In contrast, continuous precipitation results in a more regular structure. Duly found that continuous precipitation takes the form of homogeneously distributed platelets which grow parallel to the basal plane of the magnesium matrix. Duly also confirmed the following crystallographic orientation relationship observed by other authors which always exists between the precipitates and the matrix.

$$(0\,1\,1)_\beta \,//\, (0\,0\,0\,1)_\alpha$$
$$[1\bar{1}1]_\beta \,//\, [2\bar{1}\bar{1}0]_\alpha$$

In a given grain there are 12 equivalent variants which can also occur. Since the structure produced by continuous precipitation is expected to be rather easier to characterise and to model than that produced by discontinuous precipitation, this was the precipitation mode chosen for this study.

Deformation of Mg-Al alloys

Clark, 1968 studied the deformation behaviour in compression of a cast binary Mg-9wt%Al alloy by transmission electron microscopy and optical microscopy. He found that in the solution treated condition, or when there was little precipitation, basal slip and $\{10\bar{1}2\}$ twinning were the principal deformation modes. The dislocations move along the basal plane and pile up at $\{10\bar{1}2\}$ twin and grain boundaries.

As the amount of precipitation increased, cross slip occurred and $\{10\bar{1}2\}$ twinning progressively disappeared. Optical microscopy of pre-polished surfaces on specimens compressed to a strain of 4% revealed fine basal slip and wide lenticular $\{10\bar{1}2\}$ twins in the solid solution. In the fully hardened condition, however, there were almost no twins, and a second slip system identified as $\{10\bar{1}0\}\langle 11\bar{2}0\rangle$ was observed. The fine basal slip lines in the solid solution were replaced by wavy slip in the fully hardened condition and the interaction of the two slip systems produced dislocation tangles. The precipitates were never sheared by twins, and as the size and number of precipitates increased the amount of twinning decreased.

2.4.2.4 Summary

It is clear that some types of precipitation can inhibit twinning in magnesium and increase the CRSS for basal slip considerably. It is interesting to note, however, that the rate of work hardening in alloy single crystals is generally not much greater than in pure magnesium crystals. Some of the work reviewed has also raised the possibility that alloying elements can allow twinning to produce much more plastic deformation than it would in pure magnesium.

2.5 The Bauschinger Effect

This thesis is concerned with the way in which internal stresses build up and are distributed between grains of different orientations as well as between the matrix and the second phase in a magnesium alloy. Bauschinger tests provide a way of obtaining information about this stress distribution.

2.5.1 Definition

The Bauschinger effect (BE) is perhaps best defined as a dependence of the flow stress and rate of work hardening on the strain history of a metal. The main aspects of the BE are shown in Figure 2.21, in which absolute stress is plotted against absolute cumulative strain in a simple forward-reverse deformation test. The BE manifests itself by a lower initial yield point in reverse straining than in forward straining, a rounding of the stress-strain curve near the yield point in reverse straining ('transient softening'), and a lowering of the entire stress-strain relation ('permanent softening'). Various combinations of these effects may be observed. It has been found that prestraining in any direction, as defined by the principal axis of the strain tensor, will introduce an anisotropy for further deformation in any other direction. The intensity of the BE is, however, a maximum when the direction of further straining is opposite to that of the prestrain (Abel, 1986). The BE has been observed in single phase and two-phase polycrystals as well as in single crystals of BCC, FCC, and HCP metals.

In Figure 2.21, σ_{pf} denotes the flow stress in forward straining, σ_{pr} represents the flow stress in reverse straining, and $\Delta\sigma_{pps}$ denotes the permanent softening, which is the value of σ_{pf} - σ_{pr} measured at a

reverse strain sufficient to give near parallelism between the forward and reverse stress-strain curves at the same cumulative absolute strain. The parameters ε_n and $\Delta\sigma_{pn}$ are discussed in the following section.

The discovery of the BE is attributed to Bauschinger, 1886 whose paper was mainly concerned with the observed reduction in yield strength during reverse loading following prestraining. There is published evidence from the pre-Bauschinger era, however, that load reversal experiments led to the conclusion that the yield strength is history dependent. An excellent account of the history of the BE and of the work that was done to understand its origins has been provided by Abel, 1986.

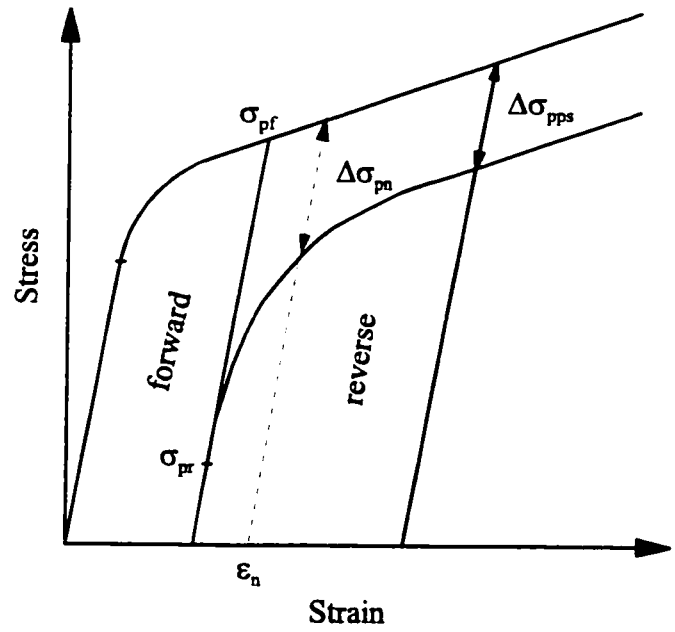

Figure 2.21: Main features of the Bauschinger Effect.

2.5.2 Interpretations of the Bauschinger Effect

The BE can arise from two different sources. On one hand, a system of internal stresses can develop in a material during forward straining which aids flow in the reverse direction. On the other hand, the dislocation structure in the material at the end of prestraining may be unstable with respect to other slip systems or may be reversible.

Heyn's model (Heyn, 1918) provides the basis of many of the macroscopic (continuum) models designed to represent the relationship between the BE and internal stresses generated during deformation. Back-stresses, which cancel the applied stress everywhere and thus prevent further movement of dislocations, are attributed to the non-homogeneous deformation of grains which leads to the piling up of slip at grain boundaries. The model assumes that the material is composed of a series of small volume elements in parallel, each having an elastic-perfectly plastic (non-hardening) flow curve. The elastic limit is

different for each volume element and does not depend on loading direction. The model can explain both transient and permanent softening. Models based on these ideas have been developed by Masing, 1922 and Mroz, 1967,1969 and variations have been used to analyse the BE in steels (Bate & Wilson, 1986) and in fibre-reinforced composites. These continuum models imply that the entire yield surface is translated (and, in some cases, distorted) in stress space during prestraining, which leads to a reduction in flow stress of the kind observed in Bauschinger tests. They are referred to as kinematic hardening models.

The first microscopic description of the BE was proposed by Orowan, 1959. He interpreted the BE in terms of the effects of two types of obstacle to slip: strong barriers and permeable obstacles. The former were expected to promote back-stress hardening due to some form of dislocation pile-up which would be wiped out to a large extent by reversed plastic deformation, thus giving rise to permanent softening. Permeable obstacles, however, could give rise to a low initial flow strength in reversed deformation without causing appreciable permanent softening. In this case, a mobile dislocation would move forward through the array of obstacles at the flow stress, overcoming individual obstacles under the pressure of only a few piled-up dislocations. At the end of prestraining, the dislocation would be held up at a row of obstacles both strong enough and sufficiently closely spaced to resist shearing. If the applied stress is then removed, the dislocation may adjust itself locally, but in the absence of sufficiently strong back-stresses it is expected to remain more or less where it was at the end of prestraining. On stress reversal, however, the dislocation would begin to move away from the obstacles at a relatively low applied stress as it samples an array of obstacles which is weaker than the array at which it was held up. Orowan's model implies that permanent softening will be much greater in dispersion hardened alloys than in single phase materials, which is in fact generally the case.

It is important to realise that macroscopic and microscopic descriptions are complementary. It should be possible to relate the magnitude of the internal stresses calculated with the macroscopic models to the internal stresses determined from a consideration of the dislocation configuration in the material.

The BE is generally interpreted in terms of the contributions from directional and non-directional components of hardening, in which case the following equation applies:

$$\sigma_{pf} = \sigma_0 + \sigma_s + \langle\sigma\rangle_m \qquad (2.8)$$

σ_0 is a derived value of the initial yield strength which excludes transient sources of flow resistance, σ_s represents the sum of the contributions from isotropic hardening components, and $\langle\sigma\rangle_m$ is the mean directional stress in the matrix. If it is assumed that neither σ_s nor $\langle\sigma\rangle_m$ relaxes significantly on unloading, the flow stress at the outset of plastic deformation in reversed straining would be:

$$\sigma_{pr} = \sigma_0 + \sigma_s - \langle\sigma\rangle_m \qquad (2.9)$$

The continuum and dislocation models described above provide a means of estimating $\langle\sigma_m\rangle$ and these values can be compared with measurements derived from the flow curves of the material.

An understanding of the BE in two-phase alloys has been well-developed by Atkinson et al., 1974, based on the experimental work of Wilson and Bate (Wilson, 1965 and Wilson & Bate, 1986). The latter performed Bauschinger tests on a series of cubic metals in order to explore the appropriateness of using measurements of permanent softening in making quantitative estimates of the contribution of back-stresses to work-hardening. The mean directional stress in the matrix , $\langle\sigma\rangle_m$, was estimated by measuring the mean lattice strains in the matrix by X-ray diffraction. $\langle\sigma\rangle_m$ increased rapidly in the early stages of deformation, but at higher strains the growth rate was limited by stress relaxation. Reverse straining first annulled the mean stress inherited from the prestrain and then developed a new distribution of internal stresses of opposite sign to the original one. Reverse strains much less than those required to produce near-parallelism between the reverse and continued forward stress-strain relationships were sufficient to annul the directional mean stress inherited from the prestrain. The reverse strain which reduced $\langle\sigma\rangle_m$ to zero (ε_n) was identified and $\Delta\sigma_{pn}$, the difference in the forward and reverse flow stresses at equivalent absolute strains corresponding to ε_n was measured. It was found that $\langle\sigma\rangle_m$, as measured by X-ray diffraction, was approximately equal to 0.5 $\Delta\sigma_{pn}$.

At the point of near parallelism, $\langle\sigma\rangle_m$ was of similar magnitude but of opposite sign to that present at the end of forward straining. These observations suggested that while the magnitude of $\langle\sigma\rangle_m$ could account in large part for the differences in forward and reverse flow strengths observed at low reverse strains, it had little direct influence on the magnitude of permanent softening. Indeed, $\sigma_{pf} - \sigma_{pr}$ at small reverse strains in the neighbourhood of ε_n would provide a much more reliable measure of $\langle\sigma\rangle_m$ than would $\Delta\sigma_{pps}$. Based on their measurements of $\langle\sigma\rangle_m$ in conjunction with the flow curves, Wilson and Bate concluded that the reversibility of σ_s was much greater in a microstructure containing a large volume fraction of non-deforming particles than in a nearly-single-phase BCC polycrystal, the difference being related to differences in the dislocation arrangements contributing to σ_s.

Atkinson et al., 1974 studied the BE in dispersion strengthened single crystals of copper containing 0.3%-1% volume fractions of silica particles for which the permanent softening is well defined. The authors argue that since the values of reverse strain required to achieve permanent softening in this system are comparable to ε_n as determined by Wilson from X-ray measurements, it follows that:

$$\Delta\sigma_{pps} = 2\langle\sigma_m\rangle \qquad \textbf{(2.10)}$$

They calculated $\langle\sigma_m\rangle$ based on a model of work hardening assuming no plastic relaxation which relied on Eshelby's analysis of the stress developed in the matrix due to the presence of a non-deforming inclusion. These values of $\langle\sigma\rangle_m$ correlated well with the results obtained from applying Equation 2.10 to their stress-

strain curves. It is important to note, however, that Equation 2.10 is only applicable in situations where permanent softening is achieved at reverse strains close to ε_n.

A complete study of the BE in a metal must include the following.

1) Mechanical tests to obtain flow curves for the material. These are usually tension-compression or compression-tension tests which produce a simple well-defined state of stress.

2) Observations of the microscopic structure of the material. These provide a description of the dislocation distribution in the material and are instrumental in determining what deformation mechanisms are contributing to the deformation.

3) Direct measurements of the stresses in the matrix and strengthening phase in two phase materials. These can be done using diffraction techniques (X-rays or neutrons). The method is described in section 2.6.

2.5.2.1 The Bauschinger effect in Mg-Al

In considering the BE in Mg-Al, there are three aspects of the deformation behaviour which must be considered. Firstly, magnesium polycrystals exhibit an inherent anisotropy with respect to loading direction, the more so if the material is textured. Woolley, 1954 performed torsion-reverse torsion tests on tubular specimens of polycrystalline magnesium to study the effect of twinning and untwinning on the deformation behaviour. The shear-stress/shear-strain curves obtained are shown in Figure 2.22.

He suggested that $\{10\bar{1}2\}$ twinning occurred along AB. On unloading, those grains which were initially unfavourably oriented for twinning (which we shall call the **T** grains) could now twin and the grains which twinned along AB (the **S** grains) could untwin. Hence yielding occurred at a relatively low reverse applied stress at D and the rate of work hardening along DE was low. If a stress were then applied in the original direction, the S grains could retwin and the **T** grains could untwin so that plastic deformation was still easy (GH). However, the untwinning of grains **T** was a limited process and the strain GH must be approximately equal in magnitude to the strain DE. At this point the **T** grains were back in their original orientation as at B and were unable to deform further in the original direction of strain by twinning. Thus at H the specimen changed from a condition in which all the grains could deform fairly easily to one in which only a fraction of them could so that the rate of work hardening increased and the stress-strain curve rose sharply from H to J and continued along JK in prolongation of curve AB.

Secondly, the plastic anisotropy of magnesium would be expected to produce high intergranular compatibility stresses which would influence the deformation behaviour of polycrystals. These are the internal back-stresses first envisaged by Heyn to give rise to the BE. In order to investigate these, it is necessary to obtain data from different components of the texture.

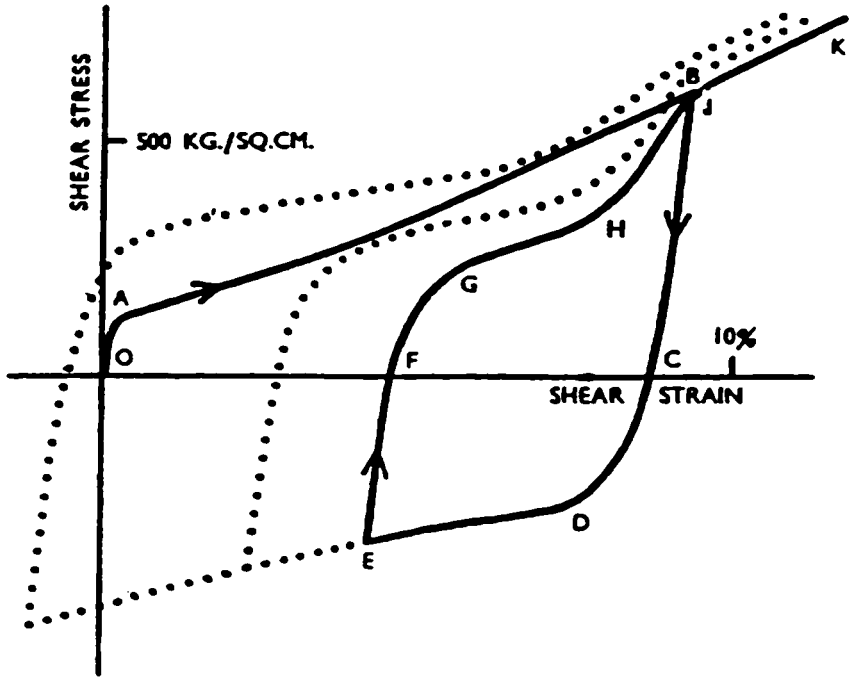

Figure 2.22: Stress- strain curve for polycrystalline pure magnesium (Woolley, 1954).

Finally, second phase particles constitute obstacles to both slip and twinning and can thus also give rise to important back-stresses. The interaction between the particles and the slip dislocations and twins must be considered and data obtained directly from measurements on the second phase.

In the present study, the mechanical response (stress-strain curves) of the material has been obtained from mechanical tests. These provide a macroscopic view of the deformation behaviour. Transmission electron microscopy and optical microscopy have been used to study particle-dislocation and particle-twin interactions on a fine scale.

In-situ neutron diffraction experiments have been performed to obtain information from various subsets of grains (defined by their orientation with respect to the stress axis) and from the second phase. The technique is described in detail in the following section.

2.6 Neutron Diffraction and Stress Analysis

Neutron diffraction was used in this study to determine the level of internal stress built up in a material during deformation. It is thus appropriate to cover some aspects of the technique. This section is divided into three parts. A brief description of neutron diffraction will first be presented. This is followed by a description of the application of neutron diffraction to the determination of internal strains. Finally, a brief overview of some of the work which has been done using neutron diffraction to measure internal strains will be presented.

2.6.1 Neutron diffraction

From wave mechanics, the wavelength of a neutron is given by the following equation:

$$\lambda = h/mv \tag{2.11}$$

where λ is the neutron wavelength, h is Planck's constant, m is the neutron mass, and v is the neutron velocity. For a nuclear reactor operating between 0°C and 100°C, the wavelength is about 1 to 2Å.

Diffraction of a beam of neutrons by a crystal is governed by Bragg's Law which can be stated as:

$$\lambda = 2d^{hkl}\sin\theta^{hkl} \tag{2.12}$$

where d^{hkl} is the spacing of a crystal plane having indices hkl, and θ^{hkl} is the angle of incidence of the neutron beam on the hkl plane. The scattering vector is defined as the bisector of the angle between the incident and scattered beams, and is parallel to the normal of the reflecting planes. The incident beam, diffracted beam, and scattering vector are coplanar.

Equation 2.12 shows that for diffraction to occur, the following condition must be satisfied:

$$\lambda < 2d^{hkl} \tag{2.13}$$

In other words, the wavelength of the radiation to be diffracted must be of the same order of magnitude as the spacing of the crystal planes, which is the case for neutrons diffracted by metal crystals.

Neutrons emerging from a reactor will have been slowed down by collisions with a moderator of graphite or heavy water and will tend to come in thermal equilibrium at the reactor temperature; the neutrons will therefore have an appropriate distribution of velocities, and thus wavelengths. The nature of the spread of wavelengths in the beams generally obtained is shown in Figure 2.23(a). The neutron spectrum is 'white', and contains nothing which corresponds to the characteristic lines in the spectrum from an X-ray tube (Figure 2.23(b)).

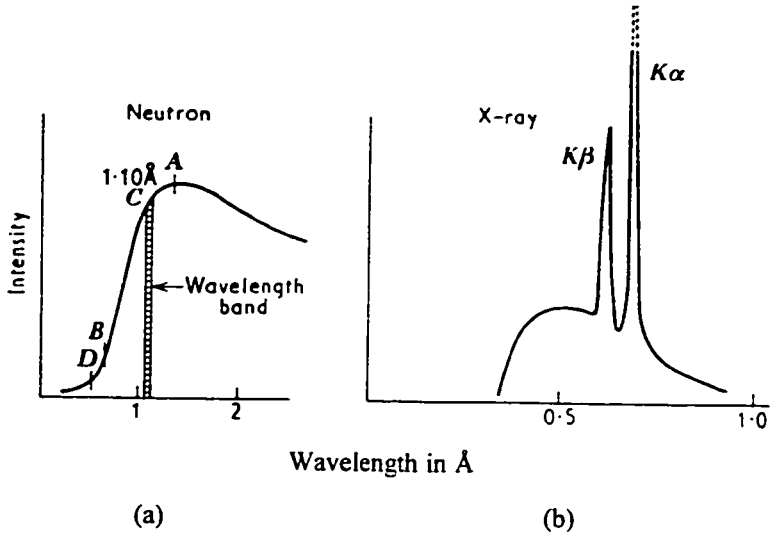

Figure 2.23: Wavelength distribution for a) neutrons, and b) X-rays (Bacon, 1975).

In order to extract a beam of a given wavelength, a monochromating crystal arrangement is generally used. The neutron beam emerging from the reactor is first collimated using Soller slits. These consist of long cadmium-lined channels which absorb neutrons which are off axis by more than a critical angle defined by the length of the channel and the width of the slits (Bacon). The collimated beam is then made to impinge on a crystal large enough to receive the whole of the beam. At any particular angle, neutrons will be diffracted into the channel if they lie within a small band of wavelength centred about a value given by Bragg's Law (Equation 2.12). The resulting monochromatic beam is then directed onto the specimen to be analysed. This method of producing a monochromatic beam of neutrons is similar to the use of a monochromator for producing crystal-reflected X-rays with one important difference. In the case of X-rays, the reflected radiation comprises solely a single line or close doublet of the X-ray spectrum. The monochromator separates this line from the general range of wavelengths which constitute the background of white radiation. For neutrons, however, since there is no equivalent of the X-ray line spectrum, the monochromator merely selects a band of wavelengths. In practice, the width of the band is of the order of 0.05Å, compared with about 0.001Å for X-rays. This width is one of the factors which limits the resolution that can be obtained from neutron diffraction experiments.

The intensity of a neutron beam emerging from a reactor is very weak, in terms of the number of quanta, compared with normal X-ray beams. Thus, in order to obtain reasonable counting statistics, a beam of large cross-section must be used, collimation can only be relatively poor, and specimen and apparatus dimensions are much greater. Fortunately, these limitations do not preclude the use of neutrons altogether because of the low absorption coefficient of most materials for neutrons. Indeed, the principal

advantage of using neutrons rather than X-rays as a probe of strain lies in the fact that neutrons can penetrate deeply (about 3 to 4 cm) into most metals to determine the internal strain within the bulk of the material, whereas X-rays can only be used non-destructively to examine stresses in near-surface regions.

When a monochromatic beam falls on a polycrystal at a fixed angle of incidence, and the area is large enough to contain a large number of crystals, every set of lattice planes will be able to diffract. This is because there is likely to be a number of grains which are correctly oriented within the aggregate for diffraction by each set of lattice planes. The beam will thus be diffracted in all directions and either a single mobile counter or a set of detectors must be used to collect data over a range of angles.

In neutron diffraction, the volume of material sampled is defined by the intersection of the incoming and outgoing neutron beams in the sample (Figure 2.24). The direction of the beams can be defined either by collimators or by a window defined by apertures at the sample. Typically the minimum volume which can be sampled is of the order of a few mm^3. The cross-section of the incident beam can be defined both vertically and horizontally by using neutron absorbing cadmium masks, and a similar mask can be used to define the horizontal extent of the scattered beam. Limiting the vertical extent of the scattered beam taken from the sample does not help define the scattering *volume* since the beam is in the form of a Debye-Scherrer cone with the incident beam as axis. However, such a restriction can help to define the angle of the scattering planes from which the scattering is accepted. This may be of importance in the study of textured samples.

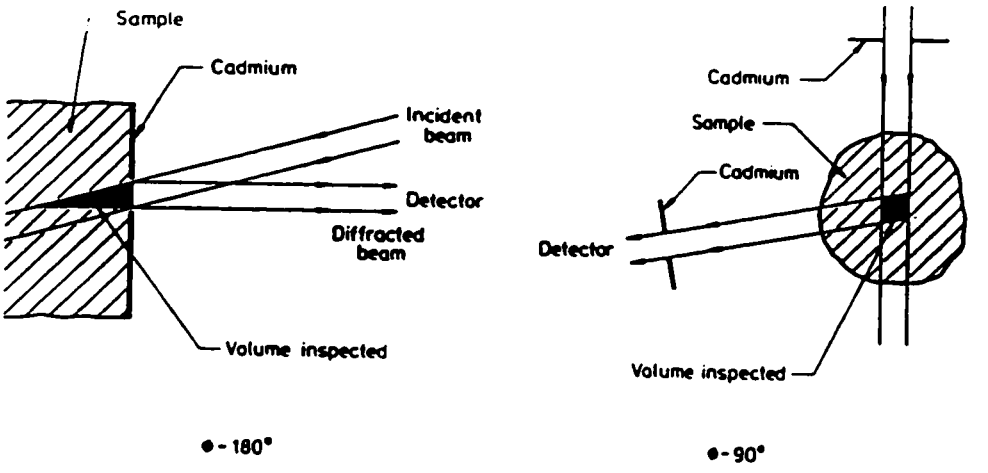

Figure 2.24: Schematic illustration of the volume over which the strain is measured by neutron diffraction (Allen et al., 1985).

2.6.2 Principle of strain measurement by neutron diffraction

2.6.2.1 Strain measurement

The principle used is the same as that of the well-known X-ray technique in which elastic lattice strain is measured. The method is based on Bragg's Law (Equation 2.12). For a monochromatic beam of neutrons (constant λ), Bragg's Law can be differentiated to yield:

$$\frac{\Delta d}{d_0} = -\cot\theta(\Delta\theta) \qquad (2.14)$$

for a given reflection (d_0 is the lattice spacing in the unstrained material). Thus a small lattice strain $\varepsilon = \Delta d/d_0$ will give rise to a change (shift) in the scattering angle for a given reflection.,

$$\Delta\varphi = 2\Delta\theta = -2\,\varepsilon\tan\theta \qquad (2.15)$$

from which the strain ε - perpendicular to the reflecting planes - can be determined. In order to measure the spacing of a given set of planes in a given sample direction, it is necessary to position the detector at the appropriate Bragg angle and orient the sample so that the desired direction is parailel to the scattering vector. Figure 2.25 shows how the detector position and sample orientation must be changed in order to measure plane spacing for two different hkl planes along the same sample direction.

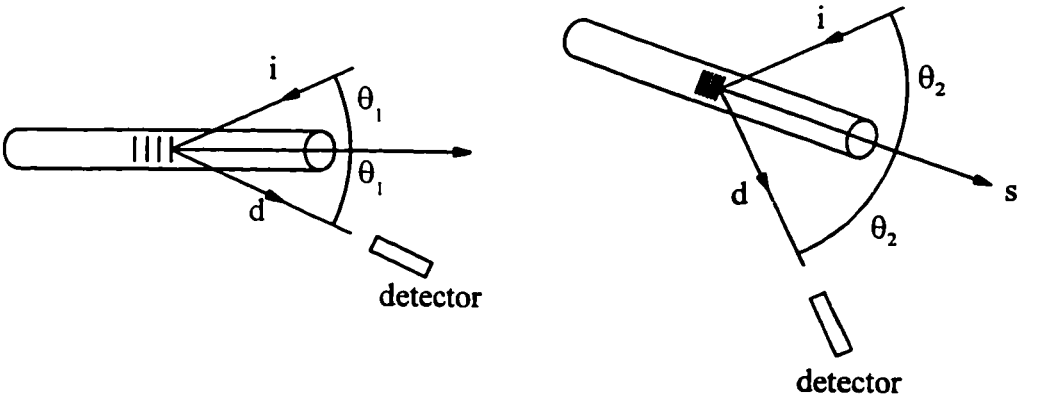

(a) $\{h_1\ k_1\ l_1\}$ (b) $\{h_2\ k_2\ l_2\}$

Figure 2.25: Diagram showing how detector position and sample orientation change when measuring the spacing of different hkl planes along the same sample direction.
($\theta_2 > \theta_1$ because $d_2 < d_1$)
i = incident beam, d = diffracted beam, s = scattering vector
The incident beam direction is the same in both figures so it is necessary to rotate the sample and the detector.

In order to obtain a complete description of the state of elastic strain in a single crystal it is necessary to measure the lattice strain in at least six different directions. These measurements yield six equations of the form:

$$\varepsilon(l,m,n) = l^2\varepsilon_{xx} + m^2\varepsilon_{yy}+n^2\varepsilon_{zz}+2lm\varepsilon_{xy}+2ln\varepsilon_{xz}+2mn\varepsilon_{zz} \qquad (2.16)$$

which can then be solved to yield the strain tensor ε_{ij} (l,m, and n are the cosines of the angles between the direction in which ε is measured and the x, y, and z axes, respectively). In a polycrystal, each diffraction signal is associated with a range of grain orientations rather than a single well-defined orientation. It is important to bear this in mind when interpreting data.

From this discussion, it is clear that the shift in Bragg angle relative to that of the stress-free material serves to determine the average lattice macrostrain over the volume sampled. The lattice microstrain, that is, the strain which is constant over only a few grains or within a grain, is reflected in the increase, above the resolution width, in the width of the diffraction peak. However, the interpretation of this information is quite complex.

Thus far, only elastically strained samples have been considered. Once the yield point has been reached, the macroscopic strain will have both an elastic and a plastic contribution. It is important to realise that the peak shift in diffraction tests measures only the elastic lattice strain, which generally continues to be proportional to the elastic component of the macroscopic strain.

2.6.2.2 Previous work

An excellent overview of neutron diffraction methods for the study of internal strain fields is provided by Allen et al., 1985. The authors describe the various set-ups possible for these experiments and present validation experiments in which they use the technique to measure the internal strain distribution in samples of 'ideal' geometry for which the stress pattern is well known from theoretical analyses or from measurements using other techniques.

MacEwen et al., 1983 used neutron diffraction measurements to study residual grain interaction stresses in Zircaloy-2. The authors strained highly textured Zircaloy-2 bars in tension and compression beyond the yield point and measured the residual lattice strain on unloading in two sets of grains (I and II) having the $\{10\bar{1}0\}$ and $\{11\bar{2}0\}$ prism planes normal to the loading direction and in a third set (III) having the (0002) basal planes normal to the loading direction. They were able to demonstrate that the residual lattice strains in grains I and II were opposite in sign to those in grains III for both tension and compression, and were consistent with the texture and anisotropic yield surface of Zircaloy.

In-situ neutron diffraction measurements have been used by Allen et al., 1992 to elucidate the extent of load transfer taking place between matrix and reinforcement in two Al-SiC metal matrix composites, one containing SiC whiskers and the other SiC particles. They proposed a model based on relaxation of thermally induced stresses which agreed quite well with the neutron diffraction results.

2.6.2.3 Summary

Neutron diffraction provides a means of obtaining information from different components of a microstructure, which can be selected by the user. The high penetrating power of neutrons makes them ideal as a probe for thick sections; the volume giving rise to the diffracted signal can be selected by using cadmium slits.

It is theoretically possible to completely characterise the state of strain in a single crystal. However, this is impossible for individual grains in a polycrystalline aggregate because each measurement represents an average over several grain orientations. Thus, generally only incomplete information is obtained which nevertheless provides very useful data for the evaluation and development of theoretical models.

3. EXPERIMENTAL METHODS

3.1 Introduction

This chapter is concerned with the preparation, characterisation, and mechanical testing of the binary Mg-Al alloy and the pure magnesium samples used in this study. The materials were first cast and extruded. This was followed by heat treatments to produce a precipitation-hardened structure in the alloy samples, and to produce the desired grain size in the pure magnesium samples. Monotonic, cyclic loading, and strain reversal tests were performed in order to obtain flow curves for a variety of strain paths. Mechanical tests were also performed while simultaneously measuring lattice spacings within the grains by in-situ neutron diffraction. All the neutron diffraction experiments were performed at Atomic Energy of Canada Limited, Chalk River Laboratories. Transmission electron microscopy and optical microscopy have been used to characterise the deformation behaviour of the material.

3.2 Materials Preparation

3.2.1 Preparation of extruded materials

The binary alloy used in this study was produced at the Pechiney Research Centre in Voreppe, France from a grade of magnesium having the composition given in Table 3.1.

Table 3.1: Composition of the magnesium used to prepare the binary alloy.

Element	Cu	Fe	Mn	Si	Al	Ni	Zn	Ca	Ti	Pb	Sn	Na
ppm	45	35	480	350	65	5	65	25	5	10	5	5

The magnesium was melted in a crucible at 650°C under an argon and sulphur hexafluoride atmosphere in order to avoid ignition. The required quantity of aluminium was then mixed in with the liquid magnesium and the resulting alloy cast in cylindrical ingots of 64mm diameter. The alloy was then extruded at 250°C under a pressure of 250 bars to a final diameter of 15mm. The bars were then annealed for 24 hours at 400°C. The magnesium bars used in this study as a reference material were prepared in exactly the same way except that no aluminium was added to the melt.

3.2.2 Heat treatments for the alloy and pure magnesium

The magnesium alloy was given a solution treatment followed by an ageing treatment to produce a microstructure containing only continuous precipitation. The mechanical test samples were machined before heat treating them in order to remove any residual stresses which might be produced. This

posed a problem, however, as the surface condition of the samples deteriorated considerably when heat treated in air. This problem was resolved by sealing the samples under approximately one half atmosphere of argon in Pyrex ampoules. The ampoules were then placed in the furnace.

In order to achieve a suitable quench in cold tap water after the solution treatment, it was necessary to remove the ampoules as quickly as possible from the furnace and break them against the side of the water bucket so that the samples would come into direct contact with the quenching medium. It was then necessary to reseal the samples in new ampoules for the ageing treatment.

3.2.2.1 Ageing schedule for the Mg-Al alloy

The first step in the ageing schedule was to solution treat the as-received alloy in order to dissolve any precipitates which may be present due to inadequate quenching of the extruded bars after annealing at Pechiney. Thus the alloy samples were left for eight hours at 415°C after which they were immediately quenched into cold water as previously described.

Figure 2.19 shows that the only way to obtain a microstructure containing only continuous precipitation in a Mg-7.7at%Al alloy is to artificially age the alloy at a temperature somewhat above 300°C. At this temperature, however, we can expect little precipitation because the difference in composition between the supersaturated solid solution and the equilibrium solid solution is very small. However, it is known that once continuous precipitation has advanced sufficiently, discontinuous precipitation is inhibited (Duly, 1992). It is thus possible to start ageing at a high temperature in order to favour continuous precipitation, then to lower the ageing temperature so that the reaction can proceed to a greater extent, thereby producing a higher volume fraction of precipitates. This approach was successfully adopted. The samples were loaded into a furnace at 330°C, held at this temperature for 10 minutes, then allowed to cool to 100°C in the furnace at a rate of 0.86 °C per hour. Once the samples reached this temperature they were removed from the furnace and allowed to cool to room temperature in air. The resulting microstructure is described in detail in section 3.3.

3.2.2.2 Heat treatment for pure magnesium

The extruded magnesium was annealed for 2.5 hours at 415°C in order to obtain the same nominal grain size as in the binary alloy. After annealing, the samples were removed from the furnace and allowed to cool to room temperature in air.

3.2.3 Preparation of the intermetallic single crystal

A single crystal of the intermetallic $Mg_{17}Al_{12}$ was prepared in order to measure the elastic constants of the material and to study its deformation behaviour. The base material was prepared as described in section 3.2.1 using the appropriate stoichiometric quantity of aluminium for the congruent-melting compound.

The material was then remelted and cast under vacuum into a graphite old which had a cylindrical shape with a tapered end (Figure 3.1). A graphite rod was then screwed into the bottom of the old to act as a support and as a heat conduit.

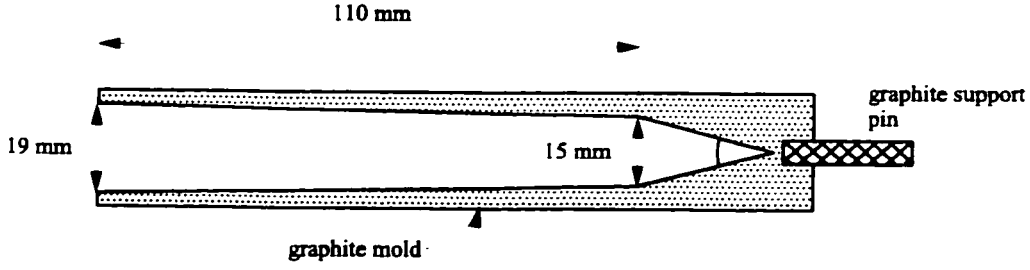

Figure 3.1: Diagram of graphite mould used for the Bridgeman single crystal growth.

The entire assembly was then placed in a quartz tube which was evacuated and back-filled with argon to a pressure of about one half atmosphere. The tube was suspended from a moving crosshead which allowed it to be lowered through a furnace. To produce the crystal, the mould was heated inside the furnace (and inside the quartz tube) until the material inside melted, then lowered at a rate of 3mm/hour through the furnace until the entire length of the mould was outside of the hot zone.

The quality of the single crystal was evaluated by X-rays. Broad beam Laue patterns were obtained for the same orientation from either end of the specimen. The patterns obtained (Figure 3.2) show that the crystal lattice has essentially the same orientation at both ends of the crystal, though there is a slight rotation (about 2°/cm) of the lattice about the long axis of the crystal. The fine structure of the spots indicates that the crystal is striated with small misorientations across its cross-section.

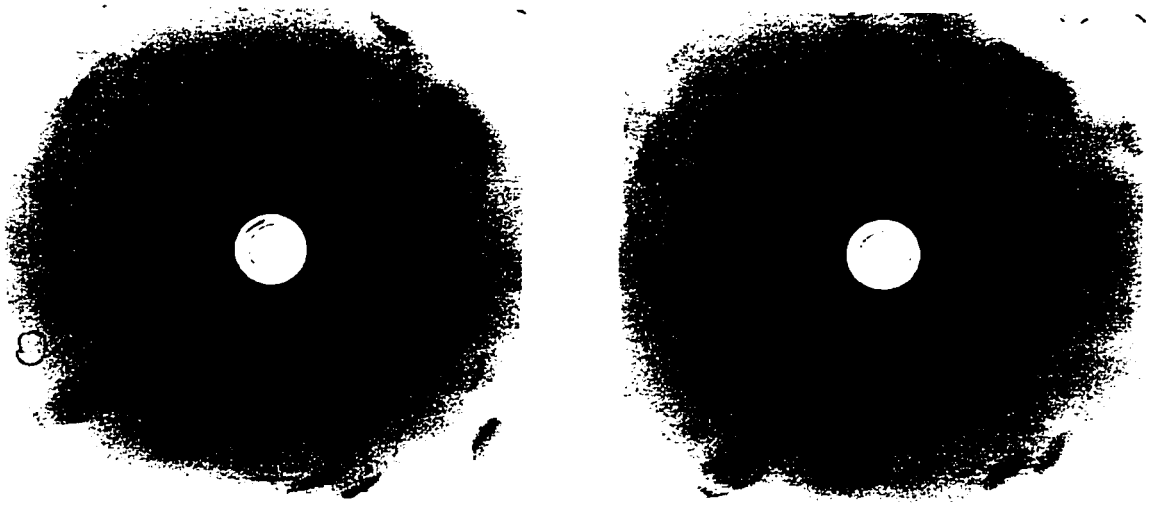

Tapered end Thick end

Figure 3.2: Broad beam Laue patterns from the intermetallic single crystal.

3.3 Materials Characterisation

The materials were characterised in terms of their grain size and texture. In addition to this, the volume fraction of precipitates in the two phase alloy was measured using a neutron diffraction technique and the average size and spacing of the precipitates was determined by transmission electron microscopy.

3.3.1 Grain size

Duly, 1992 observed that the grains obtained in the extruded binary Mg-Al alloys are equiaxed. The grain size in the aged binary alloy used in the present study was measured using the line-intercept technique on several samples. It was found to vary between 60 and 70μm. The grain size of the pure magnesium was approximately the same as for the binary alloy, though the error in the measurement is somewhat larger because the grains are not always easily distinguished from one another. Typical micrographs used to evaluate the grain size are shown in Figure 3.3.

3.3.2 Texture

Texture measurements were done by neutron diffraction using a four-circle goniometer. The variation of signal intensity with sample direction in both the pure magnesium and the aged alloy was measured for several peaks.

Stereographic pole figures are shown in Figure 3.4 for one alloy and one magnesium sample. In these figures, the extrusion axis is normal to the plane of the paper, η represents a rotation about the extrusion axis, and χ represents a rotation about a diameter of the cross section of the rod. The contour lines relate orientations showing the same diffracted intensity. The heavy contour line represents the orientations at which the intensity is that expected from a completely random distribution of grain orientations, normalised to 1. Solid and dashed contour lines represent increases and decreases in intensity, respectively. The contour separation is indicated for each figure. Thus the solid contour adjacent to the unity contour in the alloy basal (0002) plane pole figure represents orientations for which the intensity is 1.5 times that expected from a completely random sample.

The basal (0002) pole figures show pronounced cylindrical symmetry, which is a typical consequence of the extrusion process in HCP metals. The basal poles are preferentially oriented at angles greater than about 60° from the extrusion axis in both materials and the intensity of the poles increases as the normal to the extrusion axis is approached.

The $\{10\bar{1}0\}$ pole figures are essentially the reverse of the (0002) pole figures, with the prism normals concentrated in the centre of the projection rather than at the periphery, i.e. the prism poles are preferentially aligned parallel to the extrusion direction. The cylindrical symmetry is much less pronounced than in the basal pole figures, particularly for the alloy.

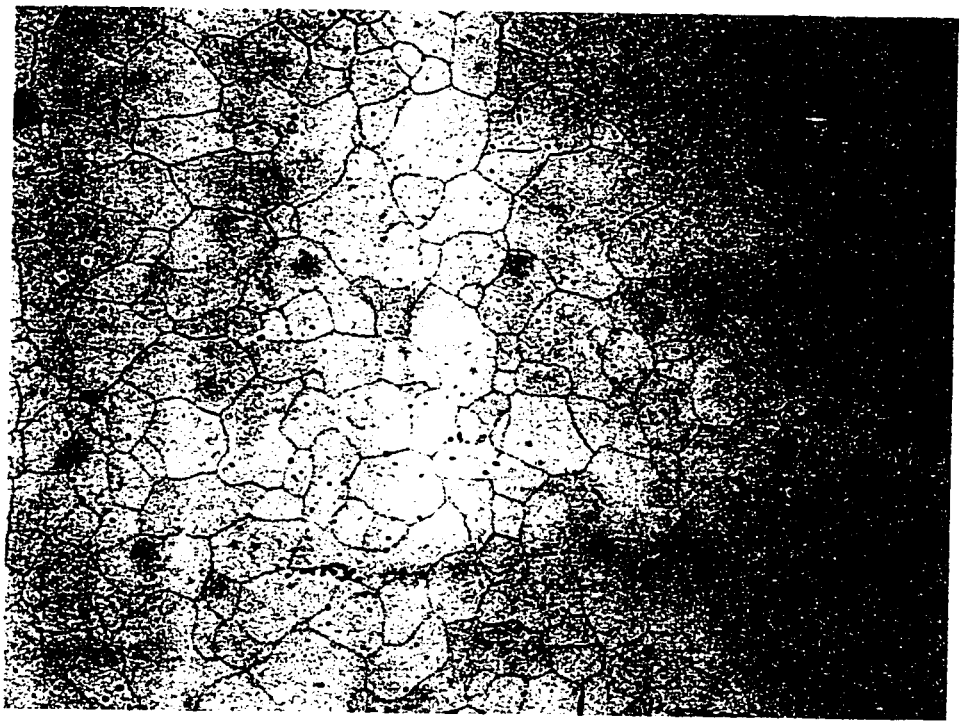

(a) x 110

(b) x 70

Figure 3.3: Optical micrographs illustrating the grain structure in (a) the alloy, and (b) pure magnesium.

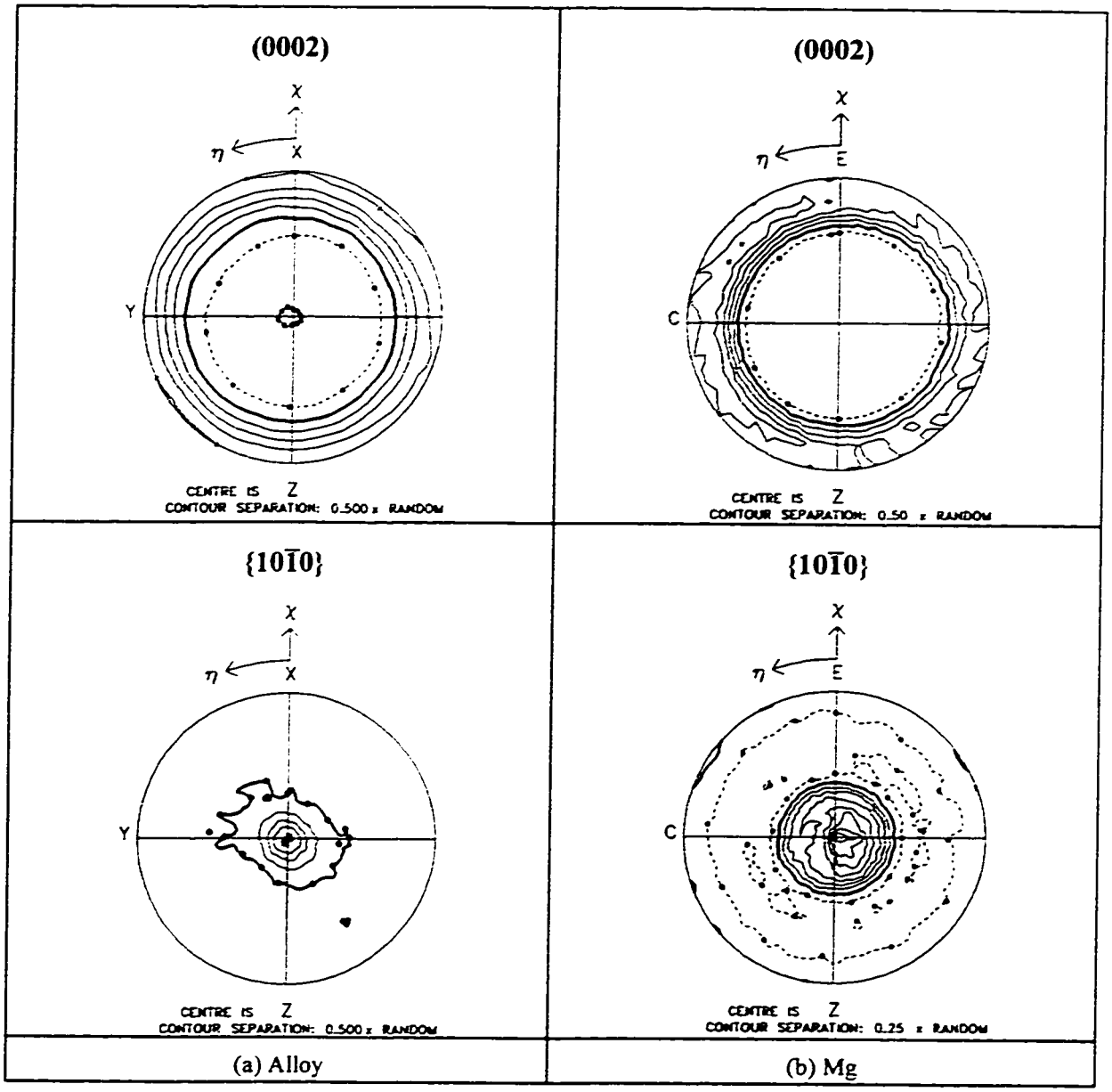

Figure 3.4: Stereographic pole figures for (a) the aged alloy, and (b) heat treated pure magnesium.

3.3.3 Volume fraction of the second phase

The volume fraction of the second phase was measured using neutron diffraction as it was difficult to do by conventional metallographic techniques due to the morphology of the precipitates. In addition, the neutrons could easily sample a large volume, thus producing a good average value. The measurement is based on the following equation:

$$I \propto V \cdot S \cdot L \cdot T \tag{3.1}$$

where I is the integrated intensity of the diffraction peak, V is the volume of material giving rise to the peak, S is the structure factor for the plane under consideration assuming it is produced by a powder sample, L is the Lorentz factor, and T is a parameter related to the texture of the material. If the intensity of a matrix peak, I_{mat} and that of a precipitate peak, I_{ppt} are measured, then the volume fraction of the precipitate will be given by the following expression:

$$V_f = \frac{\dfrac{I_{ppt}}{P_{ppt} \cdot T_{ppt}}}{\dfrac{I_{ppt}}{P_{ppt} \cdot T_{ppt}} + \dfrac{I_{mat}}{P_{mat} \cdot T_{mat}}} \tag{3.2}$$

where P is the product of the structure factor and the Lorentz factor. P can be calculated for any plane for any given structure from a knowledge of the atom positions in the unit cell. The integrated intensities are easily determined from the diffraction spectrum of the material. T is determined from texture measurements on the sample and is included as a correction of the structure factor which is computed assuming a powder i.e. a completely random distribution of grain orientations. In the present case, since texture measurements indicate that grain orientations are essentially symmetric about the specimen axis it is only necessary to measure intensity variations when the sample is tilted about a radial direction. If we let χ denote the angle of tilt where $\chi = 0$ corresponds to a diffracting plane normal which is perpendicular to the sample axis, then T is defined as follows:

$$T = \frac{I}{< I >} \text{ where } < I >= \frac{\sum I \sin\chi}{\sum \sin\chi} \tag{3.3}$$

The results of volume fraction calculations based on Equation 3.2 are shown in Table 3.2. Note that T_{ppt} was only measured on one sample (number 38 in Table 3.2). As it was identical to $T_{\{10\bar{1}1\}}$, it was assumed that this would also hold for the other samples .The results are consistent from sample to sample except for number 31 which yields a much higher volume fraction than the rest. Variations in precipitate volume fraction are likely due to inhomogeneity in the initial cast billet, which translates into inhomogeneity in the

extruded rod. In the calculations performed in following chapters, the volume fraction of intermetallic will be taken as approximately 10 ± 2%, bearing in mind that it can reach as high as 15%.

Table 3.2: Volume fraction of the second phase in the aged alloy.

Sample number	Plane	I/<I>	I	V_f (%)	Average
38	$\{411\}_{precipitate}$	1.3	252		10
	$\{10\bar{1}0\}_{matrix}$	1.16	466	10	
	$\{10\bar{1}1\}_{matrix}$	1.31	1996	12	
	$\{10\bar{1}2\}_{matrix}$	1.08	494	9	
35	$\{411\}_{precipitate}$	0.71	18		11
	$\{10\bar{1}0\}_{matrix}$	1.33	61	11	
	$\{10\bar{1}1\}_{matrix}$	0.71	143	12	
	$\{10\bar{1}2\}_{matrix}$	0.85	37	11	
33	$\{411\}_{precipitate}$	1.11	21		10
	$\{10\bar{1}0\}_{matrix}$	1.27	48	10	
	$\{10\bar{1}1\}_{matrix}$	1.11	205	10	
	$\{10\bar{1}2\}_{matrix}$	1.29	50	10	
31	$\{411\}_{precipitate}$	0.81	26		15
	$\{10\bar{1}0\}_{matrix}$	1.07	48	14	
	$\{10\bar{1}1\}_{matrix}$	0.81	146	16	
	$\{10\bar{1}2\}_{matrix}$	0.89	40	14	
30	$\{411\}_{precipitate}$	1.11	21		10
	$\{10\bar{1}0\}_{matrix}$	1.19	48	10	
	$\{10\bar{1}1\}_{matrix}$	1.11	198	10	
	$\{10\bar{1}2\}_{matrix}$	1.19	48	10	
Overall average = 10 ± 2 % (sample 31 disregarded)					

3.3.4 Size and distribution of the second phase particles

The microstructure obtained after precipitation treatment is shown in Figures 3.5(a) and (b). The plane of polish in the two micrographs is normal to the extrusion axis. The optical micrograph of the etched alloy (see section 3.4.1) in (a) shows clearly that the precipitates are homogeneously distributed within the grains, with large particles occurring at the grain boundaries. The continuous precipitation appears as thin black lines which are parallel in a given grain. Since the texture is such that the basal plane in most grains makes a small angle with the extrusion axis, and the basal plane is the precipitate habit plane, it is easy to see that the long direction of the precipitates in a given grain is parallel to the trace of the basal plane. Some coarse discontinuous precipitation is visible at the bottom right hand corner of the micrograph. Such precipitation is rare and accounts for no more than about 1% of the precipitation.

The central grain in the back-scattered SEM micrograph in Figure 3.5(b) clearly has its basal plane at a small angle from the surface of polish (the sample is not chemically etched). As a result, the precipitates appear as platelets rather than as thin parallel lines as in the surrounding grains. The coarse grain boundary precipitation is once again visible.

The precipitates thus clearly take the form of relatively thin platelets which can be

characterised by their thickness normal to the basal plane, as well as their length and width, measured within the basal plane. The thickness could easily be measured from TEM micrographs (see section 4.7 for several examples) with the incident electron beam parallel to the basal plane. Measurements done on 30 precipitates from different samples yielded an average thickness of 165 nm. The maximum and minimum were 90 and 360 nm, respectively. The length and width could not be quantified as well since it proved rather difficult to obtain thin foils for which the basal plane was normal to the incident electron beam. From SEM micrographs such as that in Figure 3.5(b), however, it can be seen that the length of the precipitates varies between about 6 and 20 μm, and that the length to width ratio lies between 2 and 6.

3.4 Metallography

Optical microscopy was used to obtain a low magnification view of the microstructure to characterise the distribution of platelets, to determine the grain size of the materials, and to reveal twinning in deformed samples.

Magnesium and its alloys are generally quite soft and thus easy to grind and polish. Metallographic surfaces were prepared by grinding on silicon carbide papers down to p600 grit, followed by diamond polishing using 6μm and then 1μm diamond pastes. The final polishing step was done with OPS-CHEM polishing fluid from Struers. This produced a mirror finish in both the aged alloy and the pure magnesium.

3.4.1 Chemical etches for optical microscopy

Several chemical etches were used to bring out different features as follows:

Observation of precipitates in the Mg-Al alloy

A solution of 10ml of 48% hydrofluoric acid in 90ml of distilled water was used to reveal the second phase in the binary alloy. The sample is dipped into the solution for one or two seconds then thoroughly rinsed in water and ethanol and dried in a blast of air. It is imperative when using this solution to wear thick rubber gloves and a face mask, and to work in a fume hood because of the hydrofluoric acid. In addition, it must be stored in a nalgene container as hydrofluoric acid will etch glass. When etched, the precipitates appear black or brown in the optical microscope. This etch is also suitable for scanning electron microscopy.

Grain boundary etchant for the binary alloy

Duly, 1992 developed an excellent method for revealing the grain boundaries in Mg-Al alloys. The material having the desired microstructure is first solution treated long enough to dissolve any precipitates at 415°C. The time required is at most about 10 minutes, which means that the grain size remains unaltered. This is followed by a 10 to 20 minute ageing treatment at 220°C. This allows discontinuous precipitation to start at all the grain boundaries but is not long enough for the reaction to

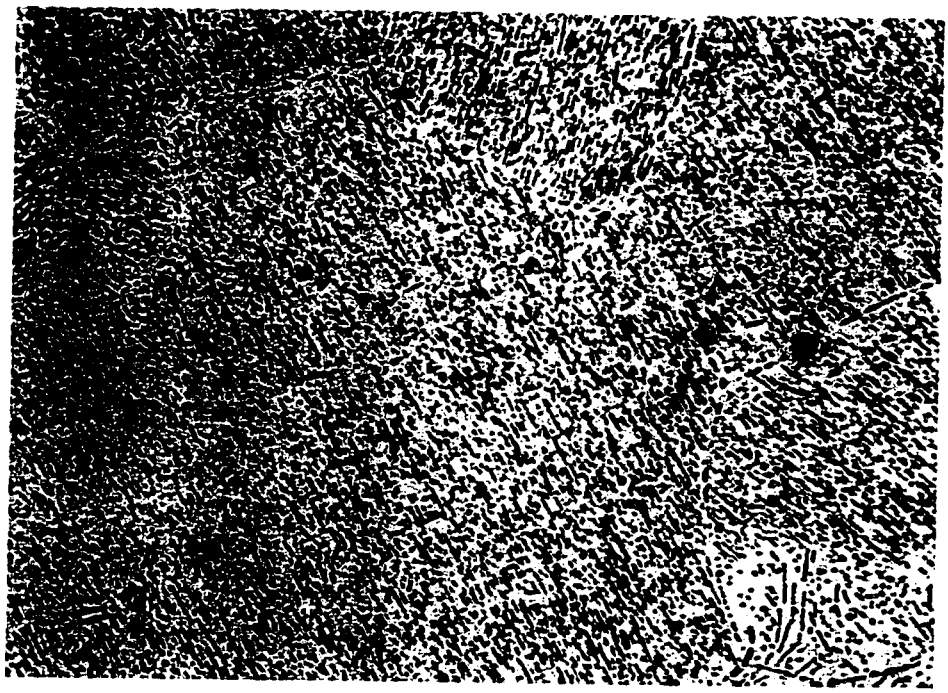

(a) x457

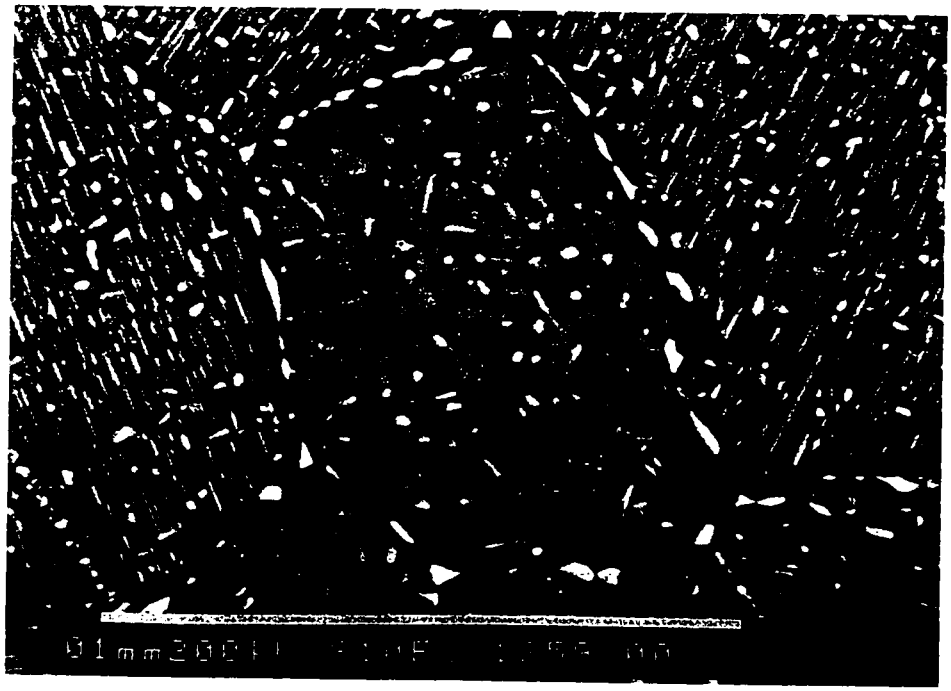

(b)

Figure 3.5: (a) Optical and (b) SEM micrographs showing the precipitate distribution in the aged alloy.

proceed appreciably into the grains. The sample is then quenched and etched using the solution described above to reveal the grain boundary precipitates which therefore act as markers.

Grain structure in pure magnesium

A solution containing 90ml of 5% picral (5g picric acid in 100ml absolute ethanol) and 10ml glacial acetic acid was used to reveal the grains in pure magnesium. The sample is immersed in the solution until its surface turns dark brown and is then rinsed with water and ethanol and dried in a blast of air. When the sample is observed in polarised light, the grain structure is revealed. Since the material is textured, as described in section 3.3.2, adjacent grains are often very similarly oriented and cannot be distinguished readily as they will appear the same under polarised light. The number of grains found in a given area is therefore somewhat dependent on personal judgement and this introduces some error in the grain size measurements.

3.4.2 Thin foil preparation for transmission electron microscopy

Transmission electron microscopy was used in this study to determine the types of twins which occur during deformation and to observe the size and spacing of the precipitates in the binary alloy. The following steps were followed to prepare the thin foils:

1) Cut a wafer about 1mm thick from the specimen of interest.
2) Cut out 3mm discs from the wafer with a spark cutter.
3) Using p600 grit silicon carbide grinding paper and kerosene as lubricant, remove equal amounts of material from both sides of the 3mm disc until a final thickness of 80 to 100μm is attained.
4) Polish one side of the foil down to 1μm diamond paste.
5) Dimple the unpolished side of the foil using a brass wheel and 4-6μm cubic boron nitride paste until a thickness of 30-35μm is reached. Finish the dimpling process by polishing with a felt-coated wheel charged with 1μm diamond paste. In all the dimpling, kerosene is used as a lubricant.
6) The final thinning is done in a GATAN duomill equipped with a cold stage using an accelerating voltage of 4kV and a gun current of 0.5mA.

Krazy glue was used to fasten the foils to the polishing jig and the holder of the dimple grinder. The samples were freed by leaving them in acetone for about one hour. Glue was used rather than mounting wax to avoid heating the sample and potentially annealing it.

3.5 Mechanical Testing

3.5.1 Sample geometry

The sample geometry used in this study is shown in Figure 3.6. This geometry was chosen because it is sufficiently squat to prevent buckling in compression. Another consideration was the fact that limited material was available so that it was necessary to avoid waste whenever possible.

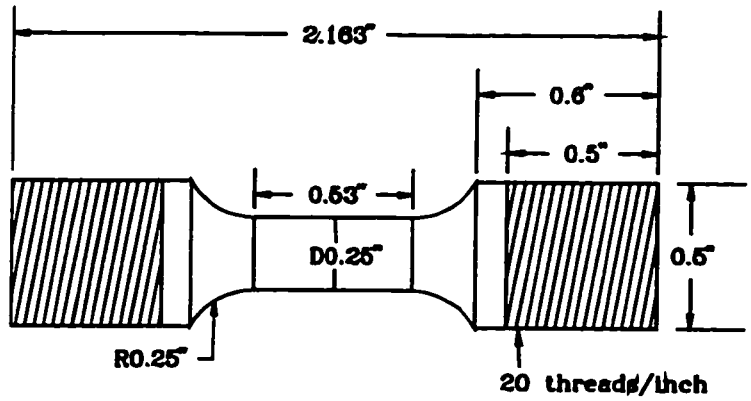

Figure 3.6: Sample geometry for mechanical tests.

3.5.2 Testing apparatus

A MTS 810 hydraulic testing machine equipped with a TESTSTAR controller, hydraulic grips, and a strain gauge extensometer was used to obtain flow curves. The controller enabled samples to be loaded into the machine without appreciable unintentional stressing.

The extensometer is intended for use at elevated temperatures and is therefore equipped with long, removable quartz rods in order to keep the body of the extensometer outside of the furnace. The gauge length of the extensometer in its high-temperature configuration is 25.4 mm (1 inch), which is too long for the samples used in this study. The quartz rods were therefore replaced with kinked stainless steel probes which reduced the gauge length and enabled the extensometer to be attached to the specimen either by metal springs or rubber o-rings. The modified extensometer was calibrated using a micrometer block. A graph of change in extensometer reading versus change in micrometer setting is shown in Figure 3.7. It is clear that the extensometer behaves very linearly over its entire range. A zero extensometer reading corresponded to a gauge length of 13.50 mm, and its range was ±2mm.

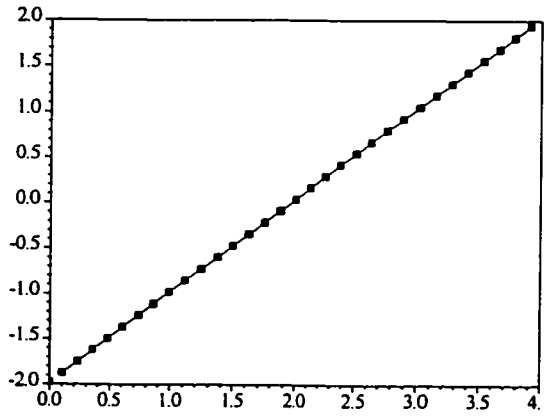

Figure 3.7: Graph showing linear behaviour of extensometer.

3.6 Neutron Diffraction Experiments

3.6.1 Spectrometer set-up

The spectrometer arrangement used for the in-situ neutron diffraction experiments is shown schematically in Figure 3.8, which represents a top view. Neutrons exit the reactor through a hole in the reactor face and enter a tube containing a set of soller slits which provide a rough initial collimation. A monochromating crystal then extracts the desired wavelength as described in section 3.5. The crystal is embedded in a large, heavily shielded drum which stops any undiffracted neutrons. The monochromatic beam then proceeds through a second soller slit collimator before it hits the sample to be analysed which is placed on a rotating sample table. Diffracted neutrons are detected using a counter which rotates about the centre of the sample table. Thus the incident and scattered beams (and therefore the scattering vector) are in the plane of the paper in Figure 3.8, which shall be referred to as the horizontal plane. The detector is controlled by a PDP-11 microcomputer connected to a VAX minicomputer. Using the software provided, the detector can be programmed to move to any desired Bragg angle and count neutrons for an appropriate length of time, thus enabling the operator to select any part of the diffraction spectrum for study. In addition to this, the sample table can be rotated so as to align the desired sample direction with the scattering vector for every measurement performed.

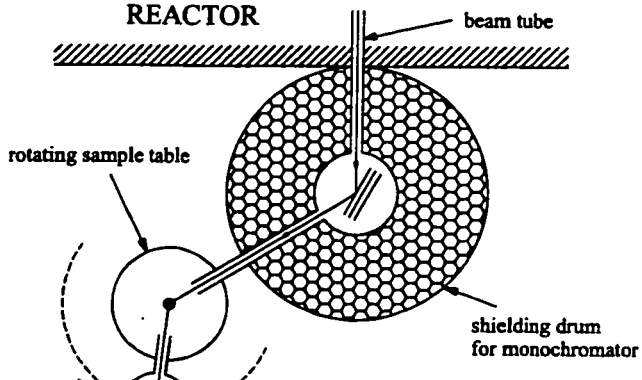

Figure 3.8: Experimental set-up for neutron diffraction experiments.

3.6.2 Mechanical test rig and strain measurement

3.6.2.1 Experimental set-up

For the in-situ tests, an ATS screw driven test rig equipped with a load cell is mounted onto the sample table. The rig is equipped with grips which are compatible with the MTS hydraulic grips mentioned

in section 3.5 so that the same sample geometry was used. In this study longitudinal (i.e. parallel to the sample axis) as well as radial (i.e. normal to the sample axis) lattice strains have been measured. Since the scattering vector defines the direction in which the lattice strains are measured, the two types of measurement necessitated different stress-rig set-ups. A photograph of the arrangement for measuring longitudinal strains is shown in Figure 3.9. The rig is placed on its side on the sample table so that the length of the sample is in the horizontal plane. For each diffracted peak, the detector is moved to the appropriate Bragg angle and the stress rig rotated so that the sample length lies along the scattering vector. The sample is mounted in the rig and the entire rig is carefully aligned so that the centre of the gauge length lies above the centre of rotation of the sample table. This is done with the aid of two telescopes which have been previously adjusted so that their crosshairs are pointing directly at the centre of the sample table. This alignment is necessary to ensure that the gauge volume does not move out of the incident beam when the stress rig is rotated. For the radial strain measurements the stress rig is set upright on the sample table so that the sample axis is normal to the horizontal plane.

Cadmium masks are used to cover the sections of the grips which may be in the path of the neutron beam in order to prevent unwanted reflections from affecting the measurements.

A MTS extensometer attached to the sample is used to measure the macroscopic strain at the same time as the diffraction data is collected. The extensometer is connected to the sample via steel springs and its body shielded from neutrons using a cadmium mask.

Since the neutron flux from the reactor can vary considerably over the course of an experiment, it is not sufficient to simply count for a predetermined time for each peak. This problem is overcome by counting until a precept number of neutrons, referred to as the monitor, have emerged from the second collimator in Figure 3.8. This ensures that the statistics are equivalent for all measurements made on a given peak.

3.6.2.2 Flow of the experiment

Once the sample is positioned in the rig and centred on the sample table, each measurement is made as follows (longitudinal strains):

1) The computer directs the stress rig to load the sample to the desired stress.
2) While the load is being maintained at the desired value by a feedback loop, the detector moves to the appropriate Bragg angle and the sample table rotates so that the sample axis lies parallel to the scattering vector.
3) The counter counts until the precept monitor value is achieved.
4) Steps 2 and 3 are repeated for each programmed Bragg reflection for the current load.
5) Steps 1 to 4 are repeated until the entire strain path has been traversed.

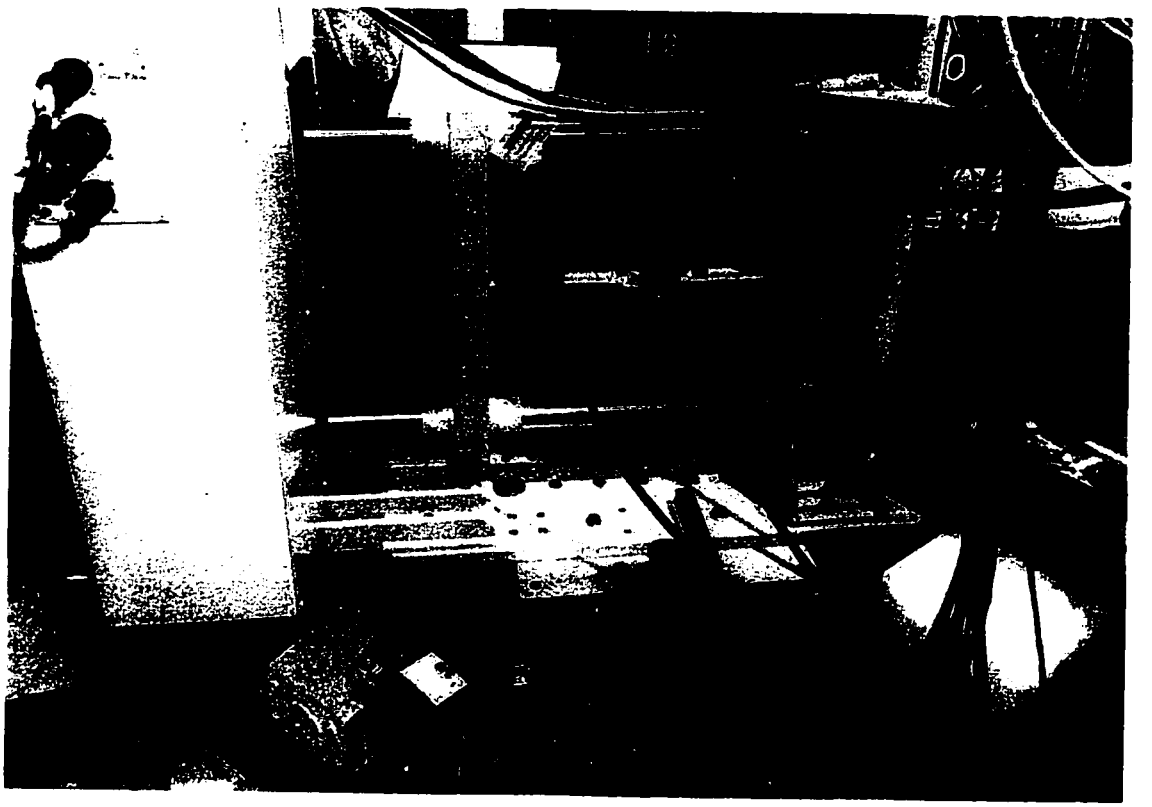

(a)

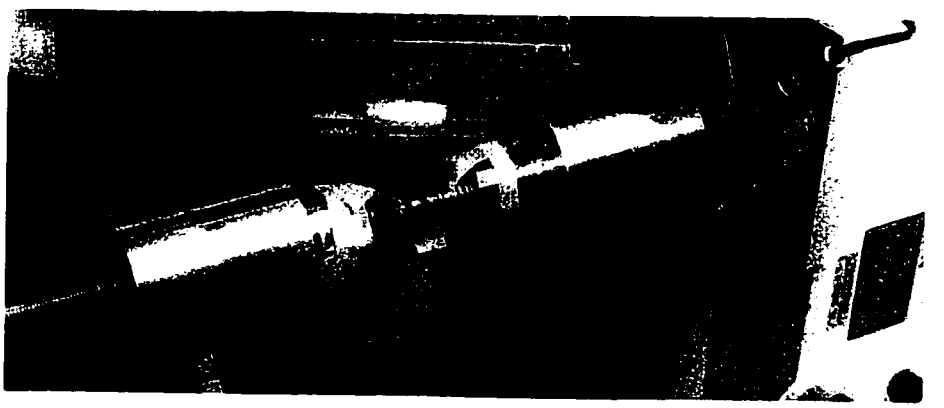

(b)

Figure 3.9: Stress-rig arrangement for longitudinal lattice strain measurements.
(a) overall view of setup.
(b) detailed view of specimen, grips, and extensometer.

All of the above steps can be programmed into the computer so that the operator need only verify that the experiment is proceeding properly every few hours. Note that at any time if the load falls outside of a precept error range during a measurement, the detector is stopped until the stress rig can readjust the load at which point the detector resumes counting. Since, as seen in section 3.3.2, the texture is symmetric about the sample axis, the sample is not rotated when measuring radial lattice strains.

3.6.3 Data analysis

A diffraction peak is defined by a set of x-y co-ordinates where x is the detector position (in degrees) and y is the number of neutrons which enter the detector during the precept monitor. In order to determine the peak position μ, the integrated intensity I, and the full width at half maximum, the following function is fitted to the data:

$$Y = b + 2m(\theta - \theta_0) + Ae^{-\frac{1}{2}\left(\frac{2\theta-\mu}{\sigma}\right)^2} \tag{3.4}$$

This represents a gaussian function, which is used to model the peak, superimposed on a linear background of intercept b and slope m. The fit is optimised by minimising the least squares error between measured values of Y and calculated values using a Newton-Raphson iterative scheme. Initial estimates of the five parameters b, m, A, μ, and σ are obtained from the raw data.

In order to determine the uncertainties in the fitted parameters, Equation (3.5) is used to determine the root mean square error (χ) as follows:

$$\chi = \sqrt{\frac{\sum_{i=1}^{N}(Y_i^{calc} - Y_i^{exp})^2}{(N-5)}} \tag{3.5}$$

where N is the number of experimental data points for the given peak. This parameter is then used to determine the error in each fitted parameter.

Once a peak has been fitted, the full width at half maximum (FWHM) and the integrated intensity (I) can be calculated from Equations 3.6 and 3.7, respectively.

$$FWHM = \sigma \cdot \sqrt{8 \cdot \ln 2} \tag{3.6}$$

$$I = A \cdot \sigma \cdot \sqrt{2\pi} \tag{3.7}$$

The lattice strain is calculated from Equation 2.14 with $\theta_0 = \mu_0/2$ and $\theta = \mu/2$ (in radians). The error in the lattice strain is determined by differentiating Equation 2.14 to yield:

$$d\varepsilon = \sqrt{\left(\frac{\cos\theta_0}{\sin\theta}(\Delta\theta_0)\right)^2 + \left(\frac{\cos\theta\sin\theta_0}{\sin^2\theta}(\Delta\theta)\right)^2} \tag{3.8}$$

where $(\Delta\theta_0)$ and $(\Delta\theta)$ are the errors in the values of θ_0 and θ, respectively.

In the set-up used for the present in-situ experiments, the error in the measured lattice strain is typically 1-2x10^{-4}. The error in the integrated intensity and in the FWHM is generally of the order of 3-4%, though it can be as high as about 7% for the precipitate peak which is relatively weak. A good fit and a poor fit are shown in Figures 3.10(a) and (b), respectively. The poor fit is for a precipitate peak which has a relatively low intensity, whereas the good fit is for a {10$\bar{1}$0} peak obtained with the scattering vector parallel to the longitudinal axis of the specimen (this peak is very strong due to the texture of the material).

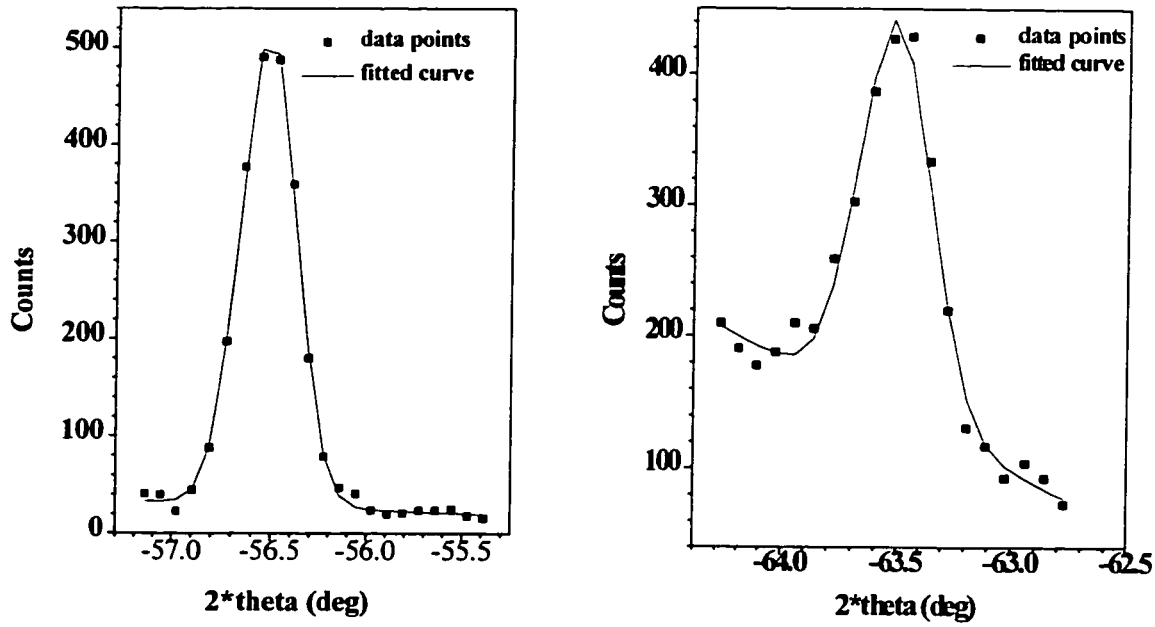

(a) (b)

Figure 3.10: Examples of (a) a good and (b) a poor fit to neutron diffraction peak data.

4. EXPERIMENTAL RESULTS

4.1 Introduction

This chapter is divided into the following sections: monotonic tension, monotonic compression, cyclic tension, cyclic compression, tension-first Bauschinger, and compression-first Bauschinger. Bauschinger tests are described in Chapter Two and provide a simple means of investigating the effect of strain path on mechanical behaviour. Each section contains a description of the results from mechanical tests (stress-strain curves) and in-situ neutron diffraction experiments. The stress-strain curves represent the average behaviour of the entire polycrystal while the neutron diffraction results yield lattice strains which are averaged over one component of the texture (see section 2.6); thus these results provide a macroscopic view of the deformation behaviour. Observations by optical and transmission electron microscopy (TEM) are presented in a separate section. The TEM observations provide complementary information at a microscopic level which relates to the nature of the debris produced by plastic flow.

It is useful to characterise the mechanical and thermal properties of the second phase to determine how it can contribute to the strength of the two-phase alloy. Results from experiments on the single crystal of the intermetallic $Mg_{17}Al_{12}$ are described in a separate section.

Throughout this chapter, the two-phase binary Mg-Al alloy samples and the pure magnesium samples are referred to as 'the alloy' and 'the Mg', respectively.

Comparison of the mechanical response of the two materials is made using true stress-true strain curves. In addition, the slope of the stress-strain curves, $d\sigma/d\varepsilon$, is plotted against true strain.

The in-situ neutron diffraction results are presented as plots of applied stress versus lattice strain, peak intensity, and peak full width at half maximum (FWHM). As discussed in Chapter Three, both axial (parallel to the stress axis) and radial (normal to the stress axis) lattice strains have been measured in this study.

For easy reference, the crystallographic planes for which the lattice strains were measured are shown in Figure 4.1. Table 4.1 contains the Young's modulus for the directions normal to the planes. This is obtained by rotating the compliance matrix S_{ij} so that the '1'-direction is parallel to the normal of the plane of interest; the desired Young's modulus is then $1/S_{11}^{rotated}$. Each of these planes corresponds to a particular grain orientation and therefore to a particular component of the texture. The angle between the basal pole and the stress axis for each component of the texture corresponding to a lattice plane is therefore also included in Table 4.1.

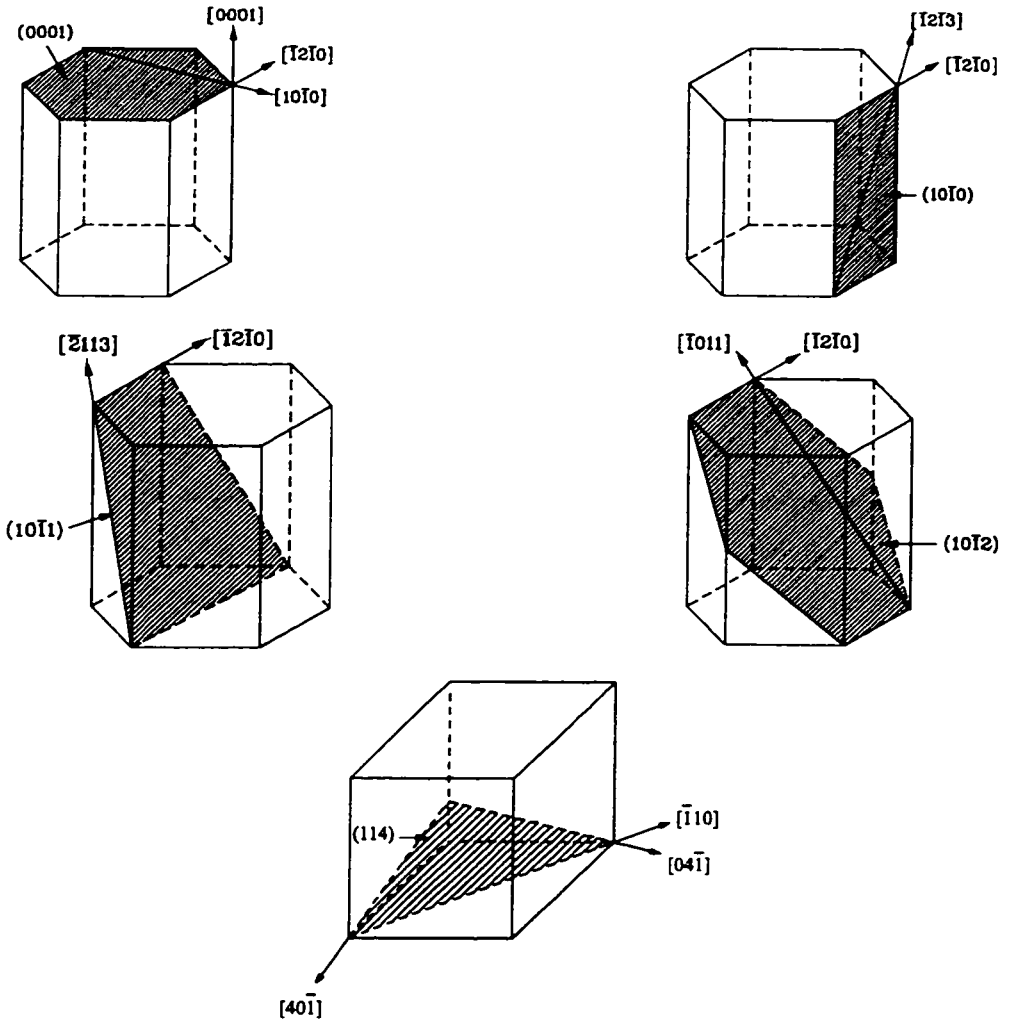

Figure 4.1: Planes for which the lattice strains have been measured.

Table 4.1: Young's modulus for directions normal to the planes in Figure 4.1.

Plane	Young's modulus normal to plane (GPa)	Angle between stress axis and [0001] (or [001])	
		Axial lattice strains	Radial lattice strains
{10$\bar{1}$0} (matrix)	45.45	90°	0°
(0002) (matrix)	50.74	0°	90°
{10$\bar{1}$1} (matrix)	43.28	62°	28°
{10$\bar{1}$2) (matrix)	43.27	43°	57°
{411} (precipitate)	83.17	76°	14°

4.2 Monotonic Tension

Since buckling does not occur in tension (in contrast to the behaviour in compression), the materials were deformed to fracture in tension. The tensile stress-strain behaviour of the alloy and the Mg is shown in Figure 4.2. The alloy is clearly much stronger than the Mg, but its ductility is comparable. Neither curve shows a well-defined linear portion corresponding to linear elastic deformation, indicating that some slip is taking place at very low applied stress. The elastic-plastic transition is difficult to define.

The $d\sigma/d\varepsilon$ vs. ε curves are shown in Figure 4.3 along with the difference between them. The results are shown only up to 1% true strain because beyond this point $d\sigma/d\varepsilon$ is the same in the two materials and varies very little. There is an inflection point in the alloy curve which is not present in the Mg curve. The difference between the two slopes is essentially constant up to about 0.5% true strain at which point it decreases until the two curves overlap.

The in-situ neutron diffraction results obtained for the alloy are shown in Figure 4.4 (axial strains) and Figure 4.5 (radial strains). The highest stress tested is 190 MPa, which is the point at which macroscopic plasticity begins.

Three horizontally arranged graphs are shown for each plane for which measurements were made. The plane corresponding to each set of graphs is identified in the first (left) graph (see Figure 4.4). Applied stress is plotted against lattice strain in the first graph, against integrated intensity in the middle graph, and against FWHM in the last graph. The lattice strain, intensity, and FWHM graphs for all the planes are vertically aligned for easy comparison between planes.

The three graphs in a given row share the same y-axis so only the axis on the first graph is labelled. Numerical labels are provided for all of the x-axes in the figure, but text is only included for the axes in the last row. Data points connected by a solid line correspond to measurements made while the absolute value of the applied load was being increased (loading) while a dashed line is used to connect points for measurements made during unloading.

A description of the salient features of the neutron diffraction results is provided for each plane in Table 4.2. The intensity always shows some variability and care must be exercised in deciding whether a given change is significant. In general, it is better to consider trends rather than looking at isolated values.

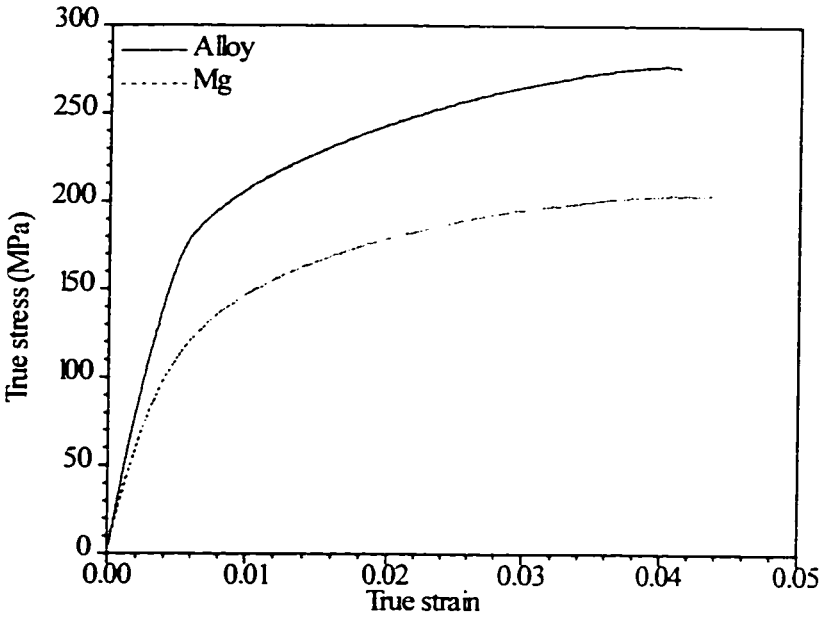

Figure 4.2: Tensile stress-strain curves for the alloy and the Mg.

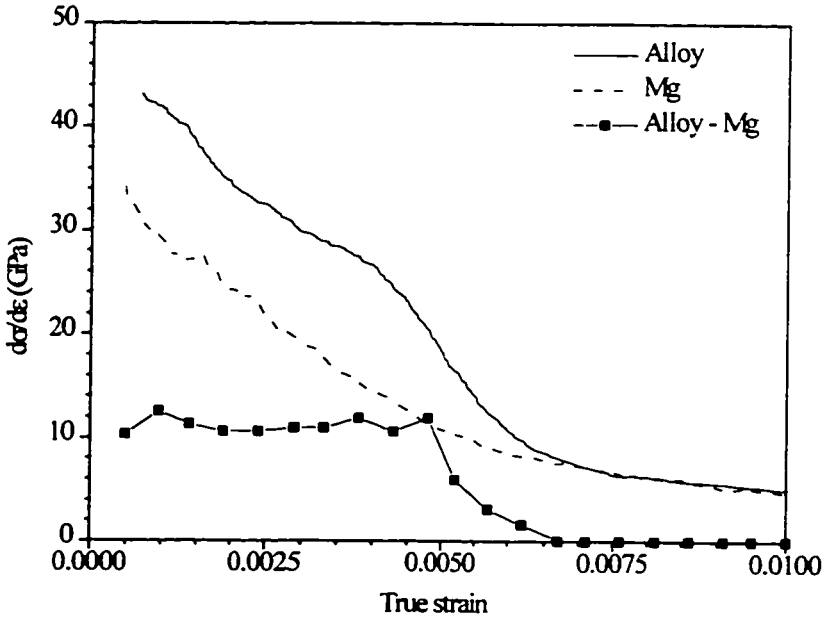

Figure 4.3: dσ/dε vs. ε curves for the alloy and the Mg deformed in tension. The difference between the two curves is also plotted.

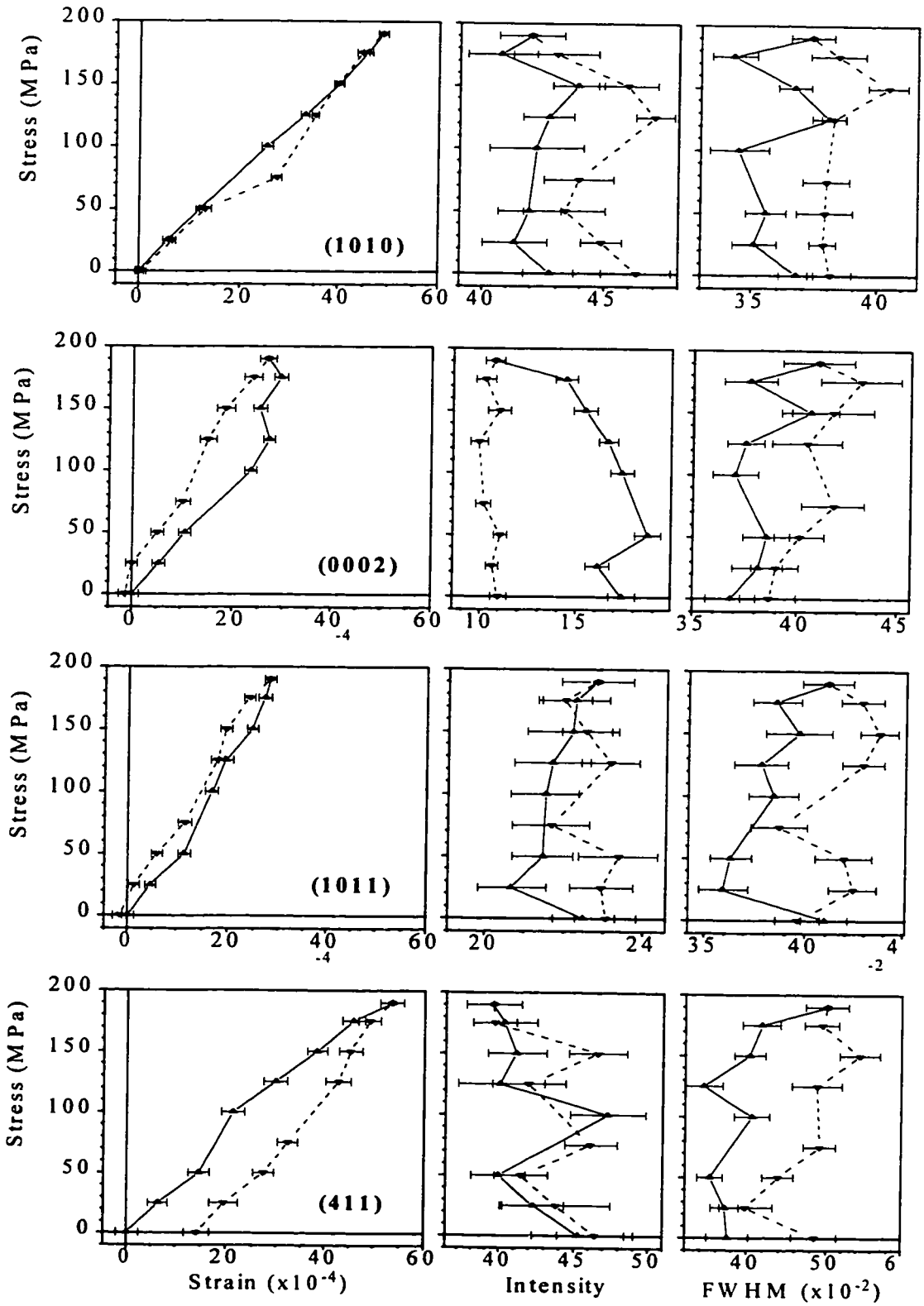

Figure 4.4: Neutron diffraction results - axial strains, monotonic tension.

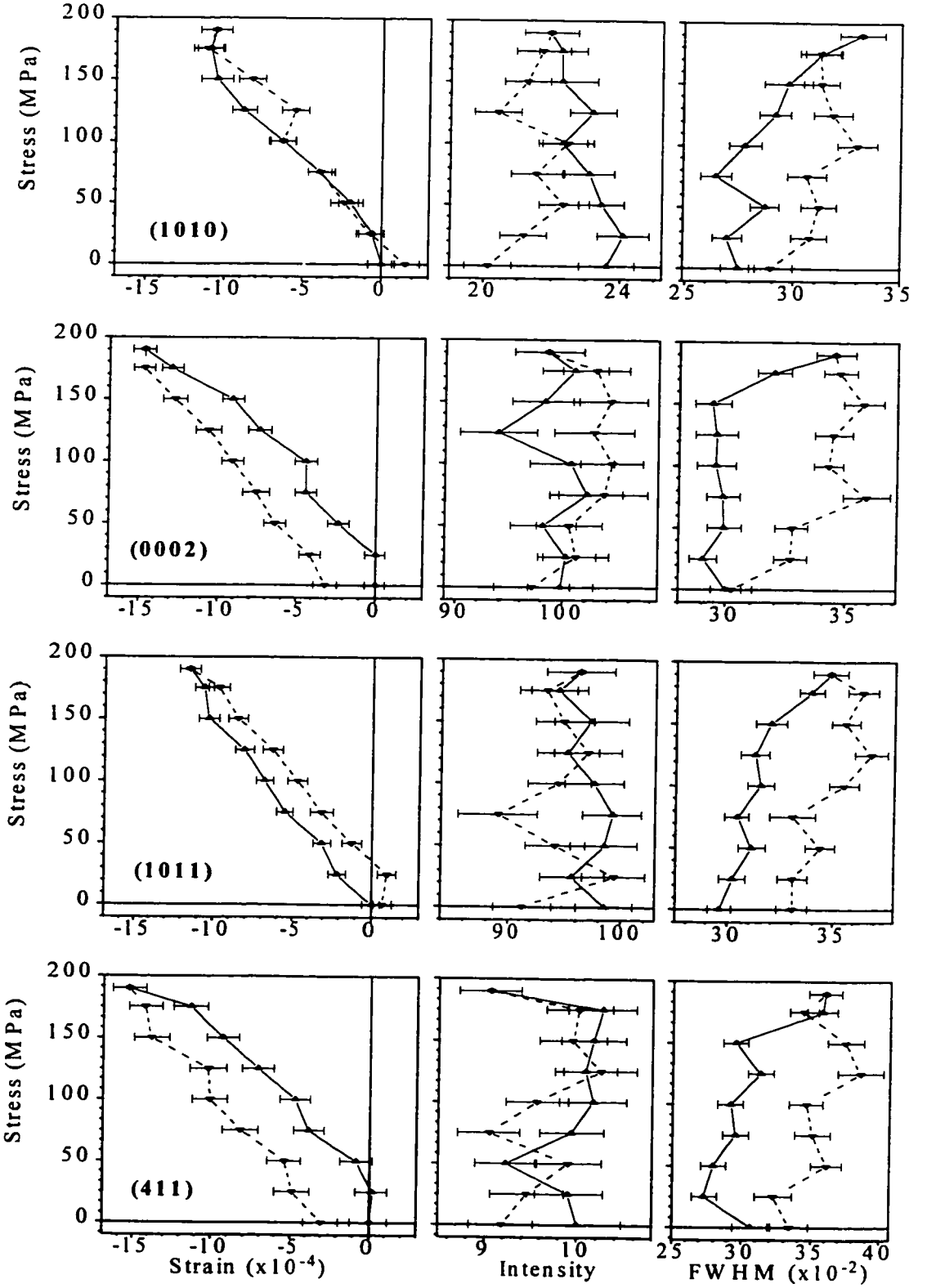

Figure 4.5: Neutron diffraction results - radial strains, monotonic tension.

Table 4.2: Neutron diffraction results - monotonic tension.

{10$\bar{1}$0} axial	• The stress strain curve is linear; the loading and unloading portions overlap so there is no residual strain at the end of the test. • There is an increase in intensity during the test (unloading line to the right of the loading line).
(0002) axial	• The lattice strain increases steadily up to 125 MPa after which it stays essentially constant. The lattice strain decreases steadily on unloading and there is a small negative residual strain at the end of the test of the order of 10^{-4}. • The intensity decreases during loading when the applied stress exceeds 125 MPa, with a large decrease occurring when the applied stress is increased from 175 to 190 MPa. The intensity is not recovered on unloading.
{10$\bar{1}$1} axial	• The lattice strain increases steadily during loading and decreases steadily during unloading. The two curves do not overlap and there is a negative residual strain of the order of 10^{-4}. • There is an increase in intensity during the test (unloading line to the right of the loading line).
{411} axial	• The lattice strain increases steadily with stress on loading. The unloading line differs markedly from the loading line and there is a positive residual strain of about $15x10^{-4}$. • There is no discernible change in intensity during the test.
{10$\bar{1}$0} radial	• The lattice strain increases during loading until about 150 MPa, beyond which it no longer increases. The unloading line deviates from the loading line at 150 MPa and 125 MPa but then follows it closely. There is a small positive residual strain of about $1\text{-}2x10^{-4}$. • There is a decrease in intensity during the test (unloading line to the left of the loading line).
{0002} radial	• The lattice strain increases steadily during loading and decreases steadily during unloading. The loading and unloading lines do not overlap and there is a small residual compressive strain. • There is an increase in intensity during the test (unloading line to the right of the loading line).
{10$\bar{1}$1} radial	• The lattice strain increases steadily during loading and decreases steadily during unloading. The loading and unloading lines overlap and there is a small residual tensile strain. • There is no discernible change in intensity during the test.
{411} radial	• The lattice strain increases steadily during loading and decreases steadily during unloading. The loading and unloading lines do not overlap and there is small residual compressive strain. • There is no discernible change in intensity during the test.

4.3 Monotonic Compression

The materials were deformed to relatively low strains in compression because of the possibility of buckling. Compressive flow curves are shown in Figure 4.6 along with the tensile flow curves for comparison. The difference between behaviour in tension and compression is very marked for both materials, with the compressive flow curves showing both a lower yield stress and a lower slope ($d\sigma/d\varepsilon$).

The compressive yield stress in the alloy is much lower than the tensile yield stress, which is similar to the behaviour of the Mg. However, the difference in $d\sigma/d\varepsilon$ in compression and in tension is not as large in the alloy as it is in the Mg. The flow curves in tension and compression are identical in the alloy until the onset of yielding in compression. The unloading lines in both tension and compression are non-linear. The strain which is recovered is much greater after a compressive strain than after a tensile strain.

The $d\sigma/d\varepsilon$ vs. ε curves are shown in Figure 4.7, along with the difference between them, up to a true strain of 1.4%. The alloy curve shows three distinct regimes. From zero to about 0.2% true strain, $d\sigma/d\varepsilon$ decreases linearly, then decreases much more rapidly from 0.2% to 0.4%. The third regime (>0.4%) shows a much slower decrease. In the Mg curve, the rate of change of $d\sigma/d\varepsilon$ decreases markedly at about 0.4% true strain as in the alloy. It is also possible to distinguish an inflection point in the curve at about 0.15% true strain.

The difference between $d\sigma/d\varepsilon$ for the two materials increases rapidly up to about 0.25% strain because the slope for the Mg decreases rapidly from the start of deformation whereas that for the alloy decreases much more slowly. The difference decreases rapidly, however, beyond 0.25%, which corresponds to general yielding in the alloy at which point $d\sigma/d\varepsilon$ decreases very rapidly. Beyond about 0.4% the slope of the Mg curve is essentially zero so that the difference curve overlaps the alloy curve. Note that this behaviour is different from that in tension where the two slopes overlap once general yielding in the alloy sets in (see Figure 4.3).

The in-situ neutron diffraction results are shown in Figure 4.8 (axial strains) and Figure 4.9 (radial strains). A description of the salient features of the neutron diffraction results is provided for each plane in Table 4.3.

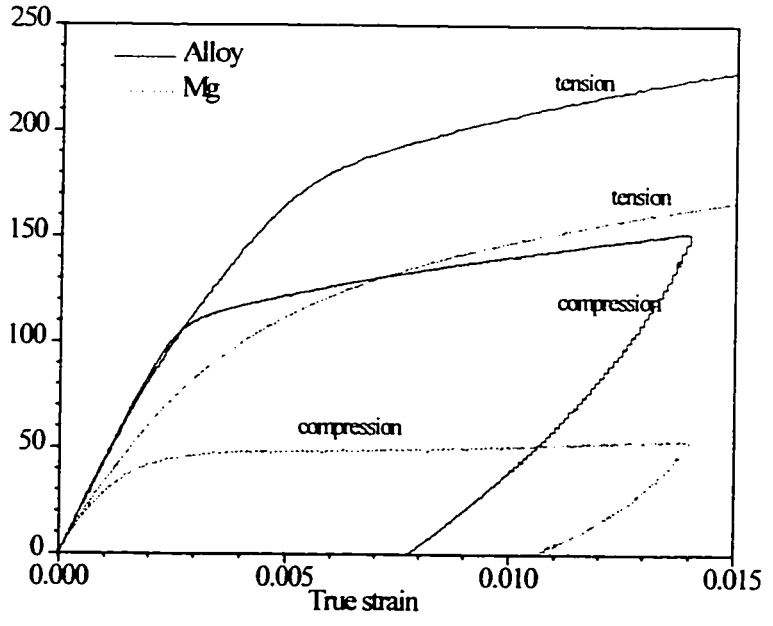

Figure 4.6: Stress-strain curves for monotonic tension and compression for the alloy and the Mg.

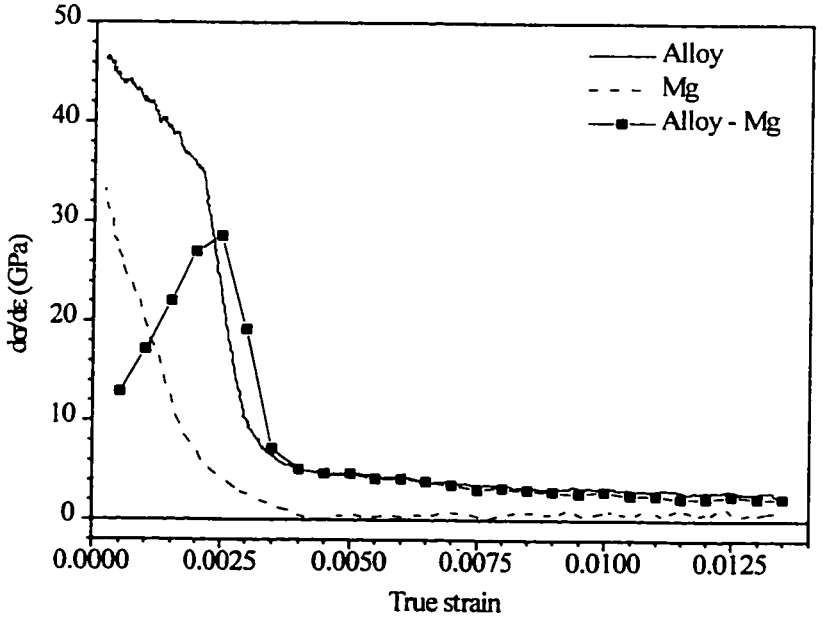

Figure 4.7: dσ/dε vs. ε curves for the alloy and the Mg deformed in compression. The difference between the two curves is also plotted.

Table 4.3: Neutron diffraction results - monotonic compression.

{10$\bar{1}$0} axial	• The stress strain curve is linear and the loading and unloading portions overlap. There may be a small residual tensile strain. • There is a decrease in intensity during the test (unloading line to the left of the loading line).
(0002) axial	• The strain increases steadily up to -115 MPa during loading, but no change is observed during the final stress increment. On unloading, the strain decreases steadily and there is a small positive residual strain of the order of 2-4x10^{-4}. • The intensity is constant during loading until the last stress increment during which there is a large increase in intensity which is not recovered on unloading.
{10$\bar{1}$1} axial	• The strain increases steadily during loading and decreases steadily during unloading. The two curves do not overlap and there is a small positive residual strain of the order of 10^{-4}. • There is no discernible change in intensity during the test.
{411} axial	• The strain increases steadily during loading. The unloading and loading lines do not differ as markedly as in the tensile test. There is a negative residual strain of about 5x10^{-4}. • There is no discernible change in intensity during the test.
{10$\bar{1}$0} radial	• The strain increases steadily during loading and decreases steadily during unloading. There is a small positive residual strain. • There is no discernible change in intensity during the test.
{0002} radial	• The lattice strain increases steadily up to -100 MPa, beyond which it no longer increases. The strain does not decrease until the stress returns to -75 MPa after which it decreases steadily. There is a small positive residual strain. • There is no discernible change in intensity during the test.
{10$\bar{1}$1} radial	• The lattice strain increases steadily during loading and decreases steadily during unloading. There is small residual tensile strain. • There is no discernible change in intensity during the test.
{411} radial	• The lattice strain increases steadily during loading and decreases steadily during unloading. There is a residual tensile strain of about 5x10^{-4}. • There is no discernible change in intensity during the test.

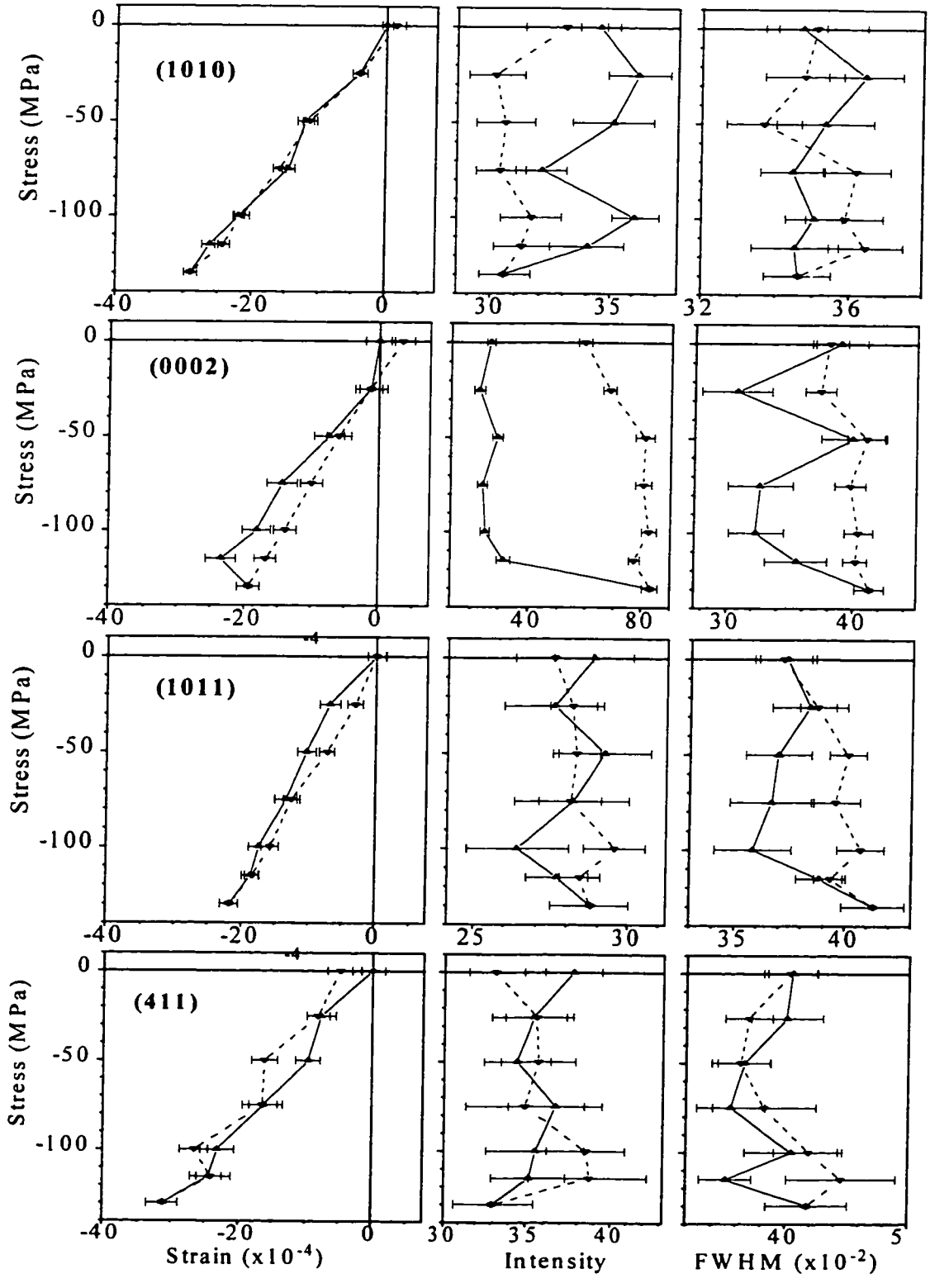

Figure 4.8: Neutron diffraction results - axial strains, monotonic compression.

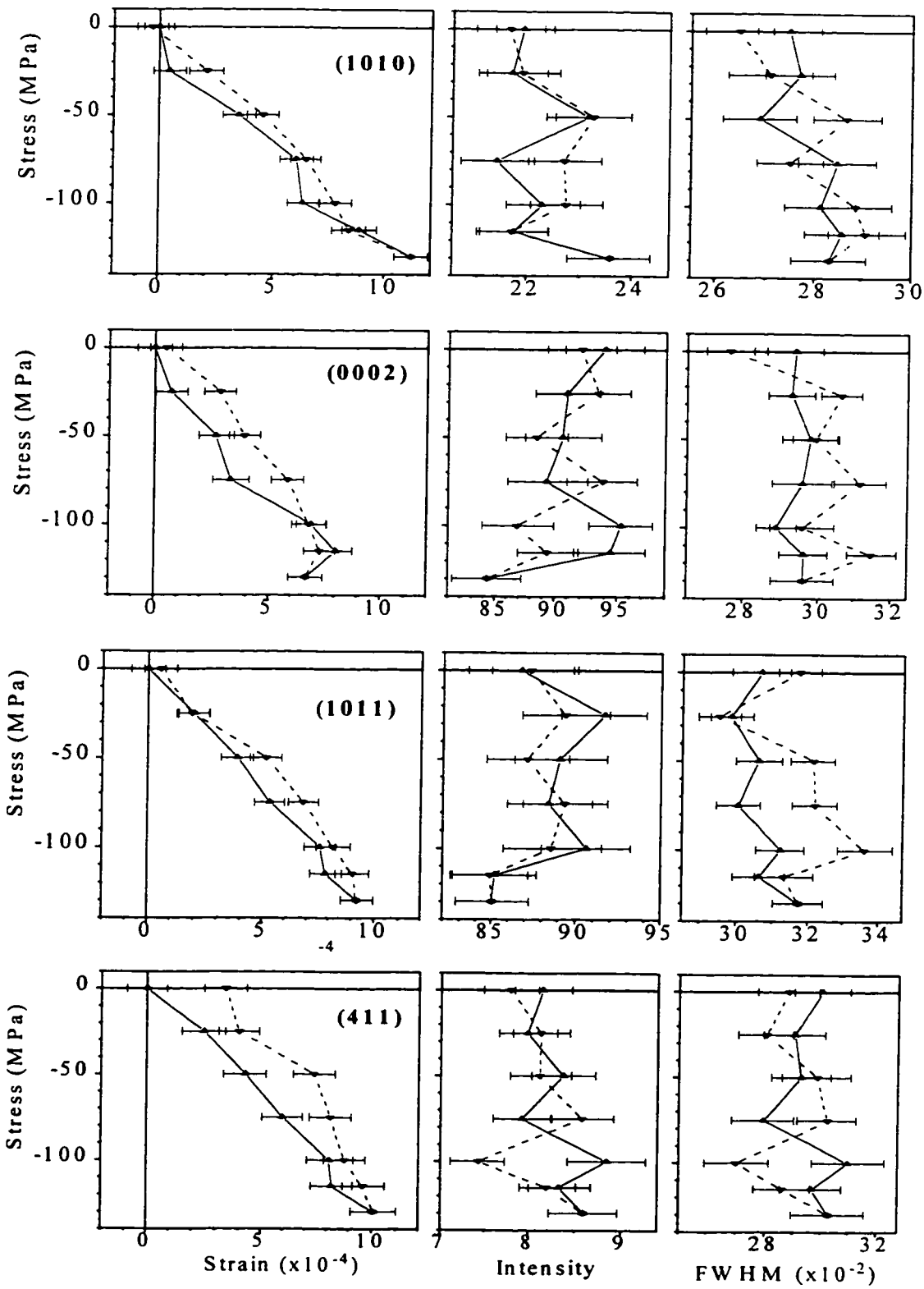

Figure 4.9: Neutron diffraction results - radial strains, monotonic compression.

4.4 Cyclic Tension

Cyclic tensile tests were performed to study the effects of unloading and reloading on the flow curve of the materials. The stress-strain curves for the alloy and for the Mg are shown in Figures 4.10(a) and (b), respectively.

The multiple loading curve for the alloy shows that no hardening is lost as a result of cycling: for all of the stresses tested, the loading line passes through the point (ε_f ,σ_f) at the end of the previous loading cycle. For stresses above about 180 MPa (i.e. in the plastic portion of the curve) a yield point appears. The failure strain of the alloy deformed cyclically is lower than that observed for the monotonic case, but this is likely due to the relatively brittle nature of the material. For the Mg, there is no yield phenomenon as for the alloy. In addition, some hardening is lost: even at low strains a given loading line crosses the unloading line of the previous cycle at a stress well below the maximum reached at the end of the previous cycle.

For both materials the loading and unloading curves are slightly rounded, giving rise to an open loop. Thus on unloading some strain beyond that due to elastic deformation is recovered.

The in-situ neutron diffraction results for axial strain measurements are shown in Figures 4.11 - 4.14 and the results for radial measurements are shown in Figures 4.15 - 4.18. A description of the salient features of these results is presented in Table 4.4. Five loading cycles were performed up to applied stresses of 100, 150, 200, 230, and 240 MPa.

For each plane for which measurements were made, five graphs of applied stress vs. lattice strain are arranged in a row. As they share the same y-axis, only that for the leftmost graph is labelled. The x-axis range is also the same for all of these graphs to enable easy comparison between cycles. As in previous sections, data points obtained while increasing the applied load are connected by a solid line and those obtained while decreasing the applied load are connected by a dashed line.

Intensity and FWHM are plotted against applied stress. The two sets of graphs share the same x-axis which is therefore labelled only once at the bottom of the figure. These graphs are drawn in such a way that the portions pertaining to a given cycle align vertically with the corresponding applied stress - lattice strain graph. All the intensity graphs share the same y-axis which is therefore labelled only once at the left of the figure. The same holds for the FWHM graphs. The significance of the solid and dashed lines is as described above.

The FWHM shows no substantial change until the third cycle (200 MPa) for all of the peaks. This corresponds to the onset of yielding as seen in Figure 4.10(a).

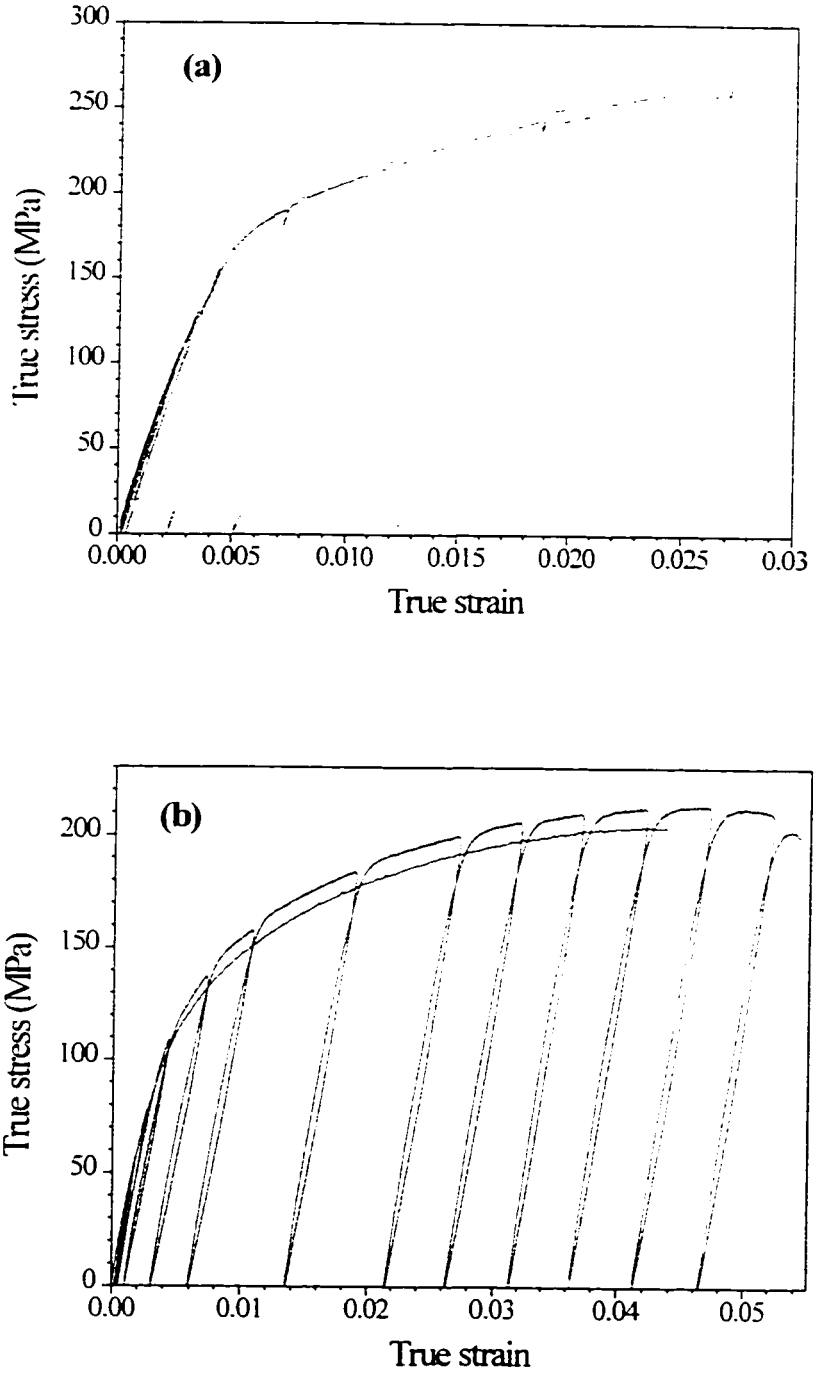

Figure 4.10: Stress-strain curves for cyclic tension for (a) the alloy, and (b) the Mg. The monotonic tensile curves are also included.

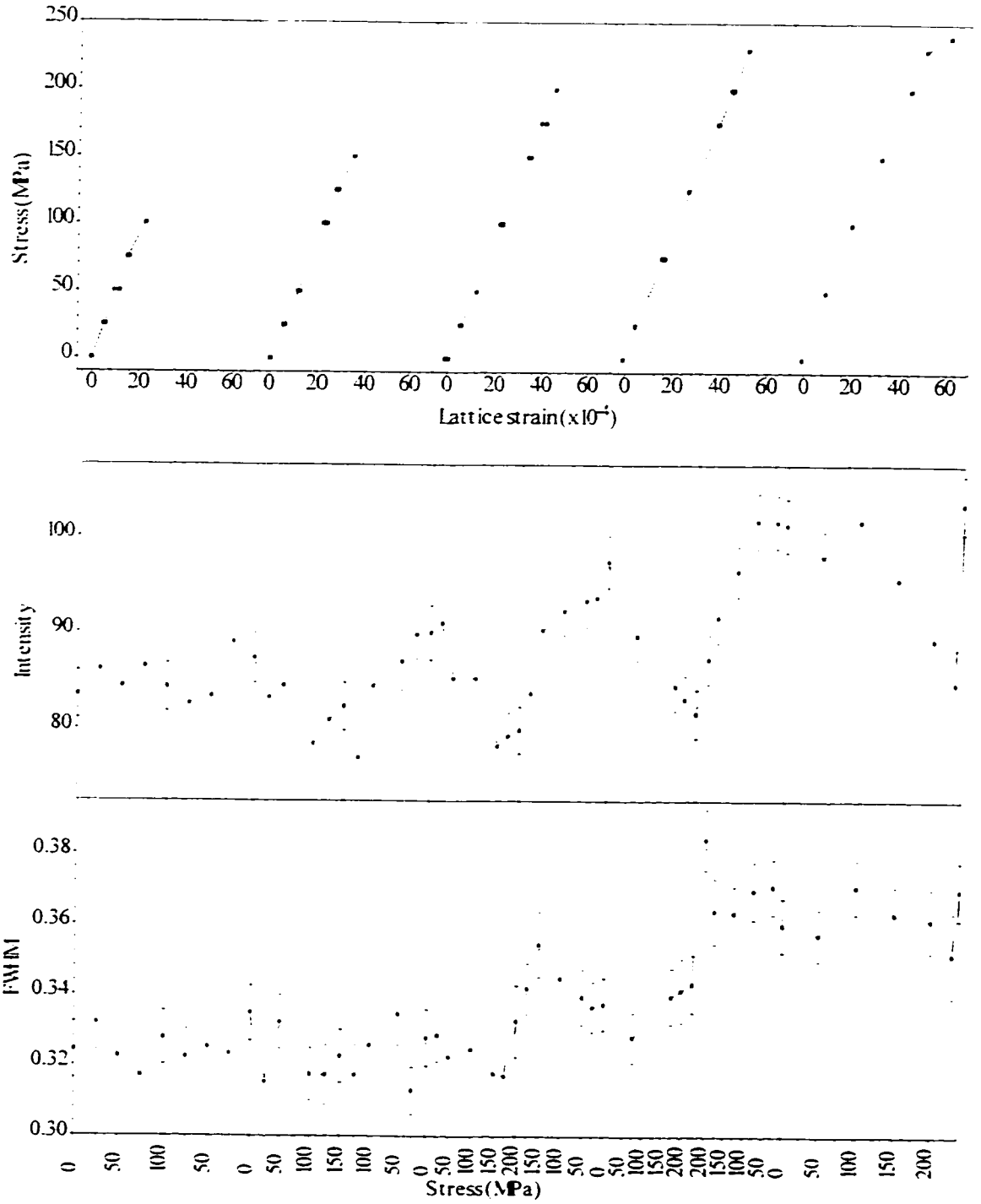

Figure 4.11: Neutron diffraction results - $\{10\bar{1}0\}$ axial lattice strains, cyclic tension.

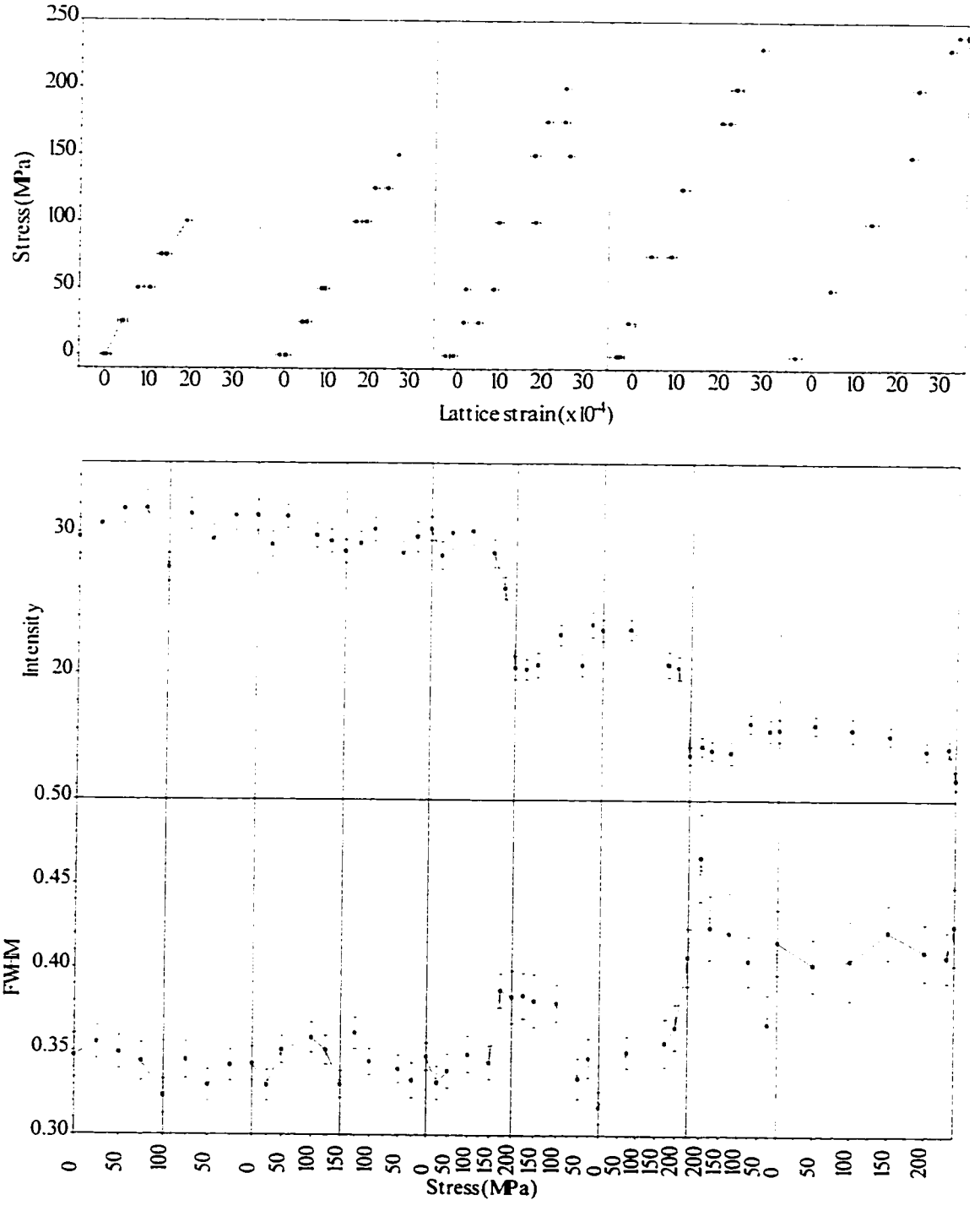

Figure 4.12: Neutron diffraction results - (0002) axial strains, cyclic tension.

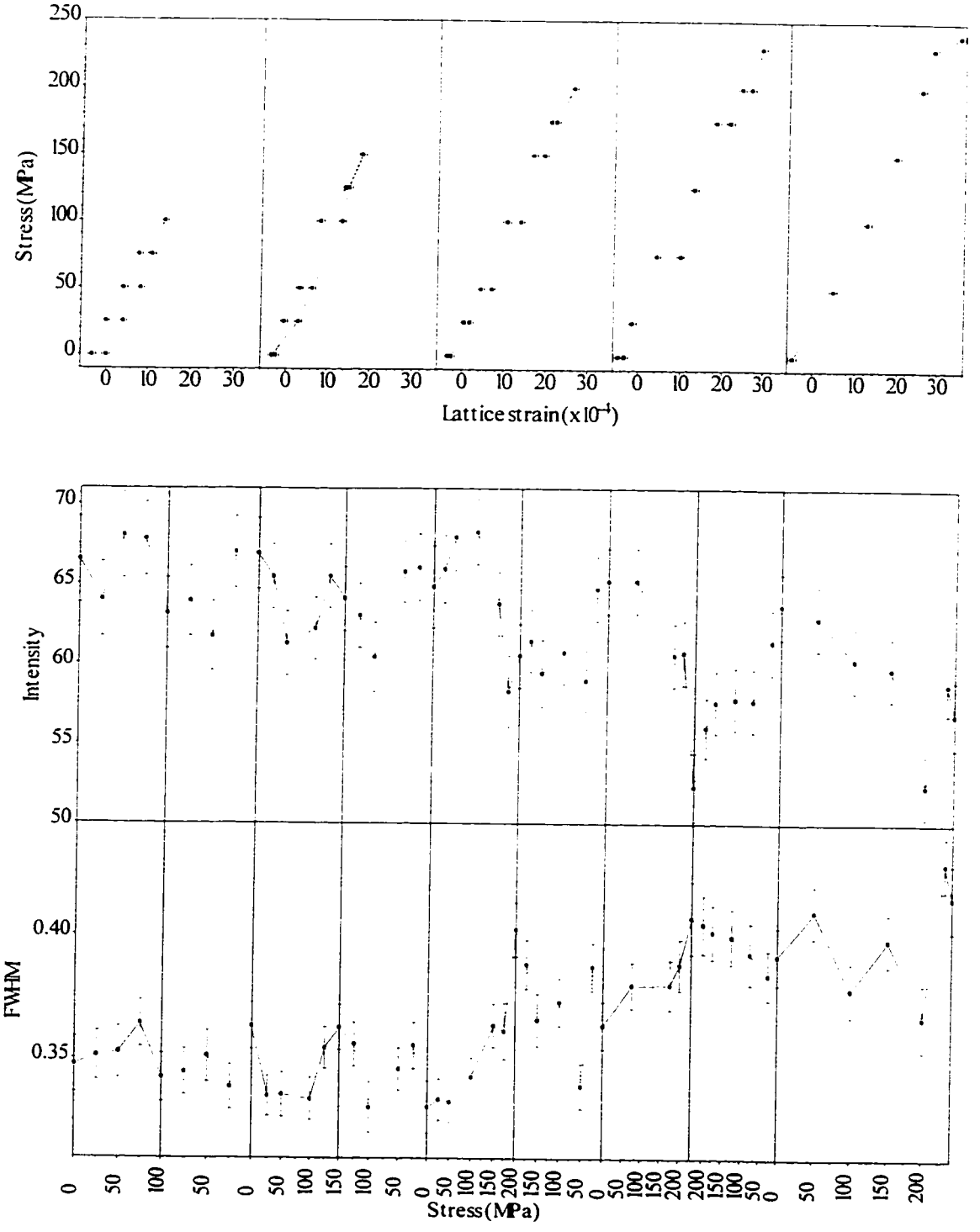

Figure 4.13: Neutron diffraction results - {10$\bar{1}$1} axial strains, cyclic tension.

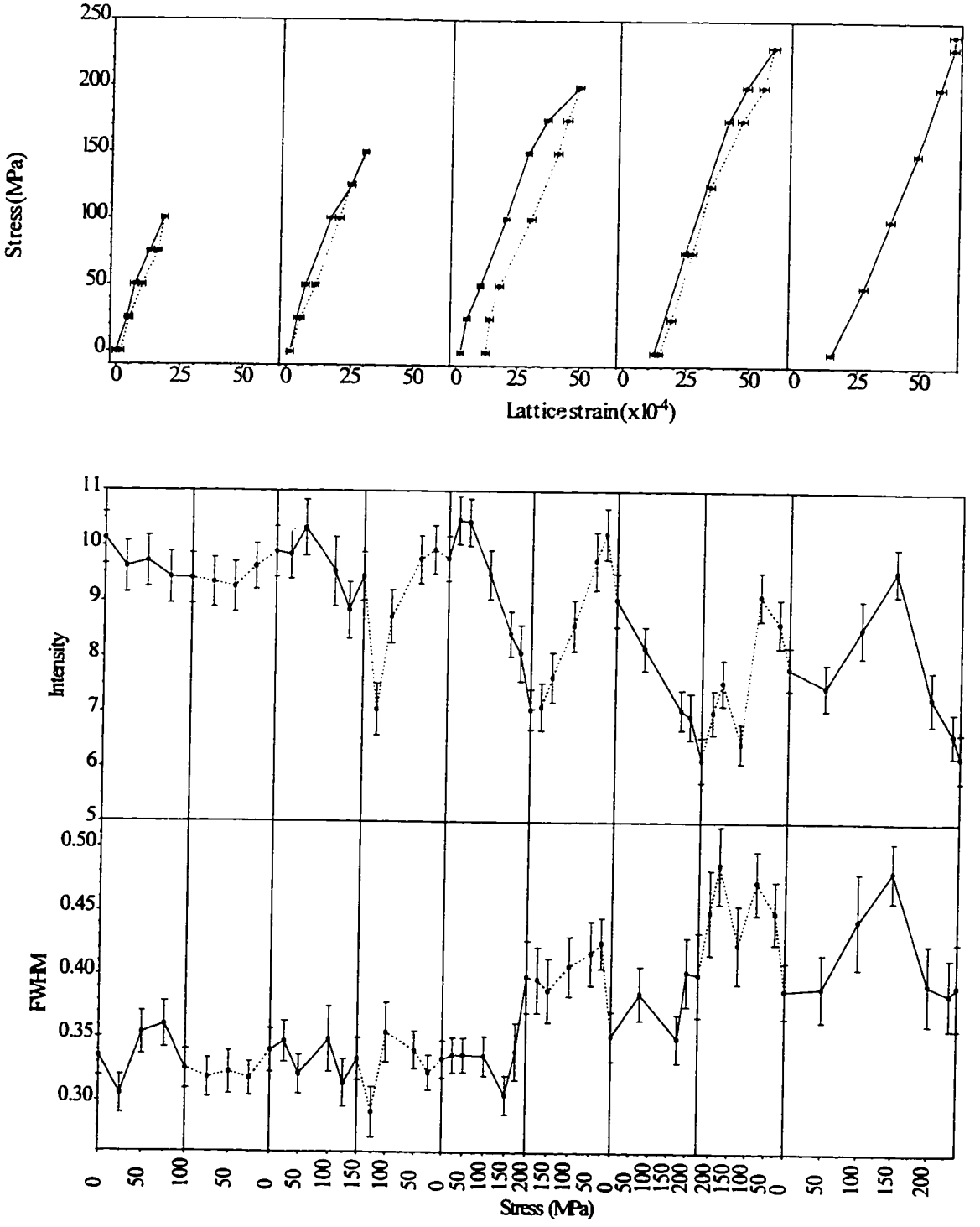

Figure 4.14: Neutron diffraction results - {411} axial strains, cyclic tension.

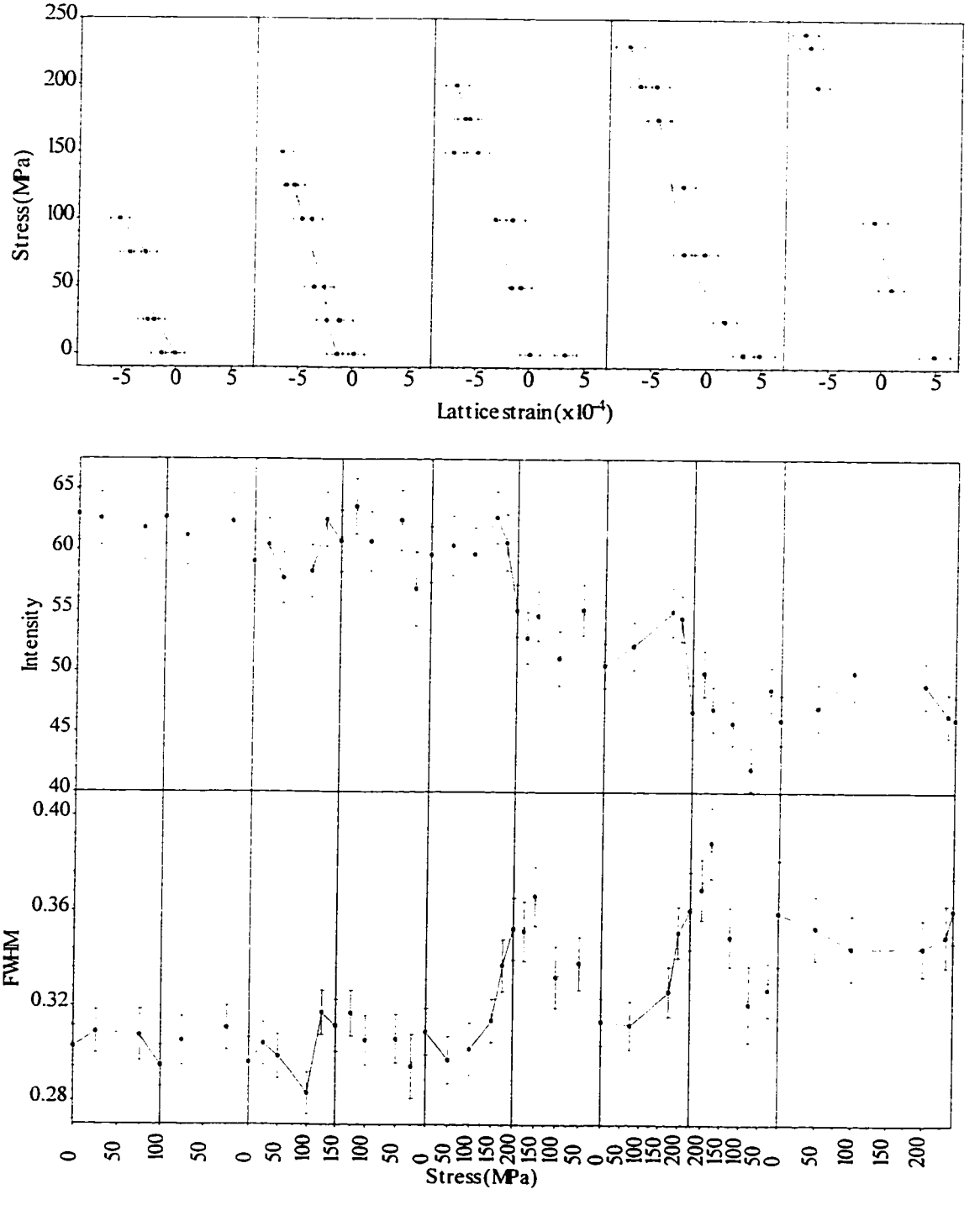

Figure 4.15: Neutron diffraction results - {10$\bar{1}$0} radial strains, cyclic tension.

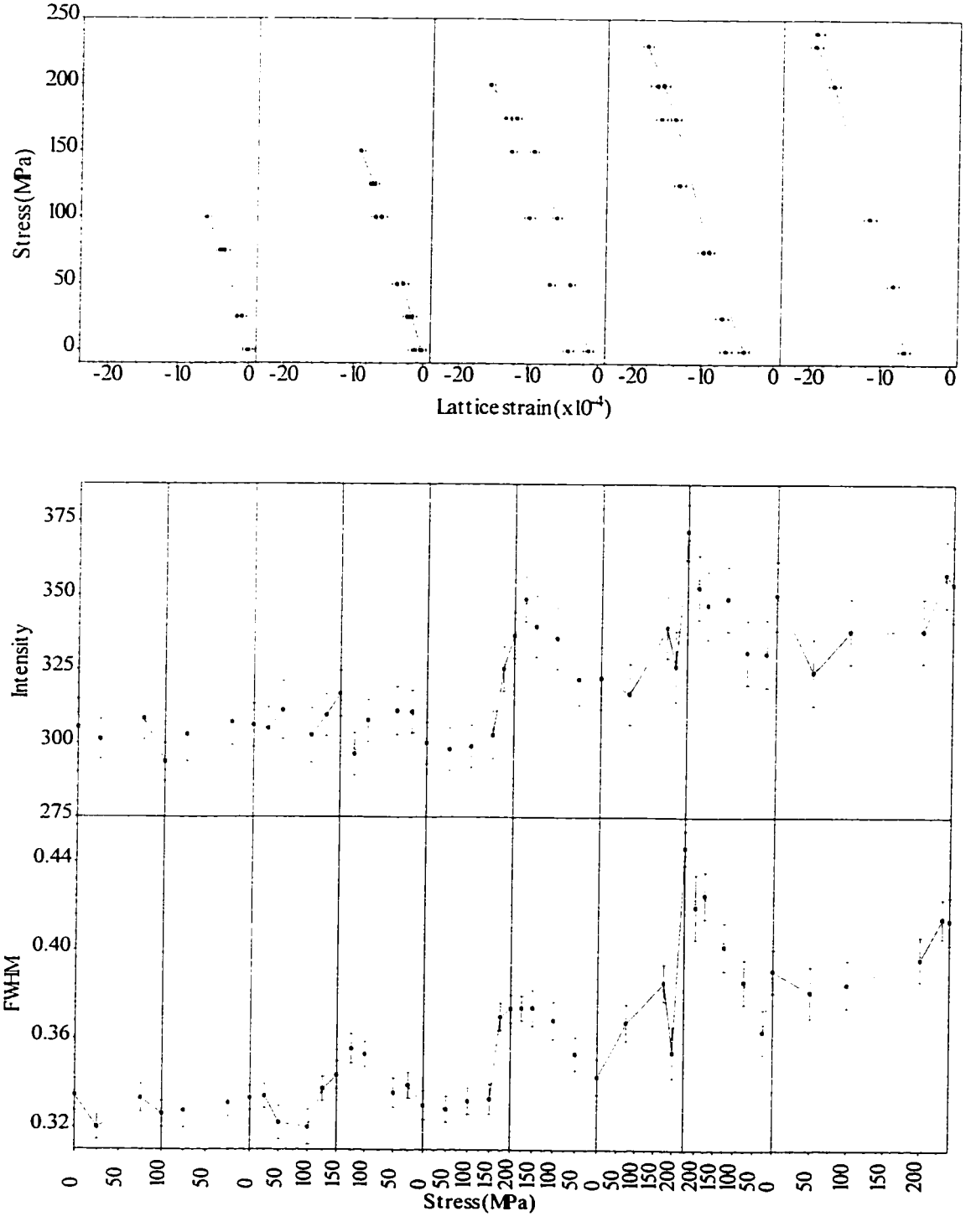

Figure 4.16: Neutron diffraction results - (0002) radial strains, cyclic tension.

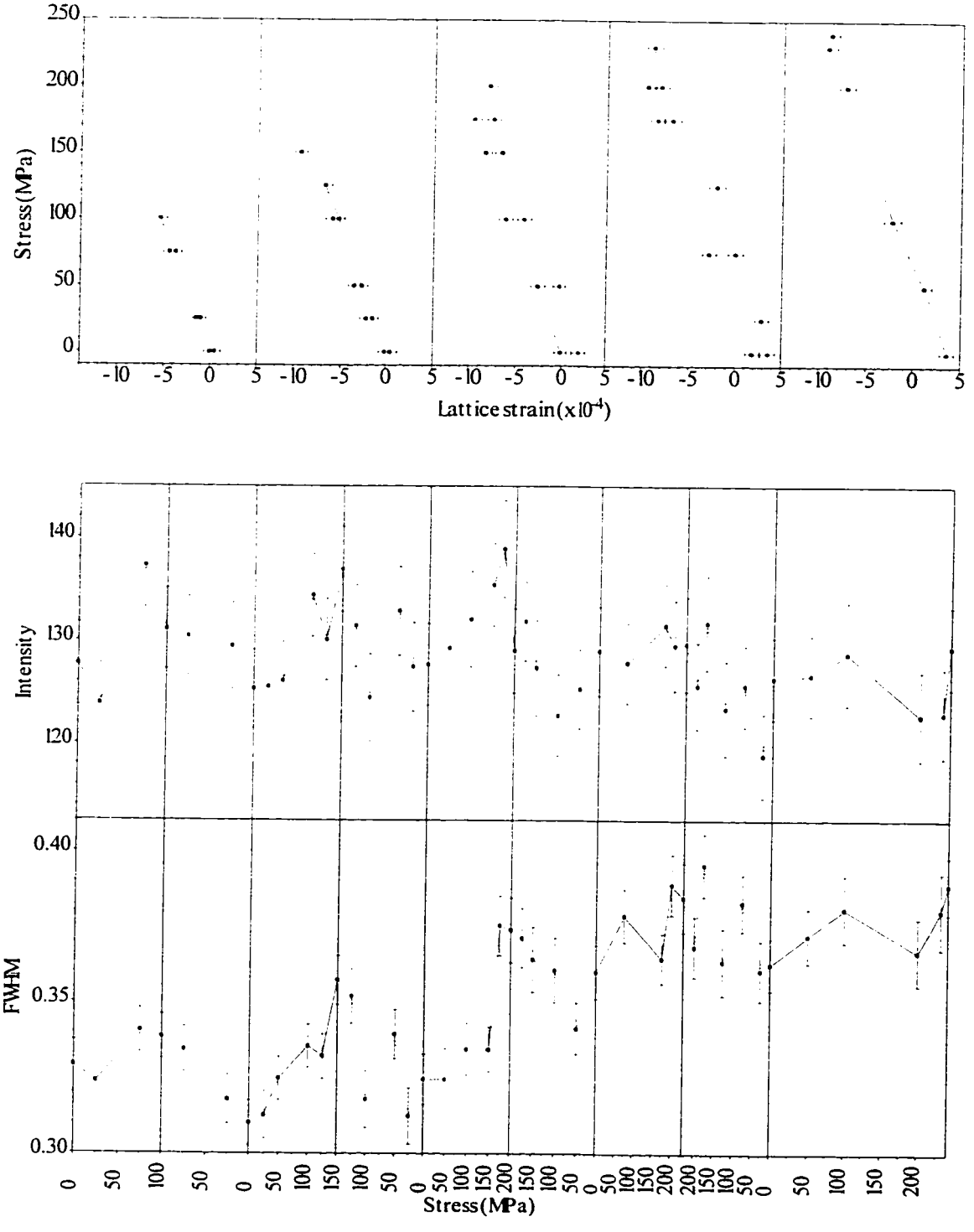

Figure 4.17: Neutron diffraction results - {10$\bar{1}$1} radial strains, cyclic tension.

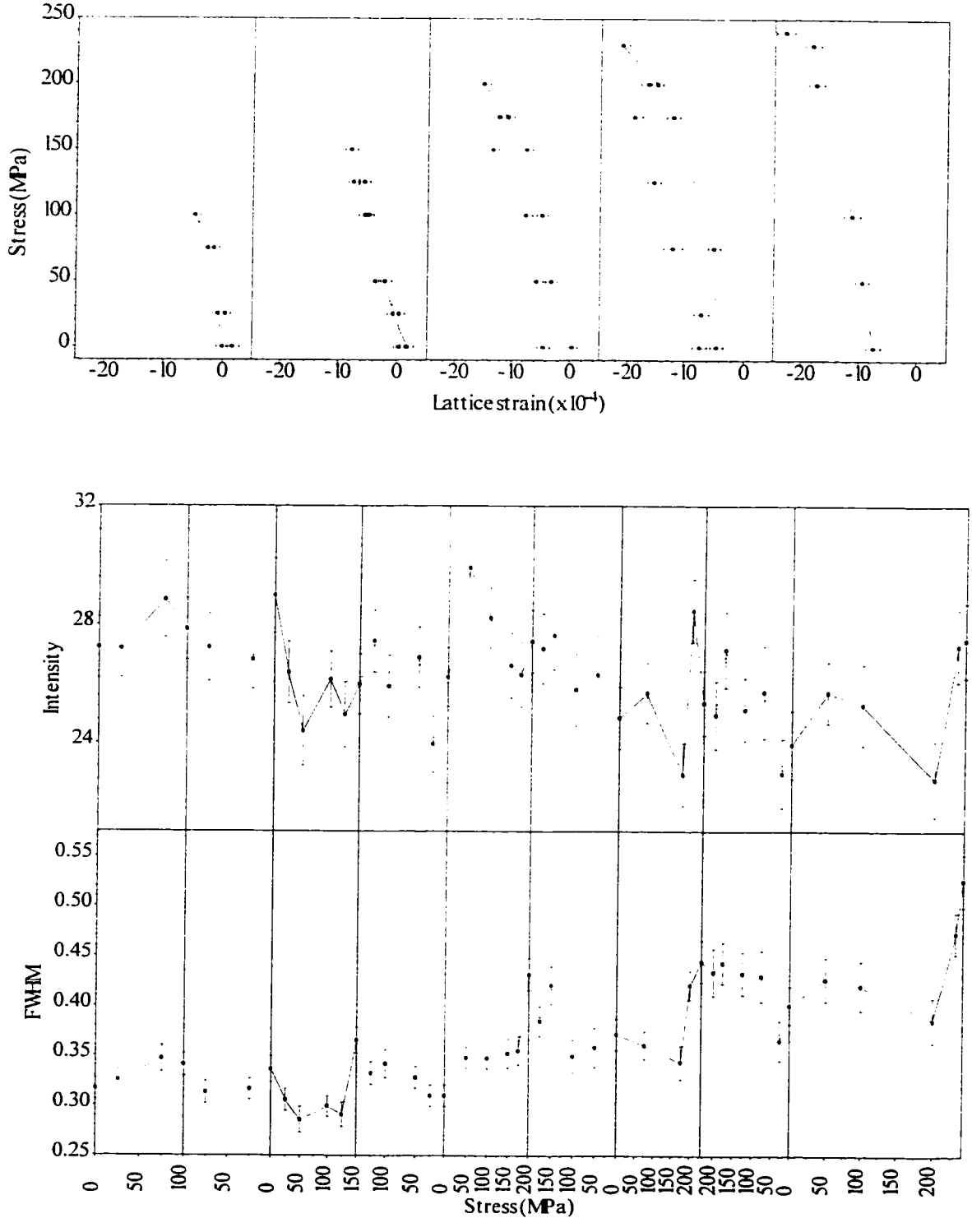

Figure 4.18: Neutron diffraction results - {411} radial strains, cyclic tension.

Table 4.4: Salient features of the neutron diffraction results for cyclic tension.

{10$\bar{1}$0} axial	• The stress-strain curves are perfectly linear throughout all of the cycles except for the deviation during the final strain increment of the last cycle. No residual strains are observed. • Starting with the second cycle, the intensity decreases during loading and increases again during unloading. The intensity measured at the end of each cycle is higher than at the end of the previous cycle as is the minimum reached during loading.
(0002) axial	• The strain varies linearly with stress in the first two cycles. In the third cycle the strain does not change during loading for stresses greater than 150 MPa and there is a compressive residual strain at the end of the cycle. In the last two cycles the strain once again varies steadily with stress and the compressive residual strain increases slightly. • In the third and fourth cycles, there is a large decrease in intensity during the last stress increment with very little recovery on unloading.
{10$\bar{1}$1} axial	• The strain varies steadily with stress throughout the test except for the large increase during the final stress increment in the last cycle. There is a compressive residual strain at the end of the first cycle which increases somewhat with each cycle. Starting with the third cycle, the intensity decreases during loading and increases again during unloading. • The intensity measured at the end of each cycle is lower than at the end of the previous cycle, as is the minimum reached during loading.
{411} axial	• The strain varies steadily with stress throughout the test except during the final stress increment of the last cycle which produces no change in strain. The loading and unloading lines deviate markedly in the third cycle, resulting in a tensile residual strain. • There does not appear to be any significant changes in intensity during this test.

Table 4.4: Salient features of the neutron diffraction results for cyclic tension. (continued)

{10$\bar{1}$0} radial	• The strain increases steadily during loading in the first two cycles. In the third cycle the strain does not change for stresses greater than 150 MPa during loading and a tensile residual strain is left at the end of the cycle. In the last two cycles the strain once again increases steadily during loading and there is little change in the residual strain. • In the third and fourth cycles, there is a significant decrease in intensity during the last stress increment with very little recovery on unloading.
(0002) radial	• The strain varies steadily with stress throughout the test except during the final stress increment of the last cycle which produces no change in strain. The loading and unloading lines deviate markedly in the third cycle, resulting in a compressive residual strain which increases somewhat in the fourth cycle. • In the third cycle, the intensity increases during loading and decreases again during unloading. A similar trend is observed in the fourth cycle but in the last cycle there appears to be no significant change in intensity.
{10$\bar{1}$1} radial	• The strain varies steadily with stress in the first two cycles. In the last three cycles, the strain does not change during the final stress increment during loading and a tensile residual strain is produced since the strain decreases steadily during unloading. • There appears to be no significant change in intensity during the test.
{411} radial	• The strain varies steadily with stress in the first two cycles. In the third and fourth cycles, the strain increases faster with stress at the higher stresses during loading; on unloading, however, the strain does not decrease substantially until the applied stress is decreased by at least 50 MPa below the maximum applied stress and a residual compressive strain results. In the last cycle, the strain increases linearly until there is an abrupt increase during the final stress increment. • There appears to be no significant change in intensity during the test.

4.5 Cyclic Compression

Cyclic compression tests were performed to study the effects of unloading and reloading on the compressive flow curve of the materials. The stress-strain curves for the alloy and the Mg are shown in Figures 4.19(a) and (b), respectively.

The cyclic and continuous loading curves for the alloy are very similar except for the elastic-plastic transition which is rather more rounded in the cyclic curve. This difference is probably due to differences in the texture of the two specimens used. In the Mg, the difference in the elastic-plastic transition is less pronounced than in the alloy, but as deformation progresses the cyclic curve starts to increase in level faster than the continuous curve. This is also likely due to a texture effect.

As in tension, no hardening is lost from one cycle to the next in the alloy. The same is true in the Mg, but this behaviour is in contrast to the marked loss of hardening observed in cyclic tension from once cycle to the next (Figure 4.10(b)).

A considerable fraction of the total strain is recovered on unloading in both materials with the effect being more pronounced in the alloy than in the Mg.

The in-situ neutron diffraction results for axial strain measurements are shown in Figures 4.20 - 4.23 and the results for radial measurements are shown in Figures 4.24 - 4.27. A description of the salient features of these results are presented in Table 4.5. Three loading cycles were performed, the first up to an applied stress of -130 MPa, and the next two up to an applied stress of -150 MPa.

For each plane for which measurements were made, three graphs of applied stress vs. lattice strain are arranged in a row. As they share the same y-axis, only that for the leftmost graph is labelled. The x-axis range is also the same for all of these graphs to enable easy comparison between cycles. As in previous sections, data points obtained while increasing the applied load are connected by a solid line and those obtained while decreasing the applied load are connected by a dashed line.

Intensity and FWHM are plotted against applied stress. The two sets of graphs share the same x-axis which is therefore labelled only once at the bottom of the figure. These graphs are drawn in such a way that the portions pertaining to a given cycle align vertically with the corresponding applied stress - lattice strain graph. All the intensity graphs share the same y-axis which is therefore labelled only once at the left of the figure. The same holds for the FWHM graphs. The significance of the solid and dashed lines is as described above.

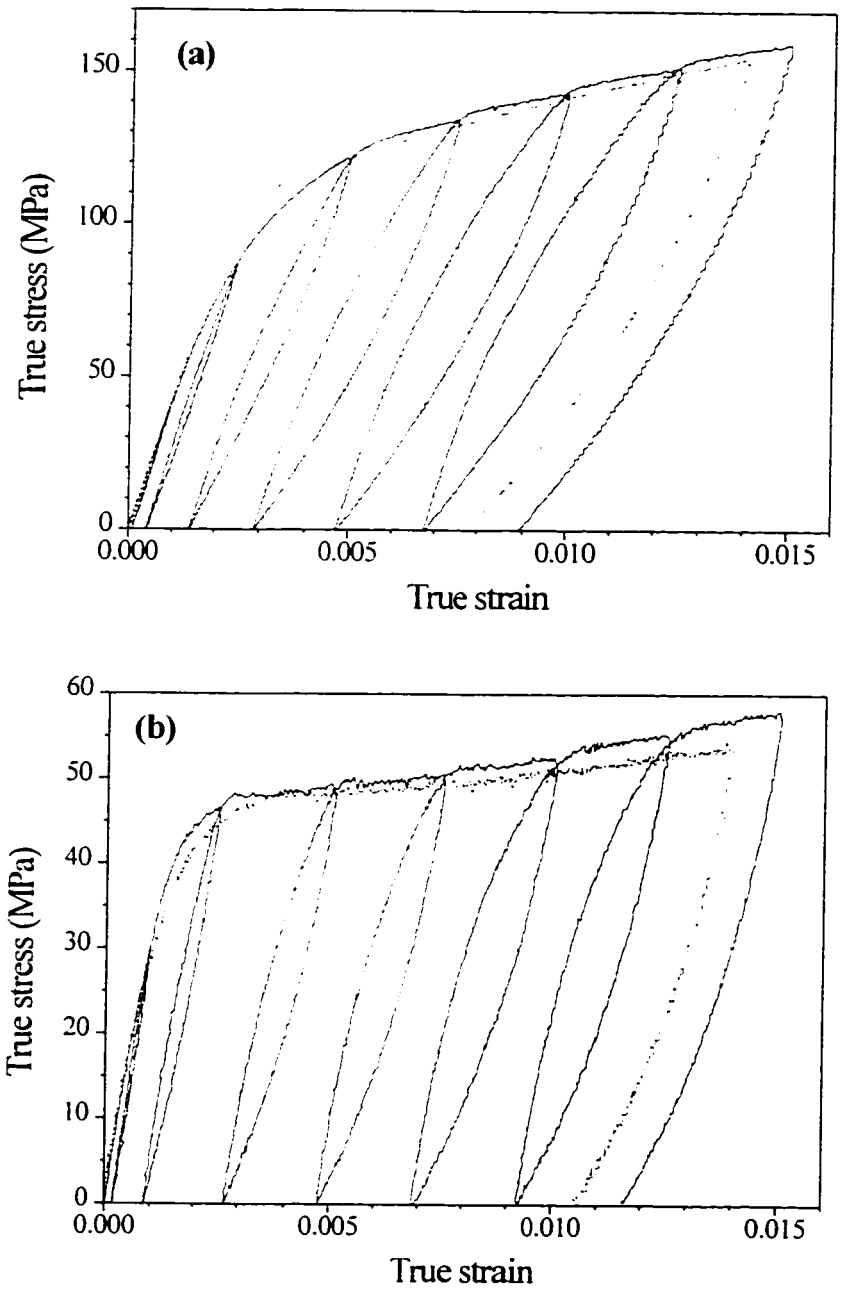

Figure 4.19: Cyclic compression curves for (a) the alloy, and (b) the Mg. The monotonic curves are also included.

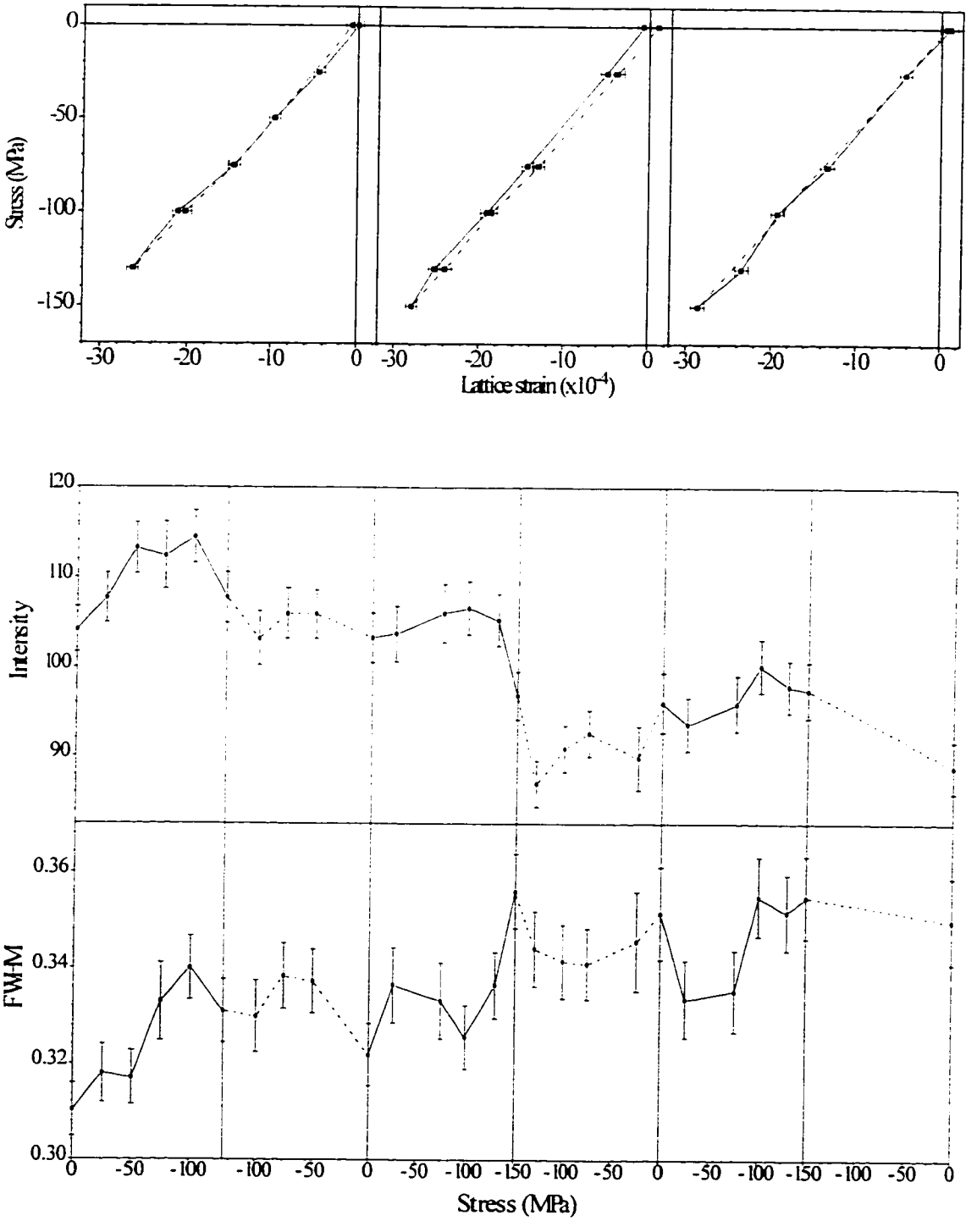

Figure 4.20: Neutron diffraction results - {10$\bar{1}$0} axial strains, cyclic compression.

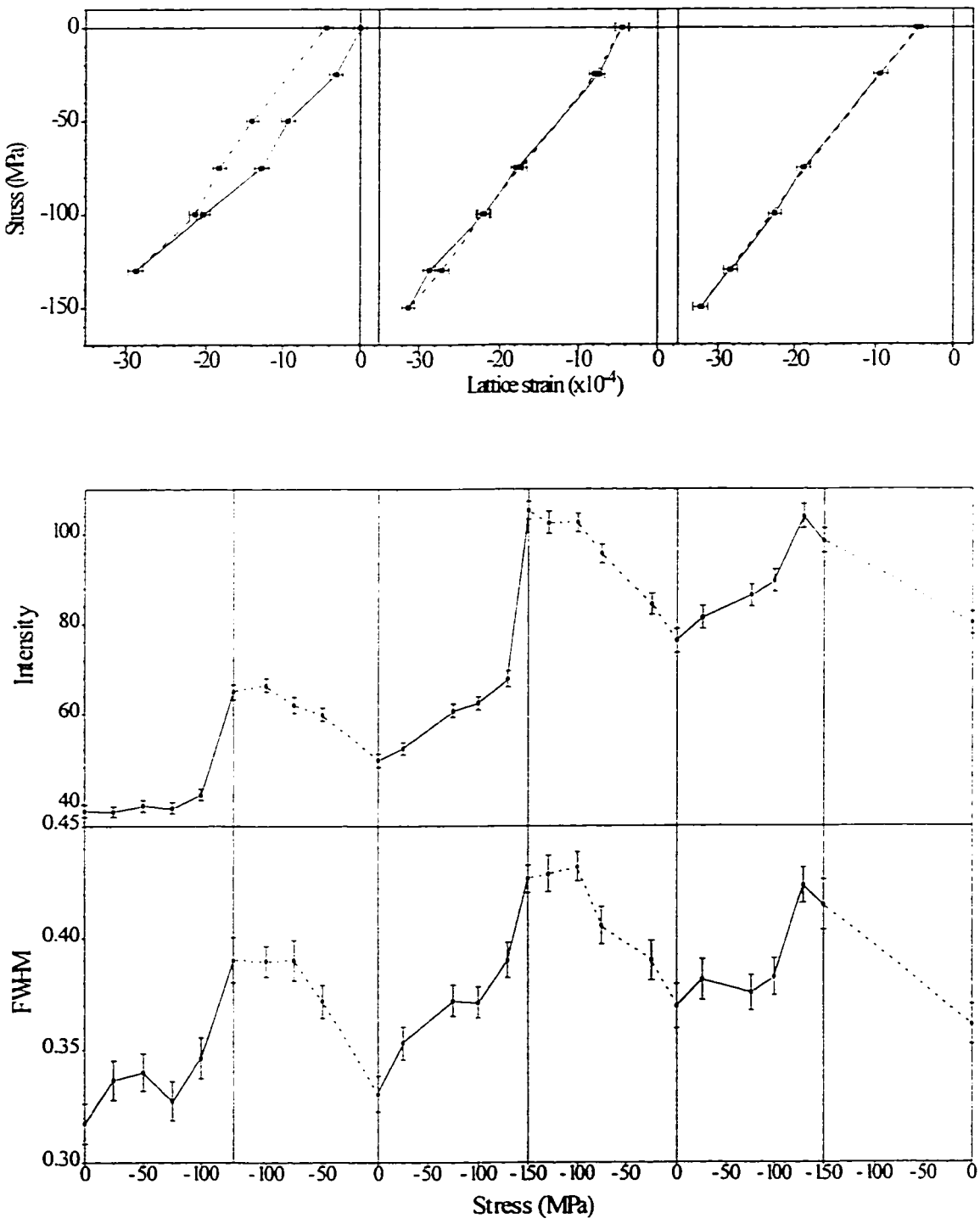

Figure 4.21: Neutron diffraction results - (0002) axial strains, cyclic compression.

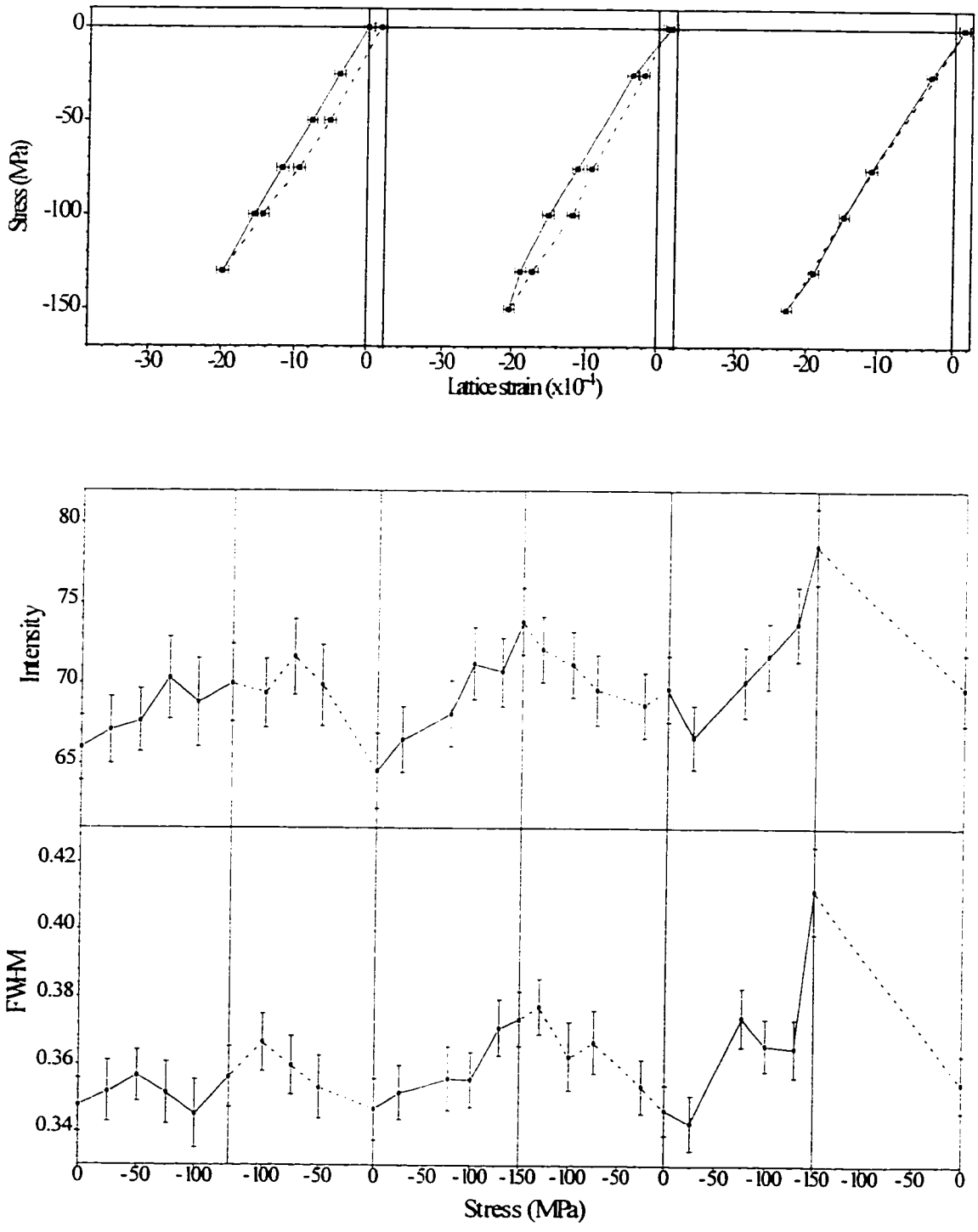

Figure 4.22: Neutron diffraction results - {10$\bar{1}$1} axial strains, cyclic compression.

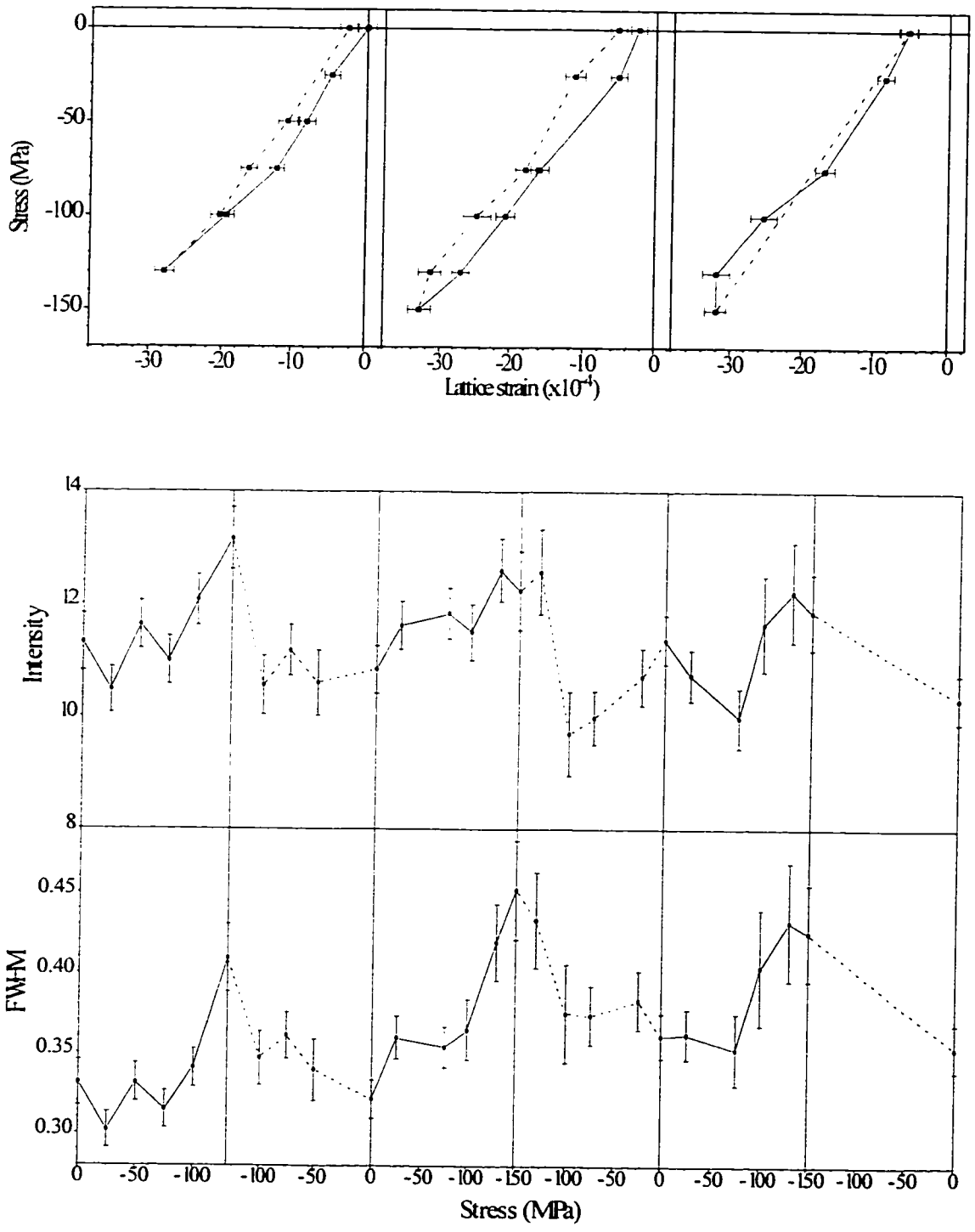

Figure 4.23: Neutron diffraction results - {411} axial strains, cyclic compression.

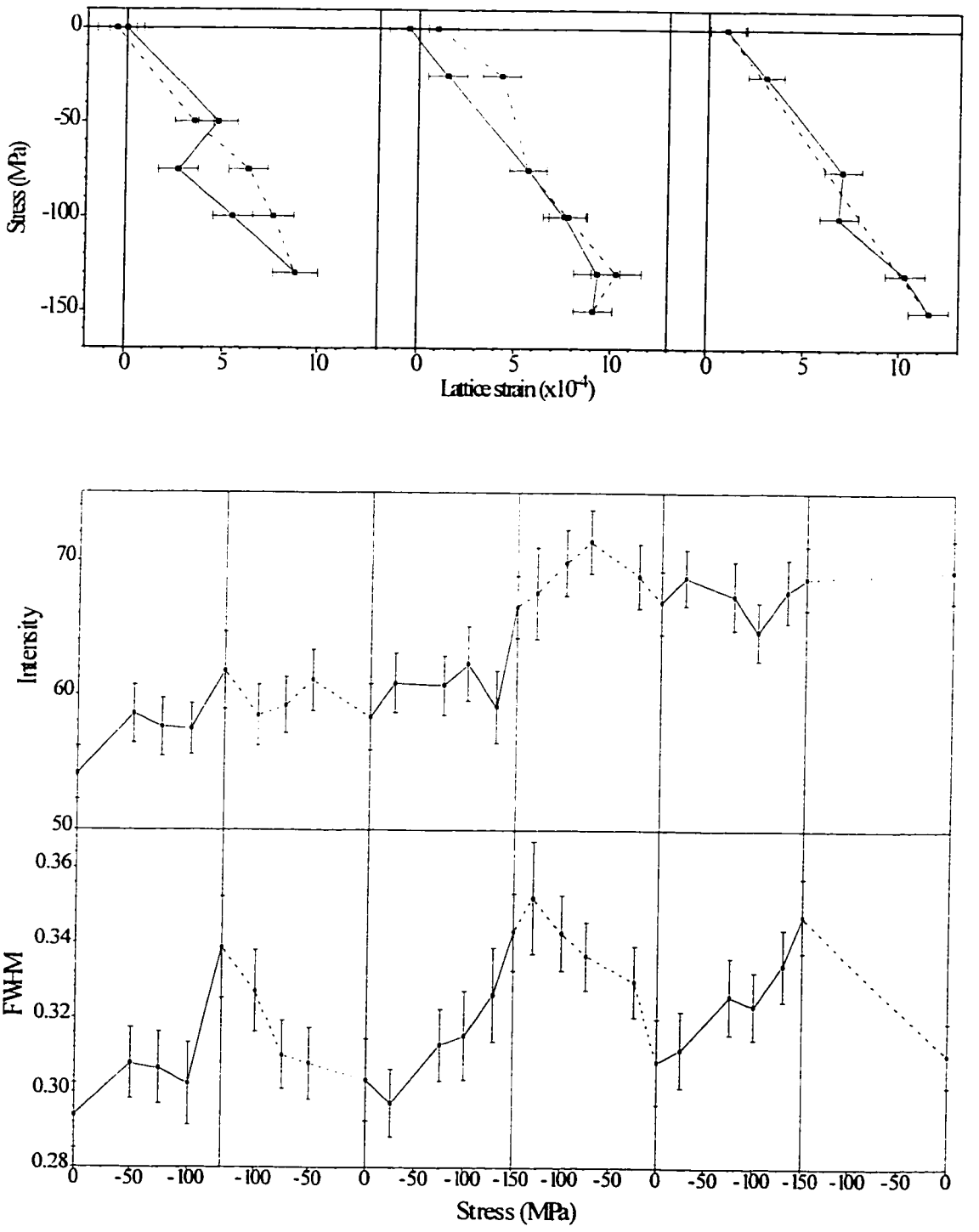

Figure 4.24: Neutron diffraction results - $\{10\bar{1}0\}$ radial strains, cyclic compression.

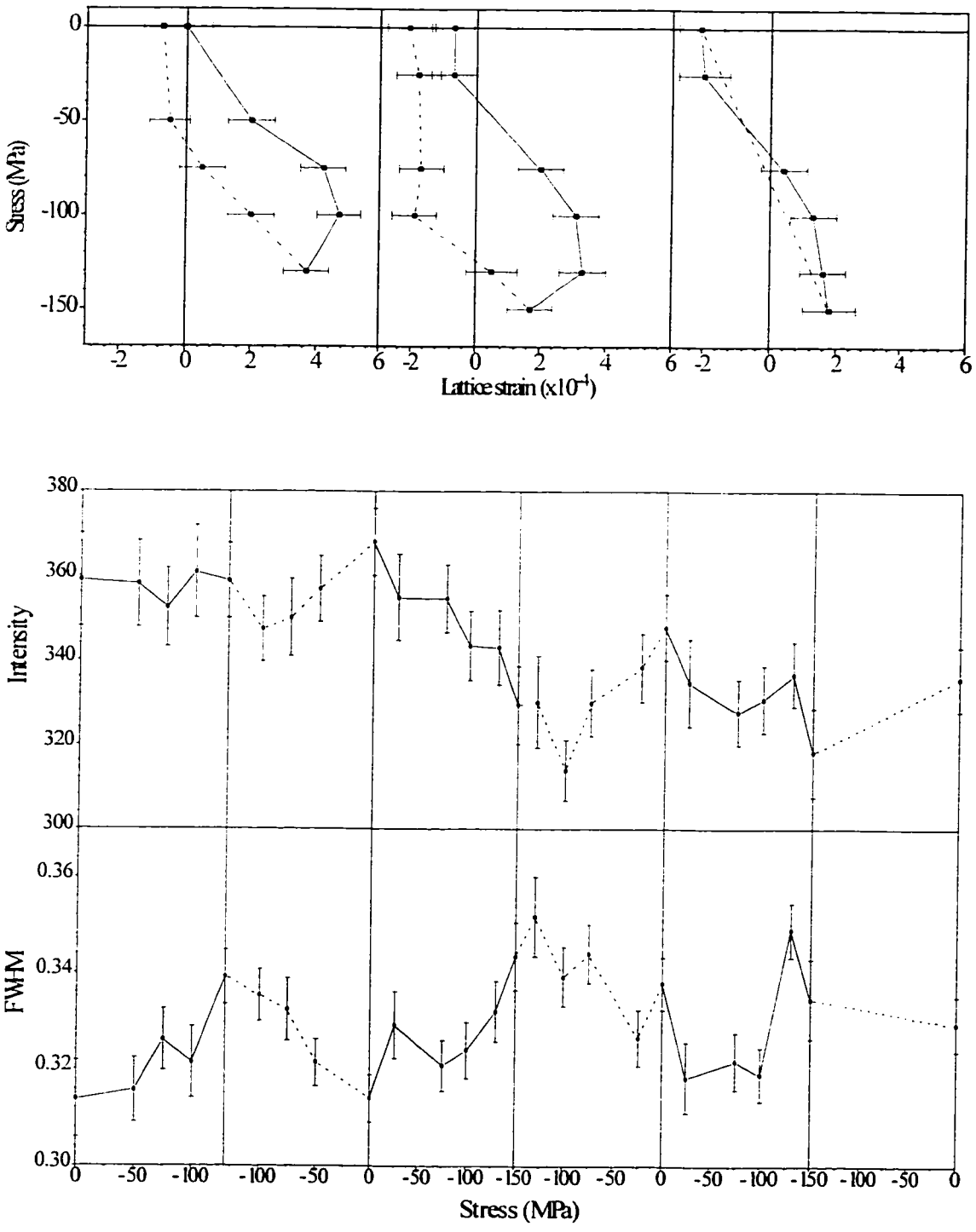

Figure 4.25: Neutron diffraction results - (0002) radial strains, cyclic compression.

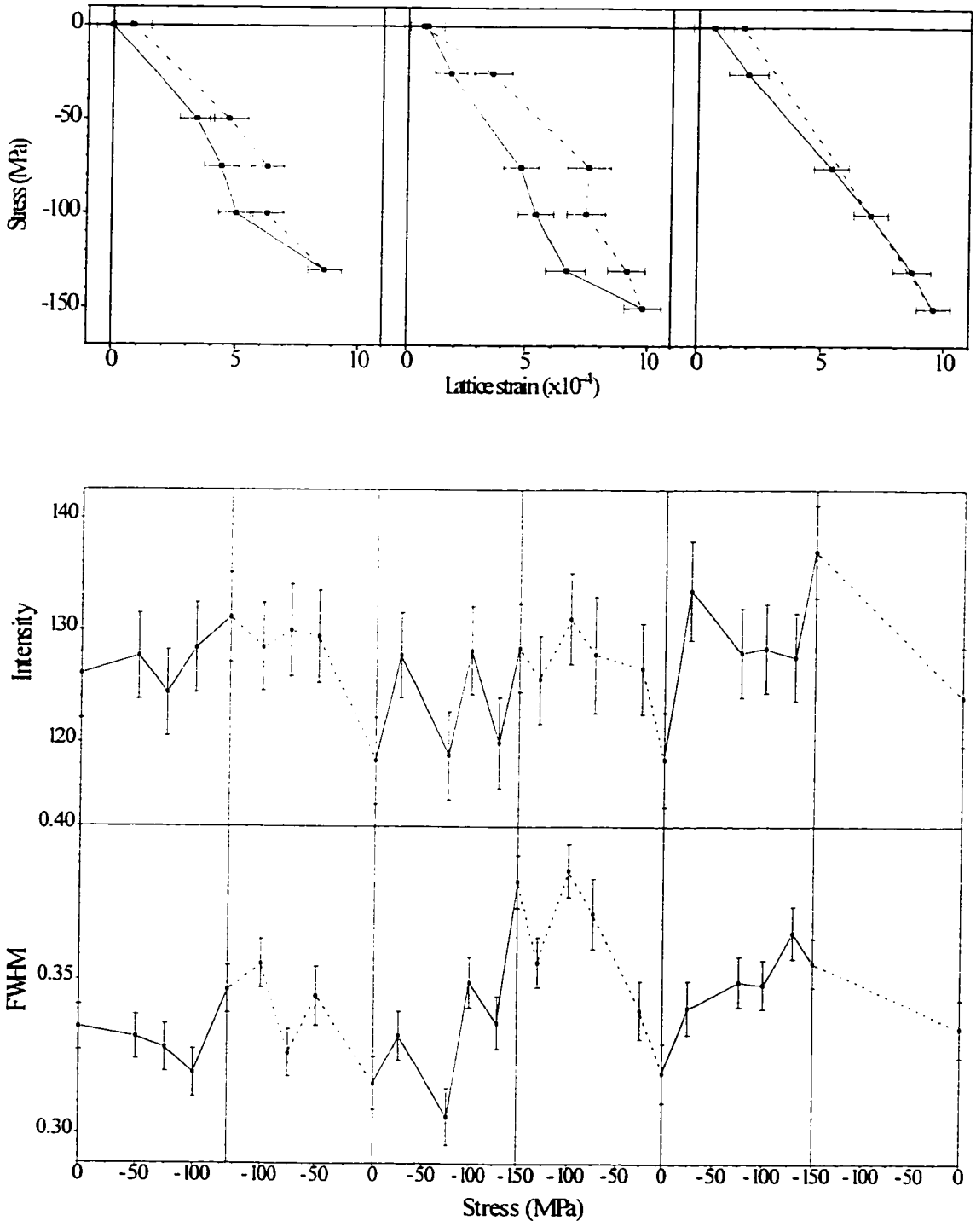

Figure 4.26: Neutron diffraction results - {10$\bar{1}$1} radial strains, cyclic compression.

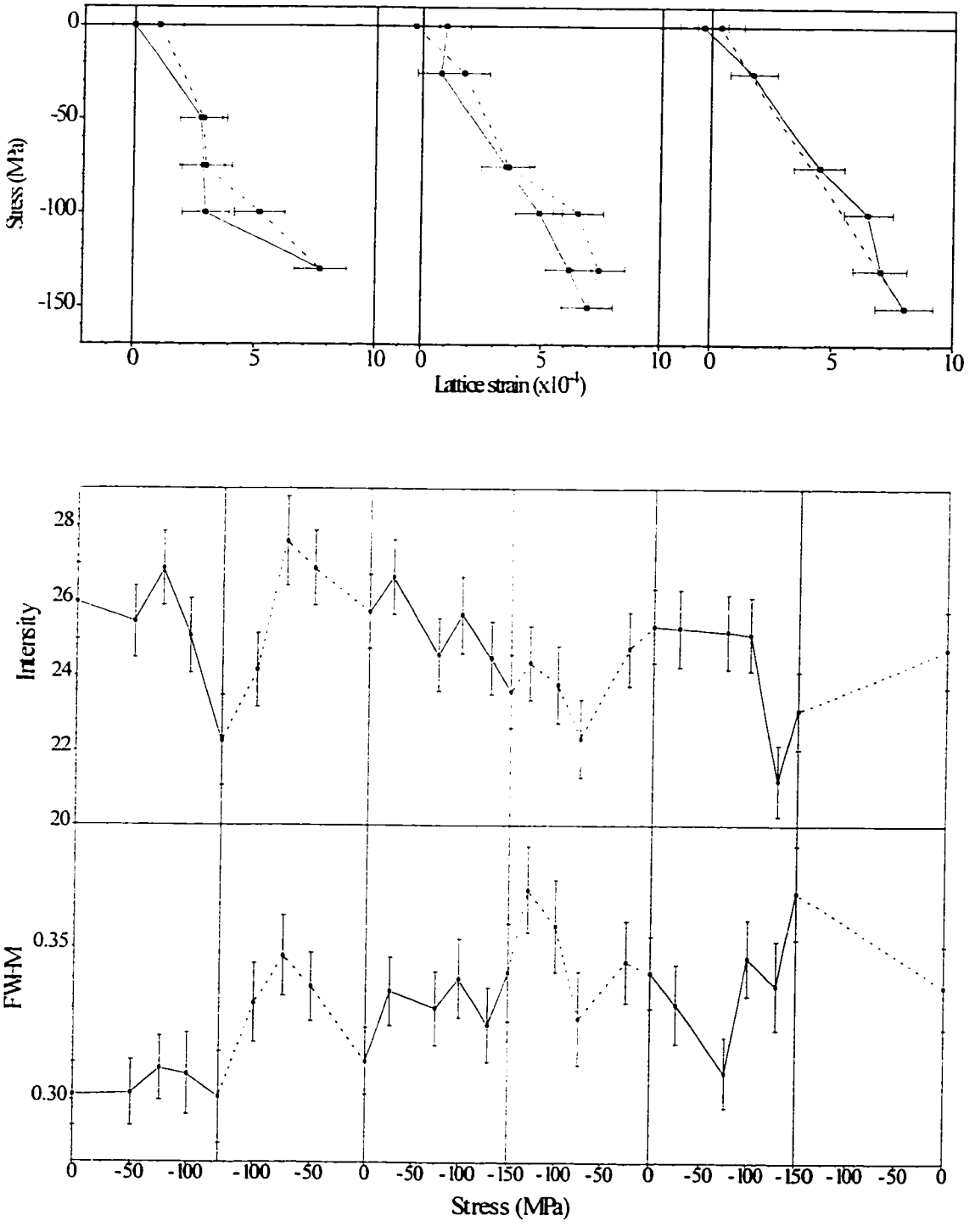

Figure 4.27: Neutron diffraction results - {411} radial strains, cyclic compression.

Table 4.5: Salient features of the neutron diffraction results for cyclic compression.

{10$\bar{1}$0} axial	• The stress-strain curves are perfectly linear throughout the entire test and there is no residual strain. In the first cycle, the intensity appears to decrease slightly on loading, with no recovery on unloading. • There is a marked decrease in intensity during loading in the third cycle with perhaps some recovery on unloading. There appears to be no change in intensity in the third cycle. • The FWHM increases during loading in the first and second cycles, but not in the third cycle.
(0002) axial	• In the first cycle, the loading and unloading lines deviate significantly and a compressive residual strain results. The stress-strain curves are linear in the second and third cycles with no change in the residual strain. • The intensity increases on loading and recovers partially on unloading in the first two cycles where the effect is very pronounced. The same trend is observed in the third cycle, but is much less pronounced. • The FWHM shows the same trend as the intensity.
{10$\bar{1}$1} axial	• The strain varies steadily with stress in all three cycles. A small tensile residual strain is left at the end of the first cycle which does not change in the second and third cycles. • The intensity appears to increase during loading and decrease during unloading in all three cycles. • The FWHM shows the same trend as the intensity in the last two cycles.
{411} axial	• The strain varies steadily with stress in the first two cycles. A residual strain is left at the end of the first cycle which increases at the end of the second cycle. The strain does not change during the final strain increment in the last cycle. • The intensity appears to increase during loading and decrease during unloading for all three cycles. • The FWHM shows the same trend as the intensity.

Table 4.5: Salient features of the neutron diffraction results for cyclic compression. (continued)

{10$\bar{1}$0} radial	• The strain varies steadily with stress in all three cycles except for the final stress increment of the second cycle which appears to produce no change in the strain. • The intensity does not change in the first and third cycles; there is an increase during loading in the second cycle. • The FWHM increases during loading and decreases during unloading in all three cycles.
(0002) radial	• In the first two cycles, the strain ceases to increase during loading beyond a given stress. On unloading, the strain decreases rapidly at first but then stays constant. A small compressive residual strain is left at the end of the first cycle which increases slightly during the second cycle. In the third cycle, the strain increases steadily with stress and there is no change in the residual strain. • The intensity does not change in the first and third cycles. There is a decrease during loading in the second cycle which is partially recovered on unloading. • The FWHM increases during loading and decreases during unloading in all three cycles.
{10$\bar{1}$1} radial	• The strain varies steadily with stress in all three cycles and a small tensile residual strain is left at the end of the test. • The intensity shows no discernible change during the test. • The FWHM increases during loading and decreases during unloading in all three cycles, though the trend is most marked in the second cycle.
{411} radial	• The strain varies steadily with strain in the first two cycles. A residual strain is left at the end of the first cycle which increases at the end of the second cycle. The strain does not change during the final strain increment in the last cycle. • The intensity appears to decrease during loading and increase during unloading for all three cycles. • The FWHM varies erratically during the test, but appears to be higher at the end of the test than at the start.

4.6 Tension-first Bauschinger

Bauschinger experiments were performed in order to investigate the effects of a simple change in strain path on the mechanical behaviour of the materials. Tension-first Bauschinger curves for the alloy and the Mg are shown in Figures 4.28(a) and (b), respectively. In both cases a tensile prestrain of 1.25% was applied, followed by a compressive strain of 1.4% The monotonic compressive curves are also included, displaced along the strain axis so that they overlap the compressive portion of the Bauschinger loops. $d\sigma/d\varepsilon$ vs. ε plots for the compressive portions of the curves in Figure 4.28 are shown in Figure 4.29.

For both the alloy and the Mg, the tensile prestrain causes a reduction in $d\sigma/d\varepsilon$ in compression prior to the start of general yielding (the effect is much less marked in the Mg) without greatly affecting $d\sigma/d\varepsilon$ at higher reverse strains. However, for the Mg, the prestrain produces an increase in the overall stress level at higher reverse strains of the order of 10 MPa which is not observed in the alloy.

Figure 4.29 shows that $(d\sigma/d\varepsilon)_{monotonic}$ is initially higher than $d\sigma/d\varepsilon_{Bauschinger}$ for both materials but decreases more rapidly right from the start of loading. At higher strains the two slopes become essentially equal. In the alloy, $d\sigma/d\varepsilon_{Bauschinger}$ decreases much more gradually to its limit value than does $d\sigma/d\varepsilon_{monotonic}$. It is worth noting that, for the Mg, $d\sigma/d\varepsilon_{Bauschinger}$ decreases slowly at the start of reverse straining, then decreases more rapidly until its limit value is reached, which is the same type of behaviour exhibited by the alloy (prestrained or not). This is in contrast to the behaviour of the Mg in monotonic compression where $d\sigma/d\varepsilon$ does not show an initial region of slow decrease.

The neutron diffraction results are shown in Figure 4.30 (axial strains) and Figure 4.31 (radial strains). The material was stressed to 190 MPa in tension and then to 130 MPa in compression. The tensile portion of the results are in fact those presented in section 4.2 and are not described in detail. Table 4.6 contains a description of the salient features of the neutron diffraction results for each plane.

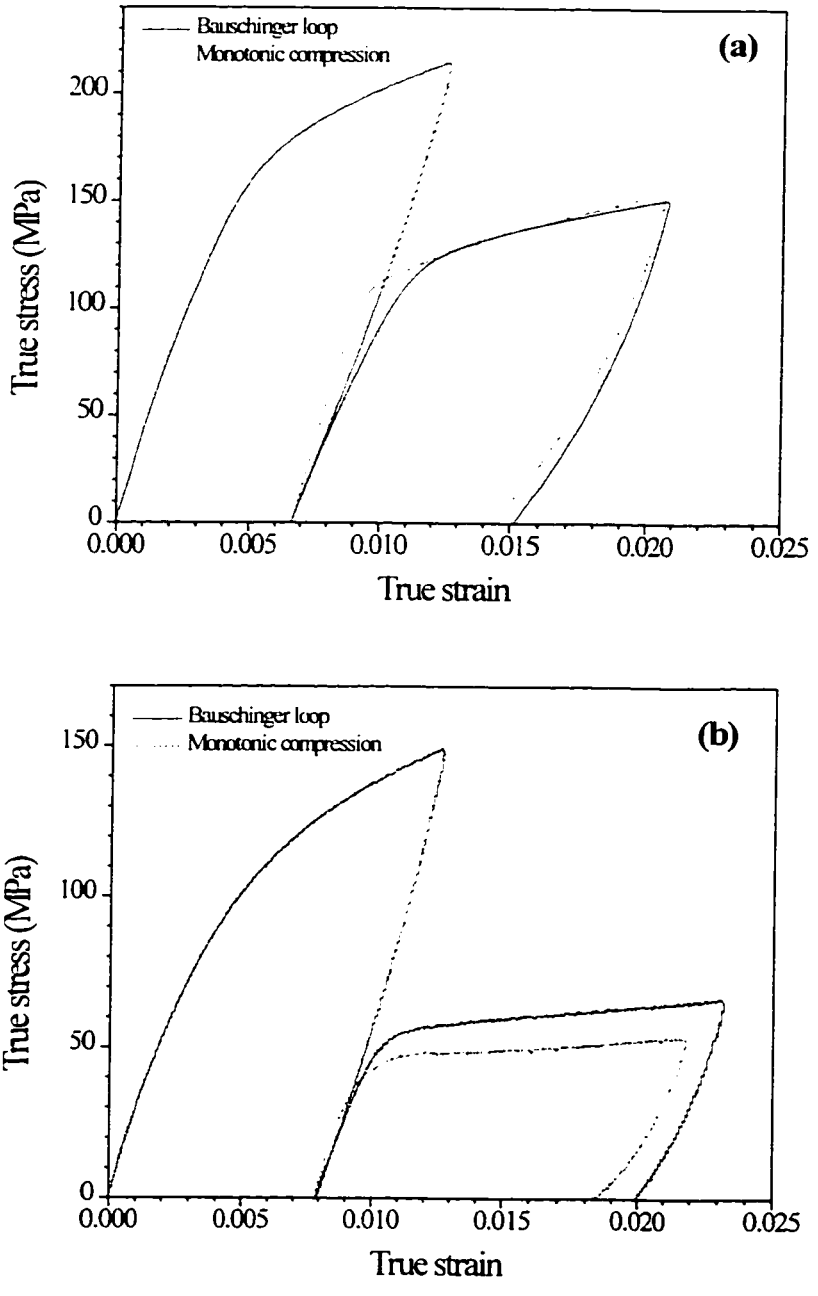

Figure 4.28: Tension-first Bauschinger loop for (a) the alloy, and (b) the Mg. The compressive half of the cycles has been flipped into the first quadrant. The monotonic compression curves are also included, superimposed on the compressive portion of the Bauschinger loops for easy comparison.

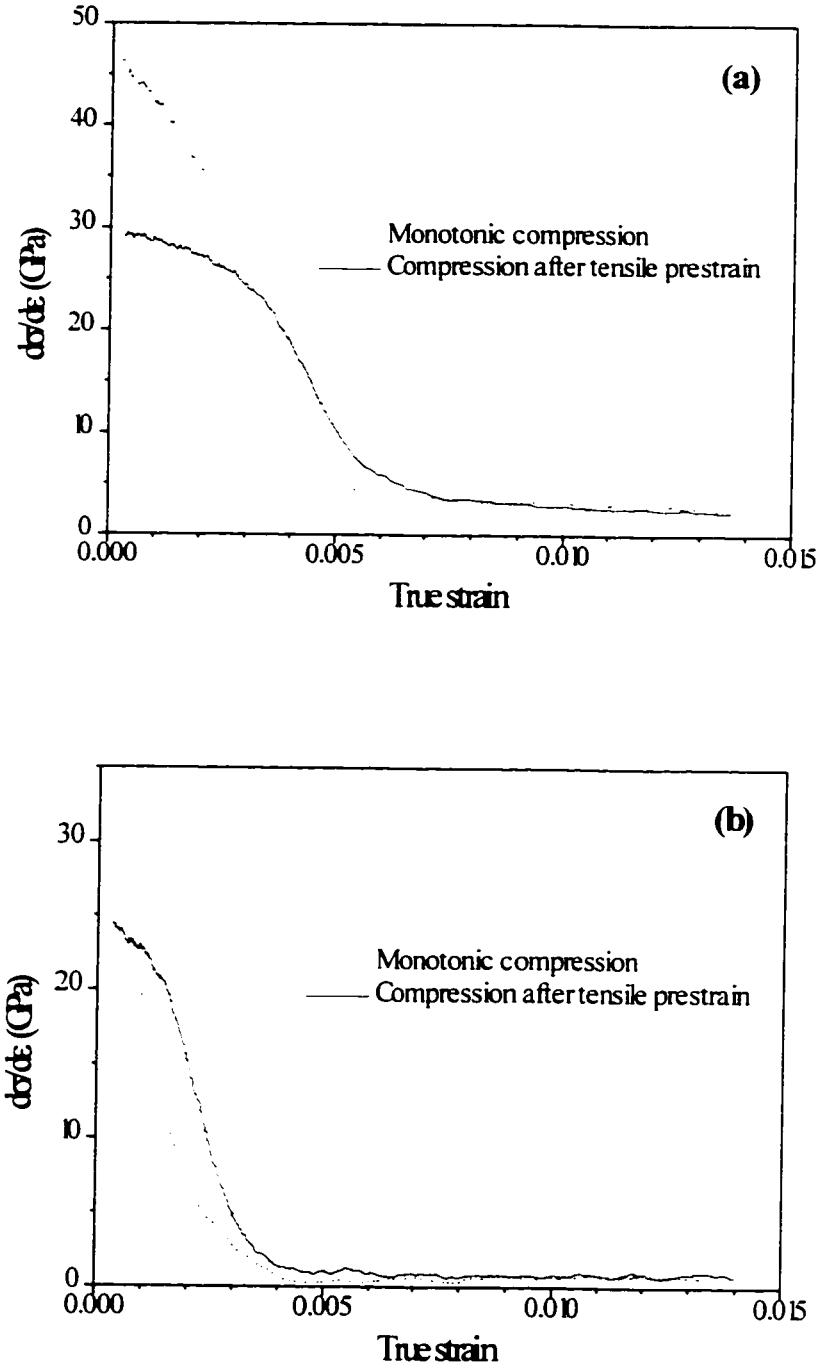

Figure 4.29: dσ/dε curves for monotonic compression and compression after a tensile prestrain for (a) the alloy, and (b) the Mg.

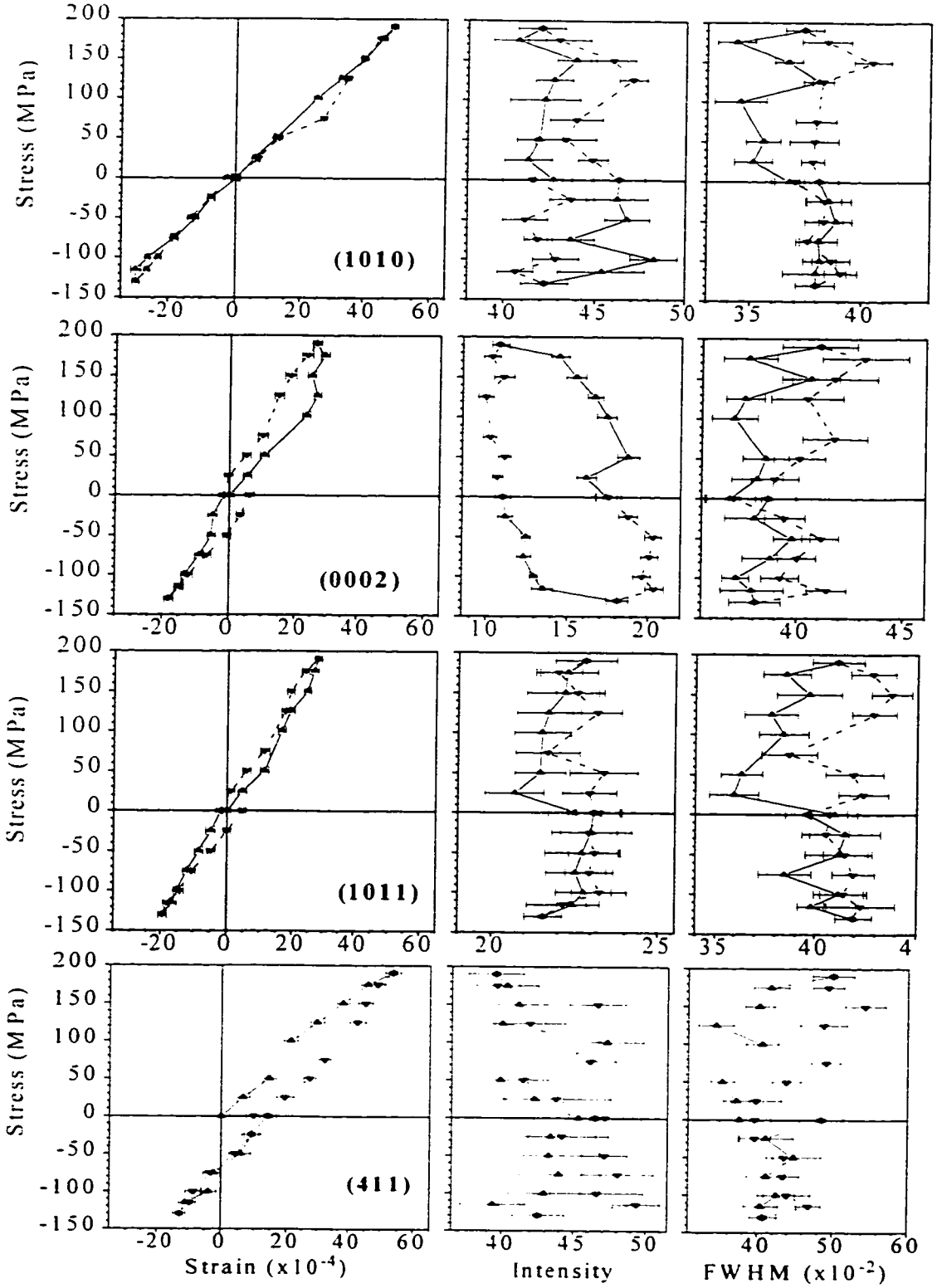

Figure 4.30: Neutron diffraction results - axial strains, tension-first Bauschinger.

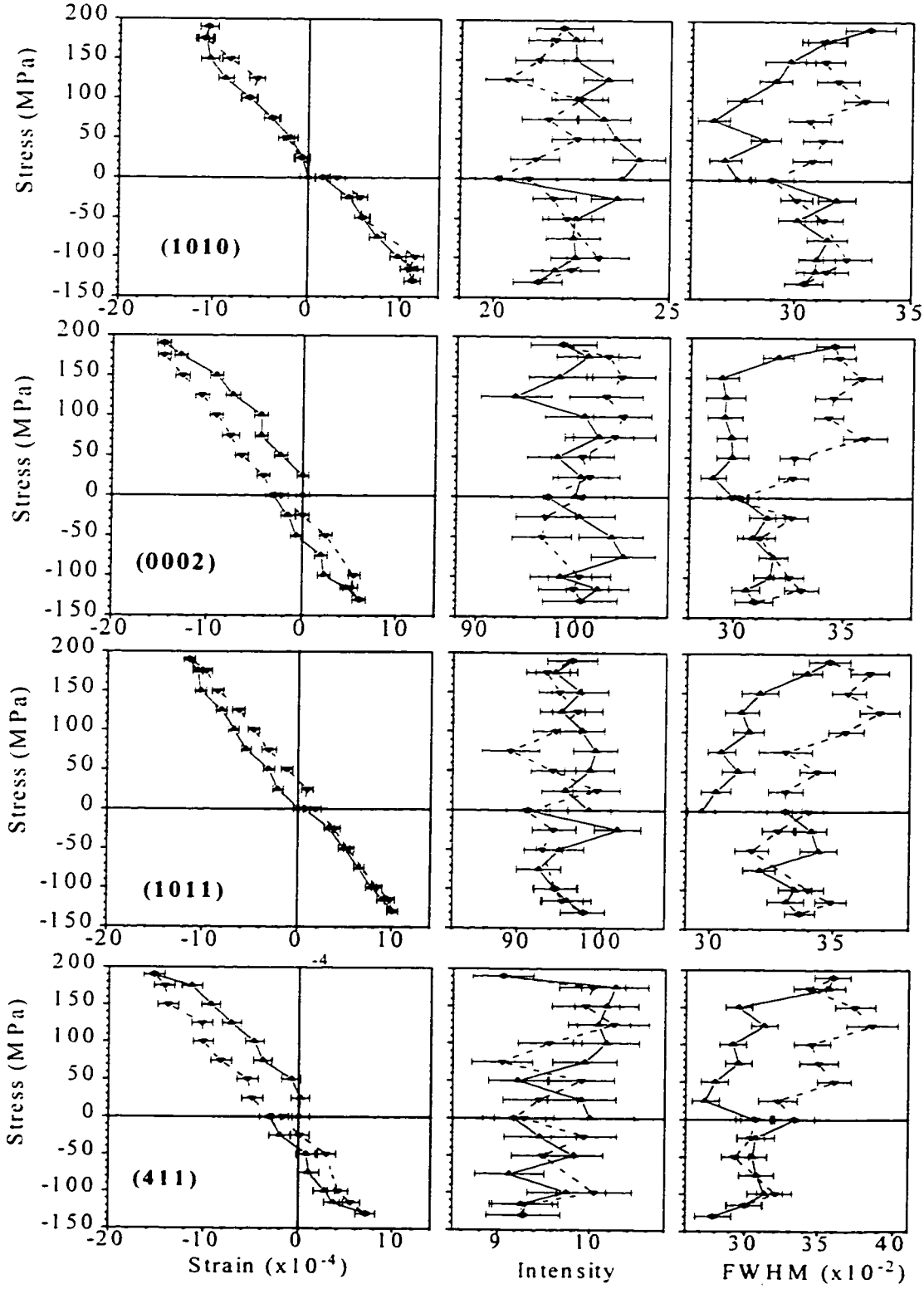

Figure 4.31: Neutron diffraction results - radial strains, tension-first Bauschinger.

Table 4.6: Salient features of the neutron diffraction results for tension-first Bauschinger.

{10$\bar{1}$0} axial	• The strain increases linearly during loading in compression except for the final stress increment which does not produce an increase in strain. The unloading line is linear and there is a small compressive residual strain. • The intensity decreases during the compressive portion of the test (unloading line to the left of the loading line) which is the opposite to what occurs in the tensile portion. The two effects cancel so that the intensity at the end of the test is the same as it was before the material was deformed. • The FWHM does not change significantly during the compressive portion of the test.
(0002) axial	• The strain varies steadily during loading and unloading in compression. However, the two lines deviate somewhat and there is a tensile residual strain at the end of the test. • A large increase in intensity occurs during the final stress increment in compression which offsets the large decrease observed in tension. • The FWHM does not change significantly during the compressive portion of the test.
{10$\bar{1}$1} axial	• The strain varies steadily during loading and unloading in compression. There is a tensile residual strain at the end of the test. • The intensity and FWHM do not change significantly during the compressive portion of the test.
{411} axial	• The strain varies steadily during loading and unloading in compression. The marked difference between the loading and unloading lines does not occur in compression as it did in tension. There is a tensile residual strain at the end of the test. • The intensity and FWHM do not change significantly during the compressive portion of the test.
{10$\bar{1}$0} radial	• The strain increases linearly during loading in compression except for the final stress increment which does not produce an increase in strain. The unloading line is linear and there is a small tensile residual strain. • The intensity and FWHM do not change significantly during the compressive portion of the test.
(0002) radial	• The strain varies steadily during loading and unloading in compression. There is a compressive residual strain at the end of the test. • The intensity and FWHM do not change significantly during the compressive portion of the test.
{10$\bar{1}$1} radial	• The strain varies linearly with stress during loading and unloading in compression (the two lines overlap). There is a tensile residual strain at the end of the test. • The intensity and FWHM do not change significantly during the compressive portion of the test.
{411} radial	• The strain varies steadily during loading and unloading in compression. There is a compressive residual strain which is inherited from the tensile portion of the test. • The intensity and FWHM do not change significantly during the compressive portion of the test.

4.7 Compression-first Bauschinger

Compression-first Bauschinger experiments were performed in order to investigate the effect of a change in strain path on the behaviour of the materials. Compression-first Bauschinger loops for the alloy and magnesium are shown in Figure 4.32. The monotonic tensile curves are also included.

The two materials show the same general trends during this deformation cycle. On unloading from compression, considerable strain is recovered. A pronounced inflection point appears in both curves after which the tensile portion of the Bauschinger loop is identical to the monotonic tensile loading curve except for being translated strictly upwards, parallel to the stress axis. The main differences between the alloy behaviour and that of the Mg are that the corresponding stress levels are higher, and that $d\sigma/d\varepsilon$ for the alloy after yielding in compression is much greater than that of magnesium which is close to zero.

The in-situ neutron diffraction results are shown in Figure 4.33 (axial strains) and Figure 4.34 (radial strains). The material was stressed to 130 MPa in compression and then to 210 MPa in tension. Table 4.7 contains a description of the salient features of the neutron diffraction results for each plane. The compressive portion of the results are in fact those presented in section 4.2 and are not described here in detail.

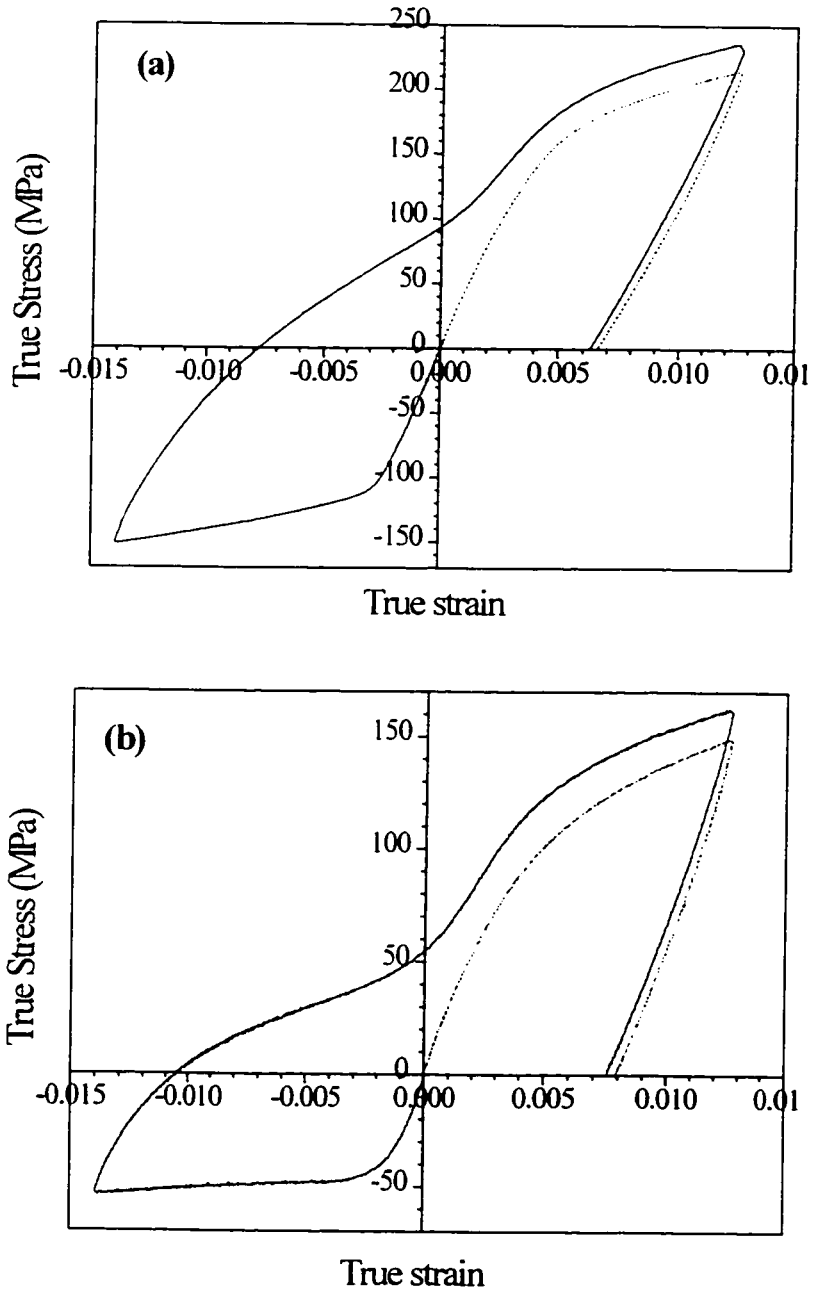

Figure 4.32: Compression-first Bauschinger loops for (a) the alloy and (b) the Mg. The monotonic tensile curves are also included.

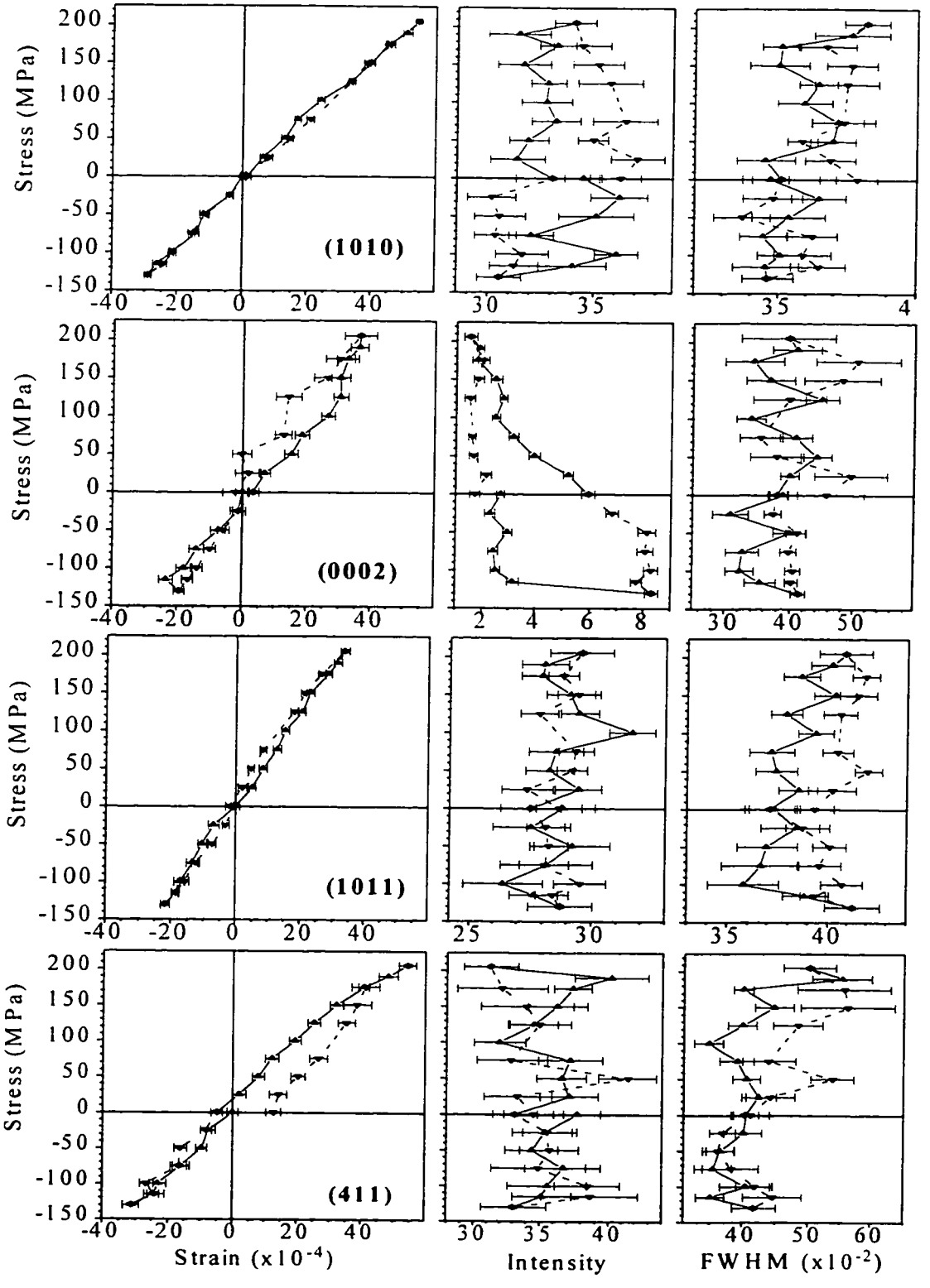

Figure 4.33: Neutron diffraction results - axial strains, compression-first Bauschinger.

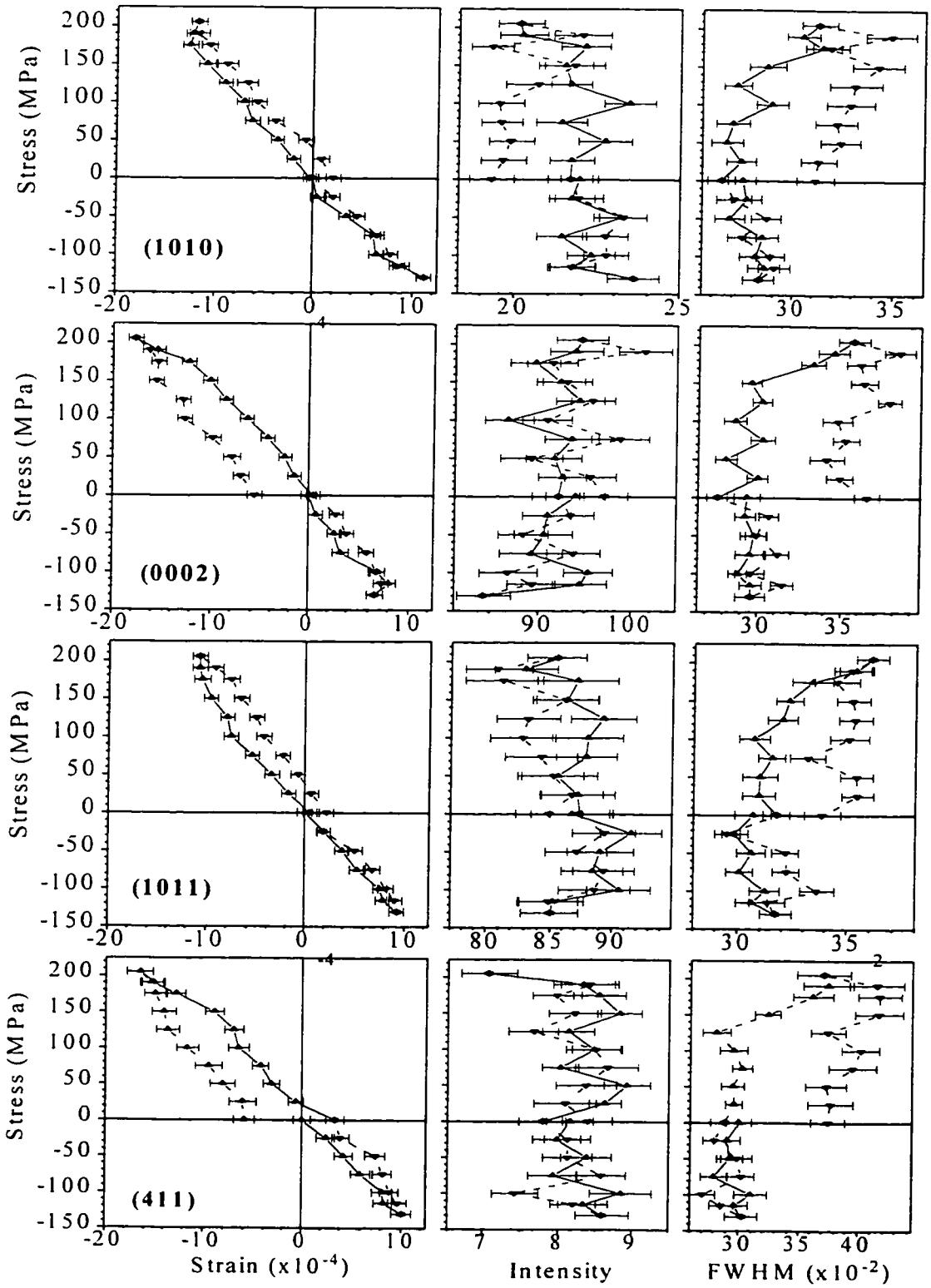

Figure 4.34: Neutron diffraction results - radial strains, compression-first Bauschinger.

Table 4.7: Salient features of the neutron diffraction results for compression-first Bauschinger.

{10$\bar{1}$0} axial	• The strain varies linearly throughout the loading cycle and there are no residual strains at the end of prestraining or at the end of the cycle. • There is an increase in intensity during the tensile portion of the cycle (unloading line to the right of the loading line). • There may be a small increase in FWHM during the tensile portion of the cycle (the average value of FWHM is higher in the tensile portion than in the compressive portion).
{0002} axial	• On loading in tension, the strain increases linearly with stress up to about 125 MPa. Beyond this level the strain increases much more slowly. The strain decreases steadily with stress down to 50 MPa where it is nil. From 50 to 0 MPa there is no change in strain. • The intensity which was lost during the compressive portion of the cycle is fully recovered at a tensile stress of about 100 MPa. It does not change from 100 to 150 MPa, then increases again to a slightly higher level than at the start of the test. No changes occur during unloading from tension. • The FWHM does not appear to change during the tensile half of the cycle.
{10$\bar{1}$1} axial	• The strain varies almost linearly during the entire cycle. However, the loading and unloading lines do not overlap perfectly. There is no residual strain at the end of the cycle. • The intensity does not appear to vary during the test. • The FWHM increases slightly at the higher applied stresses during loading in tension but does not appear to change during the final unloading.
{411} axial	• The loading line in tension can be divided into two linear regions: the first extending from 0 to 150 MPa and the second from 150 to 210 MPa. The unloading line retraces the loading line from 210 to 150 MPa, then deviates considerably resulting in a tensile residual strain of approximately 15×10^{-4}. • The intensity does not change significantly during the test. • The FWHM increases during loading in tension but appears to recover during unloading.

Table 4.7: Salient features of the neutron diffraction results for compression-first Bauschinger. (continued)

{10$\bar{1}$0} radial	• The strain increases linearly during loading in tension up to 175 MPa, beyond which the strain no longer evolves. The unloading line is essentially linear. There is a small tensile residual strain of the order of 2-4x10^{-4}. • There is a decrease in intensity during the tensile half of the cycle (unloading line to the left of the loading line). • The FWHM increases during loading in tension from 125 to 175 MPa. It is only partially recovered during unloading.
{0002} radial	• The loading line in tension can be divided into two linear regions: the first extending from 0 to 175 MPa and the second from 175 to 210 MPa. The unloading line deviates considerably from the loading line, resulting in a compressive residual strain of approximately 6x10^{-4}. • The intensity does not vary significantly during the test. • The FWHM increases steadily during loading beyond 150 MPa and is not recovered during unloading.
{10$\bar{1}$1} radial	• The loading line in tension can be divided into three regions as follows 0 to 100 MPa: strain increases linearly with applied stress. 100 to 175 MPa: second linear region (higher slope) 175 to 210 MPa: no change in strain The unloading line is essentially linear. There is a small tensile residual strain of about 2-4x10^{-4}. • There may be a small decrease in intensity during the tensile half of the cycle (unloading line to the left of the loading line). • The FWHM increases beyond about 100 MPa during loading in tension and is not recovered during unloading.
{411} radial	• The strain increases steadily during loading in tension, the rate of increase being higher beyond 150 MPa. The unloading line is linear and deviates significantly from the loading line, resulting in a negative residual strain of the order of 6x10^{-4}. • The intensity does not vary significantly during the test. • The FWHM increases steadily during loading in tension beyond about 125 MPa and is not recovered during unloading.

4.8 Microstructural Observations

Macroscopic observations are available from the mechanical tests and neutron diffraction results presented in the previous sections. Stress-strain curves represent the average behaviour of the whole polycrystal, while the neutron diffraction results for each peak reflect the behaviour of a given set of grains. HCP metals deform by a combination of slip and twinning, thus it is useful to complement these macroscopic results with microstructural observations which allow both to identify the deformation modes, and to characterise their spatial distribution and their interactions with the second phase. In this section, observations by optical and transmission electron microscopy (TEM) are presented.

4.8.1 Optical microscopy

Optical microscopy provides a relatively simple means of assessing the spatial distribution of twinning in the material. It allows comparisons to be made between the interior of grains and grain boundaries. It can also provide comparisons of the twinning behaviour of different components of the texture. Finally, it can be used to observe the effects of the sense of deformation (i.e. tension or compression) on the twinning behaviour of the material.

The anisotropy of twinning with regard to the sense of the applied stress (i.e. compression or tension) in the Mg is clearly visible in Figure 4.35 which shows etched cross-sections (i.e. normal to the stress axis) for samples deformed in tension (≈1.8% strain) and in compression (≈1.2% strain). In compression (a) very long, wide twins which can easily cross grain boundaries (e.g. at A) occur. Much smaller twins, apparently nucleated at grain boundaries, also occur (e.g. at B). In tension (b), however, only the smaller twins occur. These twins are most likely of the $\{10\bar{1}2\}\langle 10\bar{1}\bar{1}\rangle$ type, as discussed in the literature review.

In the alloy, the precipitates clearly influence the morphology of twinning, as can be seen in Figure 4.36 for a sample deformed in compression. The twins are in general much narrower than in the Mg. However, they are still transmitted through grain boundaries (at A), and small grain boundary twins still occur. In addition, precipitates do not appear to impede the propagation of the twins. This is described more fully in the following section on transmission electron microscopy.

The anisotropy of twinning in the alloy is clearly illustrated in Figure 4.37, which shows etched cross sections for samples deformed in compression (a) and in tension (b). In (a) the large central grain has its basal plane normal nearly parallel to the stress axis. This can be deduced from the appearance of the precipitates, which have their large face parallel to the plane of the micrograph. The surrounding grains, however, are more typical of the texture, with the basal pole at some large angle ($>\approx 60°$) from the stress axis. It is clear that the central grain is the only one which does not undergo copious twinning. In contrast, similarly oriented grains in (b) do undergo severe twinning, while the surrounding grains do not.

(a) x 480

(b) x 363

Figure 4.35: Anisotropy of twinning in pure magnesium (a) compression (b) tension.

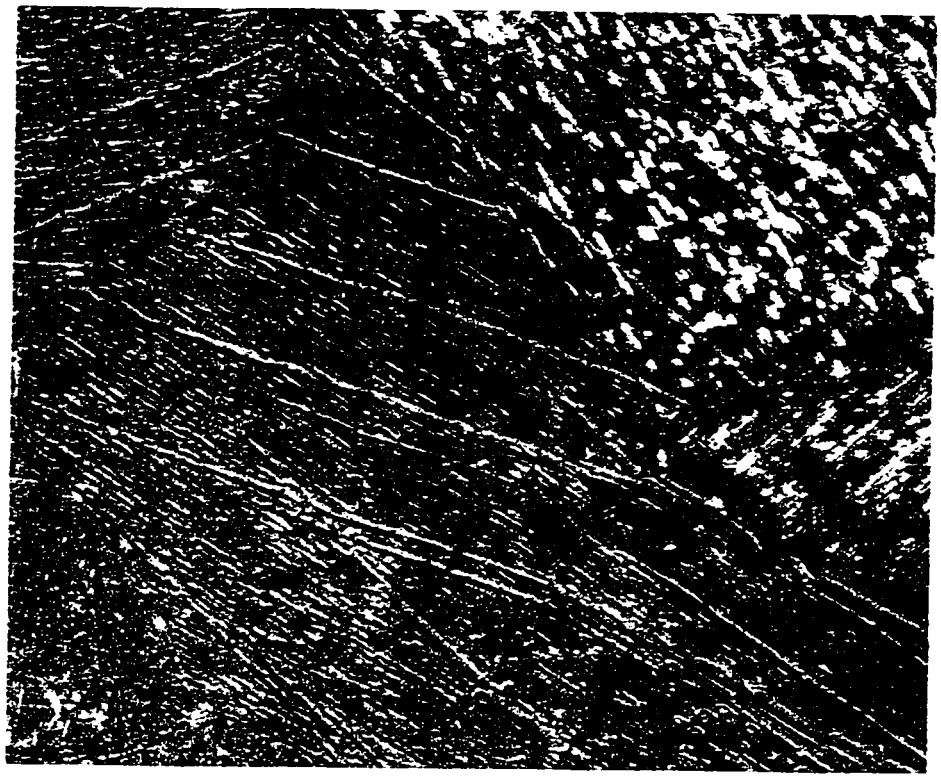

Figure 4.36: Twinning in the alloy under compressive loading (x 1018).

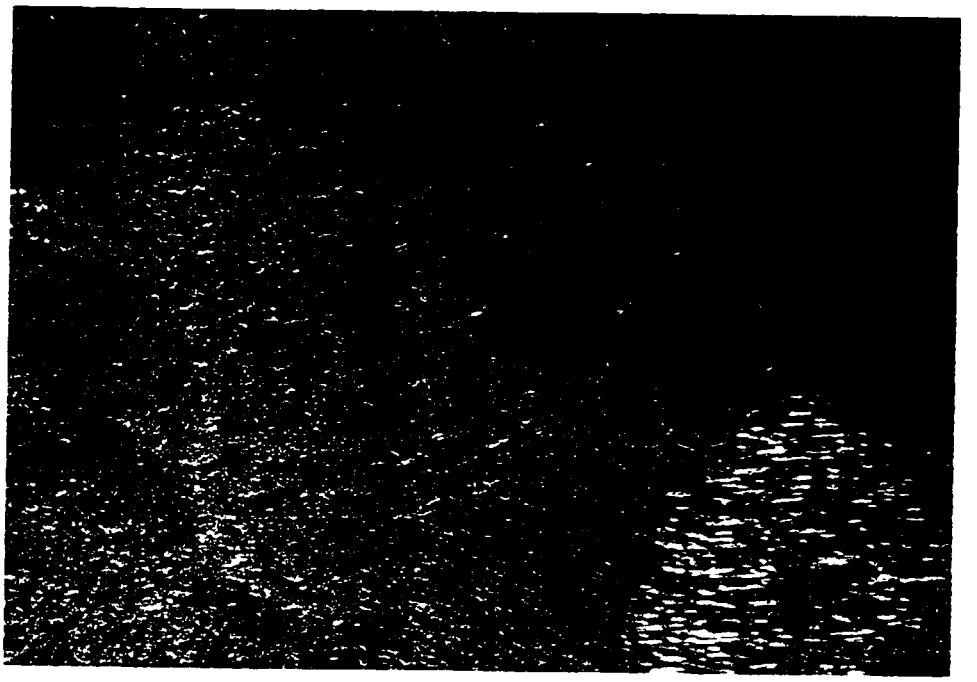

(a) x 921

(b) x 885

Figure 4.37: Anisotropy of twinning in the alloy (a) compression, (b) tension.

4.8.2 Transmission electron microscopy

TEM has been used to determine which Burgers vectors are present in the undeformed alloy and in the alloy deformed in tension and in compression in order to determine which types of dislocations contribute to deformation, and to observe how dislocations interact with second phase particles. In addition, the twinning systems which occur, and their interactions with grain boundaries and second phase particles have also been studied.

Table 4.8 contains **g.b** values for several reflections for **a**, **c**, and **c+a** Burgers vectors in a HCP metal. It is clear that **c**-type dislocations will show only weak residual contrast (**g.b**×**u**) for {10$\bar{1}$0} and {2$\bar{1}$ $\bar{1}$0} reflections (**g.b**=0) while (0002) reflections will have this effect on **a**-type dislocations.

Table 4.8: Values of g.b for several low order reflections in a HCP metal.

	Burgers vectors of perfect dislocations (x 1/3)									
g	**a**			**c+a**						**c**
	±[11$\bar{2}$0]	±[$\bar{1}$2$\bar{1}$0]	±[$\bar{1}$110]	±[11$\bar{2}$3]	±[$\bar{1}$2$\bar{1}$3]	±[$\bar{2}$113]	±[11$\bar{2}$$\bar{3}$]	±[$\bar{1}$2$\bar{1}$$\bar{3}$]	±[$\bar{2}$11$\bar{3}$]	±[0003]
10$\bar{1}$0	±1	0	∓1	±1	0	∓1	±1	0	∓1	0
01$\bar{1}$0	±1	±1	0	±1	±1	0	±1	±1	0	0
$\bar{1}$100	0	±1	±1	0	±1	±1	0	±1	±1	0
0002	0	0	0	±2	±2	±2	∓2	∓2	∓2	±2
10$\bar{1}$1	±1	0	∓1	±2	±1	0	0	±1	±2	∓1
10$\bar{1}\bar{1}$	±1	0	∓1	0	∓1	∓2	±2	±1	0	∓1
01$\bar{1}$1	±1	±1	0	±2	±2	±1	0	0	∓1	±1
01$\bar{1}\bar{1}$	±1	±1	0	0	0	∓1	±2	±2	±1	∓1
$\bar{1}$101	0	±1	±1	±1	±2	±2	∓1	0	0	±1
$\bar{1}\bar{1}$0$\bar{1}$	0	±1	±1	∓1	0	0	±1	±2	±2	∓1
11$\bar{2}$0	±2	±1	∓1	±2	±1	∓1	±2	±1	∓1	0
$\bar{1}$2$\bar{1}$0	±1	±2	±1	±1	±2	±1	±1	±2	±1	0
$\bar{2}$110	∓1	±1	±2	∓1	±1	±2	∓1	±1	±2	0

Thus the most useful zone axes, which show all **c**-type and most of the **a**-type dislocations are <2$\bar{1}\bar{1}$0>, which contain both (10$\bar{1}$0) and (0001) reflections. The diffraction pattern corresponding to one of these axes is shown in Figure 4.38.

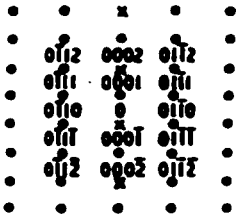

Figure 4.38: [2$\bar{1}\bar{1}$0] zone axis (crosses correspond to spots which may appear by double diffraction).

4.8.2.1 Burgers vector analysis

In the undeformed material, very straight dislocations are found which are normal to **g** = (0002), and therefore parallel to the long direction of the second phase (Figure 4.39). These dislocations disappear in a {10$\bar{1}$0} reflection and are therefore c-type. They are uniformly spaced in a grain between precipitates, and their density and distribution do not change significantly with deformation.

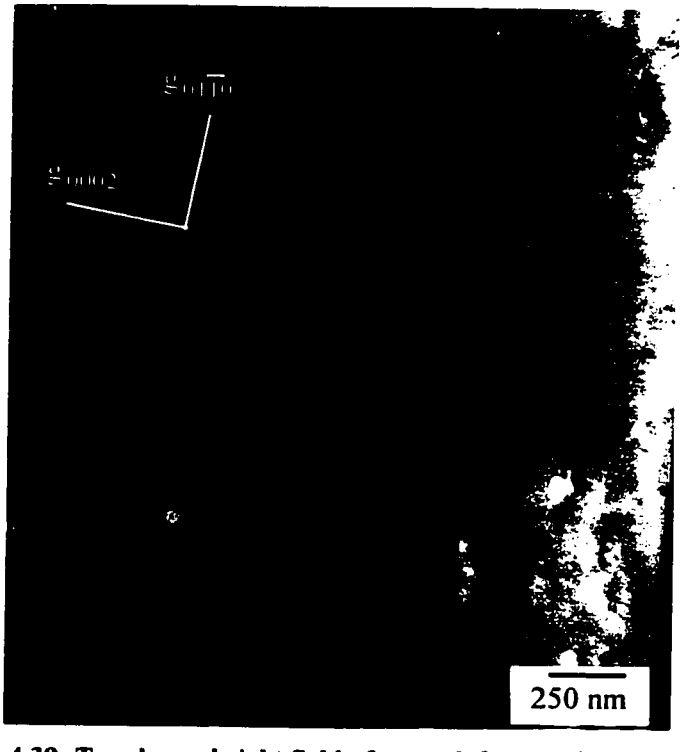

Figure 4.39: Two-beam bright field of an undeformed foil, g = (0002).

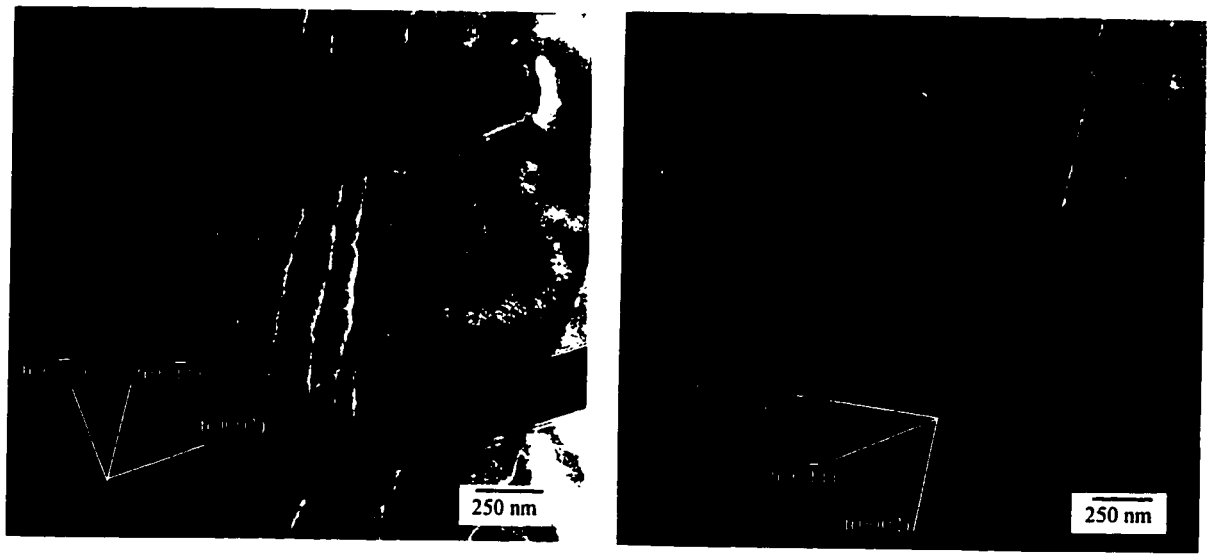

(a) (b)

Figure 4.40: Dark field image of an undeformed sample of the alloy (a) g = {10$\bar{1}$0}, (b) g = (0002).

Figure 4.40 (a) and (b) show dark field images of the same area obtained for the undeformed alloy using {10$\bar{1}$0} and (0002) reflections, respectively. It is clear that the dislocations in (a) are extinguished in (b) and are therefore **a**-type. Furthermore, the dislocation lines are parallel to the trace of a {10$\bar{1}$1} type plane, indicating that these dislocations lie on a non-basal plane. Such dislocations are not very common in the undeformed state.

Bright field images from a sample deformed in tension, using a <2$\bar{1}\bar{1}$0> type zone axis with several reflections operating, are shown in Figure 4.41. With these diffracting conditions, all the **c**-dislocations and two thirds of the **a**-dislocations should be visible. In Figure 4.41(a), dislocation lines parallel to the trace of the (0$\bar{1}$10) prism plane are easily seen (e.g. at B). In addition, at A, dislocation lines parallel to the trace of the (01$\bar{1}$3) pyramidal plane can be made out, and at C dislocation lines more or less aligned with the trace of the (0$\bar{1}$12) pyramidal plane are visible, though very faint. In Figure 4.41 (b), dislocation lines parallel to the trace of the (0$\bar{1}$10) prism plane are again easily visible. In the lower portion of the micrograph (at A), dislocation lines more or less aligned with the trace of the (0$\bar{1}$11) plane can be seen. As in Figure 4.40, the slip lines are wavy due to cross-slip on the basal plane. Dislocation lines parallel to the trace of the basal plane occur in both micrographs. In Figure 4.42, a dark field image of the same sample using a (0002) reflection is shown. Very few dislocations are visible compared with Figure 4.41, indicating that most of the dislocations are in fact **a**-type. Note also that most of the dislocation lines parallel to the trace of the basal plane also disappear in Figure 4.42 so that it is clear that the traces are due to a high density of **a** dislocations lying in the basal plane.

Near grain boundaries, areas with very high dislocation densities are easily observed, as illustrated for example in the dark field image of Figure 4.43 which shows an extremely high dislocation density in the vicinity of a large grain boundary precipitate.

Summary

The above analysis shows that although c-type dislocations are present in the alloy in the undeformed state, the density of these dislocations does not change as a result of deformation. The large majority of dislocations have a $<2\bar{1}\bar{1}0>$ type Burgers vector and lie either in the basal plane, in $\{10\bar{1}0\}$ prism planes, or (to a lesser extent) in various pyramidal planes.

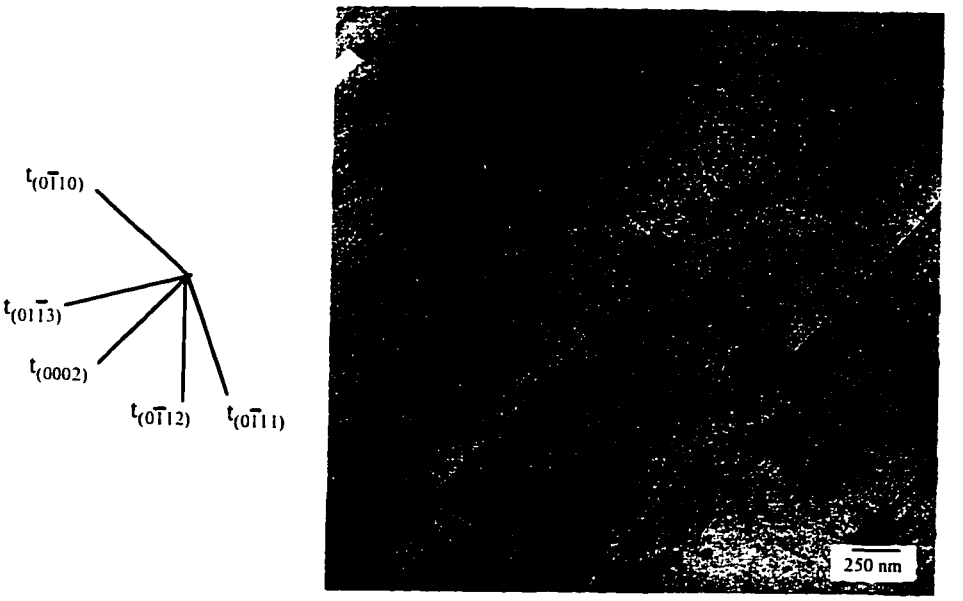

(a)

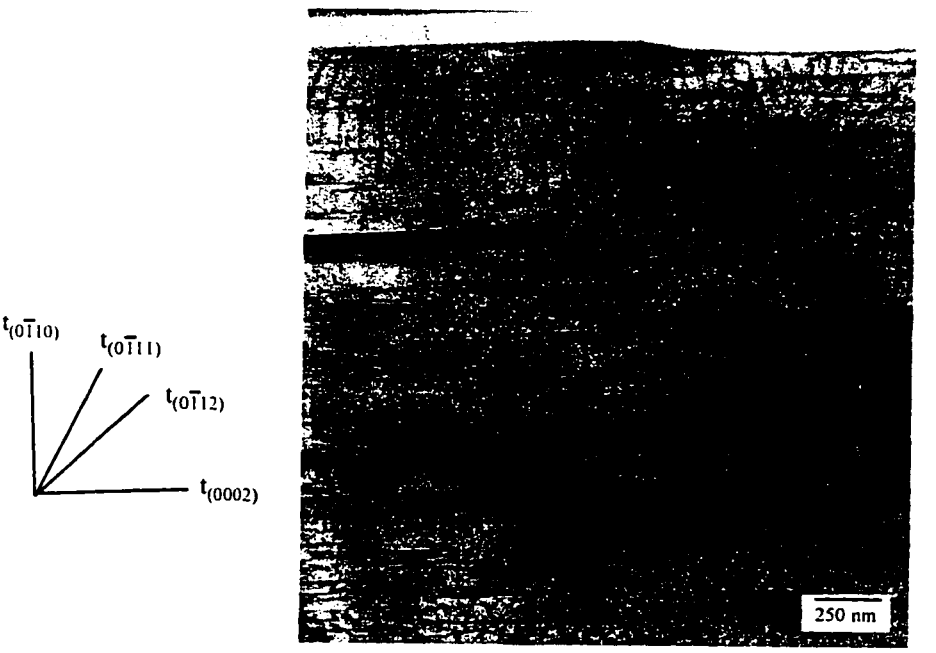

(b)

Figure 4.41: Bright field images of an alloy sample deformed in tension using a $[2\bar{1}\bar{1}0]$ zone axis (several reflections operating).

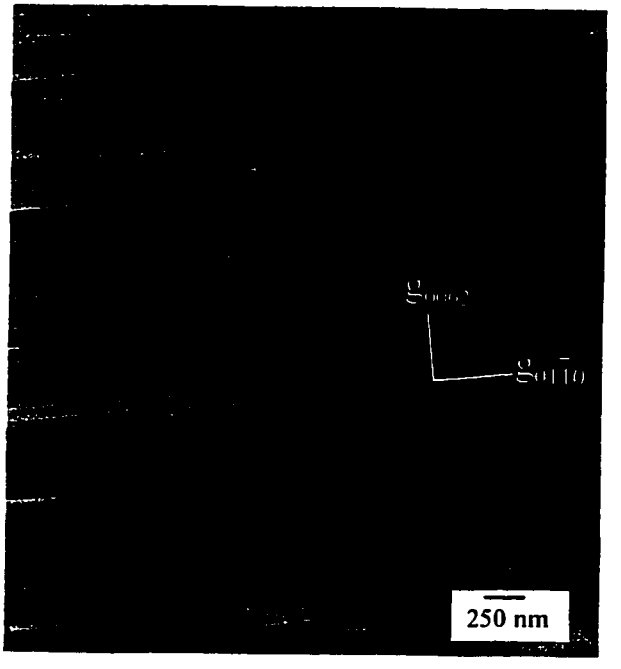

Figure 4.42: Dark field image of an alloy sample deformed in tension, g = (0002).

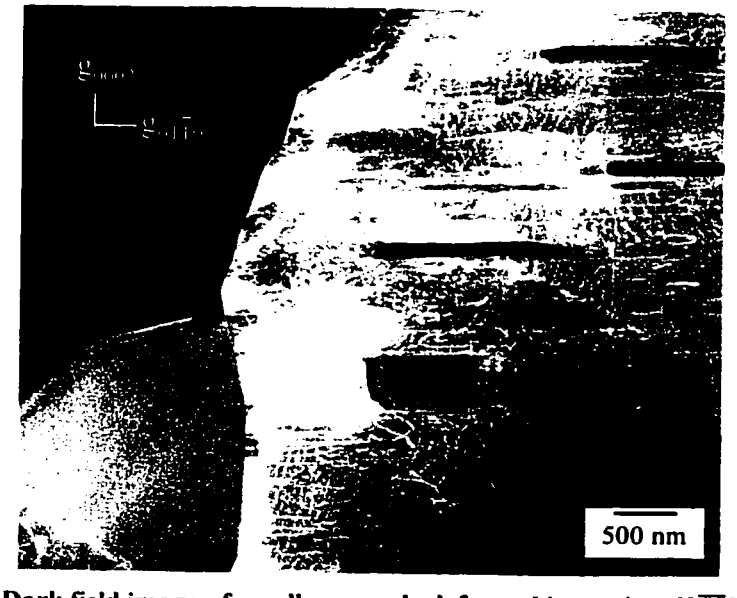

Figure 4.43: Dark field image of an alloy sample deformed in tension, $[2\bar{1}\bar{1}0]$ zone axis. ($g = (01\bar{1}0)$).

4.8.2.2 Twin observations

Optical microscopy shows clearly that twins can cross grain boundaries and interact in complex ways with precipitates in the alloy, but transmission electron microscopy (TEM) is needed to elucidate the mechanisms by which these processes occur, as well as to identify the twinning modes.

Only the $\{10\bar{1}2\}\langle 10\bar{1}\bar{1}\rangle$ twinning system referred to in the literature review has been observed in the current study. The type of twinning system obtained can be determined using selected area diffraction patterns (SADP) of the twin and matrix. If the foil is oriented such that the K_1 (mirror) plane is viewed edge on (i.e. the direction of the incident electron beam is contained in the K_1 plane), then the zone axis in the twin and matrix is the same, and the spots produced by diffraction in the twin are generated by reflection of the matrix spots across the line representing the trace of the K_1 plane in the pattern. Expressions (Reid, 1973) are also available which allow one to determine which crystallographic plane or direction in the twin should be parallel to a specified plane or direction in the matrix for a given K_1. If selected area diffraction patterns for the twin and matrix are then obtained for the same foil tilt, it is possible to determine which unique K_1 plane can account for the observed twin/matrix relationships.

Precipitates are never sheared by twins. Instead, twins generally interact with precipitates in one of three ways. A twin traversing a grain and impinging on the tip of a precipitate appears to simply bypass the precipitate without altering its course (Figure 4.44(a)). Diffraction patterns obtained for the precipitate and matrix near the precipitate-twin intersection, and for the precipitate and twin (Figure 4.44(b) and (c)) show that the orientation relationship between precipitate and matrix is unaffected by the presence of the twin. When the twin-precipitate intersection is larger, the twin can wrap around the precipitate (Figure 4.45(a)) and the precipitate is apparently bent elastically. Finally, it appears that in some cases a twin impinging on a precipitate can be stopped. A new twin then nucleates on the other side of the precipitate. This behaviour is shown by the two twins in Figure 4.45(b). The bottom twin was likely propagating from right to left when it came into contact with the precipitate, at which point it was halted, tapering down to a point where it contacted the precipitate at A. The beginnings of a new twin are visible on the other side of the precipitate at B. A similar scenario is likely for the top twin, though it appears to have propagated from left to right rather than from right to left. It is conceivable that the two twins can widen and eventually merge into a single twin.

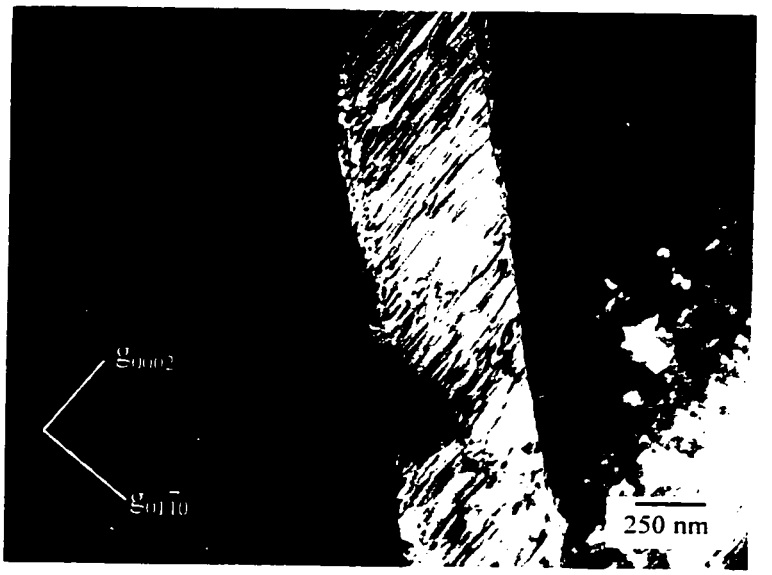

(a)

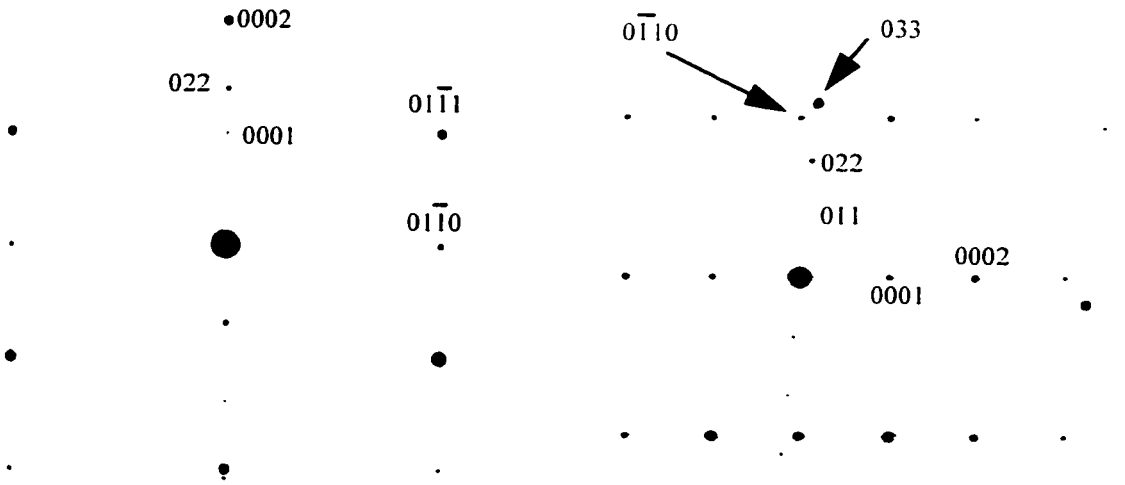

(b) (c)

Figure 4.44: (a) {10$\bar{1}$2} twin (white) impinging on the tip of a precipitate.
(b) Diffraction pattern for precipitate and matrix in (a).
(c) Diffraction pattern for precipitate and twin in (a).

(a)

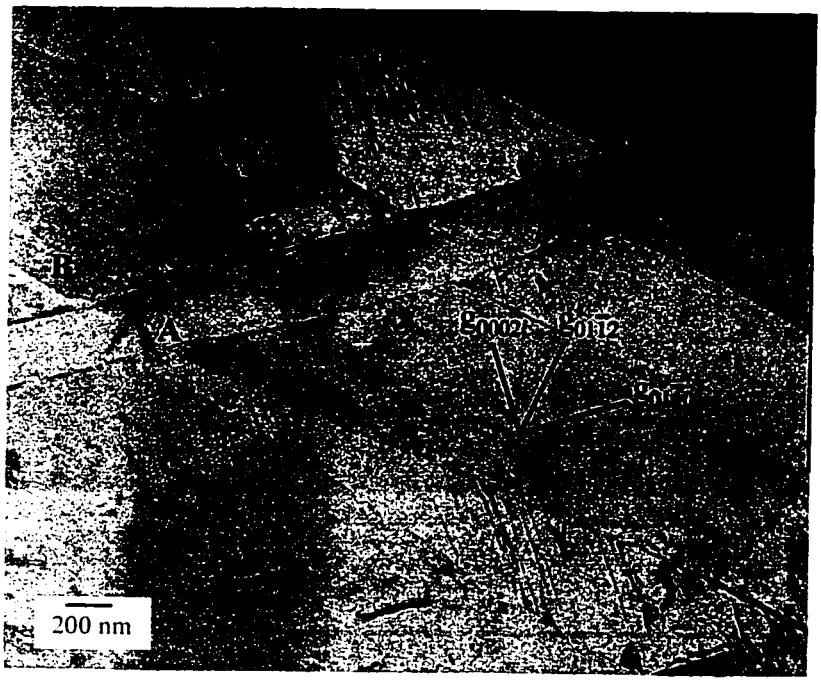

(b)

Figure 4.45: Bright field images illustrating:
(a) a twin wrapping around a precipitate, causing it to bend elastically (unknown orientation - length of precipitate is parallel to the trace of the basal plane).
(b) twins stopping on one side of a precipitate with other twins on the opposite side of the precipitate.

Twins can also engulf precipitates entirely, as shown in Figure 4.46(a) and (b). When this occurs, a high dislocation density can be observed at the tips of the precipitate (Figure 4.46(b)). In addition, the long direction of the precipitate inside the twin remains strictly parallel to that of precipitates in the matrix (Figure 4.46(b)). The SADP in Figure 4.47 for the twin in Figure 4.46 shows that it is of the $\{10\bar{1}2\}$ type. The SADP in Figure 4.48(a) for the precipitate and matrix in Figure 4.46(b) (top left corner) shows that the (0002) matrix plane is parallel to the (011) precipitate plane, as expected for the Mg-Al system based on observations by other authors (see section 2.4.1.9). The two precipitates in Figure 4.46(b) have the same crystallographic orientation with respect to the incident electron beam and by tilting the foil about $\mathbf{g} = (011)$ one easily obtains a $[\bar{1}2\bar{1}3]$ zone axis within the twin (Figure 4.48(b)) which clearly shows that the (011) precipitate plane is parallel to a $\{10\bar{1}0\}$ prism plane in the twin. The twin in Figure 4.46 contains a high density of stacking faults as shown in the dark field image in Figure 4.49.

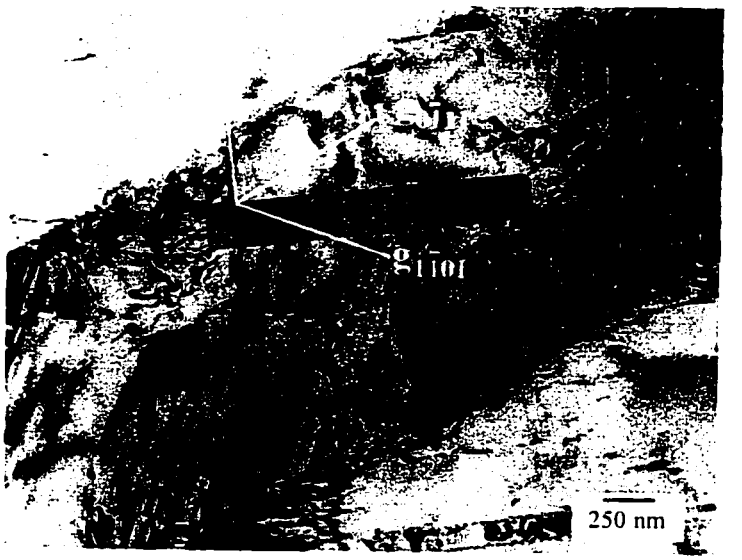

(a)

(b)

Figure 4.46: {10$\bar{1}$2} twin in an alloy sample deformed in compression. The precipitate is completely engulfed by the twin.
(a) twin zone axis = [$\bar{1}$2$\bar{1}$3]
(b) same as (a) except slightly tilted to show dislocation pileup around the precipitate.

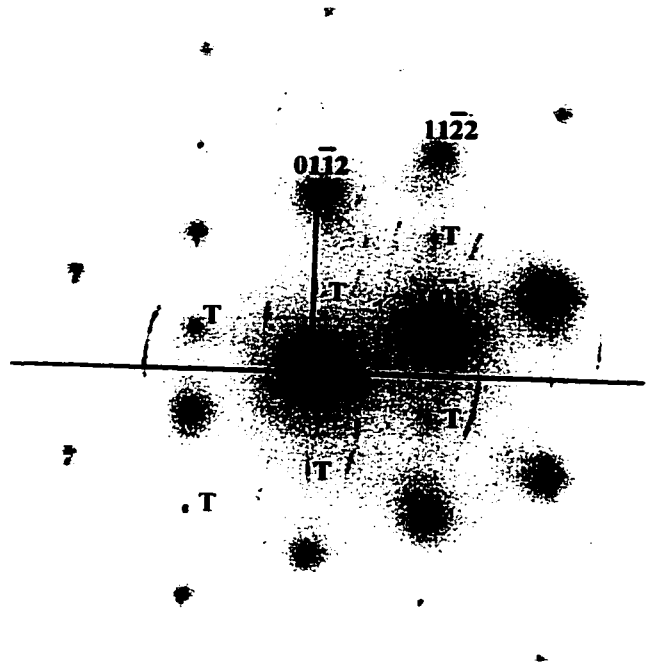

Figure 4.47: Seclected area diffraction pattern of twin and matrix in Figure 4.46. Spots marked 'T' are due to diffraction in the twin. The black line represents the trace of the $(01\bar{1}2)$ plane and is a mirror line, indicating that this is a $(01\bar{1}2)$ type twin.

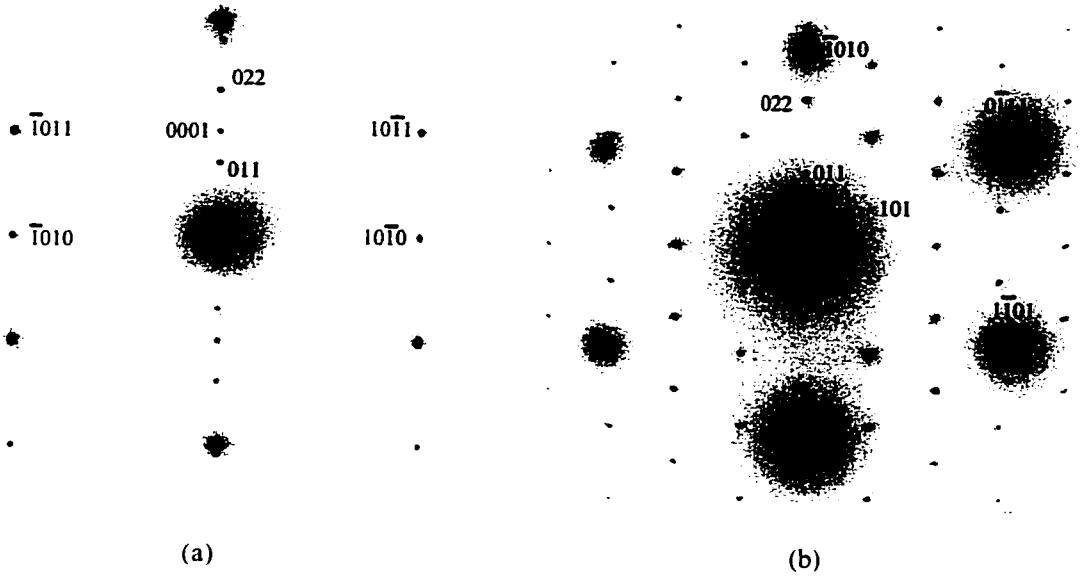

Figure 4.48: (a) Diffraction pattern for matrix and precipitate unaffected by twin in Figure 4.46(b).
(b) Diffraction pattern for matrix and precipitate engulfed by twin in Figure 4.46(b).

Figure 4.49: Dark field micrograph of the twin in Figure 4.46 showing the high density of stacking faults in the twin ($g = (\bar{1}010)$).

Finally, {10$\bar{1}$2} twins appear to be able to change their habit plane. In Figure 4.50, the twin clearly changes direction by about 15° upon encountering a precipitate. This can occur more than once along the length of a twin as shown in the figure. In order to identify the twinning system, the second method described above was used. Two foil tilts were used to obtain diffraction patterns for the twin and matrix (Figure 4.51). The orientation relationships for corresponding patterns were then catalogued (Table 4.9) and a consistent indexation of all the spots obtained. The (10$\bar{1}$2) twinning system could then be identified as the only system capable of accounting for all of the relationships observed. Table 4.9 shows that the (0$\bar{1}$1$\bar{1}$) matrix plane is unchanged in position, and has similar-type indices after twinning. This occurs for any plane in the η_1 zone (see for example Partridge, 1967).

Table 4.9: Table showing matrix planes/directions and calculated parallel twin planes/directions. The third column contains the closest indexed twin planes/directions to the matrix planes/directions. The angle indicated in the third column is the angle between the plane/direction in column 2 and that in column 3.

Matrix plane/direction	Calculated indices of parallel plane in twins	Closest indexed twin plane/direction
[2$\bar{1}\bar{1}$0]	[$\overline{0.5954}$ 1 $\overline{0.4046}$ 1.5954]	[$\bar{1}$2$\bar{1}$3] 3.52°
(0$\bar{1}$1$\bar{1}$)	($\bar{1}$10$\bar{1}$)	($\bar{1}$10$\bar{1}$) 0°
(0$\bar{1}$11)	($\overline{0.0637}$ 1 $\overline{1.0637}$ $\overline{0.8726}$	(01$\bar{1}\bar{1}$) 3.87°
(0002)	(1.6037 0 $\overline{1.6037}$ 0.1274)	(10$\bar{1}$0) 4.26°
[$\bar{1}\bar{1}$23]	[$\overline{3.2138}$ 1 2.2138 $\overline{1.7862}$]	[$\bar{7}$25$\bar{3}$] 6.37°
(1$\bar{1}$00)	($\overline{0.5319}$ 1 $\overline{0.4681}$ 0.9363)	($\bar{1}$2$\bar{1}$2) 2.40°
(10$\bar{1}\bar{1}$)	($\overline{0.5956}$ 0 0.5956 1.8089)	($\bar{1}$014) 4.42°

A dark field of the twin in Figure 4.50 is shown in Figure 4.52 with the foil tilt close to a [2$\bar{1}\bar{1}$0] zone axis. The twin is much narrower than in Figure 4.51 and a band of very high dislocation density around the twin is visible. The twin appears to be edge on in this orientation, and it is clear that the habit plane deviates considerably from a {10$\bar{1}$2} type plane. The very high dislocation density in the band is visible in the high magnification dark field images of Figure 4.53. Dislocations are visible for both (0002) and (10$\bar{1}$0) type reflections, indicating that both **c**- and **a**-type dislocations are present. In both micrographs, the dislocation lines are essentially parallel to the trace of the basal plane. The average spacing of the dislocations is approximately 10nm for both the **a**-dislocations and the **c**-dislocations. It is possible that the dislocations are **c+a**, which would account for their being visible for both diffracting conditions.

Figure 4.50: Composite bright field image showing a $(10\bar{1}2)$ twin deviating to avoid two precipitates (at P1 and P2). The indices are for reciprocal lattice vectors (t=twin, m=matrix).

*** matrix zone axis = $[7\bar{2}\bar{5}3]$**

*** twin zone axis = $[\bar{2}11\bar{3}]$**

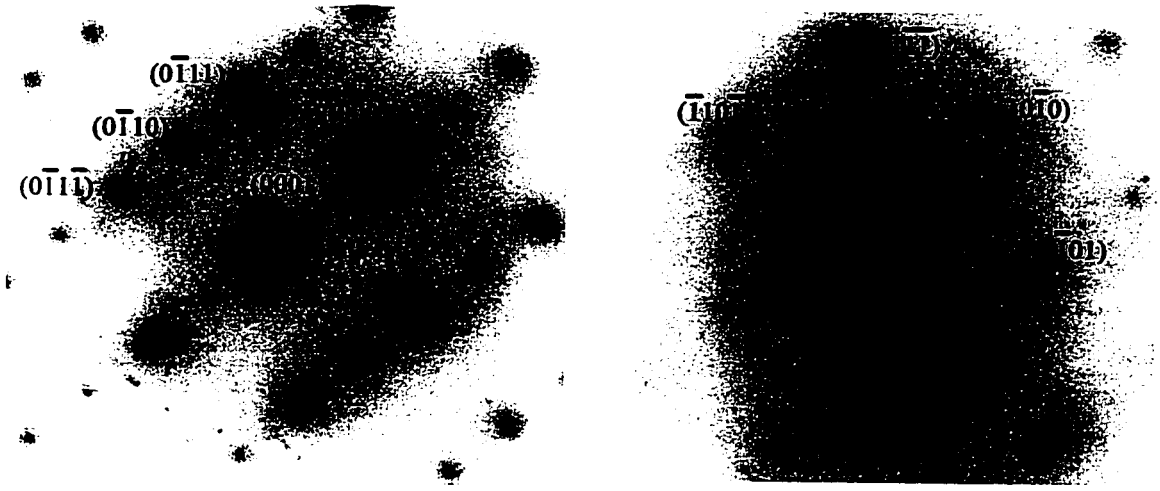

matrix (zone axis = [2$\bar{1}\bar{1}$0])

twin (zone axis = [$\bar{1}$2$\bar{1}$3])

(a) (patterns are for the same foil tilt)

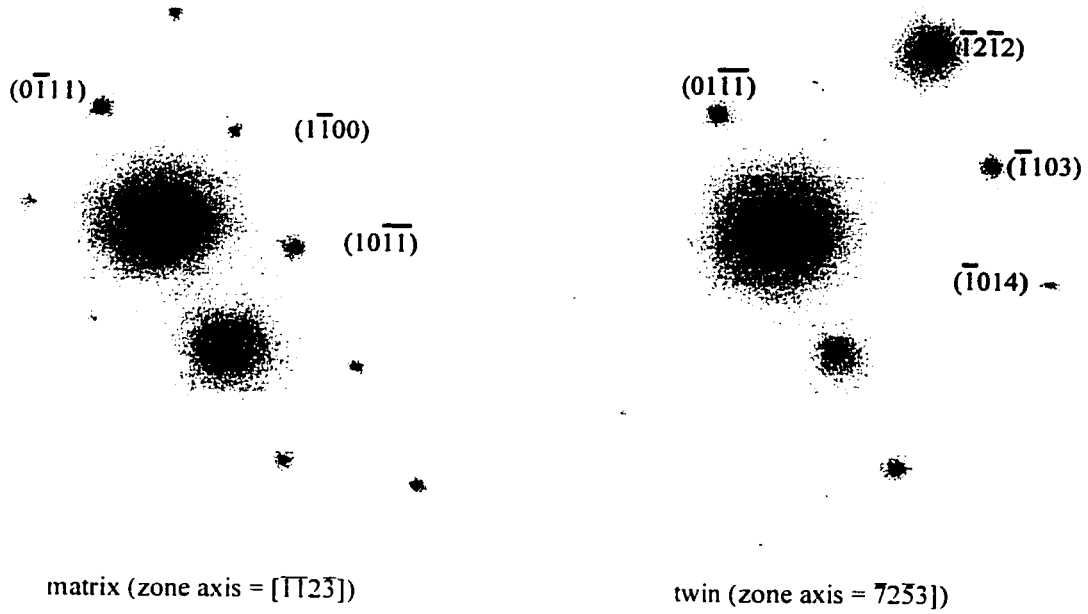

matrix (zone axis = [$\bar{1}\bar{1}$23])

twin (zone axis = $\bar{7}$253])

(b) (patterns are for the same foil tilt)

Figure 4.51: Indexed selected area diffraction patterns for the twin in Figure 4.50. The patterns in (a) and (b) are for different foil orientations.

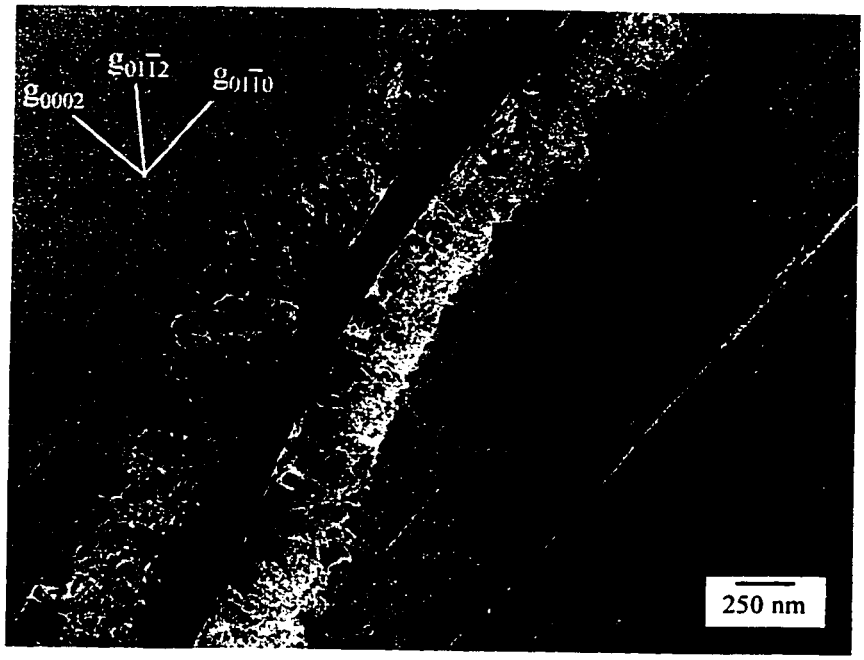

Figure 4.52: Dark field image showing that the habit plane of the $(10\bar{1}2)$ twin in Figure 4.50 deviates considerably from a $\{10\bar{1}2\}$ type plane. There is a band of high dislocation density which closely follows the twin boundary.

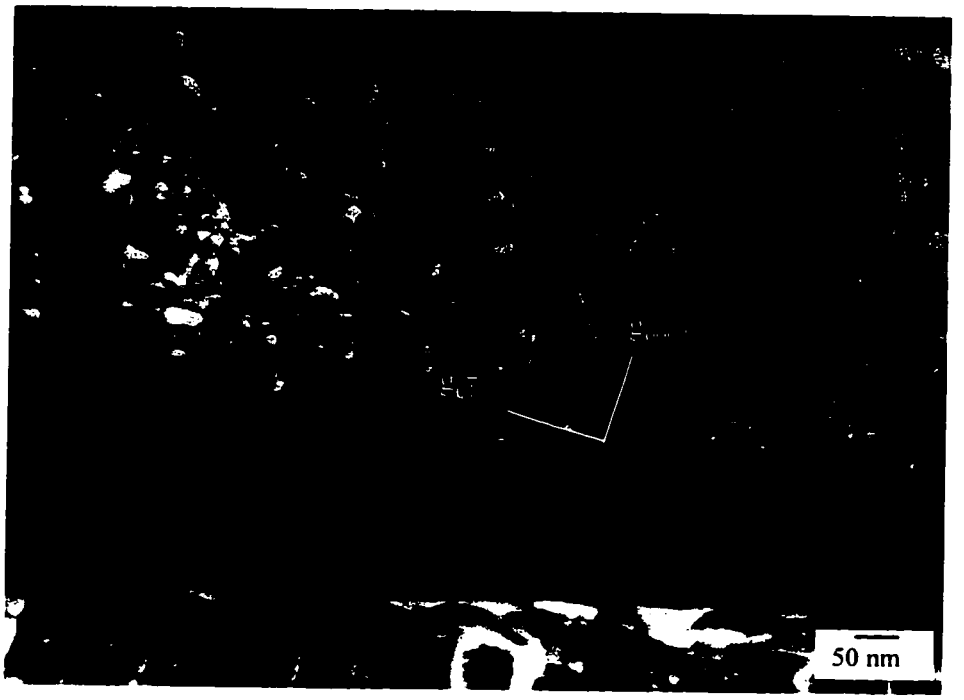

(a) g = (0002)

(b) g = (10$\bar{1}$0)

Figure 4.53: High magnification dark field images of the dislocation structure of the band around the twin in Figure 4.50 (zone axis = [2$\bar{1}\bar{1}$0]).

Summary

Microstructural observations using optical and transmission electron microscopy show that twinning is copious in samples deformed in compression but not in samples deformed in tension, for both the alloy and the Mg. Grain boundaries do not appear to constitute obstacles for twin propagation, likely because the texture of the material is such that the grain to grain misorientation is generally small. Twins never shear precipitates. Instead they either stop at the precipitate and nucleate new twins on the other side, or else they engulf the precipitates completely, or else they simply deviate to avoid coming into contact with them.

4.9 Properties of the intermetallic

It is useful to characterise the thermal and mechanical properties of the second phase in order to interpret the neutron diffraction and TEM results presented in the previous sections. To this end, the elastic constants and thermal expansion coefficient of the single crystal of the second phase described in Chapter Three have been evaluated. In addition, Vickers indentations have been used to study the deformation behaviour of the material.

4.9.1 Elastic constants

The elastic constants were evaluated using conventional ultrasonic measurement methods. The velocity of longitudinal and shear waves was measured along a [100] and a [110] direction. As there are only 3 independent elastic constants for a cubic structure, these results are sufficient to completely characterise the elastic behaviour of the material. The elastic stiffness and compliance matrices for the second phase are shown in Equations (4.1) and (4.2), respectively. Note that these matrices are expressed in the standard crystal orientation. Thus the '1', '2', and '3' axes correspond to the [100], [010], and [001] directions in the single crystal.

$$\begin{bmatrix} 86.9 & 32.6 & 32.6 & 0 & 0 & 0 \\ 32.6 & 86.9 & 32.6 & 0 & 0 & 0 \\ 32.6 & 32.6 & 86.9 & 0 & 0 & 0 \\ 0 & 0 & 0 & 19.5 & 0 & 0 \\ 0 & 0 & 0 & 0 & 19.5 & 0 \\ 0 & 0 & 0 & 0 & 0 & 19.5 \end{bmatrix} \text{GPa} \qquad (4.1)$$

$$\begin{bmatrix} 0.0145 & -0.00395 & -0.00395 & 0 & 0 & 0 \\ -0.00395 & 0.0145 & -0.00395 & 0 & 0 & 0 \\ -0.00395 & -0.00395 & 0.0145 & 0 & 0 & 0 \\ 0 & 0 & 0 & 0.0128 & 0 & 0 \\ 0 & 0 & 0 & 0 & 0.0128 & 0 \\ 0 & 0 & 0 & 0 & 0 & 0.0128 \end{bmatrix} \text{GPa}^{-1} \qquad (4.2)$$

Young's modulus (E) for any crystallographic direction can be determined by rotating the compliance matrix above such that the '1' direction lies parallel to the desired crystallographic direction. E is then given by $1/S_{11}$. The variation of E with crystallographic direction is shown in Figure 4.54. The modulus has a maximum value of 87 GPa along the <111> directions and a minimum value of 69 GPa along the <100> directions. The average value of E is 78 GPa.

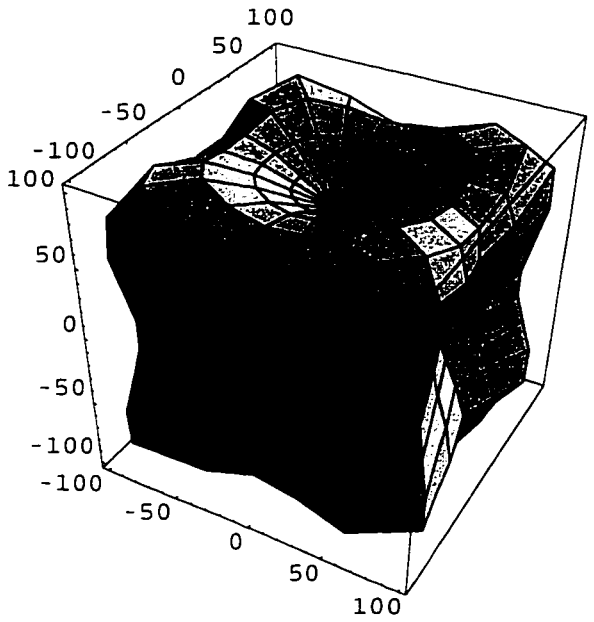

Figure 4.54: Variation of E with crystallographic direction for the intermetallic. The x, y, and z axes correspond to the three <100> directions.

4.9.2 Coefficient of thermal expansion

The coefficient of thermal expansion (α) of the intermetallic was determined using a system with an alumina reference from room temperature to 350°C. Note that cubic materials are isotropic for thermal expansion so that only one value of α need be specified. The graph of thermal strain vs. temperature is shown in Figure 4.55. α can be expressed as a linear function of temperature (in °C) using the following equation:

$$\alpha = 0.0372t + 21.14t \qquad \textbf{(4.3)}$$

An average value for α can be obtained from the best fit straight line to the thermal expansion data. The slope of the line is 28.4×10^{-6}/°C.

4.9.3 Vickers indentations

Vickers indentations were performed on a (001) and a ($1\bar{1}0$) face of the single crystal in order to have some indication of the plastic behaviour of the material, and of the possible anisotropy of this behaviour. Loads used ranged from 25g to 1000g. For each face, two indenter orientations were used. Indentations for the (110) and (100) faces are shown in Figure 4.56 and Figure 4.57, respectively. The crystallographic indices on the photographs correspond to the *traces* of the corresponding planes.

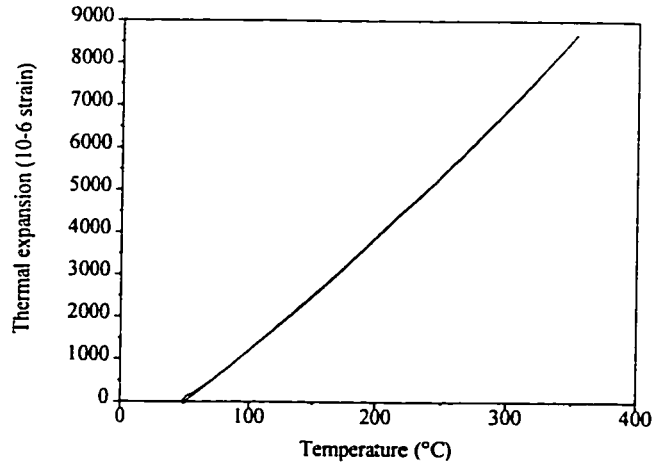

Figure 4.55: Thermal expansion of $Mg_{17}Al_{12}$ vs. temperature. Data for increasing and decreasing temperature are included.

On the (1$\bar{1}$0) face (Figure 4.56), cracks are visible for an indenter load of 25g, though this is not systematic. Well-developed cracks are easily visible for the 200g and 500g indents. In Figure 4.56(a) and (b), the cracks appear to originate at the indenter corners. The top vertical crack in (b) is very straight and follows the trace of a (100) plane. In (a), the right horizontal crack is also straight and follows the trace of a (110) plane. The other cracks in these two micrographs are quite wavy and cannot be said to correspond to any plane trace. In Figure 4.56(c) and (d), for which the indenter is rotated by 45° with respect to (a) and (b), straight cracks are visible which fall midway between the (100) and (110) plane traces. In addition, in (c) and (d), there are short, straight lines near the bottom right corner of the indent which are parallel to a (1$\bar{1}$0) plane trace.

On the (100) face (Figure 4.57), cracks are never produced for an indenter load of less than 100g. Cracks are produced systematically at a load of 200g. At 50g (Figure 4.57(b)), markings parallel to the indenter edges and therefore parallel to (100) traces are visible. In (c), long straight cracks emanating from the indent corners and parallel to (100) traces are visible. Less pronounced parallel markings originating along the indent edges are also visible. When the indenter is rotated by 45° (Figure 4.57(d)), cracks still emanate from the indent corners but they are much shorter than in (c). However, cracks parallel to the (100) traces are still very pronounced, and emanate from the midpoint of the indent edges.

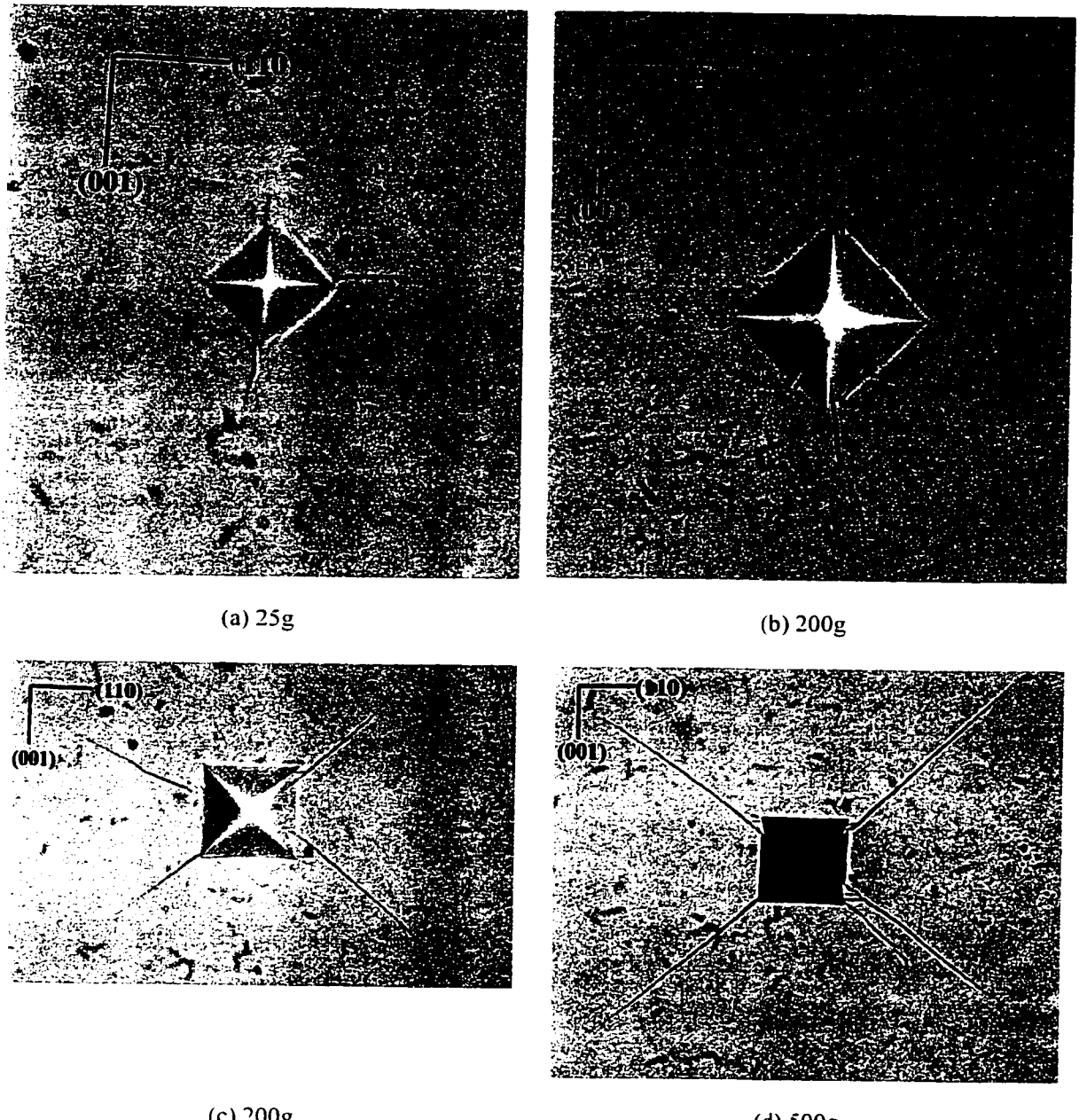

(a) 25g

(b) 200g

(c) 200g

(d) 500g

Figure 4.56: Indentations on a $(1\bar{1}0)$ face of the intermetallic for various loads and indenter orientations. The indexed lines indicate the orientation of the corresponding planes.

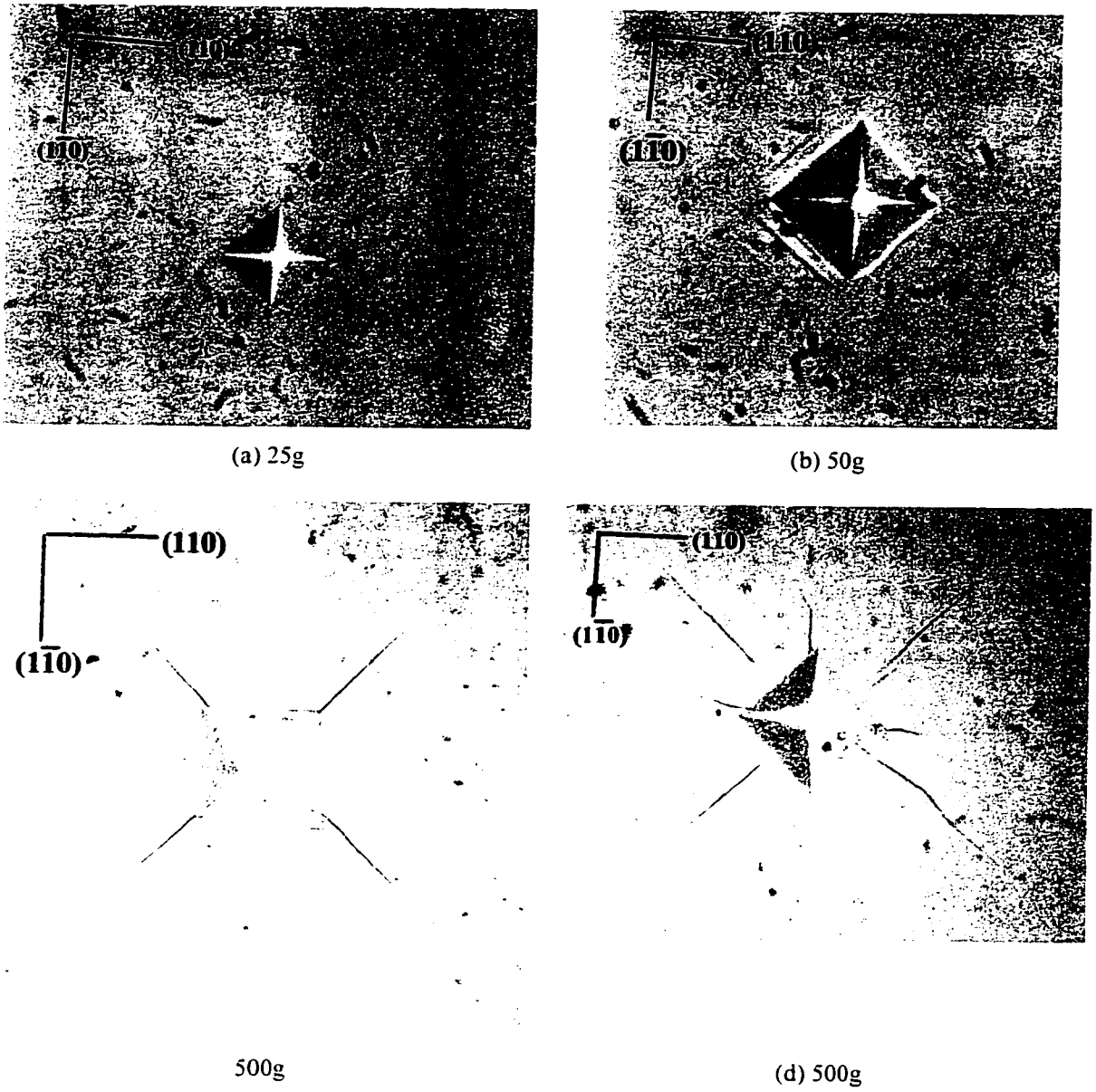

(a) 25g

(b) 50g

500g

(d) 500g

Figure 4.57: Indentations on a (001) face of the intermetallic for various loads and indenter orientations. The indexed lines indicate the orientation of the corresponding planes.

5. DISCUSSION

5.1 Introduction

In this chapter a detailed discussion of the results in Chapter Four is presented. Two types of experiments/observations have been performed. First, global information is available from the macroscopic stress-strain curves, which represent the average behaviour of the entire polycrystal, and from the in-situ ND experiments, which provide lattice strains averaged over the gauge volume for various components of the texture. In addition, optical and transmission electron microscopy reveal what deformation systems occur in each grain as well as the details of intergranular and particle-matrix interactions.

A basis for the discussion is first laid down by rationalising the general appearance of the stress-strain curves for each strain path studied through a consideration of the texture and its influence on the selection of deformation modes. The criteria for slip and twinning available in the literature are then summarised and their relevance to the present situation discussed. An analysis of how the various deformation modes identified by transmission electron microscopy can contribute to the strain tensor of each component of the texture studied by neutron diffraction is then presented.

The stress tensors for each grain orientation at each load for which measurements were made by ND are calculated and are used, in conjunction with peak intensity variations (and based on the above considerations), to derive a criterion for the activation of twinning. This is followed by a general semi-quantitative analysis of yielding in pure magnesium.

The influence of the second-phase particles on the mechanical behaviour of the alloy is then analysed. Various strengthening mechanisms are considered and their predictions compared with the alloy stress-strain curves and in-situ neutron diffraction results.

The deformation mechanisms revealed by optical and transmission electron microscopy are then discussed. Local gradients at particles and grain boundaries are discussed, as well as twin-particle interactions. The problem is extremely complex, and only general notions are presented to suggest directions for further work.

In the final section, Ashby's property correlation tables are used to rationalise the mechanical properties and behaviour of the intermetallic single crystal and to derive other properties not measured experimentally.

Throughout the chapter, lattice strains parallel and normal to the stress axis are denoted by the superscripts A and R, respectively. Thus the lattice strain normal to the $\{10\bar{1}0\}$ planes and parallel to the

stress axis is denoted $\varepsilon^{A}_{\{10\bar{1}0\}}$ while the strain normal to the $\{10\bar{1}0\}$ planes and normal to the stress axis is denoted $\varepsilon^{R}_{\{10\bar{1}0\}}$.

5.2 Macroscopic Results

5.2.1 Macroscopic stress-strain behaviour

As discussed in the literature review, the stress-strain curves obtained for materials which deform plastically by twinning can vary considerably with sense of deformation, depending on the texture. In the present case, the texture of both materials is such that $\{10\bar{1}2\}$ twinning, by far the most common mode observed in magnesium and its alloys, is favoured in compression for a majority of the grains. This is easy to understand, as most grains have the c-axis at a large angle from the stress axis. During compression, expansion is required normal to the stress axis, and therefore parallel to the c-axis for most grains, which can be obtained only by $\{10\bar{1}2\}$ twinning. In tension, however, relatively few grains are favourably oriented for $\{10\bar{1}2\}$ twinning.

Basal slip in the most important component of the texture is not particularly favoured in either tension or compression. In both cases, the resolved stress in the basal plane is very small. However, as shown in section 5.2.2, basal slip is still expected to occur easily.

Based on the above two considerations, it is possible to provide an overall interpretation of the stress-strain behaviour obtained for the two materials. In tension, most of the deformation is expected to be produced by basal slip, with perhaps some twinning and non-basal slip at regions of stress concentration and in grains oriented with the c-axis parallel to the stress axis. Since basal slip is very easy to activate, it is not surprising that the stress-strain curves show essentially no linear elastic regime in either material. In the Mg, basal slip occurs first in those grains most favourably oriented with respect to the stress axis. As the applied stress is increased, the number of grains for which the critical resolved shear stress for basal slip is achieved also increases. The number of grains for which this happens at a given applied stress level depends on the texture of the material. Eventually, all of the grains undergo basal slip, at which point the rate of strain hardening is very low. The same sequence of events probably happens in the alloy. There is no clear-cut linear elastic regime, indicating that basal slip occurs at very low applied stresses despite the presence of the reinforcing second phase. However, the presence in the stress-strain curve of a region of very high hardening rate prior to general yielding indicates that the particles must be at the origin of continuum effects which prevent extensive basal slip from spreading freely to all the grains. These effects produce a much higher general yield stress in the alloy than in the Mg, but the work hardening rate in the fully plastic regime is essentially the same as that observed in the Mg. It is also worth pointing out that the elastic-plastic transition is much more gradual in the Mg than in the alloy. The unloading behaviour is non-

linear in both materials, indicating that some deformation mechanisms are reversed under the action of internal stresses.

The situation is very different in compression. General yielding occurs at a much lower stress than in tension for both materials. In the Mg, the rate of work-hardening is essentially zero once yielding has occurred in compression. The very low yield point is due, as in tension, to the ease with which basal slip is activated, while the very low rate of work hardening can be attributed to the onset of generalised $\{10\bar{1}2\}$ twinning which spreads through the gauge section of the specimen by a Lüders process (see section 2.4). The general yield stress is much higher in the alloy than in the Mg. However, the same sequence of events must occur in the alloy, with the difference that, once begun, the propagation of twinning does not occur at a constant applied stress as it does in the Mg, due to the second phase particles which inhibit the Lüders band propagation. The elastic-plastic transition is much more gradual in the alloy than in the Mg. The unloading behaviour is very non-linear in both materials, and it may be that some untwinning takes place. This is all the more likely as a very pronounced inflection point develops as the materials are loaded in tension after a compressive prestrain, which is unlikely to be due to the reversal of basal slip.

These simple qualitative descriptions of the stress-strain behaviour of the two materials are easily arrived at by considering what is known of the predominant deformation modes in magnesium. However, in order to analyse the problem more quantitatively, and to justify these interpretations, it is necessary to consider the activation criteria that are available to predict the onset of the various deformation modes and to verify that the ND results can be interpreted based on these criteria.

5.2.2 Activation of slip in magnesium

It is generally accepted that slip is activated when a critical resolved shear stress (CRSS) is attained in the slip plane in the slip direction, and that the CRSS is essentially independent of the other stress components and also of the hydrostatic pressure. In magnesium, it is useful to distinguish between basal and non-basal slip. Values of CRSS for the observed slip systems obtained from the literature are shown in Table 5.1. Note that no value for the CRSS is available for pyramidal slip, which has only been observed at grain boundaries in polycrystalline magnesium. However, since prism slip is generally observed under the same conditions, and since the plane spacings are similar (about 12% difference) and the Burgers vector the same, it is probably reasonable to suppose that the CRSS for the two systems is quite close, and they shall be considered equal.

Clearly, basal slip is much easier to activate than non-basal slip and, in an absolute sense, very low levels of applied stress are required to activate it, even when the grain orientation is extremely unfavourable. In order to quantify this, consider the graph in Figure 5.1, which shows how the level of uniaxial applied stress required to activate basal and non-basal slip depends on the Schmid factor (S). The

stress required to activate basal slip falls below 50 MPa for an S value of only 0.05, and is less than 10 MPa for S greater than about 0.1. In comparison, for S less than about 0.1, non-basal slip can only be activated at applied stresses approximately equal to twice the tensile fracture stress of the Mg used in this study, and the minimum uniaxial applied stress necessary is 80 MPa for the most favourable condition (S=0.5).

Table 5.1: Critical resolved shear stresses for slip in pure magnesium (Partridge, 1967).

SYSTEM	Critical resolved shear stress (MPa)
Basal: (0001)<$\bar{1}2\bar{1}0$>	0.51
Prism (P_1): {$10\bar{1}0$}<$\bar{1}2\bar{1}0$>	40
Pyramidal (π_1): {$10\bar{1}1$}<$\bar{1}2\bar{1}0$>	40 (see text)

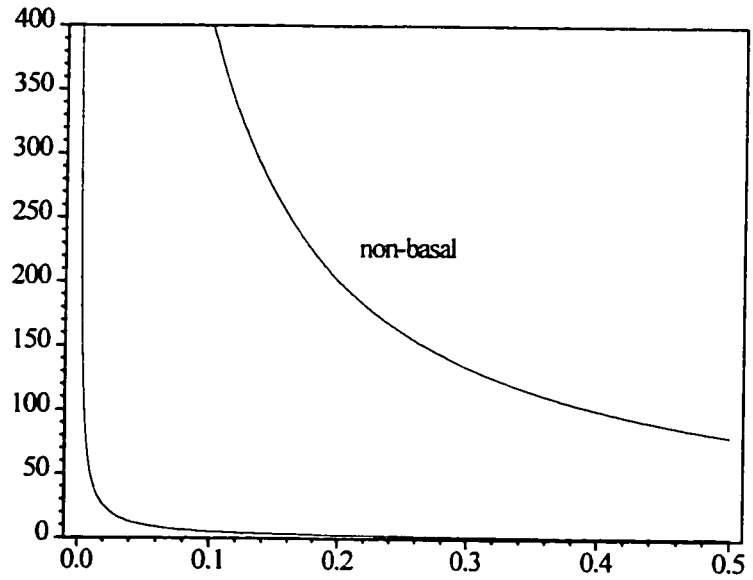

Figure 5.1: Dependence of the applied uniaxial stress to activate basal and non-basal slip on Schmid factor in pure magnesium.

The slip systems in Table 5.1 only provide four independent deformation modes, none of which can produce strain parallel to the c-axis of the hexagonal prism. Since glissile c-type dislocations have never been observed at room temperature in pure magnesium, this must be achieved by twinning.

5.2.3 Activation criteria for twinning

Although the resolved shear stress (RSS) in the twinning plane in the shear direction appears to be an important factor in the activation of twinning, experimental evidence seems to indicate that the other stress components can also play an important role. Thus Cahn, 1954 concludes from compression experiments on rutile, dypside, and baride, that twinning is favoured by the superposition of hydrostatic stress. Based on experiments on rolled, coarse-grained, silicon steel samples, Priestner & Louat, 1963 conclude that the resolved shear stress required for twinning is dependent on crystal orientation with respect to the stress axis. MacEwen et al., 1988 evaluate the internal stresses during mechanical loading of Zircaloy bar. They observe a marked relaxation of the stress normal to the basal planes at a stage of deformation which corresponds to mechanical twinning, from which they deduce that twinning may be enhanced or inhibited by superposing a normal stress to the shear component.

Lebensohn & Tome, 1993 model the twin lamella as a flat inclusion of elliptic section embedded in an elastically anisotropic medium acted on by an externally applied stress in order to derive the stress state associated with the activation of twinning. They find that a CRSS criterion can be used for twinning, provided that the normal stress components are not much larger than the CRSS. The influence of normal stresses is non-existent in an elastically isotropic medium, and becomes more important as the anisotropy increases. However, the authors indicate that their model can only take elastic effects into account. Twin growth requires the motion of twin dislocations, which shift atoms within the twinned region to the appropriate lattice positions in the twinned crystal. As discussed in the literature review, this requires that some atoms be shuffled in order to recompose the perfect lattice within the twin. The facility with which this shuffling occurs may be affected by the stress normal to the twinning plane.

In order to predict the importance of normal stresses on twin nucleation in magnesium, it is useful to consider in particular the experimental observations of Priestner & Louat, 1963. They performed their experiments at 78 K (approximately $T_m/20$) on a material having a relatively high Peierls stress. Thus dislocation motion as well as any atomic shuffling required for twin growth is not easily produced. In addition to this, the possibility of heterogeneous nucleation is also diminished as there is very little dislocation activity (no plastic deformation prior to fracture is noted by the authors).

In comparison, testing in the current study has been carried out at a high temperature ($T_m/3$), and basal slip is very easily activated, so that dislocation multiplication prior to twinning is guaranteed (even in very unfavourably oriented grains). The possibility of heterogeneous twin nucleation is thus very high. In addition, the near elastic isotropy of magnesium suggests that the influence of normal stresses described by Lebensohn & Tome, 1993 is very small. It is thus quite likely that a CRSS criterion is appropriate in the present case. In order to verify this, it is necessary to consider how twinning manifests itself in the ND

results, and to evaluate the internal stresses for each component of the microstructure considered, based on the measured lattice strains.

5.2.4 Potential contribution of deformation modes to overall strain

In the present study, three sets of grains in the magnesium matrix, defined by which plane normal is parallel to the stress axis, have been investigated by neutron diffraction. They will be referred to henceforth as A, B, and C grains, as shown in Table 5.2. The c-axis of the hexagonal prism is parallel to the stress axis in the A grains and normal to it in the B grains. The C grains represent an intermediate orientation with the c-axis approximately 62° from the stress axis.

Table 5.2: Definition of grain orientations studied by neutron diffraction.

GRAIN	ORIENTATION
A	[0002] parallel to stress axis
B	<10$\bar{1}$0> parallel to stress axis
C	normal to <10$\bar{1}$1> parallel to stress axis

The potential contribution of each slip and twinning system to the strain tensor in each family of grains can be calculated using Equation 5.1, where **n** (n_1,n_2,n_3) is the unit vector normal to the slip or shear plane, **b** (b_1,b_2,b_3) is the unit vector parallel to the shear direction, and γ is the magnitude of the shear.

$$\varepsilon_{ij} = \frac{\gamma}{2}(n_i b_j + n_j b_i) \qquad (5.1)$$

n and **b** must be expressed in a Cartesian co-ordinate system related to the specimen axes. Figure 5.2 shows how the hexagonal prism is oriented with respect to the stress axis for each set of grains. In each case, the crystallographic direction parallel to the stress axis (the x_3 axis) and two orthogonal directions normal to the stress axis (the x_1 and x_2 axes) are shown. Table 5.3 shows the calculated values of the strain parallel to the stress axis for each deformation system for each type of grain. For twinning, the value of γ is fixed: it is uniquely defined for a given twinning mode and the strains indicated correspond to a grain which is completely transformed into the twin. For slip, γ is set equal to unity so as to provide a basis on which to compare the contributions of each slip mode. The strains are all given as positive for the slip systems, but they can also be negative since slip takes place regardless of the sense of the resolved shear stress. However, the sign of the strain is meaningful for twinning due to its polar nature.

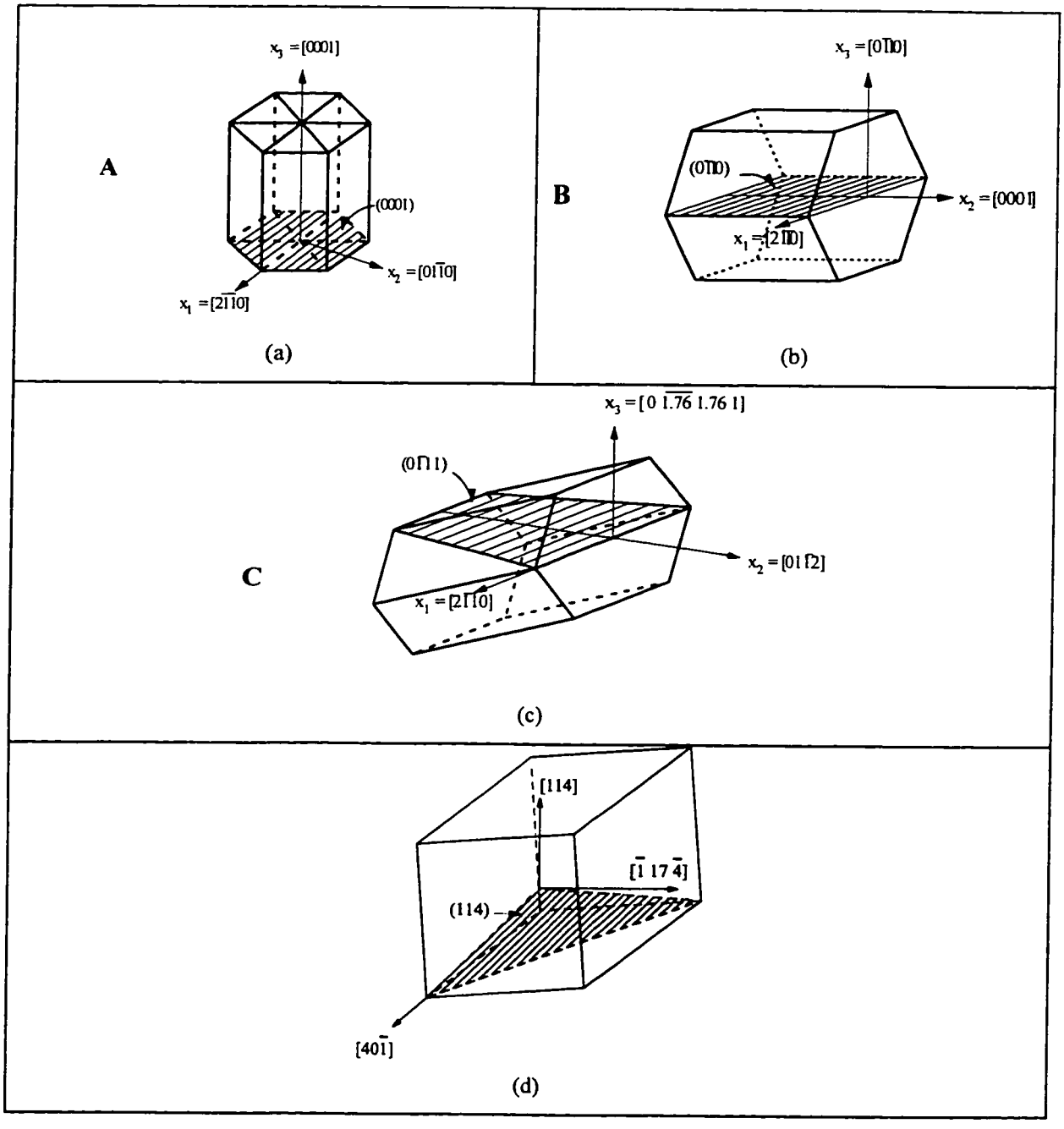

Figure 5.2: Orientation of the hexagonal prism in grains A, B, and C, and of the precipitate unit cell with respect to the stress axis.

Table 5.3: Strains along the global Cartesian axes (see Figure 5.2) for each of the possible slip and twinning systems in each family of grains (see text).

	A GRAINS			B GRAINS			C GRAINS		
	ε_{11}	ε_{22}	ε_{33}	ε_{11}	ε_{22}	ε_{33}	ε_{11}	ε_{22}	ε_{33}
			SLIP SYSTEMS						
Basal 1	0	0	0	0	0	0	0	0	0
Basal 2	0	0	0	0	0	0	0	0.3594	-0.3594
Basal 3	0	0	0	0	0	0	0	-0.3594	0.3594
Prism 1	-0.4330	0.4330	0	-0.4330	0	0.4330	-0.4330	0.0958	0.3373
Prism 2	0	0	0	0	0	0	0	0	0
Prism 3	-0.4330	0.4330	0	-0.4330	0	0.4330	-0.4330	0.0958	0.3373
Pyramidal 1	-0.3821	0.3821	0	-0.38210	0	0.3821	-0.3821	0.2535	0.1286
Pyramidal 2	0.3821	-0.3821	0	0.3821	0	-0.3821	0.3821	0.0845	-0.4667
Pyramidal 3	0	0	0	0	0	0	0	0	0
Pyramidal 4	0	0	0	0	0	0	0	0	0
Pyramidal 5	-0.3821	0.3821	0	-0.3821	0	0.3821	-0.3821	-0.0845	0.4667
Pyramidal 6	0.3821	-0.3821	0	0.3821	0	-0.3821	0.3821	-0.2535	-0.1286
			TWINNING SYSTEMS						
{10$\bar{1}$2} 1	-0.0487	-0.0162	0.0649	-0.0487	0.0649	-0.0162	-0.0487	0.0452	0.0034
{10$\bar{1}$2} 2	0	-0.0649	0.0649	0	0.0649	-0.0649	0	0.0328	-0.0328
{10$\bar{1}$2} 3	-0.0487	-0.0162	0.0649	-0.0487	0.0649	-0.0162	-0.0487	0.0452	0.0034
{10$\bar{1}$2} 4	-0.0487	-0.0162	0.0649	-0.0487	0.0649	-0.0162	-0.0487	0.0487	0
{10$\bar{1}$2} 5	0	-0.0649	0.0649	0	0.0649	-0.0649	0	0.0396	-0.0396
{10$\bar{1}$2} 6	-0.0487	-0.0162	0.0649	-0.0487	0.0649	-0.0162	-0.0487	0.0487	0
{10$\bar{1}$1} 1	0.0436	0.0145	-0.0581	0.0436	-0.0581	0.0145	0.0436	-0.0582	0.0147
{10$\bar{1}$1} 2	0.0436	0.0145	-0.0581	0.0436	-0.0581	0.0145	0.0436	-0.0258	-0.0177
{10$\bar{1}$1} 3	0	0.0581	-0.0581	0	-0.0581	0.0581	0	-0.0648	0.0648
{10$\bar{1}$1} 4	0	0.0581	-0.0581	0	-0.0581	0.0581	0	0	0
{10$\bar{1}$1} 5	0.0436	0.0145	-0.0581	0.0436	-0.0581	0.0145	0.0436	-0.0258	-0.0177
{10$\bar{1}$1} 6	0.0436	0.0145	-0.0581	0.0436	-0.0581	0.0145	0.0436	-0.0582	0.0147

It is clear that none of the slip systems can produce strain parallel to the stress axis in A grains. Since $\{10\bar{1}2\}$ twinning is not expected in A grains because of their orientation with respect to the stress axis, they probably act as hard inclusions in compression, but not in tension, in which case the $\{10\bar{1}2\}$ can contribute. It is interesting to note that the strain at fracture of both the alloy and the Mg in tension is considerably less than the maximum tensile strain obtainable in the A grains by $\{10\bar{1}2\}$ twinning.

In the B grains, prism and pyramidal slip can provide deformation parallel to the stress axis. However, these deformation modes are difficult to activate and thus likely contribute little to the overall deformation. The stress axis is within the basal plane, which means that the resolved shear stress for basal slip is very small. For orientations close to B, basal slip can provide extension and compression parallel to the stress axis, though the ratio of strain produced to basal shear would be very low. Compression parallel to the stress axis can be produced by all the $\{10\bar{1}2\}$ twin systems, two of which can contribute as much as 6.5% strain. The difference in stress-strain behaviour of magnesium in tension and compression is thus related to the polar nature of $\{10\bar{1}2\}$ twinning.

In the C grains, all three slip modes can produce appreciable strain parallel to the stress axis for a given shear. Two of the $\{10\bar{1}2\}$ twinning systems can produce compressive strain (3-4%), the others contributing at most only 0.34% tensile strain. Thus twinning is not required in the C grains, but may occur if it can be transmitted from a favourably oriented grain to ensure compatibility between grains.

Having considered how each system can contribute to the strain in each grain orientation studied, it is now possible to interpret the internal stresses obtained by in-situ neutron diffraction.

5.2.5 Internal stress calculations

5.2.5.1 Method of stress calculation

Elastic lattice strains measured by ND can be used to determine internal stresses provided the single crystal elastic constants are known. As discussed in the literature review (section 2.6.2.1), it is possible to solve for the six tensor strains in a *single crystal* if the lattice strain is measured in at least six non-coplanar directions. In polycrystals, however, each measured lattice strain represents an average over several orientations. Thus it is not possible to unambiguously determine the strain tensor for a given grain orientation in a polycrystal.

In order to determine the lattice stress tensor, it is necessary to evaluate the following equation:

$$[\sigma] = [C][\varepsilon] \qquad (5.2)$$

where matrix notation has been used and [C] is the elastic stiffness matrix, transformed appropriately according to the grain orientation. To obtain the transformed C_{ij}, it is necessary to transform the fourth order *tensor* components C_{ijkl} as follows:

$$C'_{ijkl} = a_{im}a_{jn}a_{ko}a_{lp}C_{mnop} \quad (5.3)$$

where the a_{ij} are the cosines of the angles between the new (primed) co-ordinate axes and the old (unprimed) co-ordinate axes. The matrix notation is then derived by noting that the order of the first two suffixes as well as the last two suffixes in the tensor notation is immaterial (i.e. $C_{ijkl} = C_{jikl} = C_{ijlk} = C_{klij}$). The transformed components of the stiffness *matrix* C_{ij} can then be determined by replacing each pair of suffixes of the tensor components by a single suffix according to Table 5.4.

Table 5.4: Conversion between tensor and matrix notation.

Tensor notation	11	22	33	23 or 32	13 or 31	12 or 21
Matrix notation	1	2	3	4	5	6

In this study, six measurements of lattice strain have not been made for each set of grains in Figure 5.2 from which to rigorously calculate [σ]. However, as shown in Table 5.5, ε_1, ε_2, and ε_3 have been determined or can be estimated for the three grain orientations. Note that we require $\varepsilon^R_{\{2\bar{1}\bar{1}0\}}$ and $\varepsilon^R_{\{0\bar{1}1\ 1.14\}}$ which have not been measured. The only radial strains measured in a direction within the basal plane is $\varepsilon^R_{\{10\bar{1}0\}}$. The grains giving rise to this signal include A grains, grains rotated 30° about [0001] in Figure 5.2(b), grains rotated about 30° about [01$\bar{1}$2] in Figure 5.2(c), as well as a multitude of other grain orientations so it is clear that an error will be introduced in the calculation. However, the elastic properties of materials with the hexagonal structure are isotropic in the basal plane, as can be shown by applying an arbitrary rotation about the c-axis to the tensor of elastic constants (Equation 5.3). In addition to this, the radial strains measured are very small. It is thus assumed that the measured value of $\varepsilon^R_{\{10\bar{1}0\}}$ is a reasonable approximation to the radial strains required for the stress calculations, as shown in Table 5.5.

Table 5.5: Lattice strains corresponding to the x_1, x_2, x_3 axes in Figure 5.2.

	ε_1	ε_2	ε_3
A grains	$\varepsilon^R_{\{2\bar{1}\bar{1}0\}} (\approx \varepsilon^R_{\{10\bar{1}0\}})$	$\varepsilon^R_{\{10\bar{1}0\}}$	$\varepsilon^A_{(0002)}$
B grains	$\varepsilon^R_{(0002)}$	$\varepsilon^R_{\{2\bar{1}\bar{1}0\}} (\approx \varepsilon^R_{\{10\bar{1}0\}})$	$\varepsilon^A_{\{10\bar{1}0\}}$
C grains	$\varepsilon^R_{\{2\bar{1}\bar{1}0\}} (\approx \varepsilon^R_{\{10\bar{1}0\}})$	$\varepsilon^R_{\{0\bar{1}1\ 1.14\}} (\approx \varepsilon^R_{\{0\bar{1}12\}})$	$\varepsilon^A_{\{01\bar{1}1\}}$

Finally, since the {0$\bar{1}$1 1.14} and {0$\bar{1}$12} planes are only about 15° apart, the strains normal to the two sets of planes (and therefore in the corresponding two sets of grains) are likely to be quite close in magnitude and thus it is reasonable to substitute the radial strains normal to the {0$\bar{1}$12} planes for the radial strains normal to the {0$\bar{1}$1 1.14} planes in Equation 5.3.

The matrix equations for the stress tensors for the three sets of grains are shown in Equation 5.4. It can be seen from the stiffness matrices that σ_1, σ_2, and σ_3 do not depend at all on ε_4, ε_5, and ε_6 in the A and

B grains, and are only very weakly dependent on them for the C grains so that it should be possible to determine these stresses quite accurately from the measured values of ε_1, ε_2, and ε_3.

Similarly, σ_4, σ_5, and σ_6 do not depend at all on ε_1, ε_2, and ε_3 for the A and B grains, and are only very weakly dependent on them for the C grains. Moreover, since the applied stress is uniaxial it is probably reasonable to expect that ε_4, ε_5, and ε_6 will be small in magnitude. These two observations suggest that σ_4, σ_5, and σ_6 are small compared with σ_1, σ_2, and σ_3 and they shall be considered to be zero.

$$\mathbf{A}\quad \begin{bmatrix}\sigma_1\\ \sigma_2\\ \sigma_3\\ \sigma_4\\ \sigma_5\\ \sigma_6\end{bmatrix} = \begin{bmatrix} 59.74 & 23.24 & 21.7 & 0 & 0 & 0\\ 23.24 & 59.74 & 21.7 & 0 & 0 & 0\\ 21.7 & 21.7 & 61.7 & 0 & 0 & 0\\ 0 & 0 & 0 & 16.39 & 0 & 0\\ 0 & 0 & 0 & 0 & 16.39 & 0\\ 0 & 0 & 0 & 0 & 0 & 18.25 \end{bmatrix} \begin{bmatrix} \varepsilon_1 = \varepsilon^{R}_{(10\bar{1}0)}\\ \varepsilon_2 = \varepsilon^{R}_{(10\bar{1}0)}\\ \varepsilon_3 = \varepsilon^{A}_{(0002)}\\ \varepsilon_4 = 0\\ \varepsilon_5 = 0\\ \varepsilon_6 = 0 \end{bmatrix}$$

$$\mathbf{B}\quad \begin{bmatrix}\sigma_1\\ \sigma_2\\ \sigma_3\\ \sigma_4\\ \sigma_5\\ \sigma_6\end{bmatrix} = \begin{bmatrix} 61.7 & 21.7 & 21.7 & 0 & 0 & 0\\ 23.24 & 59.74 & 23.24 & 0 & 0 & 0\\ 23.24 & 23.24 & 59.74 & 0 & 0 & 0\\ 0 & 0 & 0 & 19.02 & 0 & 0\\ 0 & 0 & 0 & 0 & 16.39 & 0\\ 0 & 0 & 0 & 0 & 0 & 16.39 \end{bmatrix} \begin{bmatrix} \varepsilon_1 = \varepsilon^{R}_{(0002)}\\ \varepsilon_2 = \varepsilon^{R}_{(10\bar{1}0)}\\ \varepsilon_3 = \varepsilon^{A}_{(10\bar{1}0)}\\ \varepsilon_4 = 0\\ \varepsilon_5 = 0\\ \varepsilon_6 = 0 \end{bmatrix} \qquad (5.4)$$

$$\mathbf{C}\quad \begin{bmatrix}\sigma_1\\ \sigma_2\\ \sigma_3\\ \sigma_4\\ \sigma_5\\ \sigma_6\end{bmatrix} = \begin{bmatrix} 59.12 & 22.7 & 23.86 & 0 & 1.94 & 0\\ 22.70 & 59.74 & 25.23 & 0 & -1.85 & 0\\ 23.86 & 25.23 & 58.02 & 0 & -0.94 & 0\\ 0 & 0 & 0 & 16.67 & 0 & -0.1235\\ 1.94 & -1.85 & -0.94 & 0 & 18.54 & 0\\ 0 & 0 & 0 & -0.1235 & 0 & 16.47 \end{bmatrix} \begin{bmatrix} \varepsilon_1 = \varepsilon^{R}_{(01\bar{1}2)}\\ \varepsilon_2 = \varepsilon^{R}_{(10\bar{1}0)}\\ \varepsilon_3 = \varepsilon^{R}_{(01\bar{1}1)}\\ \varepsilon_4 = 0\\ \varepsilon_5 = 0\\ \varepsilon_6 = 0 \end{bmatrix}$$

The precipitate stress tensor is somewhat more difficult to determine as only one crystallographic direction was measured parallel and normal to the stress axis. However, a set of axes can be set up as shown in Figure 5.2(d), and since the angle between $[1\bar{4}1]$ and $[1\bar{4}0]$ is only about 19°, we can reasonably assume that $\varepsilon^{R}_{(1\bar{4}0)} \approx \varepsilon^{R}_{(1\bar{4}1)}$. In order to perform the calculation, it is also necessary to assume that the strain tensor is symmetric with respect to the x_3 axis and therefore that $\varepsilon^{R}_{(41\ \bar{1}7)R} \approx \varepsilon^{R}_{(1\bar{4}1)}$. We then obtain the expression shown in Equation 5.5, where once again the stiffness constants have been transformed from the standard orientation to that shown in Figure 5.2(d).

Based on Equations 5.4 and 5.5 the stress tensors for the three types of grains and for the precipitates have been calculated for all of the in-situ tests performed. The results are presented in graphical form in Figures 5.3-5.10. For each test, σ_1, σ_2, and σ_3 are plotted vs. applied stress. Rather than superposing the loading and unloading curves, the sequence of stresses is plotted along the x-axis in the sequence in which they were applied during the tests. The applied stress is plotted as a dotted line for easy comparison with the calculated stresses.

$$\begin{bmatrix}\sigma_1\\ \sigma_2\\ \sigma_3\\ \sigma_4\\ \sigma_5\\ \sigma_6\end{bmatrix} = \begin{bmatrix} 85.21 & 32.69 & 34.20 & 0.39 & -3.09 & -0.75\\ 32.69 & 85.29 & 34.12 & -3.14 & 0.17 & 0.04\\ 34.20 & 34.12 & 83.78 & 2.75 & 2.92 & 0.71\\ 0.39 & -3.14 & 2.75 & 21.02 & 0.71 & 0.17\\ -3.09 & 0.17 & 2.92 & 0.71 & 21.10 & 0.39\\ -0.75 & 0.04 & 0.71 & 0.17 & 0.39 & 19.59\end{bmatrix}\begin{bmatrix}\varepsilon^{R}_{(411)}\\ \varepsilon^{R}_{(411)}\\ \varepsilon^{A}_{(411)}\\ 0\\ 0\\ 0\end{bmatrix} \quad \textbf{(5.5)}$$

5.2.5.2 Verification of calculated stresses

A simple way to verify that the calculated internal stresses are reasonable is to check whether the following expression is verified:

$$\sigma_{applied} = \sigma_A V_A + \sigma_B V_B + \sigma_C V_C + \sigma_{ppt} V_{ppt} \quad \textbf{(5.6)}$$

This is a simple force balance, where σ_A, σ_B, σ_C, σ_{ppt} are the stresses (parallel to the stress axis) in the three families of grains and in the precipitate, respectively, and V_A, V_B, V_C, V_{ppt} are the corresponding volume fractions. The volume fraction of the second phase is 10±2% (section 3.3.3). The volume fractions of the three families of grains can be obtained using Equation 3.1 (reprinted below) which relates the texture enhancement for a given plane to the measured intensity.

$$I_{hkil} \propto V_{mat} S_{hkil} L_{hkil} T_{hkil} \quad \textbf{(3.1)}$$

Since V_{mat}, the volume of magnesium matrix, is the same for all of the magnesium peaks, it can be removed from the equation. This yields a simple expression for T_{hkil}

$$T_{hkil} \propto I_{hkil} / P_{hkil} \quad \textbf{(5.7)}$$

where P_{hkil} is the product of S_{hkil} and L_{hkil} (section 3.3.3). The volume (*not* the volume fraction) of the hkil grains is then proportional to T_{hkil}. The volume fraction of each family of grains in the microstructure can then be determined using Equation 5.8 where V_{matrix} is the volume fraction of matrix material (taken as 90% in the present case).

$$V_{hkil} = \frac{T_{hkil}}{\sum T_{hkil}} V_{matrix} \quad \textbf{(5.8)}$$

The intensity of the A, B, and C peaks measured with the scattering vector parallel to the stress axis was measured for several undeformed samples and the value of T determined for each. Average values of the volume fractions for each component of the microstructure studied is shown in Table 5.6. The average internal stress is plotted against the applied stress for compression-first Bauschinger and cyclic tension in Figure 5.11. The dotted lines in these graphs have a slope of one and correspond to a perfect force balance. These graphs show that the agreement is generally very good and within the error of the calculations.

Table 5.6: Volume fractions of different components of the microstructure for which in-situ neutron diffraction data is available.

Component of microstructure	Volume fraction
A grains	0.22
B grains	0.62
C grains	0.062
Precipitates	0.1

For compression-first Bauschinger the average internal stress is slightly lower than the applied stress in compression. In tension the opposite is true. In compression, the volume fraction of B grains decreases due to {10$\bar{1}$2} twinning while the volume fraction of A grains increases. The effective volume fractions quoted in Table 5.6 should therefore be corrected and it is clear that the average internal stress is underestimated since in general the stress in the B grains is higher than that in the A grains. The opposite is true in tension and it is clear that the internal stress will be overestimated in this case. The agreement is excellent for cyclic tension, which reflects the fact that there is relatively little twinning in this type of test.

An extremely important comment must be made at this point. The lattice strains, and therefore the derived internal stresses, are calculated based on the assumption that there are no internal stresses present in the material prior to deformation. Measurements of the lattice parameters of pure magnesium after heat treatment show that they are identical to those of pure single crystal magnesium from which it is clear that there are no appreciable grain to grain interaction stresses. This is to be expected because magnesium is essentially isotropic with respect to thermal expansion.

The situation is more delicate in the aged alloy. It is unlikely that there will be residual internal stresses between grains. Furthermore, the thermal expansion coefficients of magnesium and of the intermetallic are very close ($\alpha_{Mg} = 27 \times 10^{-6}/°C$, $\alpha_{ppt} = 28.4 \times 10^{-6}/°C$). In the absence of plastic relaxation, the maximum stress on cooling from 330°C would not exceed about 21 MPa ($=(28.4-27) \times 10^{-6} * 300 * 50 \times 10^{-3}$) in the matrix. However, any such stress is almost certainly relaxed by the straight c-type dislocations parallel to the long direction of the precipitates observed by TEM in undeformed samples of the alloy. It is thus not unreasonable to assume that there are no residual stresses present in the aged alloy prior to deformation.

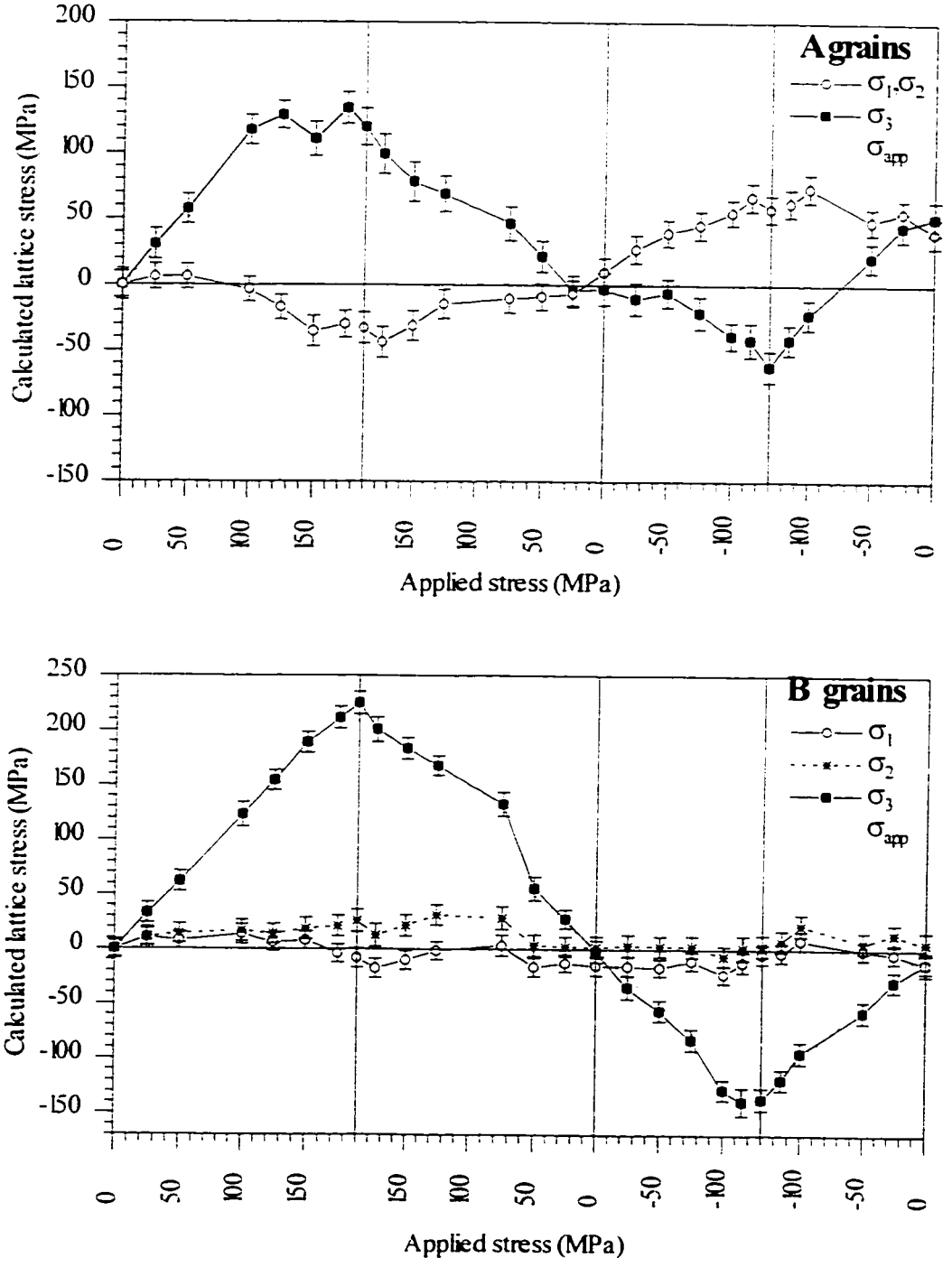

Figure 5.3: Calculated internal stress for A and B grains, tension-first Bauschinger.

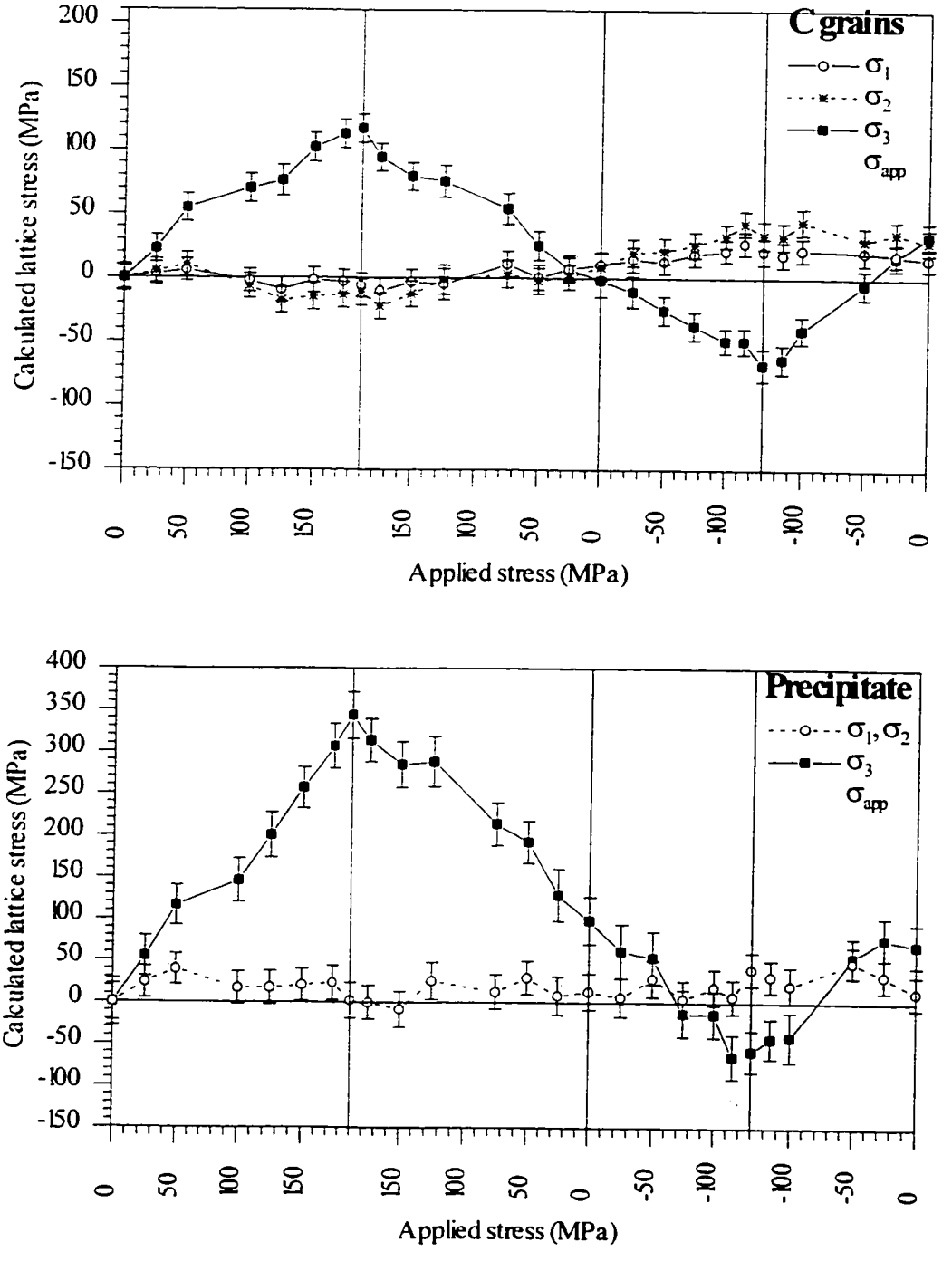

Figure 5.4: Calculated internal stresses for C grains and the precipitate, tension-first Bauschinger.

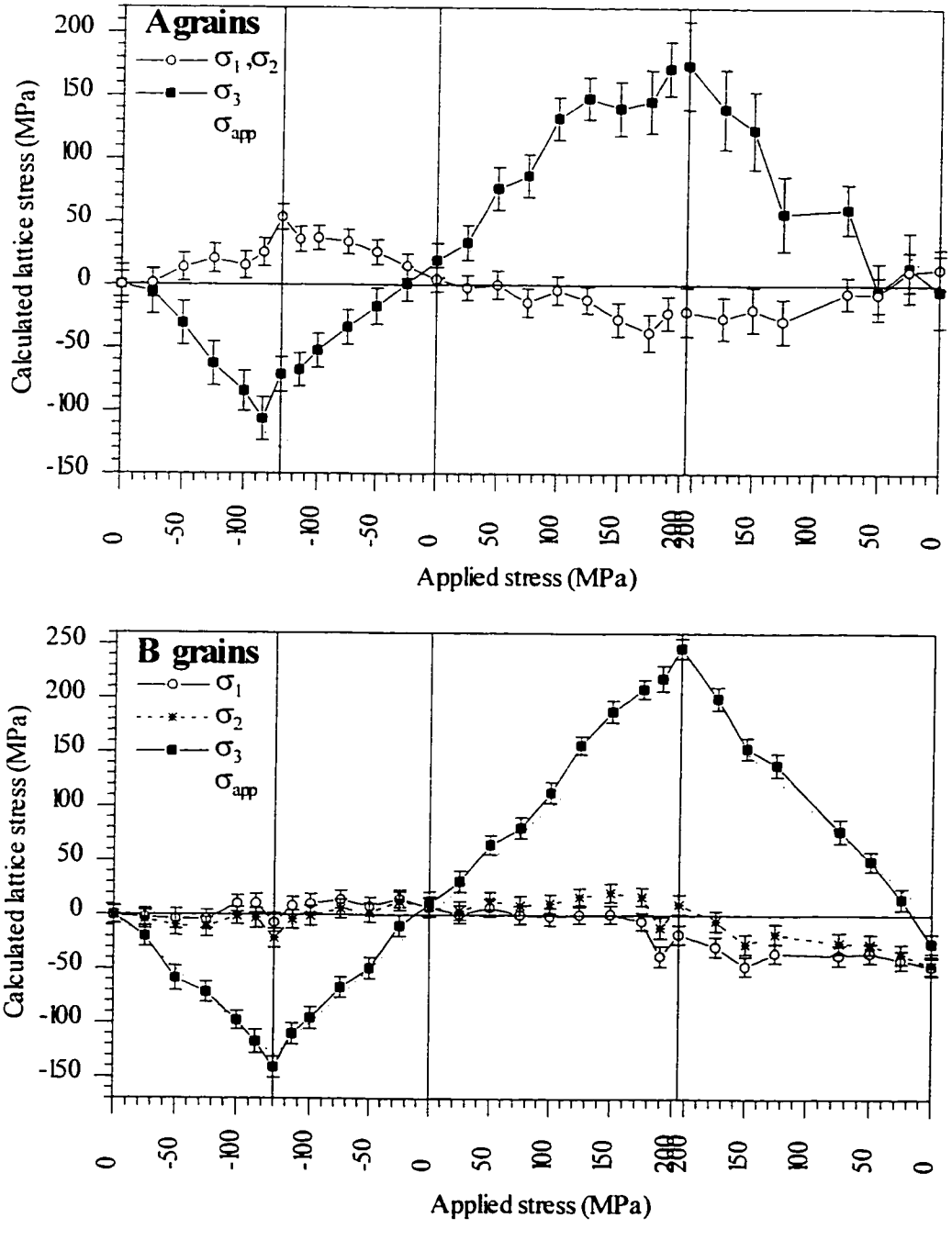

Figure 5.5: Calculated internal stresses for A and B grains , compression-first Bauschinger.

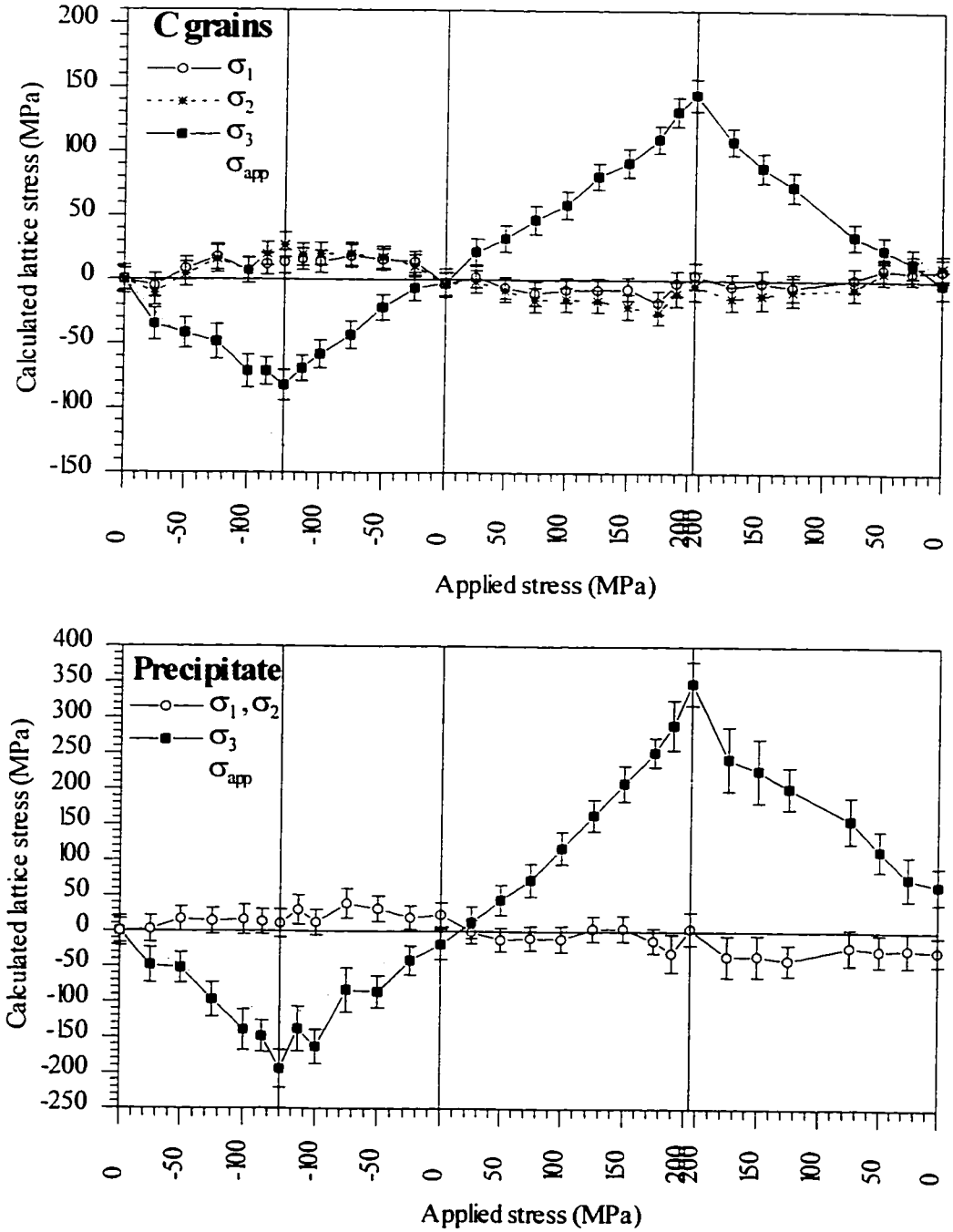

Figure 5.6: Calculated internal stresses for C grains and the precipitate, compression-first Bauschinger.

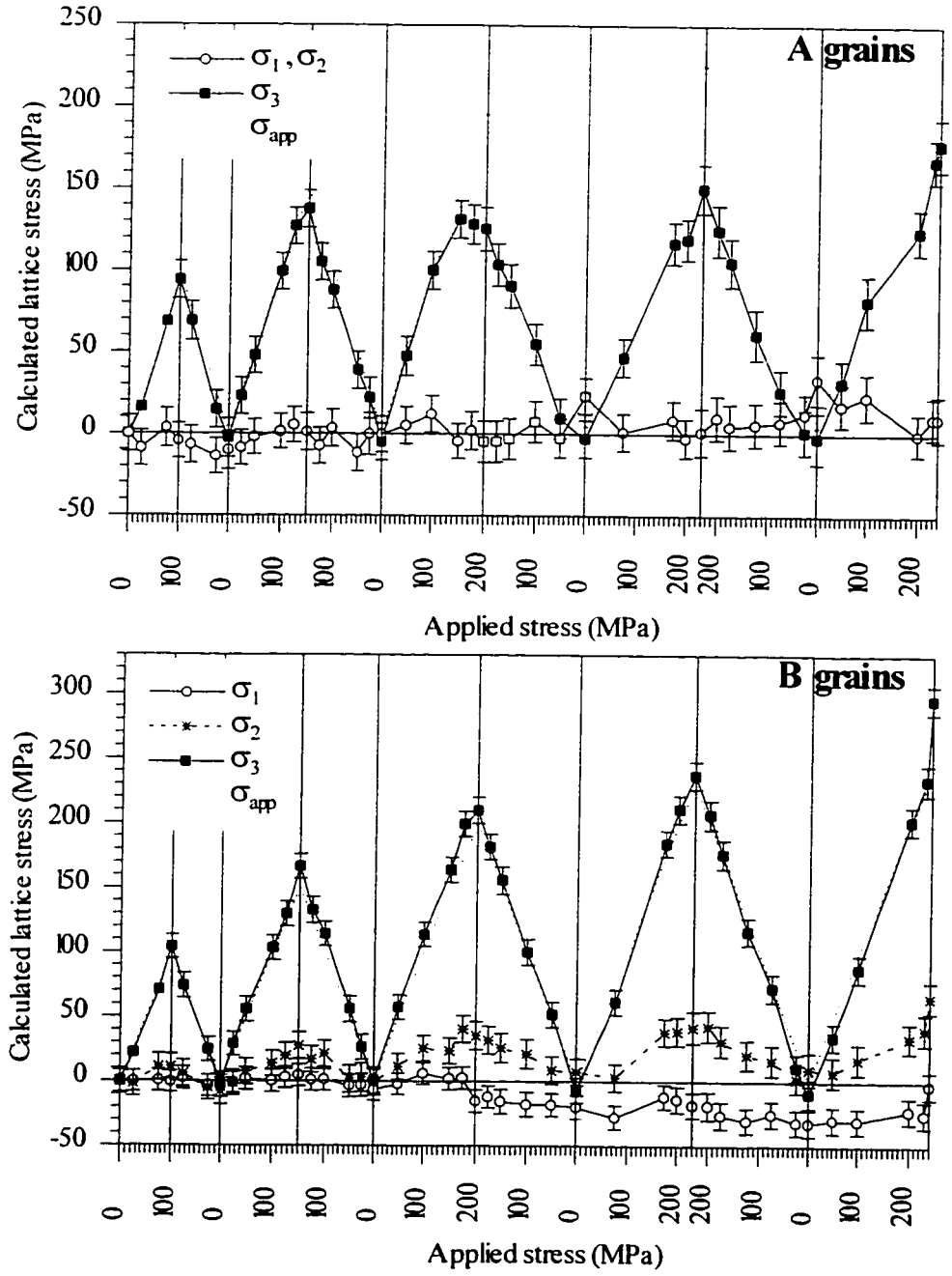

Figure 5.7: Calculated internal stresses for A and B grains, cyclic tension.

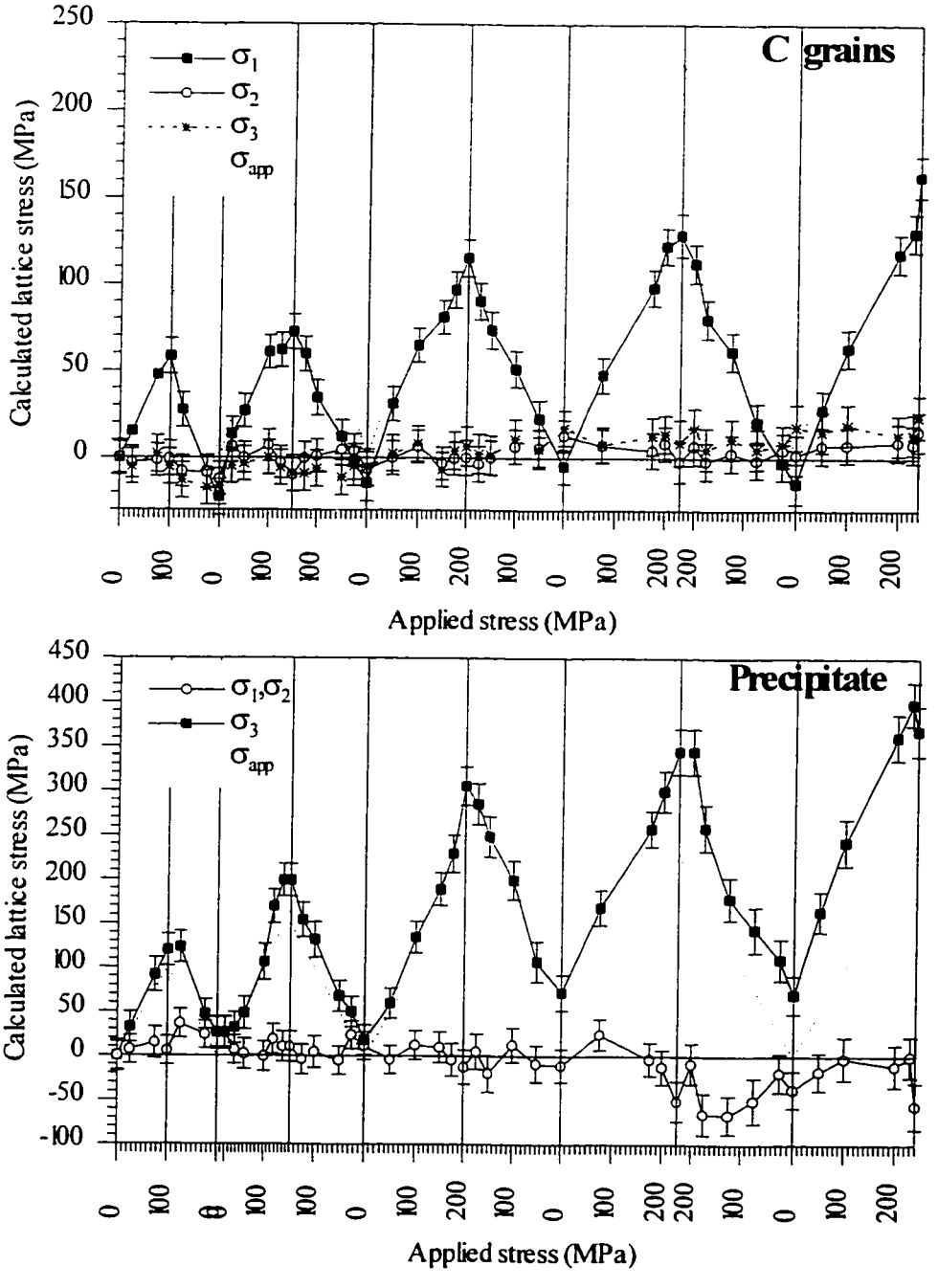

Figure 5.8: Calculated internal stresses for C grains and the precipitate, cyclic tension.

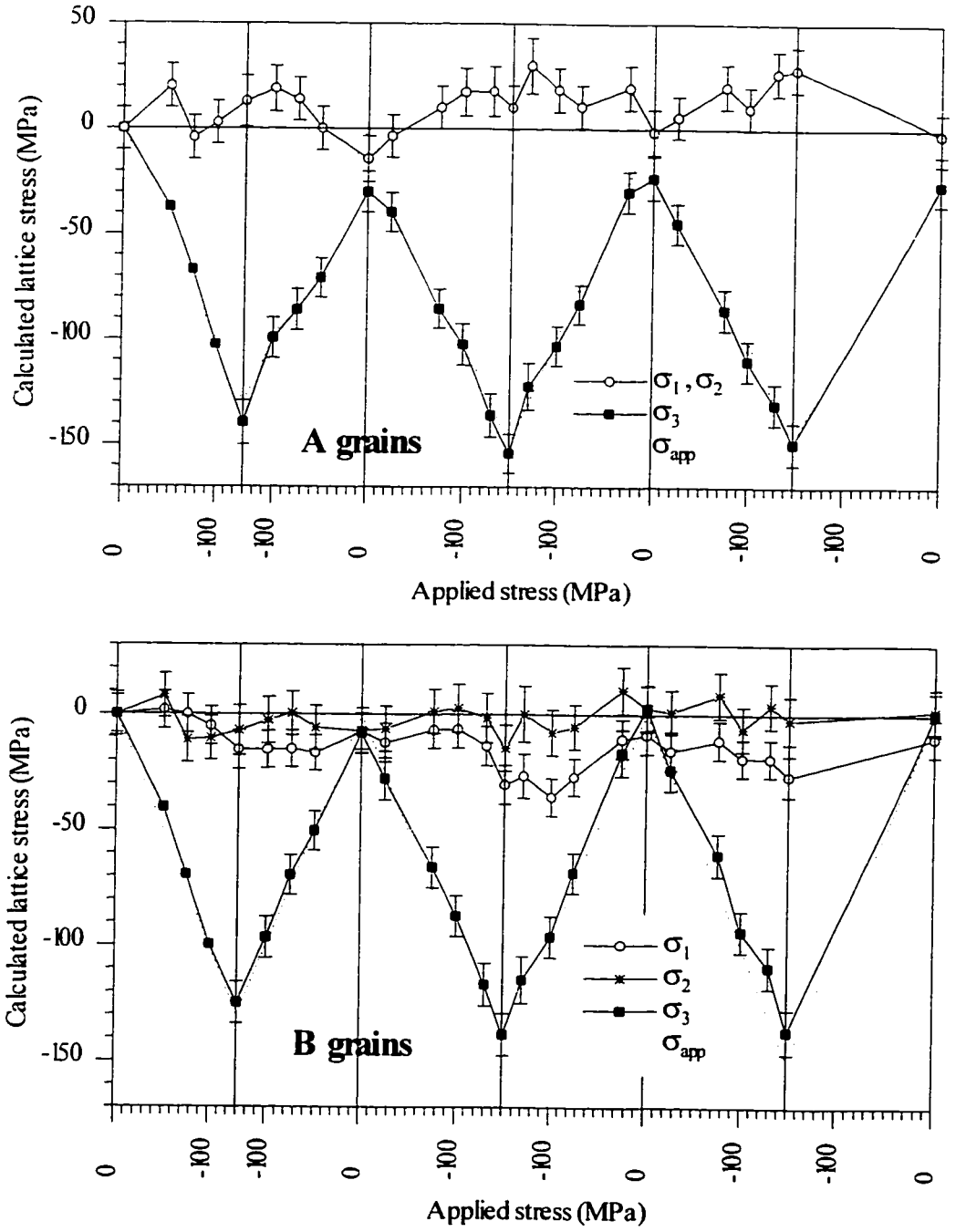

Figure 5.9: Calculated internal stresses for A and B grains, cyclic compression.

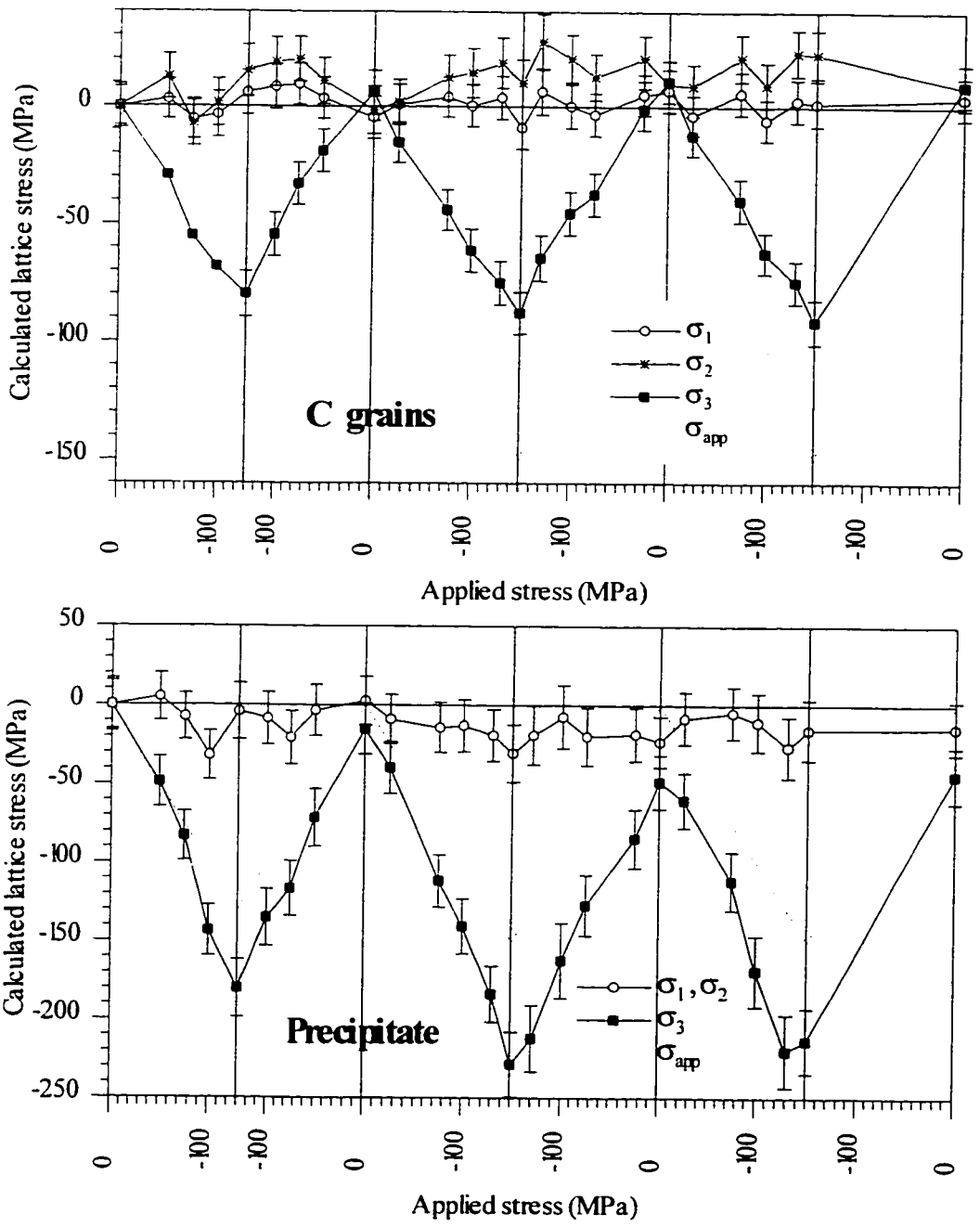

Figure 5.10: Calculated internal stresses for C grains and the precipitate, cyclic compression.

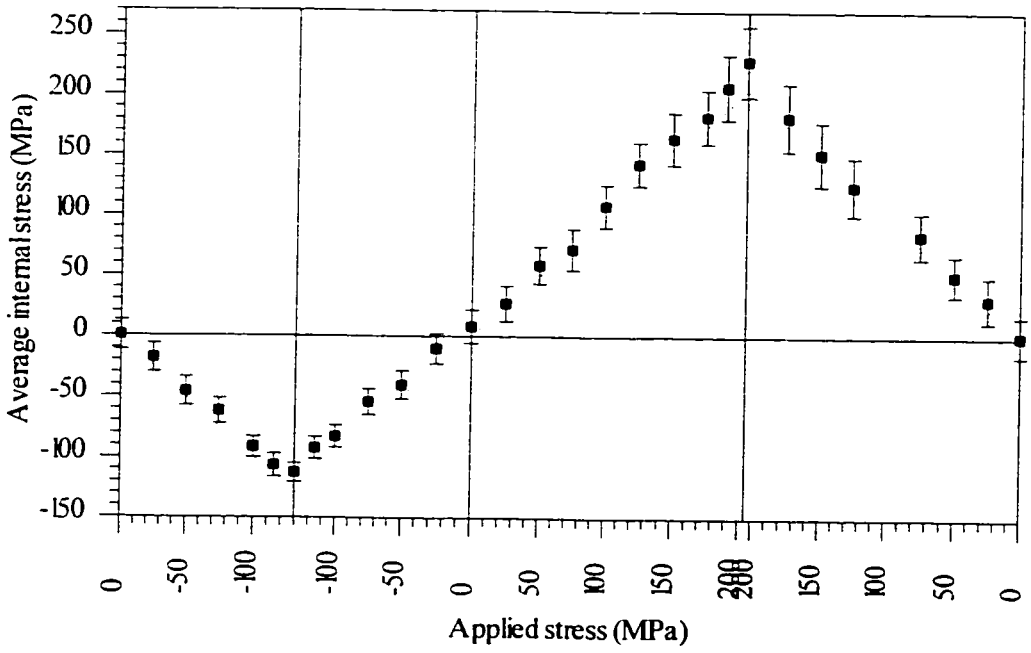

(a)

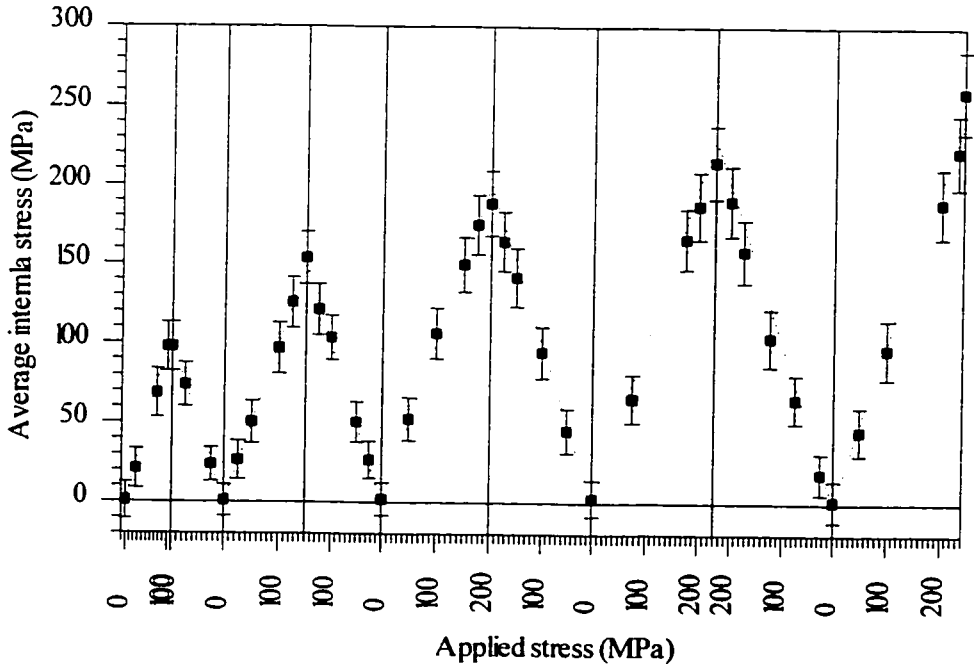

(b)

Figure 5.11: Graphs showing that the average internal stress in the matrix calculated from the neutron diffraction balances the applied stress.

a) Compression-first Bauschinger.

b) Cyclic tension.

The following preliminary remarks can be made about the calculated internal stresses:

- σ_3 is highest in the B grains (the strongest component of the texture in tension) and is either equal or slightly higher than the applied stress, except in cyclic compression.
- σ_3 in the A grains is generally smaller in magnitude than the applied stress in tension, except in the early stages (before general yielding). The situation is less clear in compression, and may depend on the extent of twinning which takes place.
- σ_3 in the C grains is always smaller in magnitude than the applied stress.
- σ_3 in the second phase particles is always much higher than in the surrounding matrix, except during the compression portion of the compression-first Bauschinger test.

It is useful at present to determine what criterion can be applied to predict the onset of twinning.

5.2.6 Critical resolved shear stress for twinning

Twinning results in an abrupt reorientation of the crystal lattice. It is thus quite easy to detect by ND since, provided it occurs in a large enough volume of the sampled material, it results in a change in peak intensity. The stress state in the grains when such an intensity change occurs can then be used to try to determine an activation criterion for twinning. When a grain twins, the intensity of the corresponding peak *decreases* since part of the grain has been rotated so that the conditions for Bragg reflection are no longer respected. When an *increase* in intensity occurs, it means that some *other* component of the texture has twinned, and in so doing has rotated the lattice so as to increase the volume of material in which the crystallographic plane giving rise to the peak is oriented appropriately for Bragg reflection. In this case, the stress tensor for the grain under study does *not* represent the state of stress at the onset of twinning.

Such intensity changes have, as seen in Chapter Four, been observed in the present study. To determine whether a CRSS criterion is suitable for twinning, it is necessary to determine the resolved shear stress at the moment of twinning (decrease in peak intensity) for at least two different loading conditions in which the internal stress tensor is appreciably different. In compression, $\{10\bar{1}2\}$ twinning is expected to occur in the B grains, which translates into a decrease in the $\{10\bar{1}0\}$ axial peak intensity. Inversely, in tension, the A grains are favourably oriented for $\{10\bar{1}2\}$ twinning and a decrease in the (0002) axial peak intensity is expected. $\{10\bar{1}2\}$ twinning converts a B grain into an orientation very close to that of an A grain (about 4° off) so any increase in (0002) axial peak intensity is due to $\{10\bar{1}2\}$ twinning in the B grains. Since the intensity of the (0002) axial peak is much smaller than that of the $\{10\bar{1}0\}$ axial peak because of the texture, it is likely to be a much more sensitive indicator of $\{10\bar{1}2\}$ twinning in B grains. In Table 5.7, the $\{10\bar{1}2\}$ twin system with the highest resolved shear stress is identified for the applied stress at which an appreciable change in intensity is observed for tension and compression. The resolved shear stress and the stress normal to the twin plane are also given.

Table 5.7: Stress states in grains at the applied stress at which an appreciable change in intensity (ΔI) of the (0002) axial peak is observed (twinning).

APPLIED STRESS STATE	ΔI	Applied stress	Shear stress	Normal stress	Twinned grains
Tension, no prestrain	↓	125 → 150	73 → 73	61 → 42	A
Compression, no prestrain	↑	-115 → -130	62 → 64	-46 → -58	B
Compression after tension	↑	-115 → -130	64 → 66	-71 → -66	B
3rd cycle of cyclic tension	↓	175 → 200	63 → 65	69 → 65	A
4th cycle of cyclic tension	↓	200 → 230	61 → 74	62 → 81	A
2nd cycle of cyclic compression	↑	-130 → -150	52 → 54	-62 → -81	B

Table 5.7 shows that in general, twinning occurs when the shear stress on the twinning plane is between 65 and 75 MPa. This is not a significant variation given the error in the stress determinations (approximately ±10 MPa), and suggests that a CRSS criterion is reasonable for $\{10\bar{1}2\}$ twinning. This is all the more convincing as the CRSS does not seem to depend at all on the sign of the normal stress, which varies from -70 to +70 MPa. Note that the CRSS may be somewhat lower after twinning has already occurred (line 6 of Table 5.7). In the following, it is thus considered that $\{10\bar{1}2\}$ twinning occurs when the RSS reaches 70 MPa.

It is also possible to estimate the shear stress when the grains 'untwin' upon changing the loading direction. The principle is the same as for twinning, except that the changes in intensity are reversed. The results of such an analysis are shown in Table 5.8.

Table 5.8: Stress states in grains at the applied stress at which an appreciable change in intensity (ΔI) of the (0002) axial peak is observed (untwinning).

APPLIED STRESS STATE	ΔI	Applied stress	Shear stress	Twinned grains
Unloading from compression (compression-first Bausch.)	↓	-50 → -25	28 → 12	B
Unloading from first cycle of cyclic compression.	↓	-50 → -25	16 → 0	B
Unloading from second cycle of cyclic compression	↓	-100 → -75	30 → 21	B
Unloading from third cycle of cyclic tension	↑	150 → 100	47 → 24	A
Unloading from fourth cycle of cyclic tension	↑	125 → 75	28 → 9	A

The scatter in the shear stress for untwinning is much greater than for twinning and it is not likely that a well-defined CRSS exists for this situation. However, the results do show clearly that untwinning likely occurs before the sign of the resolved shear stress changes during unloading.

If a CRSS for {10$\bar{1}$2} twinning is assumed for pure magnesium, then the resolved shear stress for the most favourably oriented grains (Schmid factor = 0.5) corresponding to the stress plateau in compression can be considered an upper limit. In the present case the stress plateau occurs at about 50 MPa so an upper limit for the CRSS would be 25 MPa. A better estimate can be obtained from the room temperature tensile stress strain curves of Mote & Dorn, 1960 for the asymmetric bicrystal in Figure 2.17(c). Their stress-strain curve is shown in Figure 5.12. One of the grains is oriented for basal slip and the other for {10$\bar{1}$2} twinning. Since {10$\bar{1}$2} twinning is the only system which can produce strain parallel to the stress axis, it must be activated very early in the deformation. If it is assumed that it is activated by a true plastic strain of 2% (it probably occurs earlier, but this choice should yield a relatively conservative estimate), then the CRSS would be approximately 0.5*400psi = 1.4 MPa! This is an extremely low value which is consistent with the observation that the compression curve for the pure magnesium departs from linear behaviour at an extremely low applied stress.

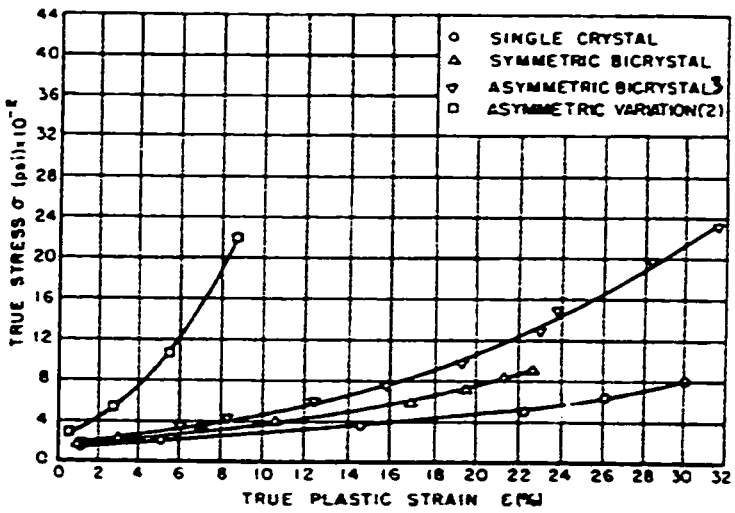

Figure 5.12: Stress-strain curves for Mg bicrystals tested at room temperature (Mote and Dorn, 1960).

It may seem odd that the presence of second phase particles can increase the CRSS of a deformation mechanism. However, as discussed in the literature review, twins first nucleate then grow. Smaller grains inhibit twinning by limiting the size of the twin, thereby increasing the surface to volume ratio and consequently the shear stress for nucleation (Equation 2.6). The precipitates in the alloy are not sheared by twins, so their presence has the same effect on the CRSS for twinning as a decrease in grain size.

5.2.7 The 'anomalous' intensity variations in cyclic tension

Most of the intensity variations observed in the neutron diffraction experiments can be easily rationalised in terms of {10$\bar{1}$2} twinning which appears to be the only bulk deformation mechanism capable of producing plastic strain parallel to the c-axis. However, the intensity variations obtained for the {10$\bar{1}$0} axial peak (i.e. B grains) in cyclic tension cannot be explained in this way (Figure 4.11, page 71). In the second, third, and fourth cycles, the intensity of this peak decreases during loading, and increases again during unloading, which means that these grains are twinning during loading and untwinning during unloading. If these grains were to twin on {10$\bar{1}$2} during loading, they would contract parallel to the tensile axis. Thus another mechanism must exist to account for these observations.

The most likely mechanism is {10$\bar{1}$1} twinning, which has been observed in pure magnesium samples deformed under highly constrained conditions (e.g. channel die compression, see section 2.4.1.3). Unfortunately, TEM analysis in the present study did not reveal the presence of such twins. This may be because the twinned volume in the unloaded condition is extremely small, making it difficult to observe. That this is so can be confirmed by comparing the overall increase in the B grain intensity with the overall decrease in A grain intensity at the end of the test. All {10$\bar{1}$2} twinning in A grains (or rather in grains very close to the A orientation) must cause an increase in B grain intensity. Equation 5.7 can be used to correlate the changes in intensity of the two orientations as shown in the table below.

Table 5.9: Analysis showing that the change in intensity of the A and B grains can be correlated for cyclic tension.

Peak	Change in intensity (ΔI_{hkil})	$\Delta T_{hkil} \propto \Delta I_{hkil} / P_{hkil}$
{10$\bar{1}$0}	+15	+673
(0002)	-18	-684

Since the magnitude of ΔT_{hkil} (proportional to the volume of twinned material) is essentially the same for the two orientations, it is clear that {10$\bar{1}$2} twinning can account for essentially all of the increase in {10$\bar{1}$0} axial peak intensity at the end of the test, and therefore that the amount of {10$\bar{1}$1} twinning left in the unloaded condition is very small. This analysis is consistent with the lack of twinning observed in B grains by optical microscopy. During loading, enough {10$\bar{1}$1} twinning occurs in each cycle (from the second on) to bring $I_{\{10\bar{1}0\}}$ close to its value at the start of the test. This decrease is of the order of 10% for the third cycle and increases as the maximum load applied is increased.

$I_{\{10\bar{1}0\}}$ increases immediately upon unloading from the maximum load for the third and fourth cycles. {10$\bar{1}$1} twinning therefore appears to behave more or less elastically, in the sense that it is reversed immediately upon reducing the applied load. Another observation which points to elastic behaviour is the remarkable linearity of the applied stress-lattice strain curve for the {10$\bar{1}$0} peak. This is in contrast to the

(0002) curve which is influenced by the occurrence of $\{10\bar{1}2\}$ twinning.

Reversible $\{10\bar{1}1\}$ twinning and untwinning could be at the root of the hysteresis observed upon unloading and reloading in tension. Upon loading the twinning process contributes to the tensile deformation, and on loading, untwinning 'takes back' some of the strain it contributed.

5.2.8 General considerations on yielding

The deformation mechanisms which can contribute to the strain tensor in a given grain have been identified, and the applicability of a CRSS criterion for the various deformation modes discussed. It is instructive now to consider how grain orientation affects which deformation mechanisms can occur, and to derive the uniaxial stress at which each can be activated, assuming no grain interaction. The equations and concepts described in section 5.2.4 are used again here, but every possible grain orientation with respect to the stress axis is considered rather than just the three studied by neutron diffraction.

The variation in Schmid factor (S) for slip and twinning (uniaxial stress) is shown in Figure 5.13. Grain orientation is characterised by the tilt angle (χ) between the stress axis and the basal pole (c-axis) of the hexagonal unit cell. For each deformation mechanism, a range of S values is shown which accounts for the multiplicity of systems for each mechanism, and for the fact that each χ corresponds to an infinite number of grain orientations obtained by rotating the unit cell about the c-axis.

Figure 5.13(a) shows that S is very low for basal slip when χ is very large or very small, and that prism and pyramidal slip are favoured for large χ, but become progressively more difficult as χ decreases. For twinning (Figure 5.13(b)) the sign of S is significant. A positive value indicates that twinning can occur in tension, while a negative value means that it is possible in compression. It is interesting to note that the range of S can be very large. For $\{10\bar{1}1\}$ twinning in particular, the maximum (absolute) value of S lies between 0.2 and 0.4 in both tension and compression for $40° \leq \chi \leq 55°$, raising the possibility that this mechanism can occur in this subset of grains regardless of the sense of straining. This is less likely for $\{10\bar{1}2\}$ twinning where S is generally very small in one sense when it becomes significant in the other.

To determine how yielding spreads to different components of the texture, it is useful to calculate the applied uniaxial stress at which each mechanism is activated as a function of χ, as well as the corresponding volume fraction of grains which yield. Thus the texture must be quantified in terms of χ. This can be done by measuring the variation in intensity of basal plane neutron scattering as the sample is rotated about a direction normal to the extrusion direction (Figure 5.14). $\chi = 0$ when the scattering vector is parallel to the extrusion axis. The intensity measured for a given χ, I_χ, is proportional to the volume of material which contributes to the signal. However, a correction must be made because the fraction of grains at a given tilt which actually contribute to the measured intensity depends on χ.

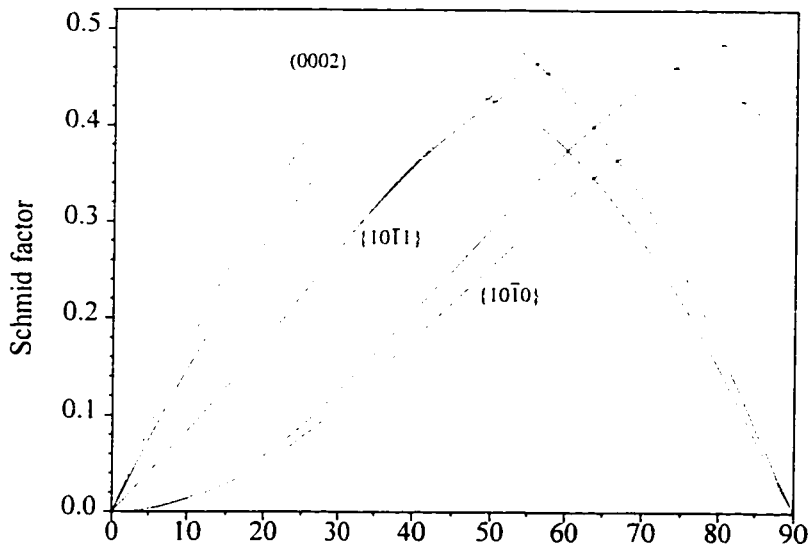

(a)

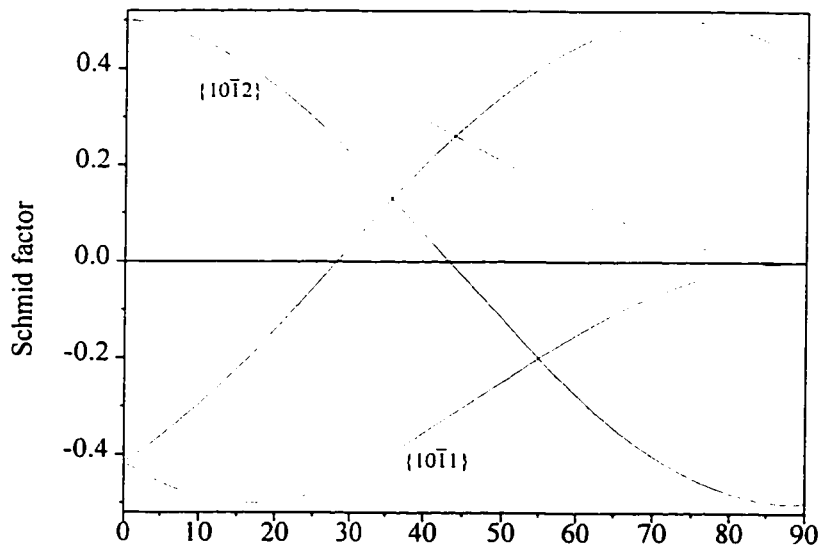

(b)

Figure 5.13: Schmid factors for the various (a) slip and (b) twinning modes expected to occur in magnesium.

This can be shown using Figure 5.15. All of the basal planes corresponding to a given tilt can be represented by a cone with the extrusion direction as axis. Two such cones, labelled A and B, are shown in the figure. Consider cone A. The sample is modelled as a point at the centre of a hemisphere of radius equal to the distance between the sample and the neutron detector (D). Note that D is fixed by the experimental apparatus. If the normals to the surface of the cone are drawn, then a new cone (A') is generated which describes all possible scattering vector directions for this tilt. D is fixed, so the locus of all such directions is the circle formed by the intersection between cone A' and the hemisphere, henceforth referred to as the locus circle for tilt A. Moreover, since the detector is of finite size, it only samples a part of this locus, δa in the figure. The fraction of grains sampled is therefore δa divided by the circumference of the locus circle for tilt A. The same geometric construction for cone B shows that the locus circle for tilt B is larger than that for tilt A. However, since the detector size is fixed, $\delta b = \delta a$, and the fraction of grains sampled for tilt B is thus smaller than for tilt A. The fraction of grains sampled for a given tilt is inversely proportional to the radius of the corresponding locus circle, which is itself proportional to $\sin\chi$. Note that when $\chi = 0°$, the locus circle reduces to a point and therefore all of the grains at this tilt are sampled. The reasoning behind the correction to be made to I_χ is then as follows:

Let I_χ = measured basal intensity at tilt χ,
V_χ = volume of grains at tilt χ,
f_χ = fraction of grains at tilt χ actually sampled ($\propto 1/\sin\chi$).

Then,

$$I_\chi \propto V_\chi f_\chi \qquad \therefore \qquad I_\chi \propto V_\chi / \sin\chi$$

$$\therefore \; V_\chi \propto I_\chi \sin\chi. \tag{5.9}$$

If I_χ is measured for several χ, then Equation 5.9 can be used to calculate the volume fraction of material corresponding to each tilt using Equation 5.10. Equation 5.9 implies that V_χ is always zero for χ=0°, which is clearly not possible. This reveals the limitation of this correction: the detector is considered a point, rather than a rectangle of finite height and width. As a result, a better correction would be to take this finite size into account. However, this is rather more complicated, and as discussed below, is not expected to significantly affect the results of the analysis.

$$V_\chi^f = \frac{I_\chi \sin\chi}{\sum_{\text{all}\,\chi} I_\chi \sin\chi} \tag{5.10}$$

I_χ was measured for tilts ranging from 0° to 90° in increments of 5° for several undeformed alloy samples. Application of Equation 5.10 then yields the results in the histogram of Figure 5.16. The bars correspond to average values, while symbols are used for the different samples used. Each calculated volume fraction corresponds to a 5° range of χ as shown in the figure. Thus the volume fraction corresponding to a given range of tilts $d\chi$ in a given 5° interval is obtained by multiplying the value for that interval by $d\chi/5°$.

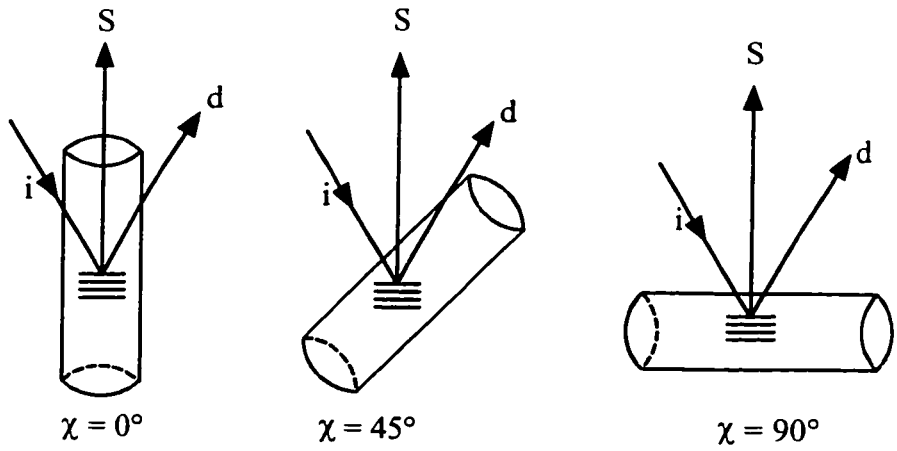

Figure 5.14: Figure illustrating how the orientation of the extrusion direction varies with respect to the scattering vector.
- **cylinder axis = extrusion direction.**
- **i,d,S = incident beam, diffracted beam, and scattering vector, respectively.**

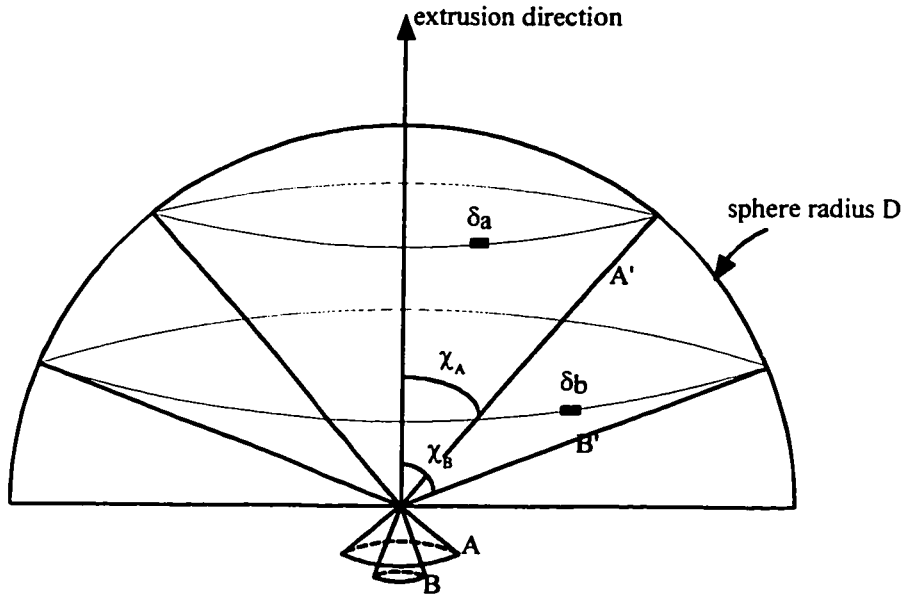

Figure 5.15: Figure used to explain how the fraction of grains corresponding to a given tilt depends on the tilt angle χ.

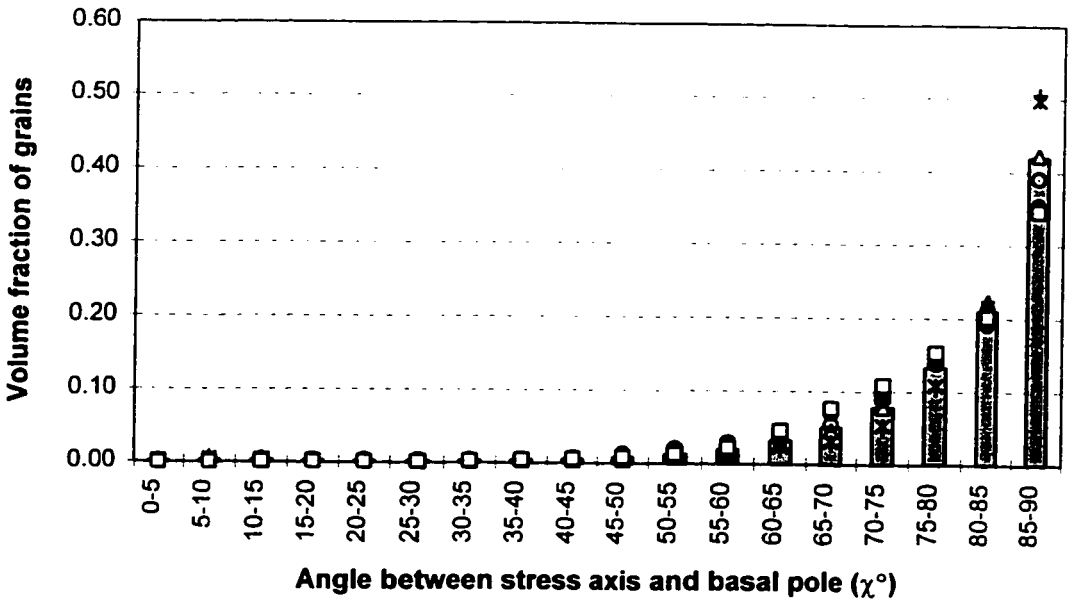

Figure 5.16: Graph showing the volume fraction of grains as a function of tilt angle χ.

Figure 5.16 shows that, as expected, most grains are oriented with the basal pole at a large angle from the extrusion axis, though the sharpness of the texture can vary considerably between samples. The volume fraction of grains with $0° \leq \chi \leq 50°$ is only about 4%. Thus, though the correction penalises the lower angles, making this part of the texture appear weaker than it really is, it is likely that this will not have a very important effect on the final distribution.

Having quantified the texture in terms of χ, and knowing how the Schmid factor varies with χ for each possible deformation mechanism, the volume fraction of grains which have yielded as a function of the applied stress can now be determined. Such a calculation neglects any grain to grain interaction, and is thus only applicable to small strains at which there is little or no plastic deformation. The results of these calculations are shown in Figure 5.17. {10$\bar{1}$1} twinning is not included in the figure because no estimate of the CRSS is available. Note that the curves in Figure 5.17 correspond to the most favourably oriented systems for each mechanism. The following reasoning applies to pure polycrystalline magnesium.

Though a large fraction of the grains are unfavourably oriented for basal slip, it could occur in about 60% of the material for a stress of about 10 MPa, and in 90% of it when the stress reaches only 25 MPa. Thus it is not surprising that the stress-strain curve shows essentially no linear elastic behaviour. This observation holds for both tension and compression, since slip is not polar. Non-basal slip, though much harder to activate than basal slip, can occur in a significant portion of the microstructure for applied stresses of the order of 80 MPa. However, such slip is not found extensively in deformed magnesium with a similar texture to that studied here. Rather it is restricted to near-grain boundary regions. This is likely a result of the fact that extensive basal slip occurs in the majority of grains before non-basal slip can become

active. The resulting long-range stress field due to basal dislocation pile-ups at grain boundaries makes further basal slip more difficult, but may also inhibit prism and pyramidal slip because the Burgers vectors are the same as for basal slip. {10$\bar{1}$2} twinning can occur in tension for a significant portion of the microstructure at fairly low applied stress. However, the contribution such twinning can make to the strain is very limited in tension in most of the grains. In addition, the boundaries associated with twin formation constitute further obstacles to slip and would increase the rate of strain hardening.

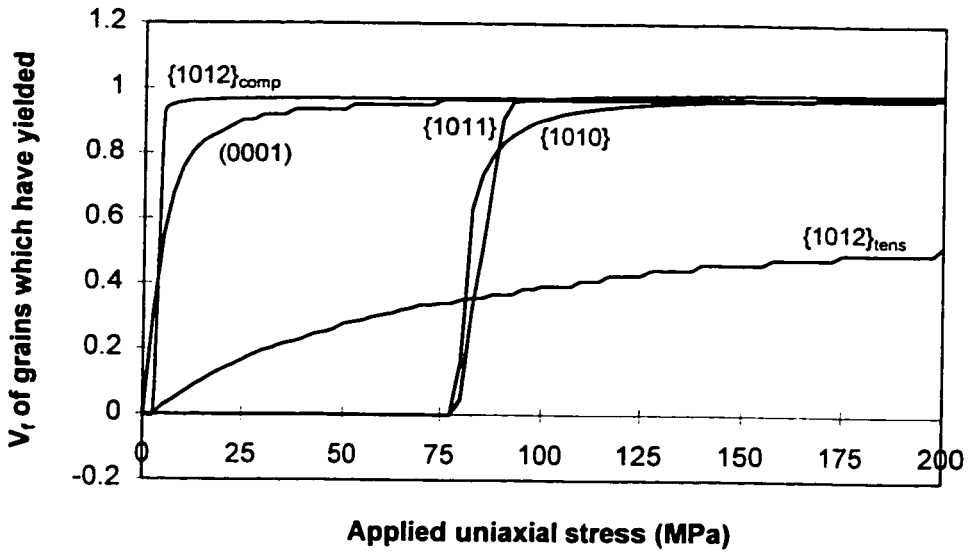

Figure 5.17: Graph showing how the volume fraction of material which yields by the various deformation mechanisms varies with the applied stress. (0001), {1011} and {1010} refer to the slip systems, whereas {1012} refers to the twinning system. Two curves are shown for twinning, one for compression, and the other for tension.

In compression, in the absence of grain interactions, {10$\bar{1}$2} twinning can potentially occur in most of the grains at stresses as low as 10 MPa. The ease with which twinning can start in most grains likely explains the difference in behaviour between yielding in tension and in compression (Figure 4.6): at an applied stress as low as 20MPa, the plastic strain in compression is measurably larger than that in tension.

This analysis is crudely semi-quantitative at best. It does, however, serve to show that basal slip occurs very easily in most of the microstructure, despite the relatively unfavourable texture. As a result, it can be asserted that the portion of the stress-strain curve prior to generalised yielding in tension (i.e. for plastic strains below about 0.2%, at stresses below about 100MPa) is not simply an extended elastic-plastic transition during which basal slip is activated in progressively less favourably oriented grains. Rather basal slip occurs in a large fraction of the material at a very low applied stress and the high value of $d\sigma/d\varepsilon$ is

probably due in large part to long range stresses produced by dislocation pile-ups at grain boundaries. There are also contributions to $d\sigma/d\varepsilon$ from grains which yield only at higher stresses, as well as additional strain hardening due to the formation of twin boundaries. In compression, dislocation pile-ups seem to play a smaller role than in tension because of the ease with which twinning can start in most of the grains.

These notions are important to understand the influence of second phase particles on the stress strain behaviour of the alloy.

5.2.9 Strengthening mechanisms in the alloy: role of the second phase particles

The alloy is significantly stronger than the polycrystalline magnesium in both tension and compression. The stress at generalised yield (i.e. 0.2% plastic strain) is higher in both cases. In addition, the slope of the stress strain curve after yielding is higher for the alloy in compression, though this is not the case in tension. Various potential strengthening mechanisms must be considered in order to explain these differences between the two materials.

5.2.9.1 Behaviour prior to generalised yielding

Solid solution strengthening can contribute to the yield strength of the alloy by raising the CRSS for slip. Given the solid solubility of Al in Mg at room temperature (about 0.5at%) and the small difference in atomic diameter between Al and Mg (about 3%), it is unlikely that this mechanism contributes significantly to the strength of the alloy.

Orowan hardening can also contribute to the alloy yield stress. In this case hardening arises because a dislocation must curve around the precipitates before it can bypass them. The closer the particles, the smaller the radius of curvature of the dislocation, and therefore the higher the shear stress required. In the present case, the distance to consider is that between particles in the basal plane since basal slip is by far the most important slip mode. This distance is of the order of 1 μm for this system. The maximum possible increase in the yield stress determined from Equation 5.11 with μ = 16.4 GPa, b=3.2Å and l=1μm, is 5 MPa.

$$\tau(\text{Orowan}) = \mu\, b / l \qquad (5.11)$$

μ = shear modulus
b = Burgers vector
l = interparticle spacing

To determine whether the Orowan mechanism can account for the increase in yield strength of the alloy with respect to pure magnesium, it is first necessary to determine how best to define this value. The 0.2% offset stress which is usually used does not seem suited to the present case. In both materials, this stress is much higher than the stress at which substantial slip has already occurred, as demonstrated by the departure from linear behaviour at very low applied stress (see also the previous section on yielding). Thus this stress is not a good measure of the stress at which dislocations bypass the precipitates.

It would seem best to consider the stress at the smallest offset possible given the sensitivity of the extensometer used. The minimum measurable strain is about $8x10^{-5}$ (i.e. 1μm in 13.5 mm). An offset of 10^{-4} can easily be measured on the stress-strain curve and yields stress values of 100 MPa and 40 MPa for the alloy and the magnesium, respectively. Thus the Orowan mechanism can contribute at most about 12% of the observed increase in yield stress.

The above two mechanisms do not seem capable of accounting for the different stress-strain behaviour of the two materials. It is thus necessary to consider continuum effects due to constraints imposed by the particles. During deformation, the elastic and plastic incompatibilities between the precipitates and the magnesium matrix result in a mean stress in the matrix which opposes the applied stress, thus contributing to hardening by opposing bulk slip and twinning. Brown and Clarke, 1960 calculate this mean back stress in a two-phase material for a number of particle geometries using Eshelby's equivalent inclusion method. They show that, provided there is no plastic relaxation around the particles, the contribution of the mean back stress to the slope of the stress-strain curve is given by Equation 5.12 for ribbons, discs, and fibres parallel to the stress axis. In this equation, E_{ppt} and V_{ppt} are the Young's modulus and volume fraction of the second phase.

$$(d\sigma/d\varepsilon)_{ppt} = E_{ppt}\, V_{ppt} \qquad \textbf{(5.12)}$$

In the present case, the precipitates can be considered as discs which have been elongated in one direction. Moreover, since most grains have the basal plane at a small angle from the stress axis, and the habit plane of the precipitates is the basal plane, they can be considered parallel to the stress axis. Thus Equation 5.12 can be used to calculate the contribution of the mean stress to the slope of the stress-strain curve. With E_{ppt} = 80 GPa, Equation 5.12 yields a back stress contribution of 8 - 9.6 GPa for volume fractions ranging from 10% to 12%. This range is in very good agreement with the constant difference in the slopes of the alloy and magnesium stress-strain curves up to a true strain of about $40x10^{-4}$ (Figure 4.3).

Equation 5.12 implies that the particles sustain elastically the applied strain. The precipitate lattice strain for the second phase at a given applied stress (Figure 4.4) does compare favourably with the corresponding plastic strain measured from the alloy stress-strain curve in Figure 4.3. In Figure 4.6 it is clear that the stress-strain behaviour of the alloy is identical in tension and compression until generalised yielding, so the same mechanism must be operative prior to this.

5.2.9.2 Behaviour after yielding

The slope of the alloy stress-strain curve in compression beyond about 0.2% strain is higher than that for the Mg. In both cases (up to the strains tested in the present study) deformation proceeds by the propagation of $\{10\bar{1}2\}$ twinning through the gauge section. In the Mg $d\sigma/d\varepsilon$ is essentially zero, indicating that both intra- and inter-granular propagation are very easy. In the alloy, intra-granular propagation is

more difficult because twins must negotiate the precipitates by the mechanisms shown in Chapter Four and discussed in section 5.3. These mechanisms require that additional energy be expended compared with the Mg, resulting in an increase in the shear stress for propagation. The large precipitates which occur at grain boundaries limit the size of twins which can be transmitted from one grain to the next and may also make it more difficult for an existing twin in one grain to nucleate a twin in a neighbouring grain.

In tension, $d\sigma/d\varepsilon$ for the alloy falls rapidly to the same level as for the Mg beyond about 0.6% strain. The particles have thus ceased to contribute significantly to hardening, indicating that one or more relaxation processes are active. The most likely process is the activation of secondary slip induced by stress concentrations near particle-matrix boundaries. Non-basal slip has been observed by transmission electron microscopy near grain boundaries. In addition, cross-slip of basal dislocations may limit the extent of eventual pile-ups at precipitates.

5.3 Microscopic Observations

In this section the interactions between various deformation mechanisms and the second phase particles and grain boundaries revealed by optical and transmission electron microscopy (TEM) are discussed. The discussion is limited to describing the more interesting features and possible explanations.

5.3.1 Slip

Though **c**-type dislocations are present in the undeformed alloy, they do not appear to glide or to multiply during deformation and so do not contribute to the general strain tensor. They are probably generated during the early (high temperature) stage of the precipitation process and act to relieve any internal stresses normal to the basal plane.

a-type dislocations on $\{10\bar{1}1\}$ pyramidal planes are also present in the undeformed material, though in small numbers. This slip system is known to be active above about 275°C (Roberts, 1960) and therefore likely also relieves any stresses associated with precipitate formation. Unlike **c**-dislocations, the density of these dislocations increases with deformation. In addition, slip can occur on higher order pyramidal planes and $\{10\bar{1}0\}$ prism planes during straining. The literature on pure magnesium indicates that non-basal slip generally occurs only near grain boundaries. As discussed above, the homogeneous distribution of non-basal slip in the alloy is likely due to the stress concentration in the matrix near particles.

High dislocation densities occur near grain boundaries. The dislocations appear to be mainly **a**-type, but it is possible that some **c**-slip also occurs in these regions. Regardless, it is clear that this high density must contribute significantly to grain to grain compatibility.

5.3.2 Twinning

Optical microscopy shows clearly that twins can be quite wide in the Mg, and can be transmitted from one grain to another very easily, as indicated by the very low rate of work hardening after generalised yielding in compression. In the alloy, though twins can traverse grains completely, their width is limited by the need to bypass precipitates in their path. In addition, transmission of twinning from one grain to another is more difficult than it is in the Mg. The large grain boundary precipitates are effective barriers, and transmitted twins must generally pass between them. Only {10$\bar{1}$2} twinning has been observed by TEM, despite the evidence from the neutron diffraction experiments which points to the existence of another twinning mechanism. These twins can bypass, engulf, or deviate around precipitates.

To see how a twin can bypass a precipitate, consider Figure 5.18. When a twin comes into contact with a precipitate, its advance is halted, but it can thicken perpendicular to the K_1 plane, and widen within the K_1 plane. If contact occurs near the tip of the precipitate, then relatively little growth enables it to be free of it. The twin wraps around the tip of the precipitate, thereby forming a twin-precipitate interface then moves on. In this case, the precipitate-twin intersection is small and the crystallographic orientation relationship between them is that obtained by taking the normal twin-matrix relationship and applying the twin transformation to the matrix lattice. The twin can continue to thicken and widen until the entire precipitate is engulfed.

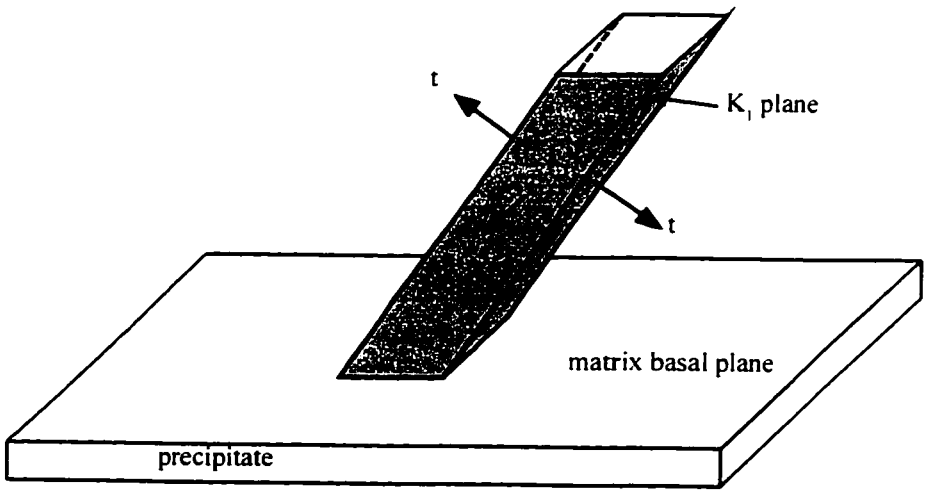

Figure 5.18: Schematic illustration of how a twin impinging on a precipitate can grow. Expansion can occur by thickening normal to the K_1 plane (direction t) or by widening parallel to the K_1 plane (direction w).

When contact occurs near the middle of the precipitate, the twin may have to widen appreciably before it reaches either extremity. The amount of widening required for this to occur depends on the size of the precipitate. If the precipitate is small, then the twin could eventually grow to wrap entirely around the precipitate, thereby engulfing it. If the precipitate is large, however, then it acts as a more formidable

obstacle to propagation. In this case a new twin may be nucleated on the other side of the precipitate. The accumulation of twinning on one side of the precipitate could exert a shear stress on the twin plane on the opposite side large enough to nucleate a new twin. This explanation is similar to that invoked to account for the transmission of slip across grain boundaries in a polycrystal.

Several variations on the above mechanisms can be envisaged. For example, it is possible for several parallel advancing twins to encounter a precipitate. In such a situation several new twins can be nucleated on the opposite side of the precipitate. All of these twins could then widen and merge to completely engulf the precipitate.

When a precipitate is completely engulfed, the twin-precipitate crystallographic orientation relationship is not that expected from applying the twin transformation to the matrix. Rather, the (011) precipitate plane initially parallel to the matrix basal plane becomes (exactly) parallel to one of the twin $\{10\bar{1}0\}$ planes. This is not very far from the expected relation given that $\{10\bar{1}2\}$ twinning results in an 86° reorientation of the lattice, and the $\{10\bar{1}0\}$ plane makes a 90° angle with the basal plane. Some accommodation mechanism must exist to account for this behaviour. It is known that continuous precipitates can form on the $\{10\bar{1}0\}$ matrix plane. This is much less frequently observed than the basal habit plane, but indicates that such an arrangement can yield relatively low interface energies. Thus it is possible that the total energy of the twin-precipitate system can be reduced by an accommodation mechanism which makes the above crystallographic relationship possible within the twin. Such a mechanism would depend on the availability of enough dislocations with a (or several) suitable Burgers vectors. As discussed in section 5.2, basal slip is certain to occur in most grains before $\{10\bar{1}2\}$ twinning even in unfavourably oriented grains. This is particularly so in the alloy because the CRSS for twinning is much higher than in pure magnesium, though this is not true for basal slip. Table 5.10 shows the effects of applying the $\{10\bar{1}2\}$ twinning transformation to the matrix a-directions.

Table 5.10: Transformation of a-directions by $\{10\bar{1}2\}$ twinning.

K_1 plane	Matrix a-direction		
	$[2\bar{1}\bar{1}0]$	$[\bar{1}2\bar{1}0]$	$[\bar{1}\bar{1}20]$
$(10\bar{1}2)$	$\overline{0.596}$ 1 $\overline{0.404}$ 1.5956	1 $\bar{2}$ 1 0	$\overline{0.404}$ 1 $\overline{0.596}$ $\overline{1.596}$
$(\bar{1}012)$	$\overline{0.596}$ 1 $\overline{0.404}$ 1.5956	1 $\bar{2}$ 1 0	$\overline{0.404}$ 1 $\overline{0.596}$ 1.596
$(01\bar{1}2)$	$\bar{2}$ 1 1 0	1 $\overline{0.596}$ $\overline{0.404}$ 1.596	1 $\overline{0.404}$ $\overline{0.596}$ $\overline{1.596}$
$(0\bar{1}12)$	$\bar{2}$ 1 1 0	1 $\overline{0.596}$ $\overline{0.404}$ $\overline{1.596}$	1 $\overline{0.404}$ $\overline{0.596}$ 1.596
$(1\bar{1}02)$	$\overline{0.865}$ $\overline{0.801}$ 1.667 0.532	$\overline{0.404}$ $\overline{0.596}$ 1 $\overline{1.596}$	1 1 $\bar{2}$ 0
$(\bar{1}102)$	$\overline{0.865}$ $\overline{0.801}$ 1.667 $\overline{0.532}$	$\overline{0.404}$ $\overline{0.596}$ 1 1.596	1 1 $\bar{2}$ 0

The new indices in the twin correspond to the direction in the twin which is parallel to the corresponding **a**-direction in the matrix. For each system, two out of three **a**-directions are converted to irrational directions in the twin. This is the reason behind the stacking faults observed within twins. The high density of debris produced by the twinning transformation may also be at the root of the twin-precipitate accommodation mechanism.

The habit plane of $\{10\bar{1}2\}$ twins can deviate considerably from the K_1 plane, enabling them to avoid contact with precipitates altogether. This appears to occur mainly when the precipitates are relatively small. The habit plane of the twin described in section 4.8 (page 122) which exhibits this behaviour is close to the basal plane, about 40° away from the twin's K_1 plane. Such deviation is accompanied by a band of very high dislocation density containing both **a**- and **c**-type dislocations. The lines for both types of dislocation are parallel to the trace of the basal plane and have similar spacing normal to the basal plane. Two scenarios are therefore possible. First, there may be a single family of **c+a** dislocations. In this case they are most likely sessile since the dislocation lines lie in the basal plane but the Burgers vector lies in a prism plane, which is not a glide plane. Second, there may be separate families of **a**- and **c**-dislocations. In this case the **a**-dislocations are glissile while the **c**-dislocations are sessile. In either case it is likely that further twin growth will be difficult.

Partridge & Roberts, 1964 have studied the formation and behaviour of incoherent twin boundaries in hexagonal metals using micro-hardness indentation within previously formed twins. They find that local stresses produced by the indenter can cause extremely incoherent twin boundary regions which are either accommodated within the twins themselves or within the surrounding matrix. The effect of an indentation is similar to that of a second phase particle: both increase the stress triaxiality in nearby regions, though the effect of the indenter is likely much stronger.

It is clear that twin-particle interactions are very complex. Further TEM is required to determine the exact nature of the accommodation bands adjacent to twins whose habit plane departs appreciably from the K_1 plane.

5.4 Mechanical Properties of the Intermetallic Phase

The elastic constants and thermal expansion coefficient for the intermetallic have been determined as described in section 4.9. In addition to this, Vickers indentations using a range of loads have been used to measure the hardness as well as to investigate the deformation and fracture behaviour. It is interesting to consider how these measurements can be used to more fully characterise the mechanical behaviour of this material, and to rationalise the behaviour of the second phase particles in the alloy during deformation.

Material properties of solids have values which lie within broadly defined ranges, depending on the structure and type of bonding. Ashby demonstrates that correlations exist between the values of

mechanical, thermal, electrical and other properties which derive from the underlying physics of the material. He expresses these correlations as dimensionless groups (DG) which, for a given class of materials, tend to have much narrower value ranges than do the individual properties themselves. He suggests that these correlations can be used to detect errors in the values of material properties which are provided as inputs for calculations, and to allow intelligent estimates to be made for missing values. These concepts are used in the present section to rationalise the properties measured for the intermetallic and to estimate other values not available in the literature.

Table 5.11 contains the property values which are known for the intermetallic. Table 5.12 contains the high and low values for metals, ceramics, and glasses for various DGs suggested by Ashby, in addition to the corresponding values for the intermetallic. Note that the ranges given are not absolute. They define the range within which it is very probable (>95% confidence) that the value of the DG will lie. The hardness (H) used to calculate the values of the last DG in Table 5.12 is expressed in MPa and is related to the Vickers number, H_v by $H = 10H_v$.

The values of the first and fourth DGs for the intermetallic fall in the ranges defined for ceramics rather than for metals, though in both DGs they are close to the high values for metals. The values fall well outside of the ranges defined for glasses, which is one indication that Ashby's technique does suggest a reasonable classification. Thus it is probable that the values of the other DGs for the intermetallic also fall within the ranges defined for ceramics.

If the sixth DG in Table 5.12 is used to estimate the yield stress of the intermetallic, it is found to lie between 1.2 and 2.3 GPa. Using this value for σ_y, the fifth DG is equal to 13×10^{-3} (using E = 78 GPa), which again lies inside the range for ceramics, and well outside the ranges for both metals and glasses. Note that this derived value of the yield stress is much larger than the maximum stress attained in the second phase particles in the alloy during deformation, as determined from the in-situ neutron diffraction experiments. Thus it is not at all surprising that transmission electron microscopy never revealed dislocations within the second phase particles.

The seventh DG can be used to estimate the fracture toughness, K_{IC}, of the intermetallic. Using the values for E and Ω in Table 5.11, K_{IC} is found to lie between 0.15 and 1.5 MPa $m^{1/2}$. This is very low, indicating that the material must be very brittle. This is in fact true, as demonstrated by the fact that Vickers indentations using loads as low as 25g are sufficient to initiate cracks in the material. Another method is available to estimate the fracture toughness if it is assumed that the intermetallic behaves essentially like a ceramic. Lawn, 1993 suggests a relatively simple way to use Vickers indentations to evaluate toughness.

Table 5.11: Values for known mechanical properties of the intermetallic.

Hardness(H) (=10 × Vickers hardness number)	2750 MPa
Young's modulus (E)	69 GPa < E < 87 GPa (average (E = 78 GPa)
Poisson's ratio (ν)	0.27 (dimensionless)
Thermal expansion coefficient (α)	28.4×10^{-6} K^{-1}
Melting point (T_m)	735 K
Average atomic volume(Ω)	2.04×10^{-29} m^3
Fracture toughness (K_{IC})	not measured (MPa $m^{1/2}$)
Yield strength (σ_y)	unknown (MPa)

Table 5.12: Value ranges of a few dimensionless property groups for metals, ceramics, and glasses. The values determined for the intermetallic are shown in the last column.

- **N_A (Avogadro's number) = 6.022×10^{23} mol^{-1}.**
- **R (gas constant) = 8.314 J mol^{-1} K^{-1}.**
- **In 1, E must be expressed in N/m^2.**
- **In 7, E is in MPa, and K_{IC} in MPa $m^{1/2}$.**

Dimensionless property group		Metals		Ceramics		Glasses		$Mg_{17}Al_{12}$
		Low	High	Low	High	Low	High	Average
1	$\frac{E.\Omega.N_A}{R.T_m}$	70	140	110	290	30	110	154
2	ν	0.2	0.42	0.19	0.35	0.17	0.24	0.27
3	K/E	0.42	2.1	0.5	1.1	0.5	0.65	
4	$\alpha.T_m$ ($\times 10^{-3}$)	12	20	18	32	0.9	15	21
5	σ_y/E ($\times 10^{-3}$)	0.2	8	10	40	25	100	****
6	H/σ_y	2.4	3.1	1.2	2.3	1.2	1.8	****
7	$\frac{K_{IC}\Omega^{-1/6}}{E}$	4	50	0.2	2	0.2	1	****

He finds that the fracture toughness evaluated using the following expression:

$$(E/H)^{1/2} \times P \times c_l^{-3/2} \qquad (5.13)$$

where: E = Young's modulus (MPa)
H = 10 x Vickers number (MPa)
P = indenter load in N
c_l = length of radial crack in μm (see Figure 5.19(a)).

can be correlated linearly with the fracture toughness measured by independent means for many different types of ceramics (Figure 5.19(b)). Thus it is only necessary to perform several indentations with loads high enough to produce cracks to obtain an average value of the parameter in Equation (5.13), then plot the parameter on the line in Figure 5.19(b) to obtain an estimate of K_{IC} for the material. If this is done for the intermetallic using the data shown in Table 5.13, it is found that K_{IC} lies between about 0.25 and 0.5 MPa $m^{1/2}$, in very good agreement with the predictions made using the DG technique proposed by Ashby.

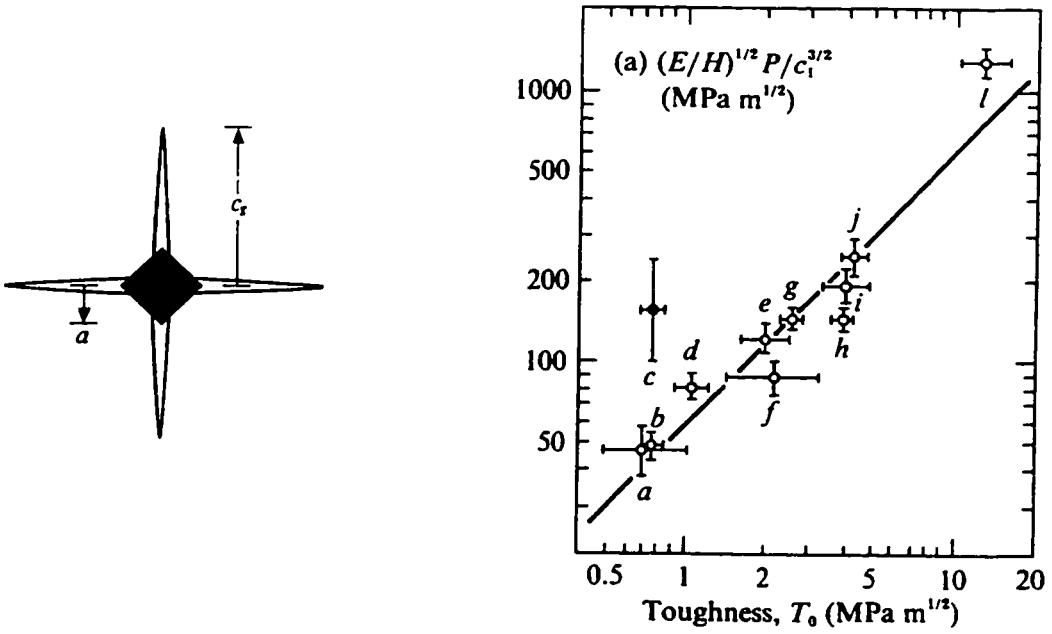

Figure 5.19: (a) Diagram showing how c_l is to be measured to evaluate the expression in Equation (5.13).
(b) Vickers indentation data illustrating that toughness evaluated using Equation (5.13) is linearly correlated with K_{IC} for ceramics. The letter associated with each data point corresponds to a given ceramic (Lawn, 1993).

Table 5.13: Measurements used to evaluate the expression in Equation. (5.13).

crystal face	Indenter load (P) g	Half crack length (c_l) μm	$(E/H)^{1/2}.P.c_l^{-3/2}$ MPa $m^{1/2}$
(100)	500	138	17
(100)	500	98	27
(100)	200	65	20
(100)	200	50	30
(100)	500	144	16
(100)	500	97	28
(100)	500	104	25
(110)	500	102	26
(110)	500	122	20
(110)	1000	219	17
(110)	2000	68	19
(110)	500	148	15
E/H = 78000 MPa / 2750 MPa = 28.4			

6. SUMMARY AND CONCLUSIONS

6.1 Summary

This study focuses mainly on the low strain behaviour of an extruded polycrystalline binary Mg-Al alloy heat-treated to obtain a coarse precipitate structure. Pure polycrystalline magnesium having nominally the same texture and grain size is used as a reference material. The experimental techniques used include uniaxial mechanical testing, in-situ neutron diffraction under load, transmission electron microscopy (TEM) and optical microscopy. In addition, the mechanical and physical properties of the second phase are obtained from a single crystal of the material using ultrasonic measurements of the elastic constants and Vickers indentations.

The mechanical behaviour of both the alloy and pure magnesium varies greatly with the sense of stressing (compression or tension). The yield stress is higher in the alloy than in pure magnesium in tension and compression. In addition, the slope of the stress-strain curve at higher strains is higher in the alloy than in magnesium in compression, though this is not so in tension.

In-situ neutron diffraction is used to follow the evolution of the elastic lattice strain with applied load in three components of the texture, having angles of 0°, 62° and 90° between the uniaxial stress axis and the basal pole, as well as in the second phase particles. The results show that the stress carried by the grains varies with grain orientation. Large and abrupt variations in scattered peak intensity are also observed during testing.

Transmission electron microscopy reveals the presence of **c**- and non-basal **a**-dislocations in undeformed samples of the alloy. Basal slip is by far the most common slip system during deformation. **c**-dislocation density does not change with strain, but non-basal **a**-slip within grains does. Only $\{10\bar{1}2\}$ twinning is observed in tension and in compression by TEM. Twins are observed to completely cross grains in the alloy, despite the presence of the precipitates. The twins can bypass, engulf, and deviate around particles.

Measurements on the intermetallic single crystal show that its elastic modulus is roughly twice that of magnesium, and that it is much harder (i.e. higher yield stress) and brittle than magnesium.

6.2 Conclusions

The shape of the stress-strain curves in tension and compression for both the alloy and pure magnesium is rationalised by considering the texture and the fact that basal slip and $\{10\bar{1}2\}$ twinning are the only commonly observed deformation mechanisms in pure magnesium.

The lattice strains measured by neutron diffraction are used, in conjunction with the single crystal elastic constants, to calculate the stress tensor in each component of the microstructure sampled, despite having at best three components of the elastic strain tensor. The average internal stress calculated by weighting the stresses for each component sampled by neutron diffraction by the texture compares very favourably with the applied stress. In general, the calculated stress is highest in grains unfavourably oriented for both basal slip and $\{10\bar{1}2\}$ twinning, lowest in grains oriented favourably for both, and in between for grains oriented favourably for $\{10\bar{1}2\}$ twinning only.

Most variations in scattered peak intensity can be explained by referring to the lattice reorientation produced by $\{10\bar{1}2\}$ twinning. The calculated stress tensors corresponding to these intensity variations are used to show that a critical resolved shear stress criterion is applicable for twinning in the magnesium alloy, and that the onset of twinning does not correlate at all with the stress normal to the K_1 plane. This is rationalised in terms of the ease with which basal slip is activated in magnesium, the essentially isotropic elasticity of magnesium, and the relatively high temperature of testing (about $T_m/3$).

Intensity variations which cannot be explained by $\{10\bar{1}2\}$ twinning occur in grains in cyclic tension, the only in-situ test in which the material is strained well beyond the elastic-plastic transition in tension. It is suggested that this is due to $\{10\bar{1}1\}$ twinning, which yields a contribution to the grain strain tensor consistent with the direction of straining. The reason such twinning is not generally observed is that it appears to be essentially elastic, in the sense that it disappears almost entirely upon removal of the applied stress. This mechanism can produce compression parallel to the c-axis, whereas $\{10\bar{1}2\}$ twinning can only produce tension in this direction.

A simple Schmid factor analysis is used, in conjunction with a quantitative knowledge of the texture, to show how the volume fraction of material which would yield by a given deformation mechanism varies with the applied uniaxial stress in pure magnesium, assuming no grain interaction. The analysis shows that pure magnesium yields first by basal slip in tension and compression, and that the early portion of the stress-strain curve should be considered a region of high strain hardening due to the accumulation of basal dislocation pile-ups at grain boundaries. In compression $\{10\bar{1}2\}$ twinning can also occur at very low applied stress.

The precipitates cause the tensile and compressive stress-strain curves to be identical in the alloy by raising the stress at which twinning starts in compression. The differences between the stress-strain curves of the alloy and pure magnesium below about 0.2% strain are explained using a simple Brown and Clarke mean-stress hardening model with no plastic relaxation. Beyond generalised yield, relaxation mechanisms, possibly cross-slip of basal dislocations and non-basal slip, reduce the mean stress contribution essentially to zero in tension. In compression, the precipitates act as obstacles to twins, thereby increasing the stress required to propagate twinning throughout the gauge section.

A simple model is proposed to explain how twins bypass precipitates, and the transformation of a-dislocations by the twinning shear is used to propose a mechanism to account for the crystallographic orientation relationship between a twin and an engulfed precipitate.

Finally, it is shown that the properties of the intermetallic can be rationalised by considering that its behaviour is similar to that of a ceramic. Property correlations are then used to calculate the fracture toughness and yield stress of the material.

6.3 Future Work

The mechanical behaviour of polycrystalline magnesium depends strongly on the texture. It would therefore be instructive to repeat some of the neutron diffraction experiments on a series of samples having different textures. In addition, much more extensive transmission electron microscopy is needed to understand the particle-twin interactions observed. The second twinning mode detected by neutron diffraction should also be investigated more carefully, and its elastic nature confirmed or rejected. A good way would be to perform SEM in-situ tensile tests using electron channelling patterns to monitor changes in lattice orientation during deformation.

7. BIBLIOGRAPHY

Abel, A., 1986, Mat. Forum, 10, pp. 11-26.

Allen, A.J., Hutchings, M.T., and Windsor, C.G., 1985, Adv. in Phys., 34, pp. 445-473.

Allen, A.J., Bourke, M.A.M., Dawes, S., Hutchings, M.T., and Withers, P.J., 1992, Acta Met., 40, pp. 2361-2373.

Atkinson, J.D., Brown, L.M., and Stobbs, W.M., 1974, Phil. Mag., 30, pp. 1247-1280.

Bacon, G.E. (1975): Neutron Diffraction, Oxford University Press, London.

Bate, P.S., and Wilson, D.V., 1986, Acta Met., 34, pp. 1097-1105.

Bauschinger, J., 1886, Mittheilungen aus dem Mechanisch-Technischen Laboratorium der K. Technischen Hochschule in Munchen, 13, p. 31.

Berghezan, A., Fourdeux, A., and Amelinckx, S., 1961, Acta Met., 9, pp. 464-490.

Brown, L.M., and Clarke, D.R., 1975, Acta Met., 23, pp. 821-830.

Burke, E.C., and Hibbard, W.R., Jr., 1952, Trans. AIME, 194, pp. 295-303.

Byrne, J.G., 1963, Acta Met., 13, pp. 1023-1027.

Cahn, R.W., 1954, Adv. in Phys., 3, pp. 363-445.

Chun, J.S., and Byrne, J.G., 1969, J. Mat. Sci., 4, pp. 861-872.

Chun, J.S., Byrne, J.G., and Bornemann, A., 1969, Phil. Mag., 20, pp. 291-299.

Clark, J.B., 1968, Acta Met., 16, pp. 141-152.

Clark, R., and Craig, G.B., 1952, Prog. Met. Phys., 3, pp. 115-139.

Couling, S.L., Pashak, J.F., and Sturkey, L., 1959, Trans. ASM, 51, pp. 94-107.

Duly, D., 1992, Etude de la precipitation discontinue dans les alliages Mg-Al, Institut National Polytechnique de Grenoble.

Frank, F.C., and Thompson, N., 1955, Acta Met., 3, pp. 30-33.

Groves, G.W., and Kelly, A., 1963, Phil. Mag., 3, pp. 877-887.

Hartt, W.H., and Reed-Hill, R.E., 1967, Trans. AIME, 239, pp. 1511-1517.

Hauser, F.E., Starr, C.D., Tietz, L., and Dorn, J.E., 1955, Trans. ASM, 47, pp. 102-103.

Heyn, E., 1918, Metall und Erz., 22, pp. 436-441 and 441-442.

Hirsch, P.B., and Lally, J.S., 1965, Phil. Mag., 12, pp. 595-648.

Hosford, W.F. (1993): The Mechanics of Crystals and Textured Polycrystals. 1st ed. Oxford University Press, New York.

Kelley, E.W., and Hosford, W.F., Jr., 1968a, Trans. AIME, 242, pp. 654-661.
1968b, Trans. AIME, 242, pp. 5-13.

Lawn, B. (1993): Fracture of Brittle Solids. 2nd ed. Cambridge University Press, London.

Lebensohn, R.A., and Tome, C.N., 1993, Philosophical Magazine A, 67, pp. 187-206.

MacEwen, S.R., Faber Jr., J., and Turner, A.P.L., 1983, Acta Met., 31, pp. 657-676.

MacEwen, S.R., Christodoulou, N., Tomé, C.N., Jackman, J., Holden, T.M., and Faber, J., Jr., 1988, Proceedings of the Eighth International Conference on the Texture of Materials,, p. 825.

Mahajan, S., and Williams, D.F., 1973, Int. Met. Rev., 18, p. 43.

Masing, G., 1922, Z. Tech. Phys., 3, p. 167.

Mote, J.D., and Dorn, J.E., 1960, Trans. AIME, 218, pp. 491-497.

Mroz, 1967, J. Mech. & Phys. Sol., 15, p. 163.

Mroz, Z., 1969, Acta Mech., 7, p. 199.

Murray, J.L., 1982, Bulletin of Alloy Phase Diagrams, 3, pp. 60-70.

Orowan, E., 1959, Internal Stresses and Fatigue in Metals,, Elsevier, .

Partridge, P.G., 1967, Met. Rev., 12, pp. 169-194.

Partridge, P.G., and Roberts, E., 1964, Acta Met., 12, pp. 1205-1210.

Poirier, J.P., and Le Hazif, R., 1976, J.Mic.Spec.Elec., 1, pp. 595-607.

Priestner, R., and Louat, N., 1963, Acta Met., 11, pp. 195-202.

Reed-Hill, R.E., 1960, Trans. AIME, 218, pp. 554-558.
1973, The Inhomogeneity of Plastic Deformation, Reed-Hill, R.E., American Society for Metals, pp. 285-311.

Reed-Hill, R.E., and Robertson, W.D., 1957a, Acta Met., 5, pp. 717-727.
1957b, Acta Met., 5, pp. 728-737.
1957c, Trans. AIME, 209, pp. 496-502.
1958, Trans. AIME, 212, pp. 256-259.

Reid, C.N. (1973): Deformation Geometry for Materials Scientists. 1st ed. Pergamon Press, Toronto. 211 pages. pp. 193-202.

Roberts, C.S. (1960): Magnesium and Its Alloys. first ed. John Wiley and Sons Inc., New York.

Schmid, E., and Boas, W. (1950): Plasticity of Crystals with Special Reference to Metals. 1st ed. Chapman and Hall, London.

Stohr, J.F., and Poirier, J.P., 1972, Phil. Mag., 25, pp. 1313-1329.

Wilson, D.V., 1965, Acta Met., 13, pp. 807-814.

Wilson, D.V., and Bate, P.S., 1986, Acta Met., 34, pp. 1107-1120.

Wonsiewicz, B.C., and Backofen, W.A., 1967, Trans. AIME, 239, pp. 1422-1431.

Woolley, R.L., 1954, J. Inst. Met., 83, pp. 57-58.

IMAGE EVALUATION TEST TARGET (QA-3)

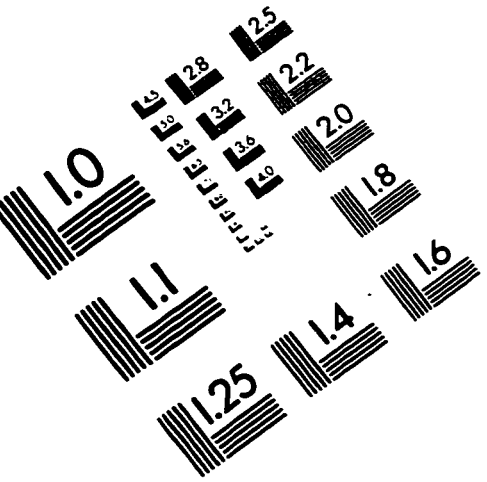

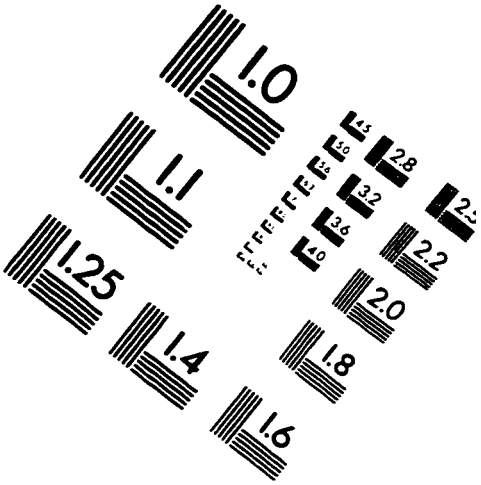

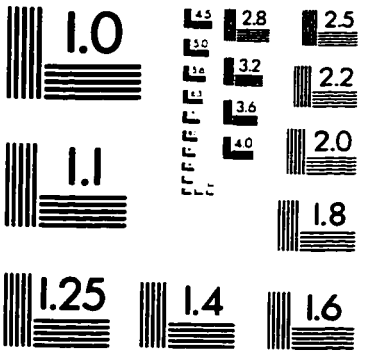

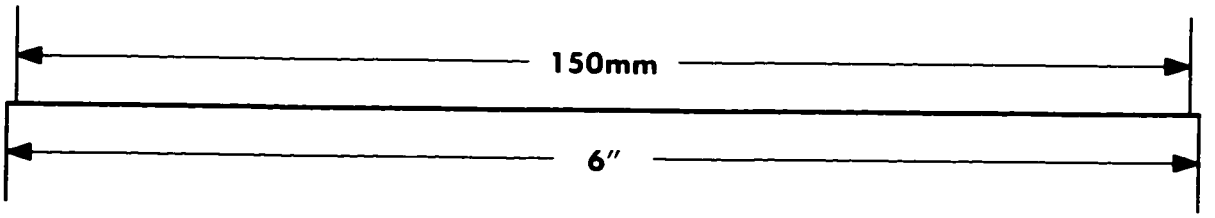

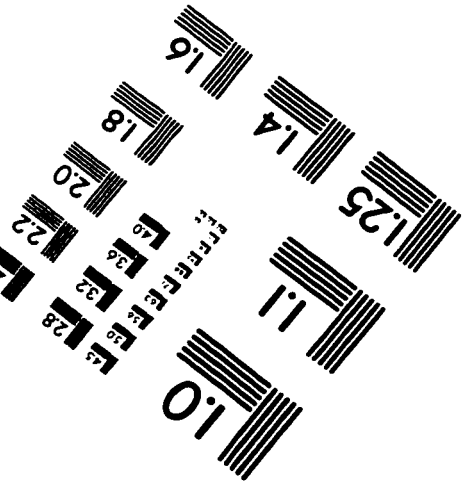

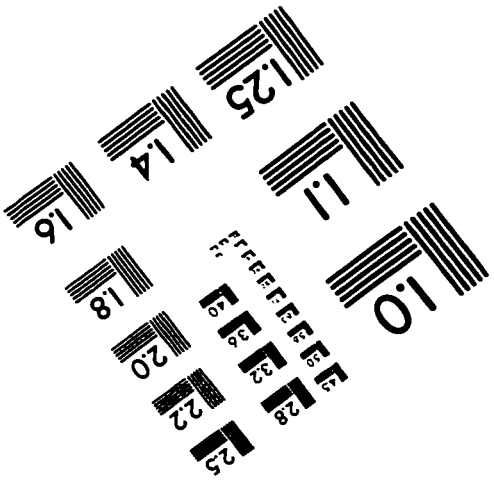

APPLIED IMAGE, Inc
1653 East Main Street
Rochester, NY 14609 USA
Phone: 716/482-0300
Fax: 716/288-5989